

Connecting ZnO to organic templates

Citation for published version (APA):

van Rijt, M. M. J. (2021). *Connecting ZnO to organic templates*. [Phd Thesis 1 (Research TU/e / Graduation TU/e), Chemical Engineering and Chemistry]. Technische Universiteit Eindhoven.

Document status and date:

Published: 08/06/2021

Document Version:

Publisher's PDF, also known as Version of Record (includes final page, issue and volume numbers)

Please check the document version of this publication:

- A submitted manuscript is the version of the article upon submission and before peer-review. There can be important differences between the submitted version and the official published version of record. People interested in the research are advised to contact the author for the final version of the publication, or visit the DOI to the publisher's website.
- The final author version and the galley proof are versions of the publication after peer review.
- The final published version features the final layout of the paper including the volume, issue and page numbers.

[Link to publication](#)

General rights

Copyright and moral rights for the publications made accessible in the public portal are retained by the authors and/or other copyright owners and it is a condition of accessing publications that users recognise and abide by the legal requirements associated with these rights.

- Users may download and print one copy of any publication from the public portal for the purpose of private study or research.
- You may not further distribute the material or use it for any profit-making activity or commercial gain
- You may freely distribute the URL identifying the publication in the public portal.

If the publication is distributed under the terms of Article 25fa of the Dutch Copyright Act, indicated by the "Taverne" license above, please follow below link for the End User Agreement:

www.tue.nl/taverne

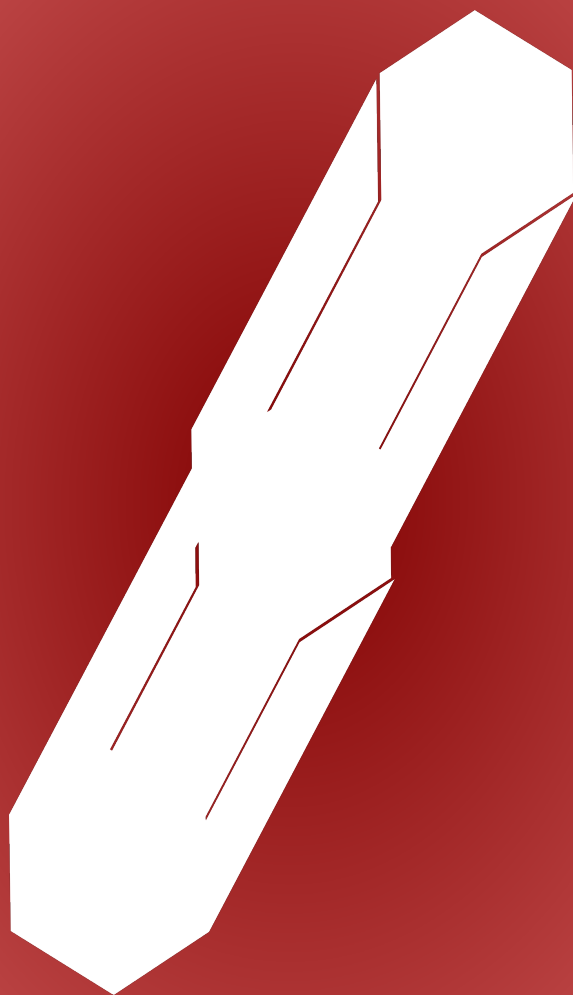
Take down policy

If you believe that this document breaches copyright please contact us at:

openaccess@tue.nl

providing details and we will investigate your claim.

Connecting ZnO to Organic Templates



Mark M. J. van Rijt

Connecting ZnO to Organic Templates

PROEFSCHRIFT

ter verkrijging van de graad van doctor aan de Technische Universiteit Eindhoven, op
gezag van de rector magnificus prof.dr.Ir F.P.T. Baaijens, voor een commissie
aangewezen door het College voor Promoties, in het openbaar te verdedigen op
Dinsdag 8 Juni 2021 om 16:00 uur

door

Marcus Maria Johannes van Rijt

geboren te Eindhoven

Dit proefschrift is goedgekeurd door de promotoren en de samenstelling van de promotiecommissie is als volgt:

Voorzitter:	prof.dr. K. Nijmeijer
Promotor:	prof.dr. G. de With
Copromotor:	dr. H. Friedrich
Leden:	prof.dr.ir. E.J.M. Hensen prof.dr. L. Estroff (Cornell University) prof.dr. J.D. Rimer (University of Houston) prof.dr. Th. Weber
Adviseur:	prof.dr. W. Noorduyn (AMOLF / Universiteit van Amsterdam)

Het onderzoek dat in dit proefschrift wordt beschreven is uitgevoerd in overeenstemming met de TU/e Gedragscode Wetenschapsbeoefening.

“ What a big book, captain, might be made with all that is known! ” And what a much bigger book still with all that is not known! ”

Jules Verne, *The Mysterious Island*, **1874**

Marcus Maria Johannes van Rijt

Connecting ZnO to Organic Templates

The research described in this thesis has been conducted at the Laboratory of Materials and Interface Chemistry (SMG), the Laboratory of Physical Chemistry (SPC) and the Eindhoven Center for Multiscale Electron Microscopy (CMEM), within the Department of Chemical Engineering and Chemistry of the Eindhoven University of Technology, the Netherlands.

This work was supported by the Dutch Research Council (NWO) as part of the TOP-PUNT Grant “Bi-Hy”, project number: 718.016.003.

A catalogue record is available from the Eindhoven University of Technology Library
ISBN: 978-90-386-5291-7

Copyright © by Mark M.J. van Rijt

Cover design by Mark M.J. van Rijt

Printed by ProefschriftMaken || www.proefschriftmaken.nl

Summary

In materials science there is a continuous strive to obtain materials with enhanced properties without introducing unwanted limitations. Inspiration for these materials can be found in nature, where the extraordinary control of biological processes results in excellent material properties, for example the impressive mechanical properties of bone, the surprising magnetic particles in magnetotactic bacteria and the beautiful iridescent colors of nacre shells. Many of these natural materials possess these properties due to a hybrid composition containing both organic and inorganic (mineral) phases. While nature has limited its choice to a few minerals, mainly silica, phosphates and carbonates, this is not the case for man-made materials. Therefore, by understanding and emulating the formation of natural materials with non-naturally incorporated minerals, a near endless range of new materials should be obtainable. An excellent candidate for this is the well-known metal oxide zinc oxide (ZnO). Its most common polymorph *wurtzite* ZnO has a wide range of relevant physical properties making it a material of interest for a multitude of technological applications including piezo-electrics, photocatalysis and solar cells. Mineralization of organic templates with ZnO should therefore allow for the expression and control over a wide range of material properties.

In this thesis we aim to combine ZnO with organic templates by developing the tools for ZnO formation under conditions that are generally compatible with organic templates using some very different approaches. The first approach, discussed in **Chapter 2**, investigates the viability of ion-exchange for the formation of ZnO mineralized collagen. As a starting mineral phase hydroxyapatite (HAp) is selected, a mineral which is able to mineralize collagen in bone. The first and crucial step in the ion-exchange process is the exchange of present calcium ions with zinc ions in order to form Zn-HAp. Using a rapid screening strategy shows that up to 20 mol% of calcium ions can be exchanged without loss in shape, size or measured crystallinity. Introducing more vigorous reaction conditions in the form of heating, sonication or extended reaction times does increase zinc incorporation but comes at the cost of byproduct formation. Control experiments show that the dissolution of the Zn-HAp crystals is directly related to the presence of zinc ions in the crystal which increases its solubility. Hence, the increased incorporation of zinc ions in Zn-HAp does not result in a more zinc-rich HAp, but in increased crystal dissolution and subsequent reprecipitation, preventing the formation of ZnO from HAp ion-exchange via a Zn-HAp intermediate.

The second part of this thesis aims to understand and control the formation mechanism of ZnO directing it towards mild “organic template friendly” reaction conditions. In **Chapter 3** a common ZnO synthesis strategy in water at mild pH using hexamethylene tetraamine (HMTA) as base release agent is discussed. Comparing the influence of the zinc salt, it is found that the counterion has a significant effect on the final product resulting in ZnO predominantly in dispersion, ZnO grown on solid reaction interfaces or layered zinc hydroxy salts (LZHS). The formation path that results in the formation of ZnO are subsequently investigated by discrete cryoTEM sampling and SEM sampling. This shows that for the formation of ZnO in dispersion, LZHS transient phases are initially predominantly formed. These LZHSs mature and grow over time in the presence of a minority ZnO phase until they rapidly and spontaneously collapse.

Especially the use of zinc acetate, with its layered basic zinc acetate (LBZA) transient phase, results in dispersed ZnO crystals, given that LBZA is rapidly formed initially and not too stable to prevent transition to a pure ZnO phase.

Using this knowledge, the formation of ZnO in dispersion was optimized by replacing the gradual HMTA hydrolysis by direct base titration as described in **Chapter 4**. Imitation of the HMTA-ZnO strategy by direct base titration shows that the hydrolysis of HMTA is in fact influenced by the formation of ZnO, preventing its exact reproduction. It is further found that the reaction results in the formation of ZnO between a pH > 5.5 up to at least 8.3 via a similar mechanism as described in chapter 3. With increasing amounts of ammonia in the system more faceted hexagonal ZnO crystals are observed, indicating that ammonia acts as a capping agent. The flexible addition of base further allows to increase the reaction yield of ZnO crystals from ~13 %, using the HMTA method, to as high as 74 %.

To improve the compatibility of the ZnO formation process with organic templates, the reaction temperature for a base titration strategy, inspired on the work in Chapter 4, was incrementally lowered as described in **Chapter 5** without introducing any post-annealing step. Depending on the concentration of zinc acetate in the reaction medium, ZnO could be formed at temperatures as low as 40 °C. Decreasing the reaction temperatures results in the formation of LBZA in the final product even with extended reaction times. This LBZA phase becomes more dominant with decreasing reaction temperatures. A more ZnO-rich reaction product could be obtained at 40 °C by introducing l-lysine (l-lys) as an additive at the start of the reaction. Moreover, in the presence of l-lys a prolonged reaction under aqueous RT conditions resulted in a more dominant ZnO phase.

The third part of this thesis focuses on the development of hierarchical organic templates and setting up the mineralization of organic templates with ZnO. To this effect, in **Chapter 6** we describe the formation of thermodynamically stable nanotubes assembled from a lysine-rich block copolypeptide (BCPP). By tuning the hydrophilic and hydrophobic domain lengths, combined with the ability of peptides to form secondary structures, high aspect ratio nanotubes can be formed that are stable between pH 2 and 12 and up to 80 °C. This stability permits their hierarchical assembly into bundled nanotube fibers by directing the pH and inducing complementary zwitterionic charge behavior, making it an excellent candidate template for mineralization.

Using collagen as a model system, the mineralization of organic templates with ZnO is investigated as discussed in **Chapter 7**. Collagen fibers are exposed to a zinc acetate and LBZA dispersion at collagen friendly reaction conditions, both in the presence and in absence of charged additives. Extended exposure of collagen to these dispersion shows no adverse effects on the collagen fibers. Although these screening experiments did not result in the mineralization of collagen with zinc species, the results indicate that with further optimization zinc (oxide) mineralized collagen should be obtainable by direct synthesis.

Samenvatting

In de materiaalkunde wordt continu gestreefd naar de vorming van materialen met geoptimaliseerde eigenschappen zonder hierbij ongewenste beperkingen te introduceren. Inspiratie voor deze materialen kan in de natuur worden gevonden, waarbij de buitengewone controle van biologische processen resulteert in uitstekende materiaaleigenschappen, zoals de indrukwekkende mechanische eigenschappen van bot, de verrassende magnetische deeltjes in magnetotactische bacteriën en de mooie iriserende kleuren van parelmoerschelpen. Veel van deze natuurlijke materialen bezitten deze eigenschappen dankzij hun hybride samenstelling van zowel organische als anorganische (mineralen) fases. Waar de natuur zichzelf beperkt tot enkele mineralen, voornamelijk silica, fosfaten en carbonaten, bestaat deze beperking niet voor synthetische materialen. Door deze natuurlijke mineralisatie processen te bestuderen en te begrijpen, en door vervolgens deze kennis te gebruiken om het mineralisatie proces te imiteren met niet in de natuur ingebouwde mineralen, kan er toegang verkregen worden tot een vrijwel oneindig bereik aan nieuwe materialen. Een uitstekend mineraal voor zo'n studie is het bekende metaaloxide zinkoxide (ZnO). De meest voorkomende ZnO-polymorf *wurtzite* bezit een scala aan relevante fysische eigenschappen waardoor het een interessant materiaal met een breed bereik aan technologische toepassingen waaronder piezo-elektriciteit, fotokatalyse en zonnecellen. De mineralisatie van organische templates met ZnO zou daarom kunnen resulteren in zowel het bereiken als het beheersen van een breed scala aan materiaaleigenschappen.

Het doel in dit proefschrift is het combineren van ZnO met organische templates door de vorming van ZnO mogelijk te maken onder omstandigheden die verenigbaar zijn met organische templates. Hierbij worden verschillende aanpakken onderzocht. In het eerste deel wordt de haalbaarheid van ionenuitwisseling onderzocht voor de vorming van met ZnO gemineraliseerde collageen. Dit wordt besproken in **Hoofdstuk 2**. Aangezien hydroxyapatiet (HAp) in collageen mineraliseert in bot is HAp gekozen als startmineraal. De eerste en cruciale stap van het ionenuitwisselingsproces is het uitwisselen van de aanwezige calciumionen met zinkionen om Zn-HAp te vormen. Snelle screeningsexperimenten laten zien dat tot 20 mol% van de calciumionen uitgewisseld kan worden zonder verlies van de kristalvorm, kristal grootte of waargenomen kristalliniteit. De introductie van extremere reactiecondities in de vorm van verwarmen, sonificatie en langere reactietijden zorgen voor een iets hogere inbouw van zinkionen, maar met als gevolg dat meer bijproduct gevormd wordt. Controle-experimenten demonstreren hierbij dat de aanwezigheid van zinkionen in Zn-HAp de kristallen destabiliseert waardoor deze beter oplosbaar worden. Dit proces resulteert dus niet in een verhoogde inbouw van zinkionen met als resultaat zinkrijker HAp, maar zorgt ervoor dat HAp kristallen oplossen en reprecipiteren waardoor de vorming van ZnO uit HAp via ionenuitwisseling met een Zn-HAp tussenfase verhinderd wordt.

In het tweede deel van deze thesis is het doel het begrijpen en beheersen van het ZnO-vormingsmechanisme, zodat dit proces kan worden aangepast naar reactiecondities die compatibel zijn met organische templates. In **Hoofdstuk 3** wordt een vaak toegepaste ZnO synthese strategie in water onderzocht met een milde reactie pH, waarbij base wordt toegevoegd door het uiteenvallen van hexamethyleen-tetramine (HMTA). Door de invloed van zinkzouten te vergelijken blijkt dat het tegenion een significante invloed heeft op het eindproduct. Selectie van het zinkzout bevordert ofwel de vorming van ZnO in dispersie, ofwel de vorming van ZnO op aanwezige oppervlakten ofwel de vorming van gelaagde zinkhydroxyzouten (LZHS). Vervolgens zijn de vormingsmechanismen van ZnO onderzocht door het nemen van aliquots voor discrete cryo-TEM en SEM metingen. Dit laat zien

dat voor de vorming van ZnO in dispersie initieel voornamelijk een LZHS-overgangsfase gevormd wordt. Deze LZHSs groeien in de tijd in aanwezigheid van een ZnO-minderheidsfase tot op het punt waarbij de LZHS-fase snel en spontaan ontleedt. Dit is vooral het geval wanneer zinkacetaat gebruikt wordt. Vanwege de snelle initiële vorming van een gelaagde basisch zinkacetaat (LBZA) overgangsfase met een beperkte stabiliteit leidt dit tot de uiteindelijke vorming van gedispergeerde ZnO kristallen.

De vorming van ZnO in dispersie kan verder worden geoptimaliseerd door de kennis uit hoofdstuk 3 te combineren met een titratie-gestuurde base additiemethode in plaats van het gebruik van HMTA. Dit wordt beschreven in **Hoofdstuk 4**. Imitatie van de HMTA-ZnO strategie via titratie-gestuurde base additie demonstreert dat de hydrolyse van HMTA wordt beïnvloed door de vorming van ZnO. Dit maakt het onmogelijk om deze reactie exact te reproduceren. Het gebruik van titratie resulteert in de vorming van ZnO, via een vergelijkbaar mechanisme zoals besproken in hoofdstuk 3, tussen een pH van >5.5 en minstens 8.3. Hexagonale ZnO kristallen met een meer uitgesproken facettering worden waargenomen met toenemende hoeveelheid ammonia in het systeem. Dit suggereert dat ammonia zich aan het ZnO oppervlak hecht en dit afdekt. Dankzij de flexibele toevoeging van base kan de ZnO reactieopbrengst verhoogd worden van ~13 %, met de HMTA methode, naar een reactieopbrengst van 74 %.

Om de compatibiliteit van het ZnO vormingsproces met organische templates te bevorderen is een titratie-gestuurde base additiemethode bij een geleidelijk verlaagde reactietemperatuur onderzocht in **Hoofdstuk 5**. Hierbij wordt geen gebruik gemaakt van een verhittingsstap na de reactie. Afhankelijk van de zinkacetaatconcentratie in het reactiemedium leidt deze methode tot de vorming van ZnO, zelfs op een reactietemperatuur zo laag als 40 °C. Het verlagen van de reactietemperatuur heeft wel als gevolg dat LBZA in het eindproduct aanwezig is, zelfs als de reactietijd verlengd wordt. Deze LBZA-fase wordt dominantier bij lagere reactietemperaturen. Door l-lysine (l-lys) toe te voegen kan een ZnO-rijker reactieproduct verkregen worden bij 40 °C. Na het uitvoeren van de reactie gaat de vorming van ZnO in het reactiemedium door op kamertemperatuur, waardoor een ZnO-rijkere fase verkregen kan worden.

Het derde deel van deze thesis is gericht op de ontwikkeling van hiërarchische organische templates en het mineraliseren van organische templates met ZnO. In **Hoofdstuk 6** wordt de vorming beschreven van thermodynamisch stabiele nanotubes gevormde uit lysinerijke blokkopolypeptiden (BCPP). Door de lengte van de hydrofiele en hydrofobe domeinen te variëren, samen met de secundaire structuur van de peptiden, kunnen nanotubes gevormd worden met een hoge aspectverhouding die stabiel zijn op 80 °C tussen pH 2 en 12. Dankzij deze stabiliteit is het mogelijk om gebundelde nanotubevezels samen te stellen uit de nanotubes door middel van de pH-geïnduceerde complementaire zwitterionischeladingen. Dit maakt dit systeem een uitstekende kandidaat om als template voor mineralisatie te dienen.

De mineralisatie van organische templates met ZnO wordt besproken in **Hoofdstuk 7**, waarbij collageen als modelsysteem gebruikt is. Collageenvezels zijn blootgesteld aan een zinkacetaatoplossing of een LBZA-dispersie onder collageen-vriendelijke reactiecondities. Dit is onderzocht zowel in de aanwezigheid als in de afwezigheid van geladen additieven. Een langere blootstelling van collageen aan deze condities heeft geen negatieve invloed op de collageenvezels. Hoewel deze screeningsexperimenten niet resulteerden in de mineralisatie van collageen met zinkkristallen, suggereren deze resultaten dat met verdere optimalisatie de mineralisatie van collageen met zink(oxide) via directe synthese mogelijk is.

Table of Contents

Summary		i
Samenvatting		iii
List of Abbreviations		vi
Chapter 1	Prologue: Bioinspired Hybrid Materials	1
Chapter 2	Stability-limited Ion-exchange of Calcium with Zinc in Biomimetic Hydroxyapatite	17
Chapter 3	Counter-ion Influence on the Mechanism of HMTA-mediated ZnO Formation	33
Chapter 4	Titration-based Strategy for Controlled Aqueous ZnO Formation	57
Chapter 5	ZnO Formation at Template Friendly Conditions	79
Chapter 6	Designing Stable, Hierarchical Peptide Fibers from Block Co-polypeptide Sequences	95
Chapter 7	Exposure of Collagen to Zinc Species	121
Chapter 8	Epilogue: Connecting ZnO to Organic Templates	131
List of Publications		136
Curriculum Vitae		137
Acknowledgements		138

List of Abbreviations

ALV	Alanine - leucine - valine sequence
ATR-FTIR	Attenuated total reflectance Fourier transform infrared spectroscopy
BCPP	Block copolypeptides
Cryo-EELS	Cryogenic electron energy loss spectroscopy
CryoET	Cryogenic electron tomography
CryoTEM	Cryogenic transmission electron microscopy
DD	Direct dissolutions
DLS	Dynamic light scattering
EDX	Energy dispersive X-ray
HAp	Hydroxyapatite, $\text{Ca}_{10}(\text{PO}_4)_6(\text{OH})_2$
HMTA	Hexamethylenetetramine or hexamine
KGE	Lysine - glycine - glutamic acid sequence
LBZA	Layered basic zinc acetate
LBZC	Layered basic zinc chloride
LBZN	Layered basic zinc nitrate
LBZS	Layered basic zinc sulfate
LDSAED	Low dose selected area electron diffraction
l-lys	Laevus lysine
LP-TEM	Liquid phase transmission electron microscopy
LZHS	Layered zinc hydroxy salts
PA	Peptide amphiphile
pAA	Poly acrylic acid
pAsp	Poly aspartic acid
pXRD	Powder X-ray diffraction
RT	Room temperature
SAED	Selected area electron diffraction
SAXS	Small angle X-ray scattering
SEM	Scanning electron microscopy
SIMS	Secondary ion mass spectrometry
SLS	Static light scattering
SS	Solvent switch
SPPS	Solid phase peptide synthesis
TEM	Transmission electron microscopy
TXM	Transmission x-ray microscopy
UV-vis	Ultraviolet-visible spectroscopy
XANES	X-ray absorption near-edge structure
Zn-HAp	Hydroxyapatite with zinc ions
ZnO	"Wurtzite" Zinc oxide

Chapter 1

Prologue: Bioinspired Hybrid Materials

"The truth." Dumbledore sighed. "It is a beautiful and terrible thing, and should therefore be treated with great caution. However, I shall answer your questions unless I have a very good reason not to, in which case I beg you'll forgive me. I shall not, of course, lie."

J.K. Rowling, *Harry Potter and the Philosopher's Stone*, 1997.

1.1. Organic-Inorganic Hybrid Materials

Inorganic materials form an essential part of the world around us. They are present in the soil, they are the building blocks of mountains and houses, they ensure cellphones can operate and they are an intricate part of many, if not all, living organisms. Due to the extraordinary control biology has over materials, living creatures cannot only incorporate inorganic materials, but they are also able to enhance the material properties, like enhanced toughness with minimal compromise on strength. Synthetically one common strategy to achieve this is via the formation of organic-inorganic *hybrid* materials^[1, 2].

In hybrid materials the organic part often templates, directs and encapsulates the inorganic minerals^[3]. Here the organic matrix can be *hierarchically* ordered over many length scales ranging from the nanometer to centimeter scale^[4, 5]. This precise control by nature over shape and size results in the exceptional properties of these materials. For example, the vivid “structural” colors^[6] of *Morpho* butterfly wings (Fig. 1.1a) are caused predominantly by the periodic nanostructured chitin of which it is composed Fig 1.1b [7, 8]. The iridescent colors and the excellent mechanical properties of nacre in shells (Fig. 1.1c) are due to ordered hybrid layers of aragonite (calcium carbonate, CaCO_3) platelets templated by β -chitin and proteins (Fig. 1.1d) [2, 9, 10]. Even magnetic properties can be directed, as exemplified in the strings of magnetite crystals grown in organic *magnetosome* vesicles in magnetotactic bacteria (Fig. 1.1e) allowing the bacteria to orient themselves^[11-13].

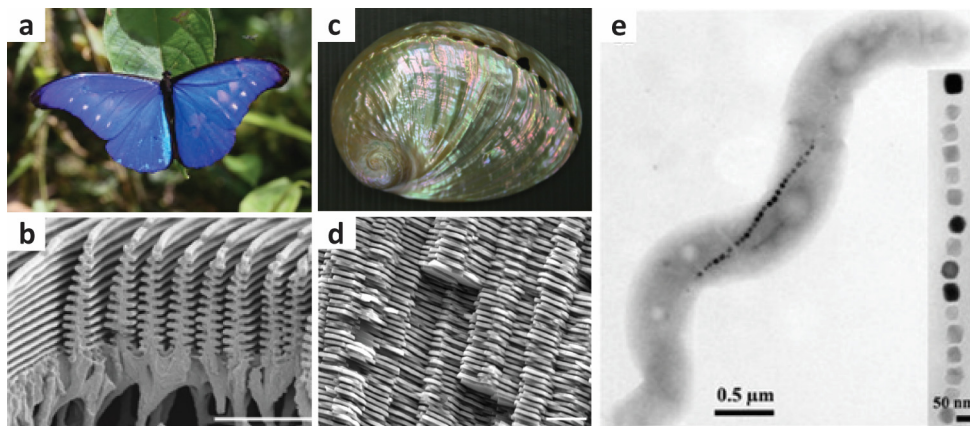


Figure 1.1 Image of a *Morpho rhetenor* butterfly with vibrant blue wings (a) and a SEM image (b) of the scales composing the *Morpho* wings^[7]. An image of the nacre shell of a *Haliotis Glabra* mollusk (c) and a SEM image (d) of its organized structure, which composed out of alternating layers β -chitin and protein with aragonite sheets^[9]. TEM image of a magnetotactic bacteria similar to the *Magnetospirillum* species, part of the magnetosome composed out of vesicles filled with individual magnetite crystals is magnified in the inset^[13]. Scale bar equals 2 μm (b) and 10 μm . (a) Photograph reproduced with permission from the photographer Adrian Hoskins. (b) Reproduced with permission.^[7] Copyright 2016, IOP Publishing. (c,d) Reproduced with permission.^[9] © The Optical Society. (e) Reproduced with permission.^[13] Copyright 2012, American Society for Microbiology.

The range of minerals used in biological systems is relatively limited. In most cases either hydroxyapatite, calcium carbonate or silica^[14] is used, there are also some less common observed minerals like magnetite^[15], iron pyrite^[16] and goethite^[17, 18]. In contrast, there is a nearly endless range of man-made inorganic materials with a wide range of properties. Indeed there are numerous examples of synthetic hybrid and even hierarchical materials taking a varying degree of inspiration from nature^[19]. A straight forward example is the mineralization of CaCO_3 or zinc oxide (ZnO) inside polymer track-etched

membrane pores [20-22]. Other, more biologically inspired systems are using mineralization of bioinspired peptide amphiphiles with magnetite[23] and hydroxyapatite[24]. However, these materials do not rival the complexity of biological materials. Therefore, understanding the formation of hybrid materials in nature and applying the lessons learned to synthetic materials is of great interest. An example of this are the attempts to imitate (and even expand) on the formation of bone[25].

1.1.1. Bone Collagen Mineralization

Bone is a hierarchical hybrid material, composed of hydroxyapatite (HAp) crystals mineralized in and around an organic collagen template[26, 27]. Collagen, which is common in the human body, be it in bone or in tendons[28] as exemplified in Fig. 1.2a, can assemble hierarchically with several length scales of order. On its smallest scale collagen is composed of procollagen, which are polypeptide sequences containing predominantly proline, hydroxyproline and glycine as amino acids. In water procollagen can self-assemble. Here, three procollagen sequences coil together into a triple helix forming a collagen molecule. These collagen molecules assemble into ordered microfibrils composed out of a repeating structure of five triple helices. This assembly results in the periodic gap and overlap zone observable in assembled collagen by electron microscopy (Fig. 1.2b)[29, 30]. The microfibrils subsequently assemble into fibrils and these fibrils assemble into collagen fibers. Finally, these collagen fibers form the final collagen structure[31-34].

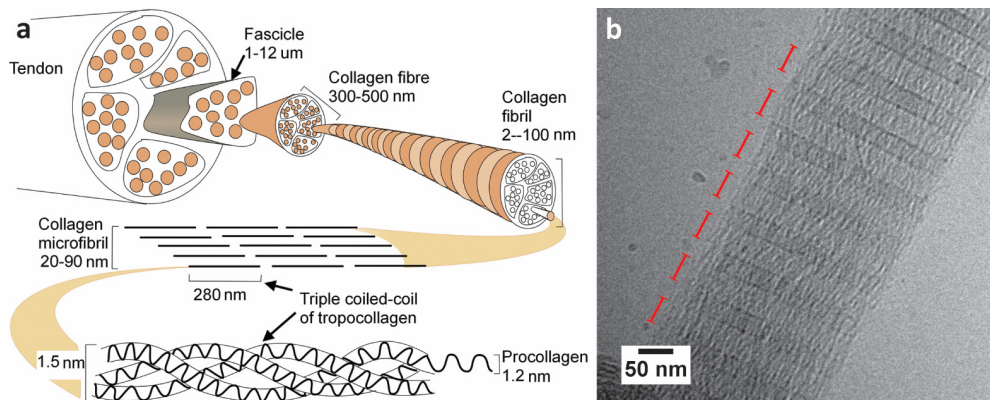


Figure 1.2 The self-assembly of procollagen into a non-mineralized tendon possessing hierarchical order from the nanometer to the micrometer scale[34]. CryoTEM image (b) of an assembled bovine Achilles tendon collagen fibril. The 40 nm gap zones in the 67 nm collagen repeating structure are indicated with red lines. (a) Reproduced with permission. [34] 2010, Elsevier Ltd.

In bone, the collagen template is mineralized both intra- and extra-fibrillary with HAp platelets. These HAp platelets combined with the collagen matrix provide bone its hardness and strength, while making sure it is not too brittle[35]. Although the exact mechanism of HAp mineralization is still poorly understood, it is presumed that a combination of small molecules plays an essential role in the mineralization process[36]. Indeed, synthetic HAp mineralization of collagen only proved possible in the presence of charged molecules. Particularly, poly aspartic acid (pAsp)[25, 37] and poly acrylic acid (pAA)[38, 39] have been used to promote the mineralization of collagen. Using these lessons from HAp mineralization, collagen could be mineralized with several other minerals including CaCO_3 [40], yttria-stabilized zirconia[41] and iron oxides [42].

Although collagen fibers are thermodynamically favored self-assembling structures, they are sensitive to reaction conditions[43]. To form and maintain the fibers, a pH between 5 – 9 is required [44]. Furthermore,

slightly increasing the reaction temperature above 37 °C results in denaturation of the collagen structure^[45]. After crosslinking, the assembled structure will maintain the general shape even outside ideal environmental conditions^[46], but it is likely not able to negate the influence of all environmental conditions which may affect collagen mineralization behavior. It is therefore important to perform any mineralization reaction of collagen under these “collagen-friendly” conditions.

1.1.2. Rules for Mineralization

To mineralize a crystal, several conditions need to be met (*Fig. 1.3*). (I) The first and most obvious is the need for template compatible reaction conditions. The mineralization protocol should preserve the organic template. As discussed above, this means that especially pH and temperature should be well controlled. (II) The precursor material should be able to enter the template and form via a gradual and controlled crystallization process. For example, in the case of HAp collagen mineralization, primary particles are initially formed^[47]. The stability of these primary particles in part allows their uptake into the collagen, which enables the formation of HAp to take place inside the collagen template^[25]. (III) Finally, mineral nucleation and growth should either be promoted in the organic template or suppressed in dispersion. A rapid formation of the mineral in dispersion will not only limit the amount of precursor available for template mineralization, but it might also drain ions from the template via osmosis. This means that before any mineralization strategy can be investigated it is essential to understand the mechanism of mineralization in the absence of a template and to have sufficient control over the reaction to perform it under “*template friendly*” conditions.

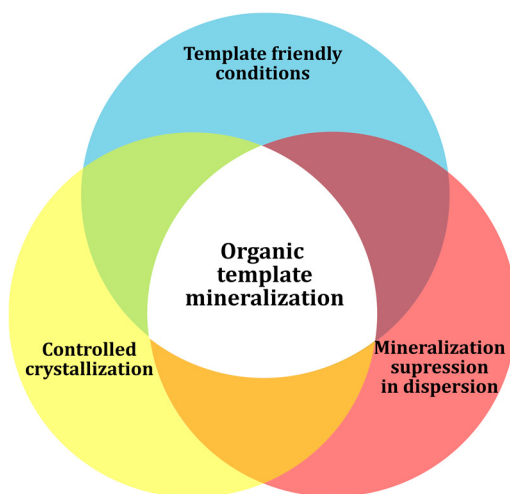


Figure 1.3 Overview of the required knowledge for mineralization.

1.2. The Targeted Inorganic Phase: Zinc Oxide

1.2.1. Crystal Structure, Physical Properties and Applications

Zinc oxide (ZnO) is an amphoteric metal oxide^[48]. Although rarely found in nature^[49], it has been synthesized and used as early as 2000 BCE^[50]. There are three known crystallographic forms of ZnO (*Fig. 1.4*): wurtzite (P6₃mc), zinc blende (F4̄3m) and rock salt (Fm3̄m)^[48, 51-53]. The hexagonal wurtzite ZnO is the thermodynamically favored polymorph, which can be readily obtained under a wide variety of

reaction conditions^[54]. Zinc blende and rock salt ZnO are metastable and require cubic epitaxial templating^[55] or high-pressures^[56] to prevent their transformation to wurtzite. Given the common formation of wurtzite ZnO, the use of “ZnO” during the remainder of this dissertation refers to wurtzite ZnO specifically.

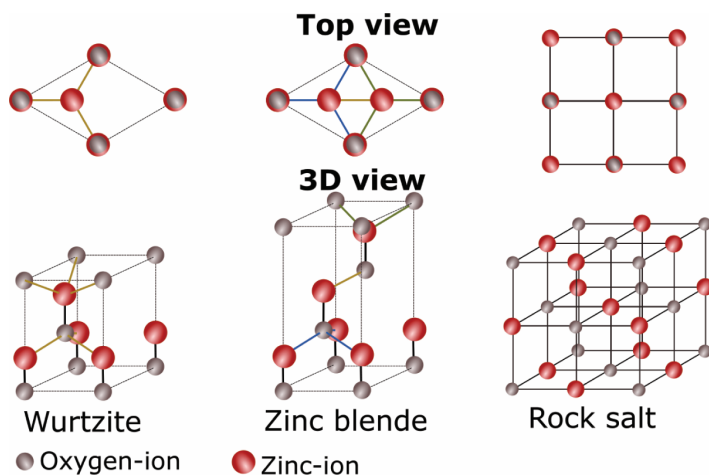


Figure 1.4 Crystal structure of wurtzite, zinc blende and rock salt ZnO shown in order.

Wurtzite ZnO has a lattice similar to a hexagonally close packed lattice. Hence, ZnO commonly forms hexagonally shaped structures including pillars^[57], platelets^[58], tubes^[59-61] and dumbbells^[62] (Fig. 1.5a,b). These structures are predominantly composed of a top and bottom c-plane (001) with rectangular m-planes (210) on the sides. Being composed of either oxygen or zinc atoms the c-planes are highly polar due^[63]. Thanks to the development of a variety in synthetic strategies, a range of alternative ZnO morphologies has been obtained. This includes: spindles^[64, 65] (Fig. 1.5c), nanobelts^[66], helices^[67], cages^[68], and even more complicated hierarchical structures including nanoplatelet columns^[69] and multileveled ZnO crystals^[70].

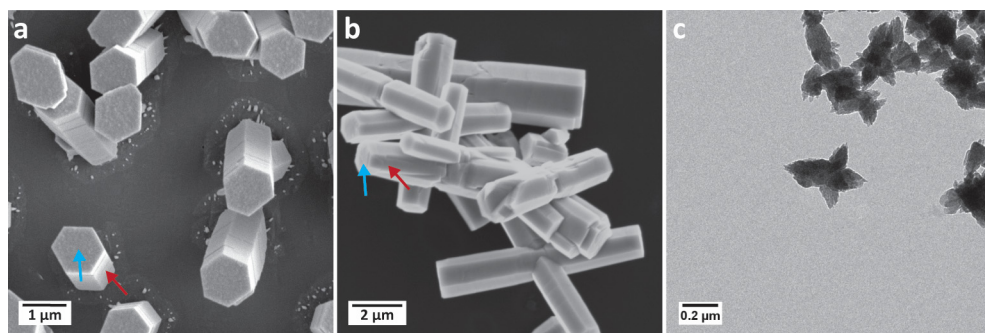


Figure 1.5 SEM (a-b) and TEM (c) images of ZnO morphologies including pillars (a), dumbbells (b) and spindles (c). In a and b, the (001) ZnO c-plane and the (210) ZnO m-plane have been indicated with a cyan and red arrow respectively.

ZnO possesses an extensive and diverse set of physical properties, due to its crystal lattice and its inherent lack of a center of symmetry. ZnO is a wide band-gap N-type semiconductor (~ 3.37 eV)^[21], it is photoluminescent^[72], has a high exciton binding energy of ~ 60 meV^[73], a high refractive index of ~ 2 ^[74], a high thermal conductivity of over 1.1 W cm⁻¹K⁻¹^[75], a reasonable electromechanical coupling coefficient of 0.24 ^[76-78], and it is biocompatible^[79] and antimicrobial^[80]. Furthermore, doping allows for changes in conductivity^[81] and a significant effort has been devoted to obtain p-type ZnO using this strategy^[82]. This makes ZnO a material of substantial interest for a wide range of technological applications including piezo-electrics^[83-85], pyroelectrics^[86-88], (O)LEDs^[89-91], sensors^[92-94], photocatalysts^[95-97], solar cells^[98, 99] and acoustic wave devices^[100, 101].

1.2.2. Synthesis of Zinc Oxide

There is a wide array of strategies for the formation of ZnO. Approaches range from chemical vapor deposition^[102, 103], pulsed laser deposition^[104], sputtering^[105], electro spinning^[106, 107] to wet chemical strategies^[65, 108]. The wet chemical methods require the mildest reaction conditions. Generally, a zinc precursor is dissolved in a solvent like methanol^[93] or ethanol^[109], though most commonly water is used. Hydroxide is provided by direct addition in the form of NaOH^[110] or ammonia^[111] or via a thermal hydrolysis of an agent like hexamethylenetetramine (HMTA)^[112]. The reaction is subsequently initiated by adding energy to the system, typically by heating (≥ 60 °C)^[113], under native or elevated (hydrothermal) pressure. After several hours reaction time this typically results in the formation ZnO crystals.

The most common wet chemical strategy for the formation of ZnO in water uses zinc acetate or zinc nitrate as the zinc source with HMTA as the base source^[114]. Upon dissolving the zinc precursor Zn²⁺ ions are released in solution (Eq. 1.1).



The reaction mixture is subsequently heated. At elevated temperature (> 50 °C) HMTA starts to thermally hydrolyse into ammonia and formaldehyde (Eq. 1.2) which are formed uniformly throughout the reaction medium^[115]. Part of the ammonia is protonated by water forming ammonium and hydroxide ions in the process (Eq. 1.3)^[116], the latter of which is consumed as base, reacting with the Zn²⁺ ions and resulting in the formation of ZnO (Eq. 1.4).



Using this strategy ZnO crystals can be grown both in dispersion^[117] and on solid interfaces exposed to the reaction solution (on-surfaces)^[118]. On-surfaces ZnO growth shows a strong preference for hydrophobic surfaces^[119]. Although, ZnO formation seems random on most surfaces the use of epitaxial seeding layers, e.g. ZnO films or gold^[108], does promote the formation of highly directed arrays of ZnO pillars or wires^[120].

1.2.3. Reaction Temperature

Whereas most wet chemical strategies require a temperature of > 60 °C, reactions at or close to room temperature (RT) have been investigated. *In vacuo*, ZnO has been formed by exposing zinc phthalocyanine to UV-light, inducing degradation of the phthalocyanine^[121]. However, UV-light exposure has been shown to cause unintentional heating^[122], rendering the actual reaction temperature ill-determined. Sonication of aqueous zinc acetate solutions has shown to produce ZnO at RT^[65, 123], typically resulting in polycrystalline spindle or flower (multiple connected spindles) shaped structures. ZnO has further been obtained at RT by using a more extreme reaction pH (> 13), both in the presence and absence of additives^[124] and in combination with alternative solvents including ethanol^[125] and DMSO^[126]. It is worth mentioning that

post synthetic annealing steps are commonly applied, making it unclear whether ZnO was formed during the reaction or during post-synthesis annealing, especially given that observed intermediates can directly transform into ZnO [127-129].

1.3. The Mechanism of Aqueous Zinc Oxide Formation

1.3.1. A Complex Interplay of Reaction Variables

Aqueous ZnO formation mechanisms have received great interest over the last decades. There is a rich literature, elucidating aspects of both the nucleation and the growth stages of formation. Due to the lack of a standard protocol for aqueous ZnO formation, however, multiple variables are varied between studies [62, 63, 113, 117, 130-132]. These variations will influence the observed formation mechanism [133], especially the initial state of the Zn^{2+} ions present in solution as in pure water, the state of zinc is pH dependent [115, 130]. Looking at a speciation diagram at room temperature, it can be observed that free (though still hydrated) ions are dominantly present below pH 6 (Fig. 1.6a). Increasing the pH above 6 results in the formation of varying species of zinc hydroxide. The selected reaction temperature or heating protocol will naturally influence the speciation.

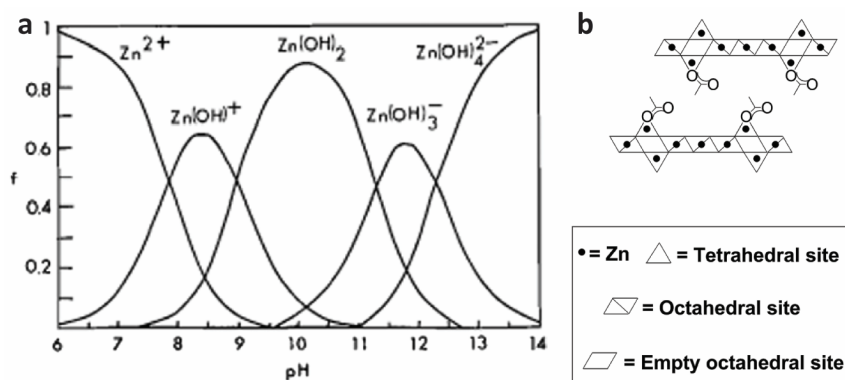


Figure 1.6 Speciation diagram based on the interaction between zinc and pure water (a) [130] and a simple scheme for the structure of LBZA [134]. (a) Reproduced with permission. [130] 2015, Elsevier Ltd. (b) Reproduced with permission. [134] 2018, Published by The Royal Society of Chemistry.

In a typical ZnO forming reaction, more components are present than simply Zn^{2+} ions and water. For instance, the counterion of the zinc salt leads to the formation of layered zinc hydroxy salts (LZHS) in many cases [134-138]. These LZHS are intercalated sheets of hexagonal unit cells. A well-known example is layered basic zinc acetate (LBZA, Fig. 1.6b) [128, 129]. Here the type and addition rate of the base also needs to be considered, for instance, when adding a significant amount of ammonia to initiate the reaction. This will (a) result in a high starting pH that decreases over the reaction, shifting the speciation of Zn^{2+} ions [115] and (b) result in a large amount of ammonia present that might directly interact with the Zn^{2+} ions or other zinc species.

In contrast, the use of an agent like HMTA will result in a more stable pH during the reaction. Still the initial concentration of HMTA will have an influence on the reaction pH. [130] As mentioned above, the ammonia and formaldehyde that are formed during the hydrolysis of HMTA might also have an effect. Besides the influence that HMTA hydrolysis products may exert, there is discussion that HMTA itself directly influences the formation of ZnO [139, 140].

1.3.2 Zinc Oxide Nucleation and Growth

Given the discussed variations in reaction conditions and their possible influences, it is not surprising that different ZnO formation mechanisms have been indicated in different studies. Generally, one of three formation mechanisms are observed or deduced: 1) ZnO is formed via a zinc hydroxide precursor phase, 2) ZnO is directly formed from the solution; and 3) ZnO is formed via a LZHS precursor phase. To expand on this, a few studies, based on *in-situ* and *ex-situ* analysis of ZnO nucleation and growth, are discussed in more detail below.

To illustrate the first mechanism, Nicholas *et al.*^[127] preheated a aqueous 0.5 M $\text{Zn}(\text{NO}_3)_2$ to 20–90 °C and initiated the reaction by adding 0.3 M ammonia hydroxide at the same temperature. The product was analyzed after 20 min reaction time with powder x-ray diffraction (pXRD). This showed the formation of ZnO at 70 °C or at higher temperatures. At lower reaction temperatures wülfingite zinc hydroxide was obtained. Increasing the reaction time at 50 °C to 140 h resulted in the formation of ZnO instead, suggesting that wülfingite acts as a precursor phase for the formation of ZnO. Using secondary ion mass spectrometry (SIMS) and isotopically labelled water (H_2^{18}O), it was found that the interior of the ZnO crystals is likely formed via a solid phase transformation from wülfingite to ZnO, whereas the ZnO edges are more likely formed via exchange with the solution. Using *ex-situ* SEM and pXRD measurements, Feng *et al.*^[130] investigated the formation of ZnO from 10 or 20 mM ZnAc_2 and 10–40 mM HMTA in water at 85 °C for 3 h. Using 10 mM ZnAc_2 and 20 mM HMTA, dominant formation of wülfingite was observed during the first 30 min of the reaction. Using liquid phase TEM (LPTEM), Wang *et al.*^[131] investigated aqueous solutions of 10 mM $\text{Zn}(\text{NO}_3)_2$ with 30–80 mM HMTA inducing the reaction by electron beam irradiation. Using 30 mM $\text{Zn}(\text{NO}_3)_2$, 200 nm ZnO crystals were formed within 70 seconds. Further growth of these crystals was limited by the LPTEM cell size. Increasing the HMTA concentration resulted in smaller ZnO particles, which in the case of 60 and 80 mM HMTA are dendritic in nature. Based on the results it is argued that zinc hydroxide is initially formed and subsequently decomposed into ZnO molecules. These monomers then aggregate into the ZnO crystals. However, no direct evidence for the zinc hydroxide formation is provided.

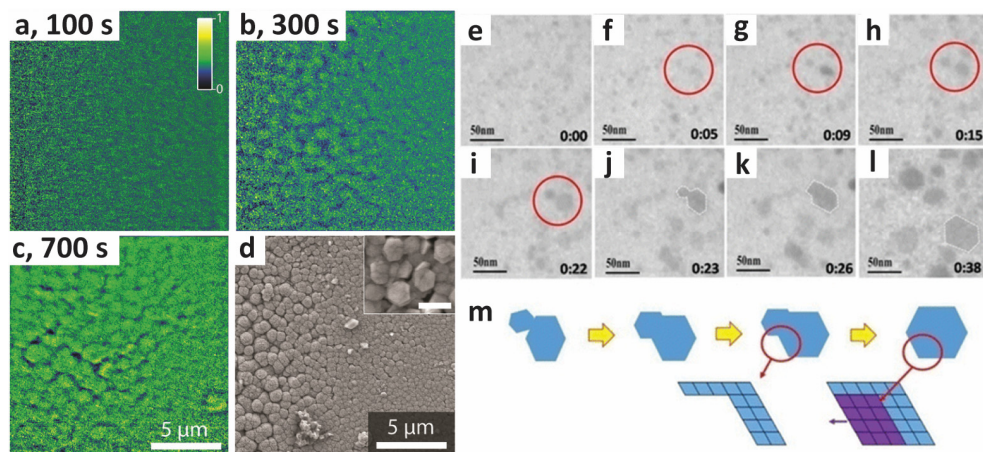


Figure 1.7 False color transmission x-ray microscopy (TXM) absorption images showing the evolution of ZnO nanorods in time (a – c) and an *ex-situ* SEM image (d) of the same area after the reaction^[141]. LPTEM series (e-h) showing ZnO particle growth by monomer attachment (e-i) and by growth via oriented attachment (i-l). Particle coalescence followed by monomer attachment is illustrated in the scheme below (m)^[117]. (a-d) Adapted from^[141] with permission from The Royal Society of Chemistry. (e-m) Reproduced with permission.^[117] 2016, American Chemical Society.

Indeed, not all studies show zinc hydroxides as an intermediate phase. Multiple studies argue that ZnO is directly formed from solution, that is, favor the second mechanism. McPeak *et al.*^[142] investigated the formation of ZnO on cadmium oxide seed layers by *in-situ* X-ray Absorption Near-Edge Structure (XANES) spectroscopy, on a 4.17, 6.25 or 12.5 mM equimolar solution of $\text{Zn}(\text{NO}_3)_2$ and HMTA at 60 or 90 °C. This showed that ZnO crystals are directly formed from $[\text{Zn}(\text{H}_2\text{O})_6]^{2+}$ without any long lived intermediates. Next, using 27 mM ZnAc_2 in ethanol in the presence of varying ligands and tetramethylammonium hydroxide as base, Zobel *et al.*^[109] studied the ZnO formation mechanism using *in-situ* Small Angle X-ray Scattering (SAXS) measurements. SAXS showed the initial formation of 1 nm ZnO clusters. These clusters subsequently form ZnO nanoparticles of 2 - 4 nm in diameter in time. Tay *et al.*^[141] investigated the formation of ZnO using an electron deposition strategy on a 5 or 50 mM $\text{Zn}(\text{NO}_3)_2$ aqueous solution with 0.1 M KCl electrolyte. Studying this process using *in-situ* transmission x-ray microscopy (TXM) showed the formation of a nanorod or nanoplate morphology of $\text{Zn}(\text{NO}_3)_2$ concentration (at 5 or 50 mM, respectively, Fig 1.7a-d). After the initial nucleation, nanorod or nanoplate growth was dominantly observed, suggesting a near instantaneous nucleation process. Due to the limited resolution of TXM, however, individual nanorods could not be resolved, consequently making it impossible to observe the very initial nucleation stages.

A combination of *in-situ* LPTM studies similarly found no preceding intermediate. Here, Liu *et al.*^[132] used an aqueous solution of 10 mM $\text{Zn}(\text{NO}_3)_2$ with 0 - 30 mM HMTA to form ZnO nanoparticles. HMTA proved essential for the formation of ZnO. Using a minimal electron flux of $< 6.3 \text{ e}^- \text{ nm}^{-2}$ ($< 1 \text{ A m}^{-2}$), ZnO formation was only observed when heating the reaction vessel to 95 °C by using a custom-made environmental stage. Hsieh *et al.*^[117] investigated the formation of ZnO using an equimolar 1 mM ZnAc_2 and HMTA solution. Here, the electron beam is proposed to act as heat source, although it is not excluded that electron beam induced radiolysis is in-fact the actual cause for reaction initiation^[143, 144]. After nucleation of clearly faceted ZnO pillars, two growth mechanism were observed: growth via monomer attachment and growth via orientated particle attachment (Fig 1.7e-m).

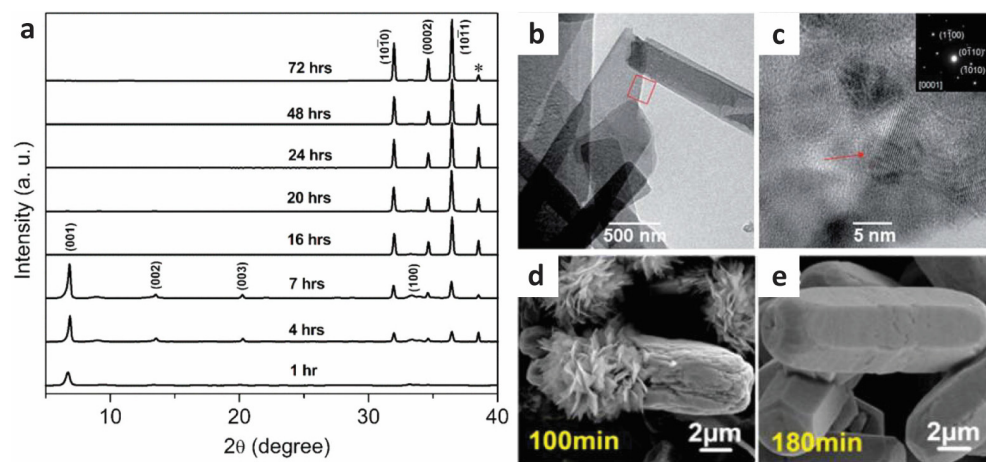


Figure 1.8 pXRD results of the formation of ZnO from 15 mM ZnAc_2 and ammonia, showing the initial formation of LBZA, at 1-7 h, preceding the formation of ZnO (a)^[113], TEM images of ZnO nuclei on LBZA sheets (b, c)^[62], SEM images of 12.5 mM $\text{Zn}(\text{DDAB})_2$ and HMTA demonstrating the initial formation of LZHS-ZnO binary structure (d) followed by the formation of ZnO crystals (e)^[128]. (a) Reproduced with permission.^[113] 2014, American Chemical Society. (b,c) Adapted from.^[62] with permission from The Royal Society of Chemistry. (d,e) Reproduced with permission.^[128] 2016, American Chemical Society.

The third formation mechanism suggests the initial formation of LZHS. Using a time resolved *ex-situ* pXRD and SEM sampling procedure, Liang *et al.*^[113] investigated the formation of ZnO using two different methods. The first method used a 50 mM equimolar concentration of $Zn(NO_3)_2$ and HMTA in water. After leaving this solution for 24 h at RT, pXRD confirmed the formation of layered basic zinc nitrate (LBZN). After subsequently heating the reaction to 65 °C for 48 h this resulted in the formation of ZnO. Secondly, $ZnAc_2$ was mixed with ammonia in an equimolar concentration of 15 mM for both compounds and preheated to 50 °C. PXRD sampling for this strategy confirmed the initial formation of LBZA, which was subsequently consumed by ZnO over increasing reaction time of up to 72 h (*Fig 1.8a*). Investigating the influence of LBZA further, Jang *et al.*^[62] looked into the transition of LBZA into ZnO by investigating a 100 mM $ZnAc_2$ and HMTA aqueous solution. Using TEM the authors concluded that ZnO nucleation sites exist on the initially formed LBZA sheets (*Fig 1.8b, c*). Assuming this, ZnO nucleates and growth occurs on both sides from these LBZA-ZnO sites and would explain the formation of dumbbell-shaped ZnO pillars.

The formation of LZHS is not limited to LBZA and LBZN. Using $ZnCl_2$ with equimolar amounts of HMTA at 95 °C for 12 h, Long *et al.*^[145] noted the formation of layered basic zinc chloride (LBZC). Notably at or above 50 mM $ZnCl_2$, pure LBZC pXRD signals were obtained from the reaction product. At lower concentrations pure ZnO signals were obtained, suggesting that also the precursor concentration can strongly influence the preferred reaction product. Song *et al.*^[128] used aqueous 50, 12.5 or 5 mM zinc N-dodecyl-N,N-dimethylammonioacetic bromide ($Zn(DDAB)_2$) solutions with an equimolar concentration of HMTA at 105 °C. Time resolved SEM sampling showed the evolution from LZHS to a stable LZHS-ZnO binary structure (*Fig 1.8d*) to ZnO (*Fig 1.8e*). The presence of these binary structures suggests that a solid-phase transformation from LZHS to ZnO can occur. Notably this binary structure was only observed at lower (12.5 and 5 mM) $Zn(DDAB)_2$ concentrations, suggesting that a dissolution and reprecipitation pathway is followed at higher 50 mM $Zn(DDAB)_2$ concentrations.

Overall, this shows that depending on the reaction conditions for the study involved, significant differences are observed for the initial ZnO formation process. This makes it challenging to predict how a specific reaction will evolve.

1.4. Objective and Outline of the Thesis

Bioinspired mineralization of complex hierarchical organic templates is already a challenge when performed with minerals that can be easily formed at template friendly conditions. ZnO is not such as mineral and hence even more difficult to deposit inside a (bio)template. Therefore, the aim of the research described in this thesis is to obtain the knowledge and the tools required for realizing ZnO formation within and on top of hierarchical organic templates under template friendly reaction conditions. Hence, three very different approaches, corresponding to the three general parts of the thesis, have been pursued. *The first part* investigates the direct ion-exchange of HAp, which can be found in biological organic templates, into ZnO without loss of size and shape. *The second part* aims to understand the nucleation and initial growth of ZnO under mild aqueous conditions and to optimize these conditions to allow for controlled “template friendly” ZnO nucleation and growth. *The third part* is dedicated to the development of a highly stable hierarchical organic mineralization template and to use the above-mentioned tools to develop new template based ZnO mineralization strategies.

The first part is dealt with in **Chapter 2**, which explores ion-exchanging from HAp into ZnO as a tool to obtain ZnO platelets in collagen. The first and crucial step in this ion-exchange pathway is the exchange of HAp into Zn-HAp. For this a near 100 % conversion of Ca^{2+} to Zn^{2+} ions is essential. Here the exchange of dispersed “biomimetic” HAp is investigated under aqueous conditions to ensure compatibility for exchange in collagen.

The second part starts by studying in detail the mechanism of ZnO formation under “typical” conditions and is discussed in **Chapter 3**. This chapter aims to elucidate the influence of the zinc counterion on both the reaction product and its formation mechanism. The primary method to achieve this is by varying only the zinc salt, present in the reaction solution, between reaction compositions. Subsequently, the reaction paths are elucidated by discrete *in-situ* CryoTEM sampling and SEM sampling.

Following this line, in **Chapter 4** a controlled titration-based strategy for the addition of base is explored, which is inspired by the thermal hydrolysis of HMTA as used in Chapter 3. This titration strategy is used to probe the influence of the added base and its addition protocol at a mild reaction pH. The flexibility of base titration is further exploited to probe the influence of reaction pH and the optimization conditions for ZnO twin-pillar structures.

The above discussed ZnO synthesis strategies lack a reaction temperature compatible with ZnO mineralization in sensitive organic templates. Therefore, in **Chapter 5** the titration strategy as used in Chapter 4 are further explored and developed for “template friendly” reaction conditions. This is done by systematically investigating the influence of the reaction temperature on the formation of ZnO at a mild reaction pH without post synthetic annealing. These results are subsequently used to further optimize the formation of ZnO at low temperatures.

For the third part the self-assembly of selectively charged block copolypeptide (BCPP) into organized structures is studied as described in **Chapter 6**. This work focusses on exploring the preferred morphologies as well as the stability of these assemblies at RT conditions, high and low pH, and at elevated reaction temperature. In particular, the pH dependent hierarchical self-assembly behavior of these BCPP is investigated in detail.

Combining the lessons learned in Chapters 3- 5, in **Chapter 7** the mineralization of bovine Achilles tendon collagen with ZnO is studied to develop a general protocol for the formation of organic-ZnO hybrid materials under “template friendly” conditions.

Finally, **Chapter 8** the *epilogue* concludes and discusses the insights gained in this thesis.

1.5. References

1. L. Mishnaevsky and M. Tsapatsis, Hierarchical Materials: Background and Perspectives. *MRS Bull* **41**, 661-666 (2016).
2. U. G. K. Wegst, H. Bai, E. Saiz, A. P. Tomsia and R. O. Ritchie, Bioinspired Structural Materials. *Nat Mater* **14**, 23-36 (2015).
3. M. R. B. M. Rejab, M. H. B. M. Hamdan, M. Quanjin, J. P. Siregar, D. Bachtari and Y. Muchlis, in *Encyclopedia of Renewable and Sustainable Materials*, S. Hashmi and I. A. Choudhury, Eds. (Elsevier, Oxford, 2020), pp. 445-455.
4. P. Fratzl and R. Weinkamer, Nature's Hierarchical Materials. *Mater Sci* **52**, 1263-1334 (2007).
5. J. A. Michel and P. J. Yunker, Structural Hierarchy Confers Error Tolerance in Biological Materials. *Proc Nat Am Soc* **116**, 2875-2880 (2019).
6. A. R. Parker, 515 Million Years of Structural Colour. *J Opt a-Pure Appl Op* **2**, R15-R28 (2000).
7. C. A. Tippets, Y. L. Fu, A. M. Jackson, E. U. Donev and R. Lopez, Reproduction and Optical Analysis of Morpho-inspired Polymeric Nanostructures. *J Optics-Uk* **18**, 065105 (2016).
8. M. A. Giraldo and D. G. Stavenga, Brilliant Iridescence of Morpho Butterfly Wing Scales is due to both a Thin Film Lower Lamina and a Multilayered Upper Lamina. *J Comp Physiol A* **202**, 381-388 (2016).
9. T. L. Tan, D. Wong and P. Lee, Iridescence of a Shell of Mollusk *Haliotis Glabra*. *Opt Express* **12**, 4847-4854 (2004).
10. J. Xu and G. S. Zhang, Unique Morphology and Gradient Arrangement of Nacre's Platelets in Green Mussel Shells. *Mat Sci Eng C-Mater* **52**, 186-193 (2015).
11. L. Yan, H. Y. Da, S. Zhang, V. M. Lopez and W. D. Wang, Bacterial Magnetosome and its Potential Application. *Microbiol Res* **203**, 19-28 (2017).
12. G. Mirabella, J. J. M. Lenders and N. A. J. M. Sommerdijk, Bioinspired Synthesis of Magnetite Nanoparticles. *Chem Soc Rev* **45**, 5085-5106 (2016).
13. C. T. Lefevre, M. L. Schmidt, N. Vilorio, D. Trubitsyn, D. Schuler and D. A. Bazylinski, Insight into the Evolution of Magnetotaxis in Magnetospirillum spp., Based on mam Gene Phylogeny. *Appl Environ Microb* **78**, 7238-7248 (2012).
14. in *Encyclopedia of Ecology*, S. E. Jørgensen and B. D. Fat, Eds. (Elsevier, 2008).
15. J. C. Weaver, Q. Q. Wang, A. Miserez, A. Tantuocci, R. Stromberg, K. N. Bozhilov, P. Maxwell, R. Nay, S. T. Heier, E. DiMasi and D. Kisailus, Analysis of an Ultra Hard Magnetic Biomineral in Chiton Radular Teeth. *Mater Today* **13**, 42-52 (2010).

16. S. Mann, N. H. C. Sparks, R. B. Frankel, D. A. Bazylinski and H. W. Jannasch, Biomineralization of Ferrimagnetic Greigite (Fe₃S₄) and Iron Pyrite (Fes₂) in a Magnetotactic Bacterium. *Nature* **343**, 258-261 (1990).
17. H. Li, S. J. Hu, M. L. Polizzotto, X. L. Chang, Q. R. Shen, W. Ran and G. H. Yu, Fungal Biomineralization of Montmorillonite and Goethite to Short-range-ordered Minerals. *Geochim Cosmochim Acta* **191**, 17-31 (2016).
18. P. Laresse-Casanova, S. B. Haderlein and A. Kappler, Biomineralization of Lepidocrocite and Goethite by Nitrate-reducing Fe(II)-oxidizing Bacteria: Effect of pH, Bicarbonate, Phosphate, and Humic Acids. *Geochim Cosmochim Acta* **74**, 3721-3734 (2010).
19. M. S. Saveleva, K. Eftekhari, A. Abalymov, T. E. L. Douglas, D. Volodkin, B. V. Parakhonskiy and A. G. Skirtach, Hierarchy of Hybrid Materials - The Place of Inorganics-in-Organics in it, Their Composition and Applications. *Front Chem* **7**, 179 (2019).
20. C. Ou, P. E. Sanchez-Jimenez, A. Datta, F. L. Boughey, R. A. Whiter, S. L. Sahonta and S. Kar-Narayan, Template-Assisted Hydrothermal Growth of Aligned Zinc Oxide Nanowires for Piezoelectric Energy Harvesting Applications. *ACS Appl Mater Inter* **8**, 13678-13683 (2016).
21. H. J. Zhou and S. S. Wong, A Facile and Mild Synthesis of 1-D ZnO, CuO, and Alpha-Fe₂O₃ Nanostructures and Nanostructured Arrays. *Acs Nano* **2**, 944-958 (2008).
22. A. S. Schenk, E. J. Albarracin, Y. Y. Kim, J. Ihli and F. C. Meldrum, Confinement Stabilises Single Crystal Vaterite Rods. *Chem Commun* **50**, 4729-4732 (2014).
23. E. D. Sone and S. I. Stupp, Bioinspired Magnetite Mineralization of Peptide-Amphiphile Nanofibers. *Chem Mater* **23**, 2005-2007 (2011).
24. J. D. Hartgerink, Self-Assembly and Mineralization of Peptide-Amphiphile Nanofibers. *Science* **294**, 1684-1688 (2001).
25. F. Nudelmann, K. Pieterse, A. George, P. H. H. Bomans, H. Friedrich, L. J. Brylka, P. A. J. Hilbers, G. de With and N. A. J. M. Sommerdijk, The Role of Collagen in Bone Apatite Formation in the Presence of Hydroxyapatite Nucleation Inhibitors. *Nat Mater* **9**, 1004-1009 (2010).
26. S. Weiner and W. Traub, Bone-Structure - from Angstroms to Microns. *Faseb J* **6**, 879-885 (1992).
27. B. M. Oosterlaken, M. P. Vena and G. de With, In Vitro Mineralization of Collagen. *Adv. Mater.*, 2004418 (2021).
28. R. B. Svensson, A. Herchenhan, T. Starborg, M. Larsen, K. E. Kadler, K. Qvortrup and S. P. Magnusson, Evidence of Structurally Continuous Collagen Fibrils in Tendons. *Acta Biomater* **50**, 293-301 (2017).
29. J. A. Chapman, M. Tzaphlidou, K. M. Meek and K. E. Kadler, The Collagen Fibril - a Model System for Studying the Staining and Fixation of a Protein. *Electron Microsc Rev* **3**, 143-182 (1990).
30. Z. J. Xu, W. L. Zhao, Z. Q. Wang, Y. Yang and N. Sahai, Structure Analysis of Collagen Fibril at Atomic-level Resolution and its Implications for Intra-fibrillar Transport in Bone Biomineralization. *Phys Chem Chem Phys* **20**, 1513-1523 (2018).
31. A. Gautieri, S. Vesentini, A. Redaelli and M. J. Buehler, Hierarchical Structure and Nanomechanics of Collagen Microfibrils from the Atomistic Scale Up. *Nano Letters* **11**, 757-766 (2011).
32. N. Reznikov, M. Bilton, L. Lari, M. M. Stevens and R. Kroger, Fractal-like Hierarchical Organization of Bone Begins at the Nanoscale. *Science* **360**, 507 (2018).
33. N. Reznikov, R. Shahar and S. Weiner, Bone Hierarchical Structure in Three Dimensions. *Acta Biomater* **10**, 3815-3826 (2014).
34. G. Scarr, Helical Tensegrity as a Structural Mechanism in Human Anatomy. *Int J Osteopath Med* **14**, 24-32 (2011).
35. J. D. Currey, Materials Science - Hierarchies in Biomineral Structures. *Science* **309**, 253-254 (2005).
36. A. K. Nair, A. Gautieri, S. W. Chang and M. J. Buehler, Molecular Mechanics of Mineralized Collagen Fibrils in Bone. *Nat Commun* **4**, 1724 (2013).
37. C. Y. Shao, R. B. Zhao, S. Q. Jiang, S. S. Yao, Z. F. Wu, B. Jin, Y. L. Yang, H. H. Pan and R. K. Tang, Citrate Improves Collagen Mineralization via Interface Wetting: A Physicochemical Understanding of Biomineralization Control. *Adv Mater* **30**, 1704876 (2018).
38. Q. Song, K. Jiao, L. Tonggu, L. G. Wang, S. L. Zhang, Y. D. Yang, L. Zhang, J. H. Bian, D. X. Hao, C. Y. Wang, Y. X. Ma, D. D. Arola, L. Breschi, J. H. Chen, F. R. Tay and L. N. Niu, Contribution of Biomimetic Collagen-ligand Interaction to Intrafibrillar Mineralization. *Sci Adv* **5**, eaav9075 (2019).
39. Y. P. Qi, Z. Ye, A. Fok, B. N. Holmes, M. Espanol, M. P. Ginebra and C. Aparicio, Effects of Molecular Weight and Concentration of Poly(Acrylic Acid) on Biomimetic Mineralization of Collagen. *Acs Biomater Sci Eng* **4**, 2758-2766 (2018).
40. H. Ping, H. Xie, Y. M. Wan, Z. X. Zhang, J. Zhang, M. Y. Xiang, J. J. Xie, H. Wang, W. M. Wang and Z. Y. Fu, Confinement Controlled Mineralization of Calcium Carbonate within Collagen Fibrils. *J Mater Chem B* **4**, 880-886 (2016).
41. B. Zhou, L. N. Niu, W. Shi, W. Zhang, D. D. Arola, L. Breschi, J. Mao, J. H. Chen, D. H. Pashley and F. R. Tay, Adopting the Principles of Collagen Biomineralization for Intrafibrillar Infiltration of Yttria-Stabilized Zirconia into Three-Dimensional Collagen Scaffolds. *Adv Funct Mater* **24**, 1895-1903 (2014).
42. Y. Xu, F. Nudelmann, E. D. Eren, M. J. M. Wirix, B. Cantaert, W. H. Nijhuis, D. Hermida-Merino, G. Portale, P. H. H. Bomans, C. Ottmann, H. Friedrich, W. Bras, A. Akiva, J. P. R. O. Orgel, F. C. Meldrum and N. Sommerdijk, Intermolecular Channels Direct Crystal Orientation in Mineralized Collagen. *Nat Commun* **11**, 5068 (2020).
43. B. R. Williams, R. A. Gelman, D. C. Poppe and K. A. Piez, Collagen Fibril Formation - Optimal Invitro Conditions and Preliminary Kinetic Results. *J Biol Chem* **253**, 6578-6585 (1978).
44. T. Hayashi and Y. Nagai, Effect of pH on the Stability of Collagen Molecule in Solution. *J Biochem* **73**, 999-1006 (1973).
45. Y. Sun, W. L. Chen, S. J. Lin, S. H. Jee, Y. F. Chen, L. C. Lin, P. T. C. So and C. Y. Dong, Investigating Mechanisms of Collagen Thermal Denaturation by High Resolution Second-harmonic Generation Imaging. *Biophys* **91**, 2620-2625 (2006).

46. L. S. Gu, T. T. Shan, Y. X. Ma, F. R. Tay and L. N. Niu, Novel Biomedical Applications of Crosslinked Collagen. *Trends Biotechnol* **37**, 464-491 (2019).
47. W. J. Habraken, J. Tao, L. J. Brylka, H. Friedrich, L. Bertinetti, A. S. Schenk, A. Verch, V. Dmitrovic, P. H. Bomans, P. M. Frederik, J. Laven, P. van der Schoot, B. Aichmayer, G. de With, J. J. DeYoreo and N. A. Sommerdijk, Ion-association Complexes Unite Classical and Non-classical Theories for the Biomimetic Nucleation of Calcium Phosphate. *Nat Commun* **4**, 1507 (2013).
48. H. Morkoç and Ü. Özgür, in *Zinc Oxide: Fundamentals, Materials and Device Technology*. (WILEY-VCH Verlag GmbH, 2009), chap. 1 General Properties of ZnO.
49. H. D. McCaskey, "Mineral Resources of the United States Part I Metals," (U.S. Department of Interior, Washington D.C., 1917).
50. A. Moezzi, A. M. McDonagh and M. B. Cortie, Zinc Oxide Particles: Synthesis, Properties and Applications. *Chem Eng J* **185**, 1-22 (2012).
51. H. J. Yearian, Intensity of Diffraction of Electrons by ZnO. *Phys Rev* **48**, 631-639 (1935).
52. C. H. Bates, R. Roy and W. B. White, New High-Pressure Polymorph of Zinc Oxide. *Science* **137**, 993 (1962).
53. A. Ashrafi and C. Jagadish, Review of Zincblende ZnO: Stability of Metastable ZnO Phases. *J Appl Phys* **102**, 071101 (2007).
54. A. Kolodziejczak-Radzimska and T. Jesionowski, Zinc Oxide-From Synthesis to Application: A Review. *Materials* **7**, 2833-2881 (2014).
55. O. Chichvarina, T. S. Herrg, K. C. Phuah, W. Xiao, N. Bao, Y. P. Feng and J. Ding, Stable Zinc-blende ZnO Thin Films: Formation and Physical Properties. *J Mater Sci* **50**, 28-33 (2015).
56. A. N. Baranov, P. S. Sokolov, V. A. Tafenko, C. Lathe, Y. V. Zubavichus, A. A. Velizhanin, M. V. Chukichev and V. L. Solozhenko, Nanocrystallinity as a Route to Metastable Phases: Rock Salt ZnO. *Chem Mater* **25**, 1775-1782 (2013).
57. L. Vayssieres, Growth of Arrayed Nanorods and Nanowires of ZnO from Aqueous Solutions. *Adv Mater* **15**, 464-466 (2003).
58. M. R. Alenezi, S. J. Henley, N. G. Emerson and S. R. P. Silva, From 1D and 2D ZnO Nanostructures to 3D Hierarchical Structures with Enhanced Gas Sensing Properties. *Nanoscale* **6**, 235-247 (2014).
59. Y. Sun, G. M. Fuge, N. A. Fox, D. J. Riley and M. N. R. Ashfold, Synthesis of Aligned Arrays of Ultrathin ZnO Nanotubes on a Si Wafer Coated with a Thin ZnO Film. *Adv Mater* **17**, 2477-2481 (2005).
60. Q. J. Yu, W. Y. Fu, C. L. Yu, H. B. Yang, R. H. Wei, M. H. Li, S. K. Liu, Y. M. Sui, Z. L. Liu, M. X. Yuan, G. T. Zou, G. R. Wang, C. L. Shao and Y. C. Liu, Fabrication and Optical Properties of Large-scale ZnO Nanotube Bundles via a Simple Solution Route. *J Phys Chem C* **111**, 17521-17526 (2007).
61. Y. B. Pyun, J. Yi, D. H. Lee, K. S. Son, G. Liu, D. K. Yi, U. Paik and W. I. Park, Synthesis of ZnO Nanotubes and Nanotube-nanorod Hybrid Hexagonal Networks using a Hexagonally Close-packed Colloidal Monolayer Template. *J Mater Chem* **20**, 5136-5140 (2010).
62. E. S. Jang, J. H. Won, Y. W. Kim, Z. Cheng and J. H. Choy, Dynamic Transition Between Zn-HDS and ZnO; Growth and Dissolving Mechanism of Dumbbell-like ZnO Bipod Crystal. *CrystEngComm* **13**, 546-552 (2011).
63. A. S. Kamble, B. B. Sinha, K. Chung, M. G. Gil, V. Burungale, C. J. Park, J. H. Kim and P. S. Patil, Effect of Hydroxide Anion Generating Agents on Growth and Properties of ZnO Nanorod Arrays. *Electrochim Acta* **149**, 386-393 (2014).
64. N. Subramanian and A. Al Ghaferi, A Green Synthetic Route for Zinc Oxide Nanoarchitectures using L-lysine. *Mater Lett* **92**, 361-364 (2013).
65. O. Carp, A. Tirsoaga, R. Ene, A. Ianculescu, R. F. Negrea, P. Chesler, G. Ionita and R. Birjega, Facile, High Yield Ultrasound Mediated Protocol for ZnO Hierarchical Structures Synthesis: Formation Mechanism, Optical and Photocatalytic Properties. *Ultrason Sonochem* **36**, 326-335 (2017).
66. X. R. Qu, S. C. Lu, J. J. Wang, Z. Q. Li and H. J. Xue, Preparation and Optical Property of Porous ZnO Nanobelts. *Mat Sci Semicon Proc* **15**, 244-250 (2012).
67. P. X. Gao, Y. Ding, W. J. Mai, W. L. Hughes, C. S. Lao and Z. L. Wang, Conversion of Zinc Oxide Nanobelts into Superlattice-structured Nanohelices. *Science* **309**, 1700-1704 (2005).
68. T. R. Chetia, M. S. Ansari and M. Qureshi, Rational Design of Hierarchical ZnO Superstructures for Efficient Charge Transfer: Mechanistic and Photovoltaic Studies of Hollow, Mesoporous, Cage-like Nanostructures with Compacted 1D Building Blocks. *Phys Chem Chem Phys* **18**, 5344-5357 (2016).
69. Z. J. Li, H. Li, Z. L. Wu, M. K. Wang, J. T. Luo, H. D. Torun, P. A. Hu, C. Yang, M. Grundmann, X. T. Liu and Y. Q. Fu, Advances in Designs and Mechanisms of Semiconducting Metal Oxide Nanostructures for High-precision Gas Sensors Operated at Room Temperature. *Mater Horiz* **6**, 470-506 (2019).
70. T. R. Zhang, W. J. Dong, M. Keeter-Brewer, S. Konar, R. N. Njabon and Z. R. Tian, Site-specific Nucleation and Growth Kinetics in Hierarchical Nanosyntheses of Branched ZnO Crystallites. *J Am Chem Soc* **128**, 10960-10968 (2006).
71. A. Mang, K. Reimann and S. Rubenacke, Band-Gaps, Crystal-Field Splitting, Spin-Orbit-Coupling, and Exciton Binding-Energies in ZnO under Hydrostatic-Pressure. *Solid State Commun* **94**, 251-254 (1995).
72. P. A. Rodnyi and I. V. Khodyuk, Optical and Luminescence Properties of Zinc Oxide (Review). *Opt Spectrosc* **111**, 776-785 (2011).
73. J. M. Hvam, Exciton Interaction in Photoluminescence from ZnO. *Phys Status Solidi B* **63**, 511-517 (1974).
74. W. L. Bond, Measurement of the Refractive Indices of Several Crystals. *J Appl Phys* **36**, 1674-1677 (1965).
75. D. I. Florescu, L. G. Mourokh, F. H. Pollak, D. C. Look, G. Cantwell and X. Li, High Spatial Resolution Thermal Conductivity of Bulk ZnO (0001). *J Appl Phys* **91**, 890-892 (2002).
76. K. Uchino, in *Ultrasonic Transducers*, K. Nakamura, Ed. (Woodhead Publishing, 2012), pp. 70-116.

77. S. Goel and B. Kumar, A Review on Piezo-/Ferro-electric Properties of Morphologically Diverse ZnO Nanostructures. *J Alloy Compd* **816**, 152491 (2020).
78. T. Yanagitani, N. Mishima, M. Matsukawa and Y. Watanabe, Electromechanical Coupling Coefficient $k(15)$ of Polycrystalline ZnO Films with the C-axes lie in the Substrate Plane. *IEEE T Ultrason Ferr* **54**, 701-704 (2007).
79. S. E. Jin and H. E. Jin, Synthesis, Characterization, and Three-Dimensional Structure Generation of Zinc Oxide-Based Nanomedicine for Biomedical Applications. *Pharmaceutics* **11**, 575 (2019).
80. M. Alavi and A. Nokhodchi, An Overview on Antimicrobial and Wound Healing Properties of ZnO Nanobiofilms, Hydrogels, and Bionanocomposites based on Cellulose, Chitosan, and Alginate Polymers. *Carbohydr* **227**, 115349 (2020).
81. A. Janotti and C. G. Van de Walle, Fundamentals of Zinc Oxide as a Semiconductor. *Rep Prog Phys* **72**, 126501 (2009).
82. Z. N. Ng, K. Y. Chan, S. Muslimin and D. Knipp, P-Type Characteristic of Nitrogen-Doped ZnO Films. *J Electron Mater* **47**, 5607-5613 (2018).
83. X. D. Wang, J. H. Song, J. Liu and Z. L. Wang, Direct-current Nanogenerator Driven by Ultrasonic Waves. *Science* **316**, 102-105 (2007).
84. J. Briscoe, M. Stewart, M. Vopson, M. Cain, P. M. Weaver and S. Dunn, Nanostructured p-n Junctions for Kinetic-to-Electrical Energy Conversion. *Adv Energy Mater* **2**, 1261-1268 (2012).
85. E. S. Nour, O. Nur and M. Willander, Zinc Oxide Piezoelectric Nano-generators for Low Frequency Applications. *Semicond Sci Tech* **32**, 064005 (2017).
86. C. C. Hsiao and S. Y. Yu, Improved Response of ZnO Films for Pyroelectric Devices. *Sensors-Basel* **12**, 17007-17022 (2012).
87. Z. N. Wang, R. M. Yu, C. F. Pan, Z. L. Li, J. Yang, F. Yi and Z. L. Wang, Light-induced Pyroelectric Effect as an Effective Approach for Ultrafast Ultraviolet Nanosensing. *Nat Commun* **6**, 8401 (2015).
88. J. Q. Dong, Z. J. Wang, X. F. Wang and Z. L. Wang, Temperature Dependence of the Pyro-phototronic Effect in Self-powered P-Si/N-ZnO Nanowires Heterojunctioned Ultraviolet Sensors. *Nano Today* **29**, 100798 (2019).
89. R. Konenkamp, R. C. Word and C. Schlegel, Vertical Nanowire Light-emitting Diode. *Appl Phys Lett* **85**, 6004-6006 (2004).
90. J. W. Stouwdam and R. A. J. Janssen, Red, Green, and Blue Quantum Dot LEDs with Solution Processable ZnO Nanocrystal Electron Injection Layers. *J Mater Chem* **18**, 1889-1894 (2008).
91. W. Q. Zhao, X. Xiong, Y. B. Han, L. Wen, Z. G. Zou, S. J. Luo, H. X. Li, J. Su, T. Y. Zhai and Y. H. Gao, Fe-Doped p-ZnO Nanostructures/n-GaN Heterojunction for "Blue-Free" Orange Light-Emitting Diodes. *Adv Opt Mater* **5**, 1700146 (2017).
92. M. R. Alenezi, A. S. Alshammari, K. D. G. I. Jayawardena, M. J. Beliatis, S. J. Henley and S. R. P. Silva, Role of the Exposed Polar Facets in the Performance of Thermally and UV Activated ZnO Nanostructured Gas Sensors. *J Phys Chem C* **117**, 17850-17858 (2013).
93. T. Park, K. E. Lee, N. Kim, Y. Oh, J. K. Yoo and M. K. Um, Aspect Ratio-controlled ZnO Nanorods for Highly Sensitive Wireless Ultraviolet Sensor Applications. *J Mater Chem C* **5**, 12256-12263 (2017).
94. A. M. Mohammed, I. J. Ibraheem, A. S. Obaid and M. Bououdina, Nanostructured ZnO-based Biosensor: DNA Immobilization and Hybridization. *Sens Biosensing Res* **15**, 46-52 (2017).
95. C. Wang, X. M. Wang, B. Q. Xu, J. C. Zhao, B. X. Mai, P. Peng, G. Y. Sheng and H. M. Fu, Enhanced Photocatalytic Performance of Nanosized Coupled ZnO/SnO₂ Photocatalysts for Methyl Orange Degradation. *J Photoch Photobio A* **168**, 47-52 (2004).
96. X. Q. Chen, Z. S. Wu, D. D. Liu and Z. Z. Gao, Preparation of ZnO Photocatalyst for the Efficient and Rapid Photocatalytic Degradation of Azo Dyes. *Nanoscale Res Lett* **12**, 143 (2017).
97. R. Sabouni and H. Gomaa, Photocatalytic Degradation of Pharmaceutical Micro-pollutants using ZnO. *Environmental Science and Pollution Research* **26**, 5372-5380 (2019).
98. M. H. Kumar, N. Yantara, S. Dharani, M. Graetzel, S. Mhaisalkar, P. P. Boix and N. Mathews, Flexible, Low-temperature, Solution Processed ZnO-based Perovskite Solid State Solar Cells. *Chem Commun* **49**, 11089-11091 (2013).
99. R. Vittal and K. C. Ho, Zinc Oxide Based Dye-sensitized Solar Cells: A Review. *Renew Sust Energy Rev* **70**, 920-935 (2017).
100. J. K. Chen, X. L. He, W. B. Wang, W. P. Xuan, J. Zhou, X. Z. Wang, S. R. Dong, S. Garner, P. Cimo and J. K. Luo, Bendable Transparent ZnO Thin Film Surface Acoustic Wave Strain Sensors on Ultra-thin Flexible Glass Substrates. *J Mater Chem C* **2**, 9109-9114 (2014).
101. J. T. Luo, A. J. Quan, G. X. Liang, Z. H. Zheng, S. Ramadan, C. Fu, H. L. Li and Y. Q. Fu, Love-mode Surface Acoustic Wave Devices Based on Multilayers of TeO₂/ZnO(1120)/Si(100) with High Sensitivity and Temperature Stability. *Ultrasonics* **75**, 63-70 (2017).
102. K. Haga, F. Katahira and H. Watanabe, Preparation of ZnO Films by Atmospheric Pressure Chemical-vapor Deposition using Zinc Acetylacetonate and Ozone. *Thin Solid Films* **343**, 145-147 (1999).
103. R. Muller, F. Huber, O. Gelme, M. Madel, J. P. Scholz, A. Minkow, U. Herr and K. Thonke, Chemical Vapor Deposition Growth of Zinc Oxide on Sapphire with Methane: Initial Crystal Formation Process. *Cryst Growth Des* **19**, 4964-4969 (2019).
104. S. Kabisch, M. Timpel, H. Kirmse, M. A. Gluba, N. Koch and N. H. Nickel, Polarity of Pulsed Laser Deposited ZnO Nanostructures. *Appl Phys Lett* **108**, 083114 (2016).
105. W. T. Chiou, W. Y. Wu and J. M. Ting, Growth of Single Crystal ZnO Nanowires using Sputter Deposition. *Diam Relat Mater* **12**, 1841-1844 (2003).
106. H. Wu and W. Pan, Preparation of Zinc Oxide Nanofibers by Electrospinning. *J Am Ceram Soc* **89**, 699-701 (2006).
107. F. Mohtaram, S. Borhani, M. Ahmadpour, P. Fojan, A. Behjat, H. G. Rubahn and M. Madsen, Electrospun ZnO Nanofiber Interlayers for Enhanced Performance of Organic Photovoltaic Devices. *Solar Energy* **197**, 311-316 (2020).
108. K. Govender, D. S. Boyle, P. B. Kenway and P. O'Brien, Understanding the Factors that Govern the Deposition and Morphology of Thin Films of ZnO from Aqueous Solution. *J Mater Chem* **14**, 2575-2591 (2004).

109. M. Zobel, A. Windmuller, E. M. Schmidt, K. Gotz, T. Milek, D. Zahn, S. A. J. Kimber, J. M. Hudspeth and R. B. Neder, The Evolution of Crystalline Ordering for Ligand-ornamented Zinc Oxide Nanoparticles. *CrystEngComm* **18**, 2163-2172 (2016).
110. K. M. Kumar, B. K. Mandal, E. A. Naidu, M. Sinha, K. S. Kumar and P. S. Reddy, Synthesis and Characterisation of Flower Shaped Zinc Oxide Nanostructures and its Antimicrobial Activity. *Spectrochim Acta A* **104**, 171-174 (2013).
111. Y. Masuda, N. Kinoshita and K. Koumoto, Morphology Control of ZnO Crystalline Particles in Aqueous Solution. *Electrochim Acta* **53**, 171-174 (2007).
112. K. Fujita, K. Murata, T. Nakazawa and I. Kayama, Crystal Shapes of Zinc Oxide Prepared by the Homogeneous Precipitation Method. *J. Ceram* **92**, 227-230 (1984).
113. M. K. Liang, M. J. Lim, A. Sola-Rabada, M. J. Roe and C. C. Perry, New Insights into the Mechanism of ZnO Formation from Aqueous Solutions of Zinc Acetate and Zinc Nitrate. *Chem Mater* **26**, 4119-4129 (2014).
114. R. Parize, J. Garnier, O. Chaix-Pluchery, C. Verrier, E. Appert and V. Consonni, Effects of Hexamethylenetetramine on the Nucleation and Radial Growth of ZnO Nanowires by Chemical Bath Deposition. *J Phys Chem C* **120**, 5242-5250 (2016).
115. M. N. R. Ashfold, R. P. Doherty, N. G. Ndifor-Angwafor, D. J. Riley and Y. Sun, The Kinetics of the Hydrothermal Growth of ZnO Nanostructures. *Thin Solid Films* **515**, 8679-8683 (2007).
116. R. G. Bates and G. D. Pinching, Acidic Dissociation Constant of Ammonium Ion at 0-Degrees to 50-Degrees-C, and the Base Strength of Ammonia. *J Res Nat Bur Stand* **42**, 419-430 (1949).
117. T. H. Hsieh, J. Y. Chen, C. W. Huang and W. W. Wu, Observing Growth of Nanostructured ZnO in Liquid. *Chem Mater* **28**, 4507-4511 (2016).
118. S. Xu, Y. Wei, M. Kirkham, J. Liu, W. Mai, D. Davidovic, R. L. Snyder and Z. L. Wang, Patterned Growth of Vertically Aligned ZnO Nanowire Arrays on Inorganic Substrates at Low Temperature without Catalyst. *J Am Chem Soc* **130**, 14958-14959 (2008).
119. Y. Masuda, N. Kinoshita, F. Sato and K. Koumoto, Site-selective Deposition and Morphology Control of UV- and Visible-light-emitting ZnO Crystals. *Cryst Growth Des* **6**, 75-78 (2006).
120. Y. G. Wei, W. Z. Wu, R. Guo, D. J. Yuan, S. M. Das and Z. L. Wang, Wafer-Scale High-Throughput Ordered Growth of Vertically Aligned ZnO Nanowire Arrays. *Nano Letters* **10**, 3414-3419 (2010).
121. D. L. G. Arellano, J. Bhamrah, J. W. Yang, J. B. Gilchrist, D. W. McComb, M. P. Ryan and S. Heutz, Room-Temperature Routes Toward the Creation of Zinc Oxide Films from Molecular Precursors. *ACS Omega* **2**, 98-104 (2017).
122. Y. H. Kim, J. S. Heo, T. H. Kim, S. Park, M. H. Yoon, J. Kim, M. S. Oh, G. R. Yi, Y. Y. Noh and S. K. Park, Flexible Metal-oxide Devices Made by Room-temperature Photochemical Activation of Sol-gel Films. *Nature* **489**, 128-U191 (2012).
123. Y. F. Zhu, D. H. Fan and W. Z. Shen, Template-free Synthesis of Zinc Oxide Hollow Microspheres in Aqueous Solution at Low Temperature. *J Phys Chem C* **111**, 18629-18635 (2007).
124. W. Zhao, X. Y. Song, Z. L. Yin, C. H. Fan, G. Z. Chen and S. X. Sun, Self-assembly of ZnO Nanosheets into Nanoflowers at Room Temperature. *MRS Bull* **43**, 3171-3176 (2008).
125. H. L. Cao, X. F. Qian, Q. Gong, W. M. Du, X. D. Ma and Z. K. Zhu, Shape- and Size-controlled Synthesis of Nanometre ZnO from a Simple Solution Route at Room Temperature. *Nanotechnology* **17**, 3632-3636 (2006).
126. Y. C. Qi, C. Zhang, S. T. Liu, Y. Q. Zong and Y. Men, Room-temperature Synthesis of ZnO@GO Nanocomposites as Anode for Lithium-ion Batteries. *J Mater Res* **33**, 1506-1514 (2018).
127. N. J. Nicholas, G. V. Franks and W. A. Ducker, The Mechanism for Hydrothermal Growth of Zinc Oxide. *CrystEngComm* **14**, 1232-1240 (2012).
128. B. Song, X. Cui, Y. Q. Wang, L. F. Si, Z. X. Kou, W. W. Tian, C. Yi and Y. M. Sun, Controllable Growth of Unique Three-Dimensional Layered Basic Zinc Salt/ZnO Binary Structure. *Cryst Growth Des* **16**, 4877-4885 (2016).
129. A. Tarat, R. Majithia, R. A. Brown, M. W. Penny, K. E. Meissner and T. G. G. Maffei, Synthesis of Nanocrystalline ZnO Nanobelts via Pyrolytic Decomposition of Zinc Acetate Nanobelts and their Gas Sensing Behavior. *Surf.Sci* **606**, 715-721 (2012).
130. W. L. Feng, B. C. Wang, P. Huang, X. D. Wang, J. Yu and C. W. Wang, Wet Chemistry Synthesis of ZnO Crystals with Hexamethylenetetramine (HMTA): Understanding the Role of HMTA in the Formation of ZnO Crystals. *Mat Sci Semicon Proc* **41**, 462-469 (2016).
131. Y. B. Wang, S. Wang and X. Lu, In Situ Observation of the Growth of ZnO Nanostructures Using Liquid Cell Electron Microscopy. *J Phys Chem C* **122**, 875-879 (2018).
132. Y. Liu, K. P. Tai and S. J. Dillon, Growth Kinetics and Morphological Evolution of ZnO Precipitated from Solution. *Chem Mater* **25**, 2927-2933 (2013).
133. G. Amin, M. H. Asif, A. Zainelabdin, S. Zaman, O. Nur and M. Willander, Influence of pH, Precursor Concentration, Growth Time, and Temperature on the Morphology of ZnO Nanostructures Grown by the Hydrothermal Method. *J Nanomater* **2011**, 1-9 (2011).
134. A. H. M. Leung, S. D. Pike, A. J. Clancy, H. C. Yau, W. J. Lee, K. L. Orchard, M. S. P. Shaffer and C. K. Williams, Layered Zinc Hydroxide Monolayers by Hydrolysis of Organozincs. *Chem Sci* **9**, 2135-2146 (2018).
135. A. Moezzi, M. Cortie and A. McDonagh, Transformation of Zinc Hydroxide Chloride Monohydrate to Crystalline Zinc Oxide. *Dalton Trans* **45**, 7385-7390 (2016).
136. A. Moezzi, M. B. Cortie and A. M. McDonagh, Zinc Hydroxide Sulphate and its Transformation to Crystalline Zinc Oxide. *Dalton Trans* **42**, 14432-14437 (2013).
137. A. Moezzi, A. McDonagh, A. Dowd and M. Cortie, Zinc Hydroxyacetate and Its Transformation to Nanocrystalline Zinc Oxide. *Inorg Chem* **52**, 95-102 (2013).

138. B. Song, Y. Q. Wang, X. Cui, Z. X. Kou, L. F. Si, W. W. Tian, C. Yi, T. Wei and Y. M. Sun, A Series of Unique Architecture Building of Layered Zinc Hydroxides: Self-Assembling Stepwise Growth of Layered Zinc Hydroxide Carbonate and Conversion into Three-Dimensional ZnO. *Cryst Growth Des* **16**, 887-894 (2016).
139. V. Strano, R. G. Urso, M. Scuderi, K. O. Iwu, F. Simone, E. Ciliberto, C. Spinella and S. Mirabella, Double Role of HMTA in ZnO Nanorods Grown by Chemical Bath Deposition. *J Phys Chem C* **118**, 28189-28195 (2014).
140. R. Devaraj, K. Venkatachalam, K. Saravanakumar, P. M. Razad and K. Mahalakshmi, Role of Hexamine: Growth of Multiarmed ZnO Nanorods and Evidence of Merging due to Lateral Growth. *J Mater Sci-Mater El* **27**, 12201-12208 (2016).
141. S. E. R. Tay, A. E. Goode, J. N. Weker, A. A. Cruickshank, S. Heutz, A. E. Porter, M. P. Ryan and M. F. Toney, Direct in Situ Observation of ZnO Nucleation and Growth via Transmission X-ray Microscopy. *Nanoscale* **8**, 1849-1853 (2016).
142. K. M. McPeak, M. A. Becker, N. G. Britton, H. Majidi, B. A. Bunker and J. B. Baxter, In Situ X-ray Absorption Near-Edge Structure Spectroscopy of ZnO Nanowire Growth During Chemical Bath Deposition. *Chem Mater* **22**, 6162-6170 (2010).
143. P. Abellan, T. H. Moser, I. T. Lucas, J. W. Grate, J. E. Evans and N. D. Browning, The Formation of Cerium(III) Hydroxide Nanoparticles by a Radiation Mediated Increase in Local pH. *RSC Adv* **7**, 3831-3837 (2017).
144. H. Su, B. L. Mehdi, J. P. Patterson, N. A. J. M. Sommerdijk, N. D. Browning and H. Friedrich, Growth Kinetics of Cobalt Carbonate Nanoparticles Revealed by Liquid-Phase Scanning Transmission Electron Microscopy. *J Phys Chem C* **123**, 25448-25455 (2019).
145. T. F. Long, S. Yin, K. Takabatake, P. Zhnag and T. Sato, Synthesis and Characterization of ZnO Nanorods and Nanodisks from Zinc Chloride Aqueous Solution. *Nanoscale Res Lett* **4**, 247-253 (2009).

Chapter 2

Stability-limited Ion-exchange of Calcium with Zinc in Biomimetic Hydroxyapatite

The exchange of Ca^{2+} ions in hydroxyapatite (HAp) with Zn^{2+} ions into Zn-HAp is of interest for applications ranging from bone tissue engineering to the use as a precursor in subsequent ion-exchange reactions. Previous studies, using direct synthesis, showed that ~ 20 mol% Zn^{2+} ions can be incorporated into HAp, before byproducts are observed. However, this is realized at the cost of a loss in crystallinity and control over crystal size and shape with an increasing amount of Zn^{2+} ion incorporation. In this work we investigate a simple post synthetic ion-exchange strategy for the formation of Zn-HAp. By merely exposing HAp to high concentrations of zinc nitrate in water, up to 22 mol% of the Ca^{2+} ions could be displaced by Zn^{2+} ions without any measured loss in crystallinity and preservation of crystallite size and shape. It was found that the incorporation of Zn^{2+} ions destabilizes the HAp crystals resulting in their gradual dissolution and reprecipitation. Consequently, promoting the exchange of Ca^{2+} with Zn^{2+} ions using increased reaction times, sonication and increased temperature results in an increased dissolution of HAp and precipitation of hopeite crystals, thereby preventing the formation of more zinc rich Zn-HAp.

This chapter has been adapted from:

M. M. J. van Rijt[‡], S. W. Nootboom[‡], A. van der Weijden, W. L. Noorduyn and G. de With, Stability-limited Ion-exchange of Calcium with Zinc in Biomimetic Hydroxyapatite, *Materials & Design*, 2021, *under peer review*.

“Would you tell me, please, which way I ought to go from here?” “That depends a good deal on where you want to get to” said the Cat. “I don’t much care where-” said Alice “Then it doesn’t matter which way you go,” said the Cat “so long as I get somewhere,” Alice added as an explanation. “Oh, you’re sure to do that,” said the Cat, “if only you walk long enough.””

Lewis Carroll, *Alice’s Adventures in Wonderland*, 1865.

2.1. HAp Ion-exchange

Hydroxyapatite (HAp, $\text{Ca}_{10}(\text{PO}_4)_6(\text{OH})_2$) is one of the most abundant minerals in biology. In both bone and teeth HAp is mineralized *intra* and *inter* fibrillary in collagen providing strength to these materials^[1, 2]. Synthetically highly crystalline HAp can be formed in dispersion^[3], although biological HAp is rather ill-defined^[4]. While HAp is the naturally occurring mineral in collagen^[5], collagen has thus far only been mineralized to a limited extent via direct synthesis^[6] with other materials including calcium carbonate^[7], silica^[8], yttria-stabilized zirconia^[9] and iron oxides^[10].

To extend the range of materials that can be incorporated into collagen and other organic templates, an alternative strategy would be the use of ion-exchange^[11, 12]. The preservation of crystallite shape and location should allow for a post-synthetic ion-exchange of the mineral inside the template, avoiding the need to investigate new mineralization protocols. The substitution of both PO_4^{3-} and Ca^{2+} ions in HAp with a range of respective anions and cations is possible^[13]. However, the relatively high lattice energy of HAp and apatite species in general will make anion exchange challenging^[11, 14-16]. The substitution of Ca^{2+} ions with Zn^{2+} ions (further on referred to as Ca and Zn), leading to Zn-HAp, has been investigated for a range of applications including its (antimicrobial) coatings^[17-19], dental applications^[20], drug or DNA delivery^[21, 22], bone tissue engineering^[23-25], improvement in bio-activity and selective protein adsorption^[26, 27]. By substituting Ca with Zn during HAp synthesis 15 – 20 mol% of the Ca could be replaced with Zn^[20, 23, 28-30]. Increasing the amount of Zn in the reaction medium results in a progressive increase in Zn substitution, but with an associated decrease in crystallinity and control over the crystal size and shape^[20, 28]. Furthermore increasing the concentration of Zn in the reaction medium above 15 – 20 mol% leads to the undesired formation of $\text{CaZn}_2(\text{PO}_4)_2 \cdot 2\text{H}_2\text{O}$ ^[23, 29, 30] and $\text{Zn}_3(\text{PO}_4)_2 \cdot 2\text{H}_2\text{O}$ (hopeite)^[29].

Apart from its use as an heavy metal remover as e.g. discussed by Oliva et al.^[31], substituting Ca by Zn via post-synthetic ion-exchange for the specific goal of obtaining Zn-HAp has received limited attention. Hayakawa et al.^[26] exposed HAp to up to 11.5 mM of aqueous $\text{Zn}(\text{NO}_3)_2$ solutions for 24 h at 80 °C and they exchanged 2.3 mol% of Ca with Zn without loss in crystallinity. Wang et al.^[32] exposed a HAp slurry to 1 M $\text{Zn}(\text{NO}_3)_2$ solution for 7 days at 37 °C resulting in a 9.5 mol% exchange of Ca with Zn for HAp with the formation of β -tricalcium phosphate as a byproduct. Using organic solvents, Chen et al.^[33] were able to incorporate a range of cations in HAp including Zn. A maximum of 20.5 mol% could be exchanged in the case of iron^[33]. These processes generally result in a very limited Zn incorporation of less than 20 mol%, require significantly longer than 24 h reaction times or need to be performed in organic solvents.

Here ion-exchange^[11, 12] of Ca with Zn in HAp to Zn-HAp in an aqueous dispersion was investigated by a combination of fast screening experiments, directly performed on TEM grids, in combination with more traditional ion-exchange experiments on dispersed HAp powders. Exposing synthetic HAp to a significant concentration of $\text{Zn}(\text{NO}_3)_2$, it was found that ~ 20 mol% of Ca can be exchanged with Zn within a minute while preserving morphology and crystallinity. Further promoting the incorporation of Zn into Zn-HAp by using increased exposure time or increased temperature only results in a minimal increase in incorporated Zn. The main reason for this seems to be the destabilizing effect of the Zn incorporated into the HAp crystals close to 20 mol%. This causes the gradual dissolution of the Zn-HAp crystals, followed by the precipitation of hopeite. Nevertheless, the method used leads to the rapid incorporation of what seems to be the maximum of Zn in HAp.

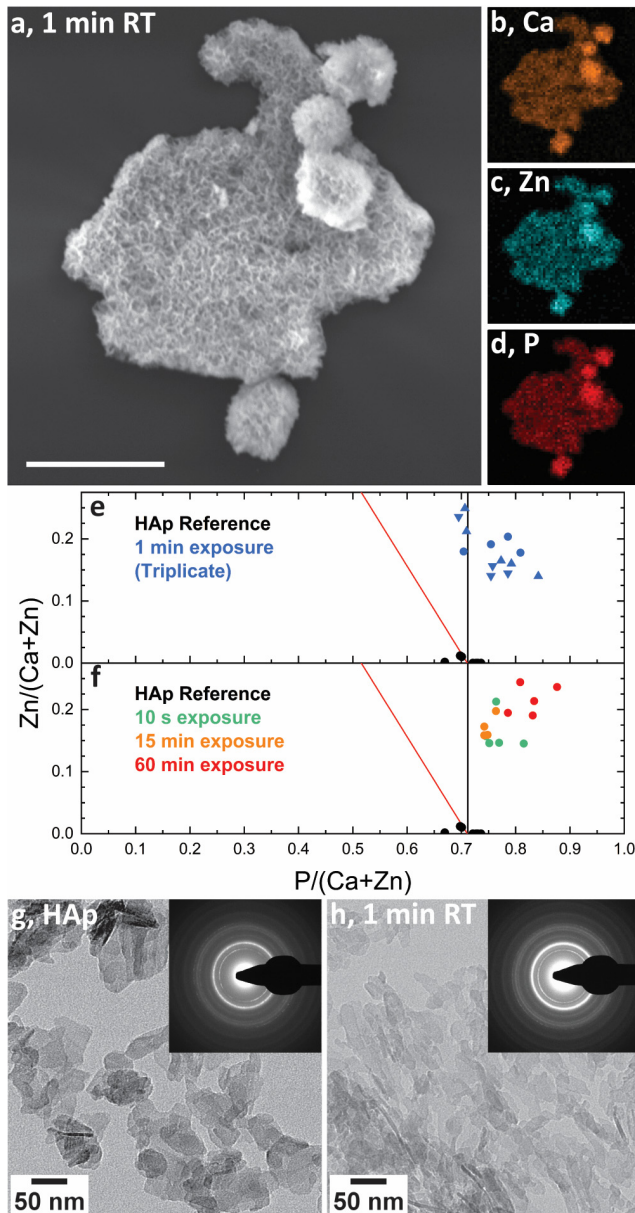


Figure 2.1 SEM image of HAp clusters after exposure to 1M $\text{Zn}(\text{NO}_3)_2 \cdot 6\text{H}_2\text{O}$ solution (a, scale bar: 5 μm) and the corresponding EDX signals of Zn, Ca and P (b-d). quantified EDX atomic ratios of $\text{Zn}/(\text{Ca}+\text{Zn})$ against $\text{P}/(\text{Ca}+\text{Zn})$ for apatite exposed to $\text{Zn}(\text{NO}_3)_2 \cdot 6\text{H}_2\text{O}$ at RT for 1 min in triplicate (e, using a different symbol for each sample) and varying exposure time at RT (f). The black line corresponds to Ca - Zn ion-exchange, whereas the red line indicates maximum Zn adsorption to the HAp crystals. Conventional TEM images of as synthesized HAp (g) and after exposure to $\text{Zn}(\text{NO}_3)_2 \cdot 6\text{H}_2\text{O}$ solution for 1 min (h); performed directly on a TEM grid. Inset: SEAD results of similar regions, observed spacings match with HAp (g-h).

2.2. Incorporation of Zinc into HAp

Ion-exchange was performed by exposing HAp to a 1 M $\text{Zn}(\text{NO}_3)_2 \cdot 6\text{H}_2\text{O}$ solution set to pH 2.9 by adding 0.1 M nitric acid. To rapidly probe the incorporation of Zn into HAp, HAp-coated continuous carbon TEM grids were floated on a droplet of $\text{Zn}(\text{NO}_3)_2$ solution for 1 min, followed by washing (Section 2.7). SEM imaging showed the presence of clusters of HAp before and after the reaction (Fig. 2.1a). SEM-EDX mapping on these clusters was used to investigate the chemical composition. From the EDX data quantitatively two values were compared (Fig. 2.1b-e): the ratio of $\text{P}/(\text{Ca}+\text{Zn})$ to identify the occurrence of ion-exchange versus adsorption and the $\text{Zn}/(\text{Ca}+\text{Zn})$ which indicates the rate of ion-exchange. No drop in $\text{P}/(\text{Ca}+\text{Zn})$ ratio was measured suggesting that Ca is exchanged for Zn rather than the adsorption of Zn to the HAp exterior. Nevertheless, the $\text{P}/(\text{Ca}+\text{Zn})$ ratio increased, possibly indicating the introduction of cation hole defects. After 1 min exposure time, a $\text{Zn}/(\text{Ca}+\text{Zn})$ ratio of about 0.18 ± 0.07 could be obtained, implying that Zn ion-exchange has occurred replacing approximately 20 mol% of the Ca with Zn.

The influence of the procedure on crystallite shape was investigated using conventional TEM. This showed that nanometer-sized platelets were present both before and after the reaction (Fig. 2.1g,h), with a similar length (before 400 ± 138 nm, after 380 ± 171 nm) and width (before 170 ± 70 nm, after 170 ± 64 nm). The crystallinity was further probed by using Selective Area Electron Diffraction (SAED) measurements. No changes in diffraction spacings could be observed before and after ion-exchange, indicating that the crystalline structure remains intact (insets of Fig. 2.1 g,h). Note that, given the accuracy of the SAED measurements, this does not exclude that minor shifts in specific spacings might have occurred (ESI section 1).

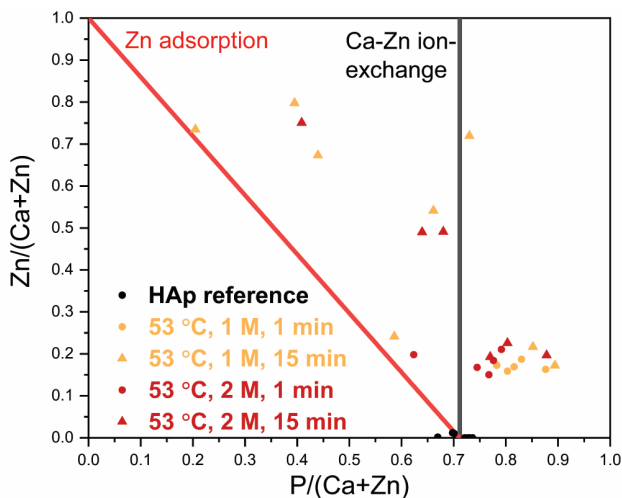


Figure 2.2 Quantified EDX atomic ratios of $\text{Zn}/(\text{Ca}+\text{Zn})$ against $\text{P}/(\text{Ca}+\text{Zn})$ for apatite exposed to $\text{Zn}(\text{NO}_3)_2 \cdot 6\text{H}_2\text{O}$ at 53°C at varying concentrations and time.

To determine if the incorporation of Zn can be modulated by the exposure time to the $\text{Zn}(\text{NO}_3)_2$ solution, the reaction was repeated at 10 s, 15 min and 60 min. Again SEM-EDX measurements showed a slightly increased $\text{P}/(\text{Ca}+\text{Zn})$ value for all reaction times, indicating the predominant occurrence of ion-exchange over that of adsorption. With increasing reaction time, a $\text{Zn}/(\text{Ca}+\text{Zn})$ ratio of 0.16 ± 0.03 (10 s), 0.18 ± 0.07 (1 min), 0.17 ± 0.01 (15 min) and 0.22 ± 0.02 (60 min) was obtained (Fig. 2.1f). This shows that most of the ~ 15 mol% Zn is incorporated rapidly within the first 10 s of exposure. After significantly

increasing the exposure time to 60 min only a minor increase in the incorporated amount to ~22 mol% Zn can be achieved. This suggests that there is either a diffusion or ion-exchange barrier, preventing the incorporation of more Zn. Overall it shows that close to 20 mol% of Zn can be incorporated into HAp by exposure to $\text{Zn}(\text{NO}_3)_2$ under aqueous RT conditions, a result which is comparable to direct Zn-HAp synthesis.

2.3. Temperature Effects

Generally, reaction and diffusion barriers can be overcome by elevating the reaction temperature. Therefore the experiments were repeated at 53 °C using $\text{Zn}(\text{NO}_3)_2 \cdot 6\text{H}_2\text{O}$ solution concentrations of both 1 M and 2 M using either 1 min or 15 min exposure time (Fig. 2.2, Section 2.7). SEM-EDX studies after exposure showed that in all cases the Zn concentration in solution had no effect and therefore the given averages are combinations from both concentrations. EDX studies after 1 min ion-exchange at 53 °C showed a $\text{Zn}/(\text{Ca}+\text{Zn})$ ratio of 0.18 ± 0.02 , similar to the value obtained at RT experiments. After 15 min reaction time, however, a strong increase in $\text{Zn}/(\text{Ca}+\text{Zn})$ ratio was observed to 0.44 ± 0.24 . The $\text{P}/(\text{Ca}+\text{Zn})$ ratio showed a strong variation between 0.2 and 0.9. In most regions a measured increase in $\text{Zn}/(\text{Ca}+\text{Zn})$ ratio corresponded with a strong decrease in $\text{P}/(\text{Ca}+\text{Zn})$ ratio (Fig. 2.2), suggesting that adsorption of Zn is at least in part responsible for the relative increase in Zn. Notably multiple regions were identified that only had a minimal decrease in $\text{P}/(\text{Ca}+\text{Zn})$ ratio indicating minimal adsorption, while showing a $\text{Zn}/(\text{Ca}+\text{Zn})$ ratio as high as 0.8. TEM studies after ion-exchange further showed large populations of relatively small Zn-HAp crystals (Fig. A2.1, 200 ± 79 nm by 80 ± 32 nm) compared to the original crystal (400 ± 138 nm by 170 ± 70 nm). This could indicate that the stress induced by Zn substitution induces cracking or that at elevated temperature dissolution of the Zn-HAp starts to occur. Performing the procedure at 80 °C only showed the incidental presence of particles (Fig. A2.2), preventing further EDX studies. Overall, the data does suggest that a higher incorporation might be obtained, both by increasing exposure time and temperature. However, this is at a notable cost of uniformity throughout the sample, indicating full Zn incorporation may not be feasible.

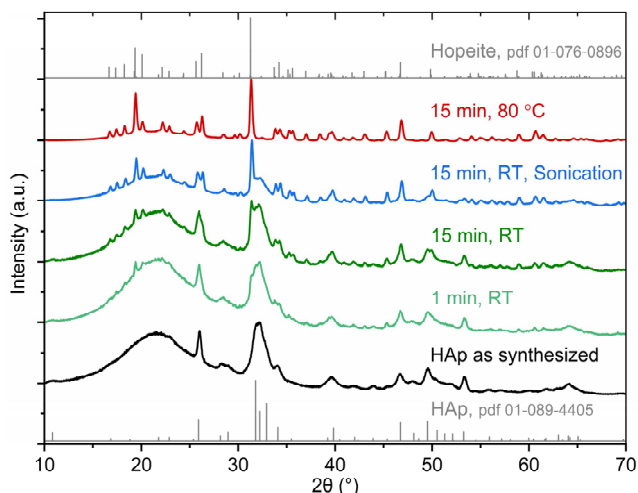


Figure 2.3 pXRD pattern of as synthesized HAp (black) and HAp dispersed in 1M $\text{Zn}(\text{NO}_3)_2 \cdot 6\text{H}_2\text{O}$ solution for 1 min at RT (light-green), 15 min at RT (dark-green), 15 min at RT while sonicating (blue) and 15 min at 80 °C (red). The broad pXRD signal visible at about 20° is due to the substrate.

2.4. Exchange of Dispersed HAp Crystals

To supplement on-grid studies, the exchange procedure was also performed on dispersed HAp crystals exposed for 15 min at 80 °C to a preheated 1 M $\text{Zn}(\text{NO}_3)_2 \cdot 6\text{H}_2\text{O}$ solution (Section 2.7). Powder X-Ray Diffraction (pXRD) of the purified product (Fig. 2.3) showed the dominant formation of hopeite with no (Zn-)HAp signals being identified. SEM studies on the product dominantly showed highly faceted micrometer-sized hopeite sheets with an ill-defined shape. (Fig. 2.4a-b). The observation of hopeite is in sharp contrast with the incidentally observed HAp particles when using the on-grid procedure.

Further experiments on dispersed HAp crystals show that the formation of hopeite is not restricted to high temperature conditions. pXRD analysis of HAp exposed to a $\text{Zn}(\text{NO}_3)_2$ solution shows the presence of hopeite signals after as little as 1 min exposure time at RT (Fig. 2.3). These hopeite signals become more pronounced with increasing exposure time (15 min) and sonication. SEM studies (Fig. 2.4c-d) show, in contrast to the experiments performed at 80 °C, micrometer-sized sheets that are rectangular in shape, very similar to previously synthesized hopeite crystals by Parhi et al.^[34] The sheets formed at RT are generally clean. Many of the hopeite sheets formed under sonication at RT are covered with small particles, presumably (Zn-)HAp. The presence of the latter could be due to better dispersion due to sonication.

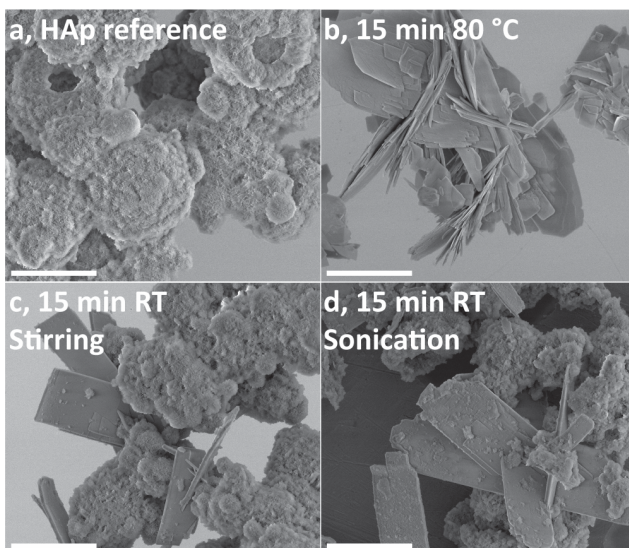


Figure 2.4 SEM images of HAp before ion-exchange (a) and Zn-HAp and Hopeite crystals obtained after HAp exposure to 1 M $\text{Zn}(\text{NO}_3)_2 \cdot 6\text{H}_2\text{O}$ solution at pH 2.7 for 15 min at 80 °C (b), 15 min stirring at RT (c), and 15 min sonication at RT (d). Scale bar: 10 μm .

2.5. Transformation to Hopeite

There are two possible pathways for the transformation of Zn-HAp to hopeite. The first is the dissolution of Zn-HAp followed by reprecipitation into hopeite. A second route would be the direct transformation into hopeite. The initial nanometer-sized Zn-HAp crystals are significantly smaller than the formed micrometer-sized hopeite crystals, which is highly unusual for a direct transformation strategy. Furthermore, hopeite crystals were not observed when using the on-grid exchange procedure although

their presence would be expected for a direct transformation. Given that the grids are floated on or suspended in the $\text{Zn}(\text{NO}_3)_2$ solution (Fig. A2.3), dissolution and recrystallization to hopeite probably predominantly takes place in the solution phase with the crystals subsequently sedimenting in the liquid phase, a process matching observations. This leaves dissolution and reprecipitation as the most likely mechanism.

A dissolution reprecipitation mechanism, however, does not preclude local interaction between hopeite and Zn-HAp crystals. It is possible that local dissolution of the Zn-HAp crystals is required for the formation of the large hopeite sheets. Indeed, using conventional TEM on the powder sample formed at 15 min at RT showed Zn-HAp crystals aggregated on hopeite crystals. Specifically, not well developed crystal facets were covered with Zn-HAp crystals (Fig. 2.5). One suggestion is that the dissolution reprecipitation process occurs locally. Unfortunately, the hopeite crystals proved too thick for cryoTEM imaging, preventing the time-resolved studies of their formation *in-situ*. This makes it unclear whether these Zn-HAp filled defects are due to drying effects, the presence of Zn-HAp or a local mineralization process.

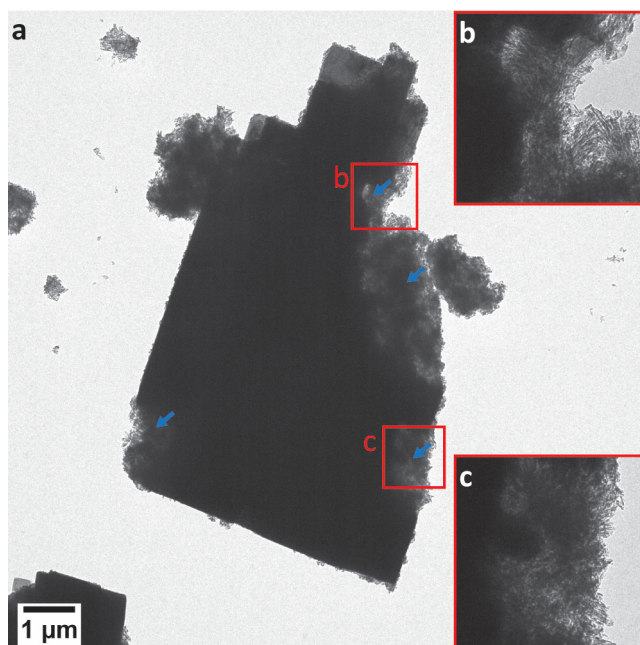


Figure 2.5 Conventional TEM image (a) of a hopeite crystal with Zn-HAp crystals in observed crystal defects (blue arrows) in a 15 min RT experiments. Higher magnification insets (b-c) of hopeite Zn-HAp interface regions.

Parhi et al.^[34] demonstrated that, at low pH, hopeite can be synthesized in water at room temperature by mixing ZnCl_2 and sodium phosphate solutions. This suggests that, if Zn and PO_4^{3-} ions are present in solution, hopeite is the preferred crystallization product although not necessarily the thermodynamically most stable one. Therefore, to identify whether the formation of hopeite at higher reaction temperatures is a simple dissolution and reprecipitation process caused by the natural dissolution of HAp under these conditions, a control experiment at 80 °C at pH 2.7 in the absence of Zn was performed. After the reaction a significant amount of white powder was collected. pXRD and TEM studies (Fig. A2.4) showed the presence of pure HAp crystals. This demonstrates that Zn is essential for the dissolution process.

Previously mentioned EDX studies show that roughly 20 mol% of the Ca can be exchanged with Zn. Since the spatial resolution of SEM-EDX analysis is limited it cannot distinguish between ions present on the surface or throughout the crystal. The HAp crystals investigated have a thickness of about 4.2 ± 0.69 nm based on measurements on tilted crystals observed by cryoTEM (Fig. A2.5). A HAp unit cell has a c-axis of $\sim 7 \text{ \AA}$ ^[35], meaning a single crystal is ~ 6 unit cells in thickness. If 20 mol% of the Ca in HAp is exchanged with Zn in a surface layer, this would give a layer thickness of about half a unit cell on either side. To support such an assumption, a value of the diffusion constant of Zn in HAp would be helpful. However, direct data are absent and given the broad range of experimentally determined activation energies for other ions which do not uniquely relate to the ionic radius, it also appeared to be unfeasible to reliably estimate the diffusion constant of Zn into apatite^[36, 37]. Hence it is not realistic to determine the positioning of Zn throughout the Zn-HAp crystals based on experimental evidence or calculations. Therefore, to gain more insight the results were compared to existing literature.

In literature, using direct synthesis, a HAp exchange limit of ~ 20 mol% Ca with Zn was obtained, the distribution of which is expected to be homogenous. Furthermore, increasing the Zn fraction above 20 mol% during synthesis results in increased amounts of hopeite. In addition, performing ion-exchange with a range of cations in organic solvents, a similar degree of cation incorporation was achieved by Chen et al.^[33] These observations combined with the results from our work suggest that the Zn is homogeneously distributed throughout the crystal. This indicates that the incorporation of Zn into HAp is limited to about 20 mol%. The ionic radius of Zn (0.88 Å) is smaller than of Ca (1.14 Å)^[38]. Incorporating Zn therefore results in internal stress in the crystal. If the crystal is unable to reconfigure to release this stress, its stability decreases, and, when in contact with water, possibly resulting in dissolution eventually. Calculations by Flora et al.^[17] indicate that fully converted Zn-HAp ($\text{Zn}_{10}(\text{PO}_4)_6(\text{OH})_2$) has a negative Gibbs energy of dissolution, matching our inference. This would mean that hopeite is not only formed because it is the most preferred crystal at this low pH and Zn-rich conditions, but that the Zn-HAp is simply too unstable to exist under experimental conditions. It also means that it is highly unlikely that more than about 20 mol% of Zn incorporation in Zn-HAp can be achieved in absence of any stabilization agents in water.

2.6. Conclusion

Exposing HAp to a simple aqueous ion-exchange strategy, up to ~ 20 mol% of the Ca atoms could consistently be replaced with Zn atoms without influencing the morphology or crystallinity. The initial exchange with Zn occurs rapidly reaching ~ 16 mol% exchange within seconds. A larger amount of Zn could be incorporated with increasing reaction time (up to 22 mol% after 60 min) or by elevating the reaction temperature (incidental high conversion). The incorporation of Zn decreases the stability of the resulting Zn-HAp, resulting in an increased dissolution of these crystals and reprecipitation into hopeite crystals with increasing Zn incorporation. The limited stability of the Zn-HAp crystals under aqueous conditions in the absence of stabilization agents, therefore, does not permit the homogenous formation of a more Zn-rich Zn-HAp.

2.7. Materials and Methods

2.7.1. Materials

Acetone (99%, Technical) was acquired from VWR, sodium chloride (NaCl, > 99,5%, BioXtra), sodium hydroxide (NaOH, > 98%, BioXtra) and hydrochloric acid (HCl, 37%, ACS reagent) were acquired from Sigma Aldrich, zinc nitrate hexahydrate ($\text{Zn}(\text{NO}_3)_2$, 98%, ACS reagent) was acquired from Acros organics, calcium carbonate (CaCl_2 , 90%, anhydrous), di-potassium hydrogen phosphate (K_2HPO_4 , 99 %, pro

analysis), Trizma® base ($\text{NH}_2\text{C}(\text{CH}_2\text{OH})_3$, 99.7%, pro analysi), Nitric acid (HNO_3 , 65 % EMSURE) were acquired from MERCK. All chemicals were used as received unless stated otherwise.

2.7.2. Synthesis of HAp Nanoplatelets

HAp nanoplatelets were synthesized according to the procedure described by Habraken et al.^[3] A buffer solution was prepared by dissolving 50 mM Trizma base and 150 mM NaCl in pure water. The pH was set to 7.4 using concentrated HCl solution. Phosphate and calcium stock solutions were prepared by adding either 10 mM K_2HPO_4 or CaCl_2 to the buffer solution. Both stock solutions were set to pH 7.4 by dropwise addition of 0.1 M HCl or NaOH. The reaction was initiated by adding phosphate stock solution to calcium stock solution in a ratio of 0.7:1.0 in a beaker. The reaction mixture was stirred for at least 4 h depending on volume under magnetic stirring. The HAp nanoplatelets were isolated by centrifugation using either an Optima L-90K ultracentrifuge equipped with a Type 70 Ti rotor at 20,000 rpm for 20 min or an Eppendorf MiniSpinPlus equipped with a F-45-12-11 rotor at 14,500 rpm for 15 min. The so-obtained pellets were redispersed in pure water followed by another centrifugation step. This procedure was performed twice. After centrifugation the product was dried overnight in a 60 °C oven.

2.7.3. On-grid Ion-exchange Experiments

Several mg of HAp was dispersed in pure water and 10 μl of the resulting HAp dispersion was placed on a glow discharged continuous carbon Au grid for 40 s. The droplet was removed by sideling manual blotting using a filter paper. The pH of the $\text{Zn}(\text{NO}_3)_2 \cdot 6\text{H}_2\text{O}$ ion-exchange solution was preadjusted to pH 2.9, unless otherwise stated, by dropwise addition of 0.1 M nitric acid. For RT experiments a HAp-loaded grid was placed on a 300 μl droplet of $\text{Zn}(\text{NO}_3)_2 \cdot 6\text{H}_2\text{O}$ solution for the targeted amount of time. For on-grid exchange at higher temperature, a HAp loaded grid clamped in Teflon coated tweezers was submerged vertically using for the targeted amount of time in a preheated $\text{Zn}(\text{NO}_3)_2 \cdot 6\text{H}_2\text{O}$ solution. After either ion-exchange reaction procedure, excess Zn was removed by washing in freshly prepared acetone and pure water (twice).

2.7.4. Powder Ion-exchange Experiments

For ion-exchange on HAp powder, > 10 mg of HAp was dispersed in 1 mL of pure-water, which was injected in fluent motion into 15 mL of 1 M $\text{Zn}(\text{NO}_3)_2 \cdot 6\text{H}_2\text{O}$ solution. For short reactions (< 1 min) the dispersion was dispersed by shaking. For reactions longer than 1 min the dispersion was either stirred or sonicated (the latter at room temperature only) to prevent sedimentation. After a reaction time of 1 to 15 min (and cooling on an ice bath in case of heated reactions), the powder was purified and dried by centrifugation, similar to as during the synthesis of HAp, or by rapid filtration over a GE Whatman® 7 μm filter paper.

2.7.5. Analysis

pH measurements were performed using a Metrohm (6.0234.100) 125 mm unitrode pH probe.

Scanning Electron Microscopy (SEM) and Energy Dispersive X-ray (EDX) measurements were conducted using either a Phenom ProX (Thermo Fischer Scientific) operated at 5 kV (for imaging) using a backscattering detector and at 15 kV (for EDX mapping) or on a Verios 460 (Thermo Fischer Scientific) operated at 5 kV and 100 pA (for imaging) and using an circular Everhart-Thornley backscatter detector at 30 kV (for EDX analysis). Elemental quantification was performed using the built-in Phenom software or AZtec 2.4, respectively, based on internal device calibrations. For every reaction condition at least 5 different areas were mapped using EDX. Regular SEM imaging was conducted using a Quanta 3D (Thermo Fischer Scientific) operated at 5.0 kV which was equipped with a field emission gun and an ETL secondary electron detector.

Transmission Electron Microscopy (TEM) and selected area electron diffraction (SAED) images were collected on a Tecnai T20 (Thermo Fischer Scientific) operated at 200 kV, equipped with a 4096×4096 pixels CETA CMOS camera.

Size analysis of the HAp particles was performed by judiciously choosing representative particles in representative images, and measuring their length, width and thickness manually using an in-house Matlab script.

Powder X-ray diffraction (pXRD) measurements were performed on a MiniFlex 600 diffractometer operated at 40 kV and 15 mA using Cu $K\alpha$ radiation. Automatic peak assignments were made by the PDXL 2 software.

Cryogenic transmission electron microscopy (CryoTEM) samples were prepared by depositing 3 μ l of a dispersion on a 200 mesh Au grid covered with a Quantifoil R 2/2 holey carbon films (QuantifoilMicro Tools GmbH, part of SPT Life Sciences group). An automated vitrification robot (TFS, Vitrobot Mark III) was used for blotting and plunging in liquid ethane. All TEM grids were surface plasma treated for 40 s using a Cressington 208 carbon coater prior to use. CryoTEM studies were performed on the TU/e cryoTITAN (Thermo Fischer Scientific) equipped with a field emission gun (FEG), a postcolumn Gatan Energy Filter (model 2002) and a post-GIF $2k \times 2k$ Gatan CCD camera (model 794). The microscope was operated at 300 kV acceleration voltage in bright field mode and with zero-loss energy filtering.

2.8. Appendix A2

A2.1 Selected Area Electron Diffraction Resolution

In literature the exchange of Ca^{2+} with Zn^{2+} or other ions can result in a small observed pXRD shift of up to 0.2° for the (002) plane, e.g. from 26.0° to 26.2° in 2θ .^[26, 33] Using SAED the reciprocal of the lattice D spacing is measured $1/D$. The D spacing is related to the angle 2θ measured in pXRD as shown in Eq. 2.1, using a wavelength λ of 1.5406 \AA and a reflection order n of 1.

$$n\lambda = 2D\sin(\theta) \quad (2.1) \quad D = \frac{n\lambda}{2\sin(\theta)} \quad (2.2)$$

Rewriting Eq. 2.1 into Eq. 2.2 a reciprocal D spacing of 2.92 1/nm^{-1} and 2.94 nm^{-1} is obtained for a 2θ of 26.0° to 26.2° , respectively. At a pixel size is 0.0165 nm^{-1} , this shift would then roughly equal only 1 pixel. In acquired SAED data the signal arising from this spacing is measured between a reciprocal D spacing of 2.85 nm^{-1} and 2.98 nm^{-1} making it unrealistic to determine this minor shift.

A2.2 Figures

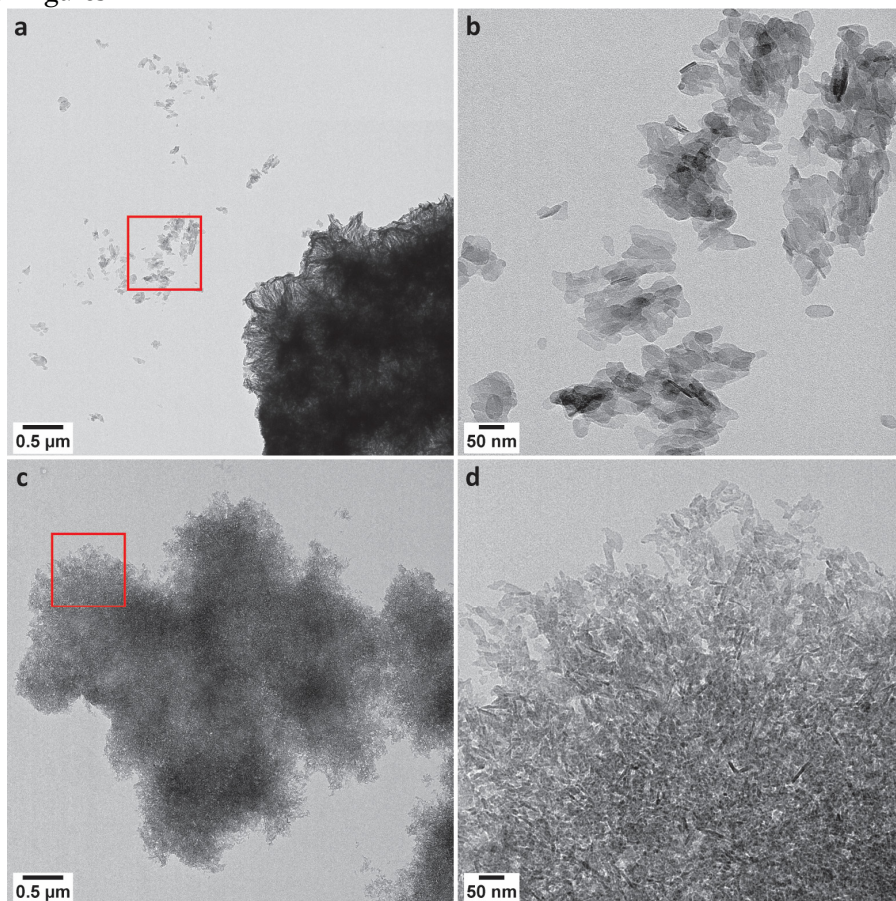


Figure A2.1 TEM images of HAp crystals before (a,b) and after (c,d) 15 min exposure to $1 \text{ M Zn(NO}_3)_2 \cdot 6\text{H}_2\text{O}$ at 53°C . Panels b and d are higher magnifications of the indicated regions in figure a, c, respectively.

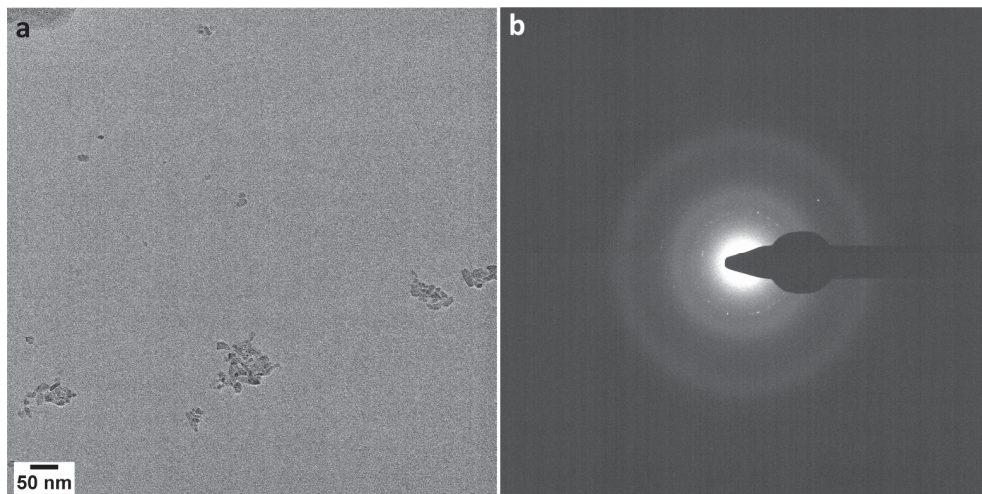
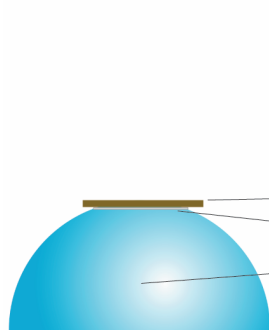


Figure A2.2 TEM image (a) and the corresponding SAED (b) of incidentally observed HAp platelets after on-grid exposure of HAp to 1 M $\text{Zn}(\text{NO}_3)_2 \cdot 6\text{H}_2\text{O}$ for 15 minutes at 80 °C.

On-grid exchange at RT



On-grid exchange at elevated temperatures

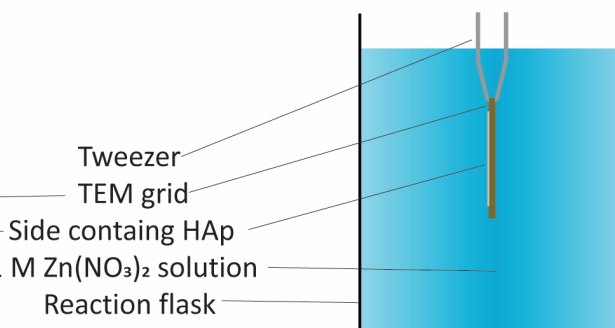


Figure A2.3 Sketch of the grid position during the exposure to $\text{Zn}(\text{NO}_3)_2 \cdot 6\text{H}_2\text{O}$ solution at RT (left) and at elevated temperatures (right).

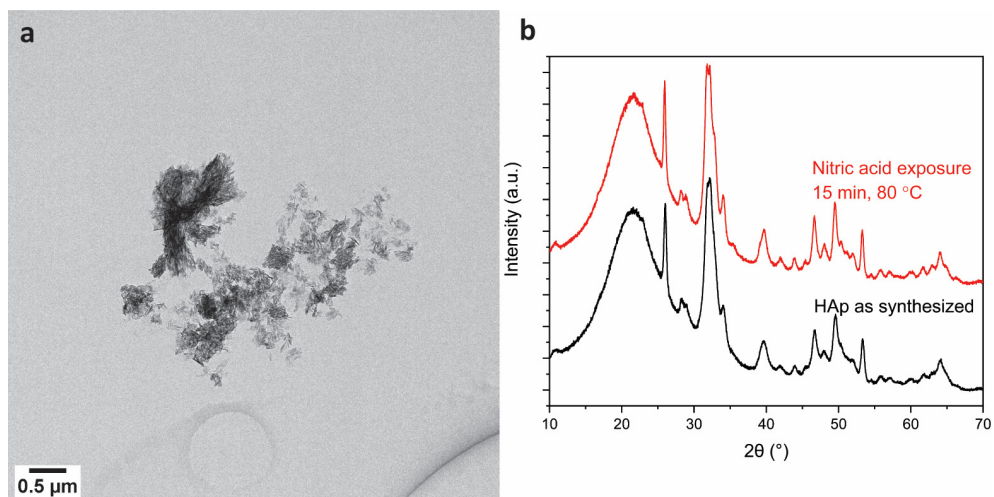


Figure A2.4 TEM image (a) and pXRD of the HAp crystals after exposure for 15 min to a nitric acid solution set to pH 2.7 at 80 °C. Comparing pXRD of the product (red) to HAp before exposure (black) shows no change in crystalline species. The broad signal around 20 deg corresponds to the measuring substrate.

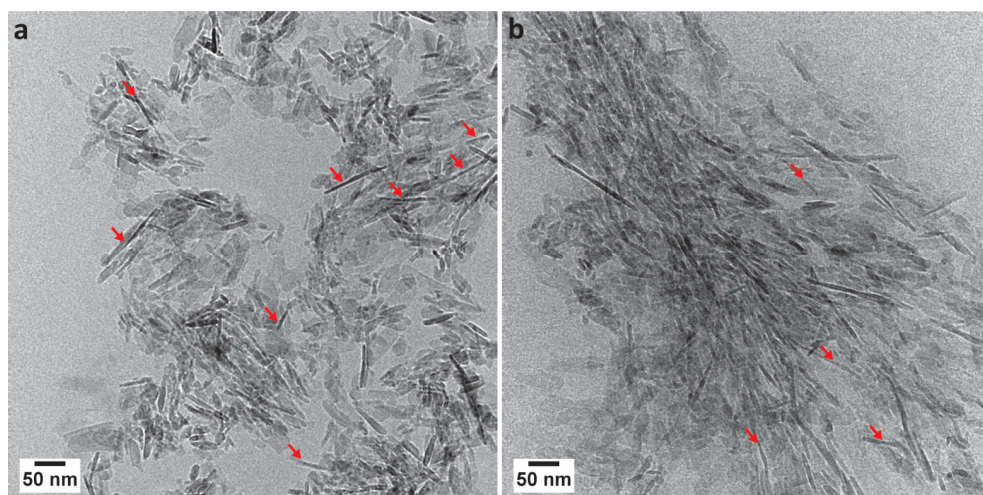


Figure A2.5 CryoTEM image of HAp platelets after exposure to 1 M $\text{Zn}(\text{NO}_3)_2 \cdot 6\text{H}_2\text{O}$ at RT. Size measurements at the indicated region (red arrows) give a platelet thickness of 4.2 ± 0.69 nm.

2.9. References

1. M. Pandya and T. G. H. Diekwisch, Enamel Biomimetics-fiction or Future of Dentistry. *Int J Oral Sci* **11**, 8 (2019).
2. Y. Liu, D. Luo and T. Wang, Hierarchical Structures of Bone and Bioinspired Bone Tissue Engineering. *Small* **12**, 4611-4632 (2016).
3. W. J. Habraken, J. Tao, L. J. Brylka, H. Friedrich, L. Bertinetti, A. S. Schenk, A. Verch, V. Dmitrovic, P. H. Bomans, P. M. Frederik, J. Laven, P. van der Schoot, B. Aichmayer, G. de With, J. J. DeYoreo and N. A. Sommerdijk, Ion-association Complexes Unite Classical and Non-classical Theories for the Biomimetic Nucleation of Calcium Phosphate. *Nat Commun* **4**, 1507 (2013).
4. L. C. Bonar, A. H. Roufosse, W. K. Sabine, M. D. Grynypas and M. J. Glimcher, X-Ray-Diffraction Studies of the Crystallinity of Bone-Mineral in Newly Synthesized and Density Fractionated Bone. *Calcified Tissue Int* **35**, 202-209 (1983).
5. F. Nudelman, K. Pieterse, A. George, P. H. H. Bomans, H. Friedrich, L. J. Brylka, P. A. J. Hilbers, G. de With and N. A. J. M. Sommerdijk, The Role of Collagen in Bone Apatite Formation in the Presence of Hydroxyapatite Nucleation Inhibitors. *Nat Mater* **9**, 1004-1009 (2010).
6. B. M. Oosterlaken, M. P. Vena and G. de With, In Vitro Mineralization of Collagen. *Adv. Mater.*, 2004418 (2011).
7. H. Ping, H. Xie, Y. M. Wan, Z. X. Zhang, J. Zhang, M. Y. Xiang, J. J. Xie, H. Wang, W. M. Wang and Z. Y. Fu, Confinement Controlled Mineralization of Calcium Carbonate within Collagen Fibrils. *J Mater Chem B* **4**, 880-886 (2016).
8. L. N. Niu, K. Jiao, H. Ryou, A. Diogenes, C. K. Y. Yiu, A. Mazzoni, J. H. Chen, D. D. Arola, K. M. Hargreaves, D. H. Pashley and F. R. Tay, Biomimetic Silicification of Demineralized Hierarchical Collagenous Tissues. *Biomacromolecules* **14**, 1661-1668 (2013).
9. B. Zhou, L. N. Niu, W. Shi, W. Zhang, D. D. Arola, L. Breschi, J. Mao, J. H. Chen, D. H. Pashley and F. R. Tay, Adopting the Principles of Collagen Biomimetalization for Intrafibrillar Infiltration of Yttria-Stabilized Zirconia into Three-Dimensional Collagen Scaffolds. *Adv Funct Mater* **24**, 1895-1903 (2014).
10. Y. Xu, F. Nudelman, E. D. Eren, M. J. M. Wirix, B. Cantaert, W. H. Nijhuis, D. Hermida-Merino, G. Portale, P. H. H. Bomans, C. Ottmann, H. Friedrich, W. Bras, A. Akiva, J. P. R. O. Orgel, F. C. Meldrum and N. Sommerdijk, Intermolecular Channels Direct Crystal Orientation in Mineralized Collagen. *Nat Commun* **11**, 5068 (2020).
11. L. De Trizio and L. Manna, Forging Colloidal Nanostructures via Cation Exchange Reactions. *Chemical Reviews* **116**, 10852-10887 (2016).
12. T. Holtus, L. Helmbrecht, H. C. Hendrikse, I. Baglai, S. Meuret, G. W. P. Adhyaksa, E. C. Garnett and W. L. Noorduin, Shape-preserving Transformation of Carbonate Minerals into Lead Halide Perovskite Semiconductors based on Ion Exchange/Insertion Reactions. *Nat Chem* **10**, 740-745 (2018).
13. S. J. Omelon and M. D. Grynypas, Relationships between Polyphosphate Chemistry, Biochemistry and Apatite Biomimetalization. *Chemical Reviews* **108**, 4694-4715 (2008).
14. D. J. Zhang and A. Tamilselvan, Lattice Energy and Mechanical Stiffness of Hydroxyapatite. *J Mater Sci-Mater M* **18**, 79-87 (2007).
15. N. J. Flora, C. H. Yoder and H. D. B. Jenkins, Lattice Energies of Apatites and the Estimation of $\Delta H-f^{\circ}(\text{PO}_4(3-), \text{g})$. *Inorg Chem* **43**, 2340-2345 (2004).
16. L. Glasser and H. D. B. Jenkins, Lattice Energies and Unit Cell Volumes of Complex Ionic Solids. *J Am Chem Soc* **122**, 632-638 (2000).
17. R. Sergi, D. Bellucci, R. T. Candidato, L. Lusvarghi, G. Bolelli, L. Pawlowski, G. Candiani, L. Altomare, L. De Nardo and V. Cannillo, Bioactive Zn-doped Hydroxyapatite Coatings and their Antibacterial Efficacy against Escherichia Coli and Staphylococcus Aureus. *Surf Coat Tech* **352**, 84-91 (2018).
18. L. Robinson, K. Salma-Ancane, L. Stipniece, B. J. Meenan and A. R. Boyd, The Deposition of Strontium and Zinc Co-substituted Hydroxyapatite Coatings. *J Mater Sci-Mater M* **28**, 51 (2017).
19. R. Rogojan, E. Andronescu, M. Necula, C. Cercel, R. Popescu and G. Stoian, Calcium Phosphate Nanoparticles Substituted with Zn²⁺/Cu²⁺ - as Antibacterial Systems. *Rom Biotech Lett* **23**, 13425-13438 (2018).
20. J. R. Guerra-Lopez, G. A. Echeverria, J. A. Guida, R. Vina and G. Punte, Synthetic Hydroxyapatites Doped with Zn(II) Studied by X-ray Diffraction, Infrared, Raman and Thermal Analysis. *Journal of Physics and Chemistry of Solids* **81**, 57-65 (2015).
21. H. Kim, S. Mondal, S. Bharathiraja, P. Manivasagan, M. S. Moorthy and J. Oh, Optimized Zn-doped Hydroxyapatite/Doxorubicin Bioceramics System for Efficient Drug Delivery and Tissue Engineering Application. *Ceram Int* **44**, 6062-6071 (2018).
22. C. Kojima, K. Watanabe, H. Murata, Y. Nishio, R. Makiura, K. Matsunaga and A. Nakahira, Controlled Release of DNA from Zinc and Magnesium Ion-doped Hydroxyapatites. *Res Chem Intermediat* **45**, 23-32 (2019).
23. M. O. Li, X. F. Xiao, R. F. Liu, C. Y. Chen and L. Z. Huang, Structural Characterization of Zinc-substituted Hydroxyapatite Prepared by Hydrothermal Method. *J Mater Sci-Mater M* **19**, 797-803 (2008).
24. G. L. Meng, X. L. Wu, R. J. Yao, J. He, W. Yao and F. Wu, Effect of Zinc Substitution in Hydroxyapatite Coating on Osteoblast and Osteoclast Differentiation under Osteoblast/Osteoclast Co-culture. *Regen Biomater* **6**, 349-359 (2019).
25. N. Lowry, M. Broly, Y. Han, S. McKillop, B. J. Meenan and A. R. Boyd, Synthesis and Characterisation of Nanophase Hydroxyapatite Co-substituted with Strontium and Zinc. *Ceram Int* **44**, 7761-7770 (2018).

26. S. Hayakawa, K. Ando, K. Tsuru, A. Osaka, E. Fujii, K. Kawabata, C. Bonhomme and F. Babonneau, Structural Characterization and Protein Adsorption Property of Hydroxyapatite Particles Modified with Zinc Ions. *J Am Ceram Soc* **90**, 565-569 (2007).
27. E. Fujii, M. Ohkubo, K. Tsuru, S. Hayakawa, A. Osaka, K. Kawabata, C. Bonhomme and F. Babonneau, Selective Protein Adsorption Property and Characterization of Nano-crystalline Zinc-containing Hydroxyapatite. *Acta Biomater* **2**, 69-74 (2006).
28. X. Zhao, Y. Zhu, Z. Zhu, Y. Liang, Y. Niu and J. Lin, Characterization, Dissolution, and Solubility of Zn-Substituted Hydroxylapatites [(Zn_xCa_{1-x})(PO₄)₃OH] at 25°C. *J Chem* **2017**, 1-13 (2017).
29. F. Z. Ren, R. L. Xin, X. Ge and Y. Leng, Characterization and Structural Analysis of Zinc-substituted Hydroxyapatites. *Acta Biomater* **5**, 3141-3149 (2009).
30. F. Miyaji, Y. Kono and Y. Suyama, Formation and Structure of Zinc-substituted Calcium Hydroxyapatite. *MRS Bull* **40**, 209-220 (2005).
31. J. Oliva, J. De Pablo, J. L. Cortina, J. Cama and C. Ayora, The use of Apatite II (TM) to Remove Divalent Metal Ions Zinc(II), Lead(II), Manganese(II) and Iron(II) from Water in Passive Treatment Systems: Column Experiments. *J Hazard Mater* **184**, 364-374 (2010).
32. Q. Wang, P. F. Tang, X. Ge, P. F. Li, C. Lv, M. H. Wang, K. F. Wang, L. M. Fang and X. Lu, Experimental and Simulation Studies of Strontium/Zinc-codoped Hydroxyapatite Porous Scaffolds with Excellent Osteoinductivity and Antibacterial Activity. *Appl Surf Sci* **462**, 118-126 (2018).
33. G. Y. Chen, X. Y. Zheng, C. Wang, J. F. Hui, X. X. Sheng, X. X. Xu, J. C. Bao, W. J. Xiu, L. H. Yuwen and D. D. Fan, A Postsynthetic Ion Exchange Method for Tunable Doping of Hydroxyapatite Nanocrystals. *RSC Adv* **7**, 56537-56542 (2017).
34. P. Parhi, V. Manivannan, S. Kohli and P. McCurdy, Room Temperature Metathetic Synthesis and Characterization of Alpha-hopeite, Zn-3(PO₄)(2)·4H(2)O. *MRS Bull* **43**, 1836-1841 (2008).
35. J. C. Elliott, R. M. Wilson and S. E. P. Dowker, Apatite Structures. *Adv. X-Ray Anal.* **45**, 172-181 (2002).
36. D. J. Cherniak, W. A. Lanford and F. J. Ryerson, Lead Diffusion in Apatite and Zircon Using Ion-Implantation and Rutherford Backscattering Techniques. *Geochim Cosmochim Acta* **55**, 1663-1673 (1991).
37. D. J. Cherniak, Uranium and Manganese Diffusion in Apatite. *Chem Geol* **219**, 297-308 (2005).
38. R. D. Shannon, Revised Effective Ionic-Radii and Systematic Studies of Interatomic Distances in Halides and Chalcogenides. *Acta Crystallographica Section A* **32**, 751-767 (1976).

Chapter 3

Counter-ion Influence on the Mechanism of HMTA-mediated ZnO Formation

Crystalline materials are often formed via transient phases. Here we focus on ZnO which is a widely used and investigated material for technological applications. Although the literature for the wet chemical synthesis of ZnO is extensive, its formation pathway using these strategies has gained limited attention so far and is poorly understood. To gain insight in these pathways, a HMTA-mediated ZnO synthesis protocol with a variety of zinc salts was employed using in-situ pH measurements combined with discrete cryoTEM and SEM sampling studies, in addition to more typical pXRD and SEM product analysis. These results indicate a significant effect of counterions on the reaction product. Using acetate, nitrate, chloride and sulphate as counterions all result first in the formation of a layered zinc hydroxy salt (LZHS), the exact composition of which depends on the counterion. Rather stable LZHSs are formed using chloride and sulphate, preventing the eventual formation of ZnO. Only acetate and nitrate result in the formation of ZnO. For acetate, ZnO is preferably grown in-dispersion, while for nitrate it is formed on exposed solid interfaces to the reaction medium (on-surfaces). For the latter the nucleation of its LZHS precursor requires an additional incubation time, resulting in heterogenous nucleation instead.

This chapter is adapted from:

M. M. J. van Rijt, B. M. Oosterlaken, R. R. J. Joosten, L. E. A. Wijkhuijs, P. Bomans, H. Friedrich and G. de With, Counter-ion influence on the mechanism of HMTA-mediated ZnO formation, *CrystEngComm*, 2020, **22**, 5854-5861.

“Even as a young officer he was such a hard drinker that his name, Tiberius Claudius Nero, was displaced by the nickname ‘Biberius Caldius Mero’: ‘Drinker of wine with no water added’”

Suetonius, The twelve Caesars, **121CE**.

3.1. HMTA-mediated ZnO Formation

Non-classical crystallization pathways, i.e. the multi-step progression from transient phases^[1] has been observed for multiple minerals including magnetite^[2], hydroxy apatite^[3] and calcium carbonate^[4]. Similarly, for the synthesis of zinc oxide (ZnO) under aqueous conditions, it is generally accepted that either zinc hydroxide^[5-8] or layered zinc hydroxy salts (LZHS)^[9-13] are formed as a transient phase.

A common strategy for the formation of high quality ZnO uses the gradual thermal decomposition of hexamethylenetetramine (HMTA) into ammonia and formaldehyde, where after the ammonia reacts with water resulting in the formation of hydroxide. The released hydroxide is subsequently consumed resulting in the formation of ZnO after several hours at temperatures above 60 °C^[9, 10, 14, 15]. The thermal decomposition rate of HMTA increases with the concentration of protons in the system, making the release of hydroxide in the system pH dependent^[16]. Several *ex-situ* studies on the mechanism of ZnO formation have been conducted using both zinc acetate^[9, 10, 13, 14] and zinc nitrate^[10, 17-20] as a zinc source. For these reactions either layered basic zinc acetate (LBZA, $Zn_5(OH)_8(CH_3COO)_2 \cdot 2H_2O$) or layered basic zinc nitrate (LBZN, $Zn_5(OH)_8(NO_3)_2 \cdot 2H_2O$) have been observed in the early reaction stages, suggesting they are transient species. It has been postulated by *Jang et al.*^[13] that these LZHS act as a seeding template for ZnO dumbbell structures that are frequently formed in dispersion. *In-situ* studies have been performed including LPTEM^[14, 21] and STXM^[22], focusing on the growth stage, and XANES^[7], showing the initial formation of $[Zn(OH)_6]^{2+}$ instead of LZHS.

The formation of ZnO using HMTA is not limited to the use of zinc acetate or zinc nitrate, as other zinc salts such as zinc N-dodecyl-N,N-dimethylammonioacetic bromide^[11], zinc formate^[5], zinc chloride^[23, 24] and zinc sulphate^[25], have been successfully used. However, only a few papers used similar reaction conditions for different zinc salts to investigate the influence of the counterion^[5, 23] so that a general understanding of the counterion role during the ZnO formation is currently lacking. To date counterions are mainly described as capping agents, e.g. resulting in the formation of hexagonal platelets when using zinc sulphate, in contrast to the typically formed hexagonal rods for > 4 nm ZnO crystals^[25-27]. Given the observation of counter-ion specific intermediates, it is highly likely that the counterion will have a significant influence on the reaction.

Here we investigate the influence of various zinc counterions on the formation of ZnO using a mild HMTA-based reaction strategy. We show that the selection of the counterion has a strong influence on the process and the final reaction product. Furthermore, for the formation of ZnO the counter-ion, dependent on reaction conditions, can direct the growth of ZnO in-dispersion or on-surfaces. Finally, *in-situ* pH measurements are combined with discrete cryoTEM and SEM sampling to gain insight in the underlying formation mechanism of ZnO.

3.2. Counter-ion Influence on the Reaction Product

The influence of zinc counterions on ZnO crystallization was investigated using a protocol similar to *Ou et al.*^[28]. In brief, by reacting 50 mM zinc salt and 25 mM hexamine (HMTA) in pure water at 80 °C for 6 h at ambient pressure, see *section 3.6*. Four different zinc salts were investigated: zinc acetate ($ZnAc_2$), chloride ($ZnCl_2$), nitrate ($Zn(NO_3)_2$) and sulphate ($ZnSO_4$). In all cases a white precipitate was obtained after the reaction (*Fig. A3.1*). For $Zn(NO_3)_2$ the precipitate formed dominantly on the flask wall and on the pH probe, resulting in a clear solution. In contrast, for the other three salts most (all in the case of $ZnSO_4$) of the precipitate was formed in dispersion.

For all zinc salts, *in-situ* pH measurements (*Fig. 3.1a*) showed an initial rapid decrease in pH with increasing reaction temperature. The observed pH minima show a counter-ion dependence with the highest pH minima being observed for $ZnAc_2$ (5.8) followed by $Zn(NO_3)_2$ (5.6), $ZnCl_2$ (5.5) and

ZnSO₄ (5.4). Following the initial drop in pH, a stabilization or gradual increase in pH is observed over time. Only when ZnAc₂ is used this constant pH trend is interrupted by a distinct second drop in pH of 0.1 - 0.2 pH points. This drop is typically observed after 2 h reaction time (*section A3.1*). After 6 h reaction time the pH of the reaction solution has raised to 5.8 for ZnAc₂, 5.7 for ZnCl₂ and 5.6 for both Zn(NO₃)₂ and ZnSO₄.

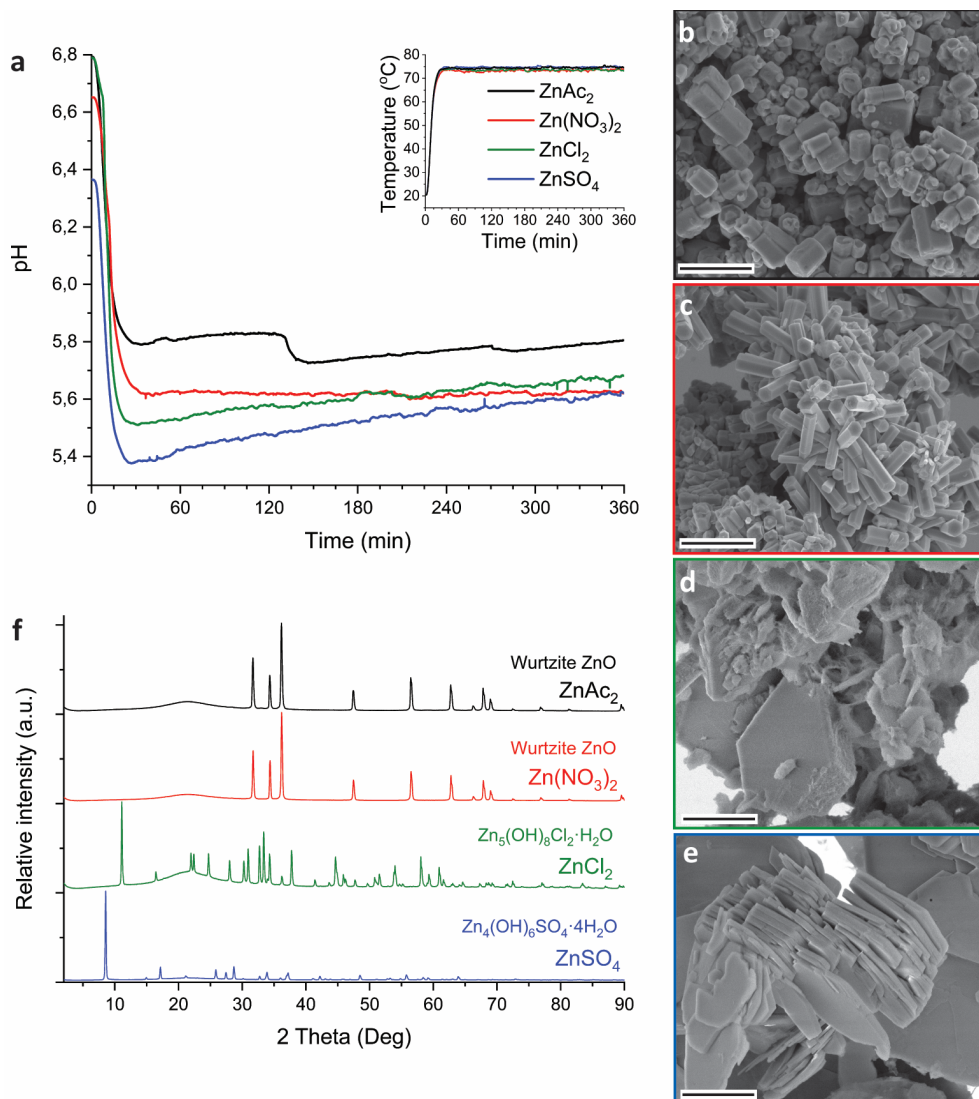


Figure 3.1 HMTA-mediated synthesis of ZnO showing pH (a) and temperature (inset) profiles, combined with SEM images (b-e) and pXRD data (f) of the reaction products when using ZnAc₂ (b, black), Zn(NO₃)₂ (c, red), ZnCl₂ (d, green) and ZnSO₄ (e, blue). SEM scales equal 2 μm. The pXRD data are normalized on the highest intensity signal and the broad pXRD signal visible at about 20° is from the substrate.

The morphologies and crystallinity of the purified reaction products were investigated using SEM (Fig. 3.1b-e) and pXRD (Fig. 3.1f). For both ZnAc_2 and $\text{Zn}(\text{NO}_3)_2$ hexagonal pillar-shaped wurtzite ZnO crystals were formed. Use of ZnAc_2 typically resulted in a dumbbell structure. The reactions using ZnCl_2 and ZnSO_4 resulted in the formation of frequently hexagonally faceted plate-shaped crystals of $\text{Zn}_5(\text{OH})_8\text{Cl}_2 \cdot \text{H}_2\text{O}$ (LBZC) and^[29] $\text{Zn}_4(\text{OH})_6\text{SO}_4 \cdot 4\text{H}_2\text{O}$ (LBZS), respectively^[30]. The plate-shaped crystals are not dissimilar to crystals observed by Govender *et al.*^[5] Thus for ZnCl_2 and ZnSO_4 no evidence of ZnO formation was observed using pXRD and this was supported by the observation of only one morphology by SEM. When comparing the reaction pH profiles, it can be observed that for ZnCl_2 and ZnSO_4 the reaction pH is slightly lower than when using the ZnO forming zinc salts. Furthermore, when ZnO pillars formed from ZnAc_2 and $\text{Zn}(\text{NO}_3)_2$ were left in the reaction solution for over 24 h, they became hollow (Fig. A3.2). This is indicative of pH-induced etching due to prolonged exposure to the low pH reaction solution at RT after synthesis^[31]. This suggests that the reaction pH when using ZnAc_2 and $\text{Zn}(\text{NO}_3)_2$ is close to the pH stability limit of ZnO. In an attempt to raise the reaction pH, base (0.1 M ammonia) was added dropwise to the ZnSO_4 reaction. This led to the formation of a white precipitate at RT without resulting in an increase in pH. After performing the reaction, pXRD showed the formation of a mixture of zinc hydroxy sulphate salts (Fig. A3.3). As an alternative to raise the reaction pH, the reaction temperature was lowered for both ZnCl_2 and ZnSO_4 . This increased the observed minima in reaction pH to 5.7 and 5.8, respectively (Fig. A3.4a). After purification pXRD analysis still showed the dominant formation of LBZC and LBZS without any evidence for ZnO formation (Fig. A3.4b). This indicates that the reaction pH is not the main cause for the formation of LZHS instead of ZnO when using ZnCl_2 or ZnSO_4 .

3.3. Mechanism of HMTA-mediated ZnO Formation in Dispersion

To understand how ZnAc_2 transforms in dispersion into ZnO, discrete cryoTEM sampling studies were conducted (Fig. 3.2). Given that the features in the pH curve tend to shift in time between experiments due to the stochastic nature of nucleation and crystallization (section A3.1), cryoTEM sampling points are chosen and indicated based on curve features rather than absolute time points (Fig. 3.2a I). Dissolving ZnAc_2 and HMTA in water yielded a transparent solution. CryoTEM prior to the start of the reaction showed the presence of ~ 200 nm sized sheets (Fig. 3.2b). These sheets tend to orient with the TEM grid and are predominantly observed in clusters. Low Dose Selected Area Electron Diffraction (LDSAED) of such clusters showed the presence of two diffuse rings originating from vitreous water and three faint but sharp rings, which include stronger diffraction spots, matching the (010), ($\bar{1}20$) and (020) spacing of either wurtzite ZnO or LBZA (Fig. 3.3; A3.5). When the temperature is gradually increased to initiate the reaction, cryoTEM imaging shows that the lateral size of the sheets increases significantly (Fig. 3.2c) concomitant with a decrease in pH from 6.8 to 5.8. LDSAED shows that these sheets are single crystals (Fig. A3.5b,e), in agreement with previous observations on LBZA^[32, 33], with a preferred growth in the [010] direction. The maxima of the most prominent diffraction signals match with those of the ~ 200 nm sheets (Fig. 3.3). This clearly shows that LBZA is formed when dissolving the reactants prior to the start of the reaction at RT. Upon temperature increase, which initiates the reaction, growth of LBZA sheets accelerates resulting in increased hydroxide consumption and a concomitant decrease in pH.

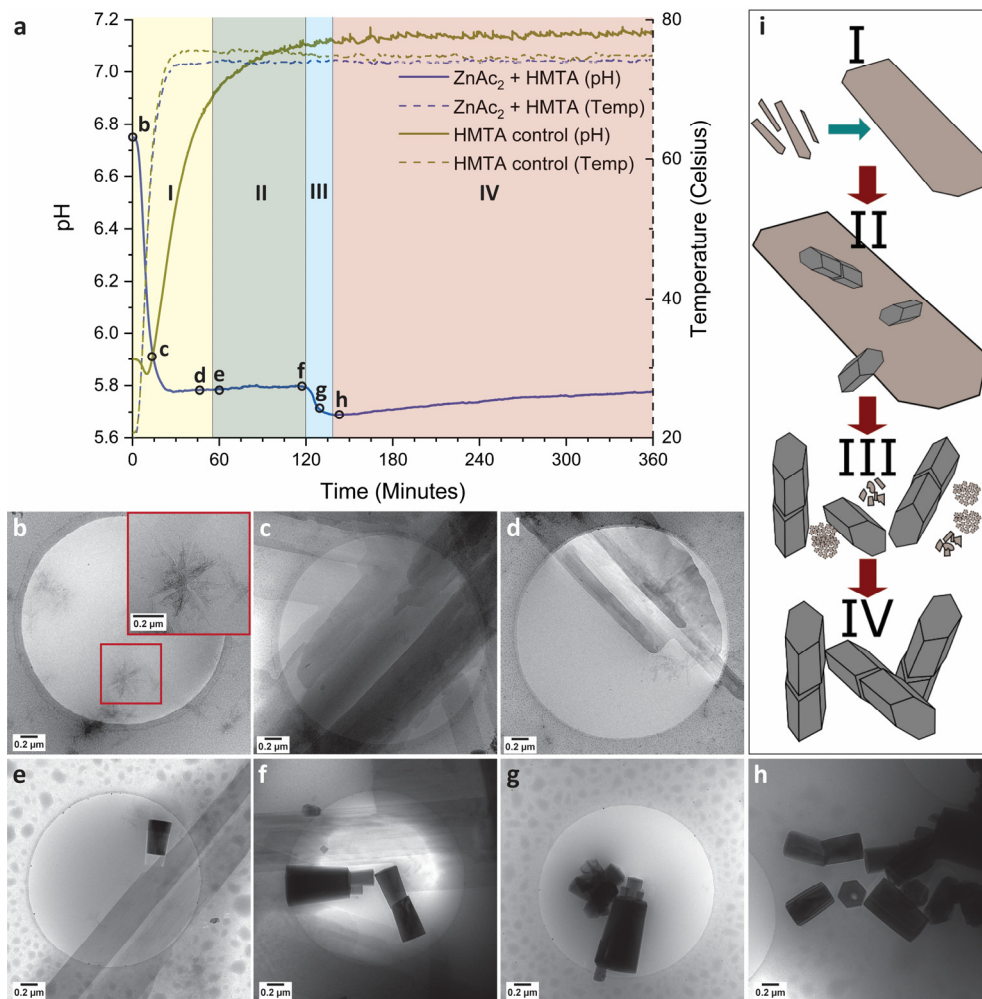


Figure 3.2 pH (continuous) and temperature (dashed) profiles of the ZnAc₂ / HMTA reaction (blue) versus HMTA decomposition (gold) (a). CryoTEM images (b-h) obtained from discrete sampling, selected points are indicated in the pH curve. Sketch of products observed by cryoTEM at different time points (i) showing only LBZA sheets (region I, a), nucleation of ZnO in presence of LBZA (region II, a), fast disintegration of LBZA (region III, a) and of the final ZnO reaction product (region IV, a).

The initial pH drop lasts for about 30 min when the temperature has reached approximately 75 °C. Thermal decomposition of HMTA, which starts at 50 °C, does not impact the slope of the pH drop. This suggests that the hydroxide, released by HMTA decomposition – ammonia formation – is immediately consumed by the formation of LBZA. Subsequently, the pH stabilizes close to 5.8 with only a slight increase being observed in time. At the beginning of the first pH plateau, LBZA sheets with a width of over 1 μm in some cases (Fig. 3.2d) can be regularly observed by cryoTEM. It should be noted that even at this stage small nanometer-sized sheets, like those observed at RT, are still present.

CryoTEM imaging at 60 min reaction time shows that the LBZA sheets have even further increased in size, with some having a width of more than $5\ \mu\text{m}$ (Fig. 3.2e,f; A3.6). From this timepoint onward, ZnO pillars can be observed in dispersion using cryoTEM (Fig. 3.2a II), suggesting that the ZnO nucleation takes place after formation of large LBZA sheets. Given above findings and the similar lattice spacings of wurtzite ZnO and LBZA, it seems reasonable to assume that LBZA plays a role in the formation of ZnO. However, cryoTEM provides no direct evidence for this hypothesis. Furthermore, it is striking that the formation of ZnO crystals does not rapidly consume all available LBZA, in fact, it seems that LBZA sheets continue to increase in size during the nucleation and initial growth of ZnO pillars.

The first pH plateau ends with a spontaneous second decrease in pH (Fig. 3.2a III). Under typical reaction conditions this pH drop occurs after about 2 h reaction time. Surprisingly, during cryoTEM sampling experiments this pH drop occurred earlier (as early as 75 min reaction time), and in several cases directly after sampling (section A3.1) as will be discussed in more detail later. The spontaneous decrease in pH, which consequently will again accelerate the proton catalyzed decomposition of HMTA and subsequent release of hydroxide^[34], can only be explained by a spontaneous increase in the consumption of hydroxide by the reaction.

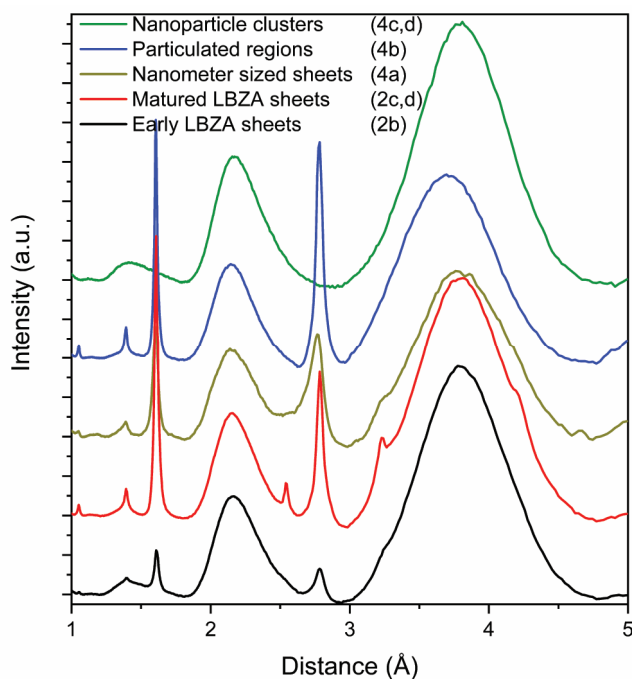


Figure 3.3 Radial averaged LDSAED data at different time points showing the initially observed small $\sim 200\ \text{nm}$ LBZA (black), the large “matured” LBZA sheets (red) and species observed after the second pH drop; nanometer-sized sheets (gold), high-contrast particulated regions (blue), and amorphous nanoparticle clusters (green). The full LDSAED patterns are shown in Fig. A3.5. The sharp signals at 1.1, 1.4, 1.6, 2.6, 2.8 and 3.2 Å match with LBZA.

After the onset of this second pH drop no rectangular shaped LBZA crystals were observed by cryoTEM (Fig. 3.2g; 3.4), indicating that the pH drop corresponded with a rapid decrease in the number of LBZA crystals present. Simultaneously, the size of ZnO crystals increased from $470 \pm 330\ \text{nm}$ to $660 \pm 380\ \text{nm}$ in length, \pm standard deviation, during the first 9 minutes of the pH drop (Fig. A3.7; A3.8), while

the aspect ratio stayed almost constant at 2.4 vs 2.3, respectively. Simplifying the shape of ZnO crystals as cylinders, this corresponds to a ZnO volume increase of 2.8 times. At the end of the second pH drop (27 min in the process), a ZnO rod length of 650 ± 250 nm is measured with an aspect ratio of 2.2. This shows that ZnO crystal growth is most pronounced at the start of the second pH drop. Given that LBZA contains hydroxide moieties, spontaneous dissolution of LBZA would result in a strong pH increase. The rapid increase in ZnO size and the corresponding decrease in pH indicate that the LBZA is not gradually dissolved, but instead rapidly consumed by accelerated ZnO crystal growth.

Although ZnO has become the main phase after the onset of the second pH drop, other transient phases are present. Throughout the pH decrease a variety of coexisting phase are observed including folded sheets (Fig. 3.4a) and high contrast regions, that appear to be particulated on a higher magnification (Fig. 3.4b). LDSAED of both phases matches with the earlier observed LBZA spacings (Fig. 3.3). Furthermore, clusters of amorphous nanometer-sized particles are also observed at multiple time points (Fig. 3.3; Fig. 3.4c,d).

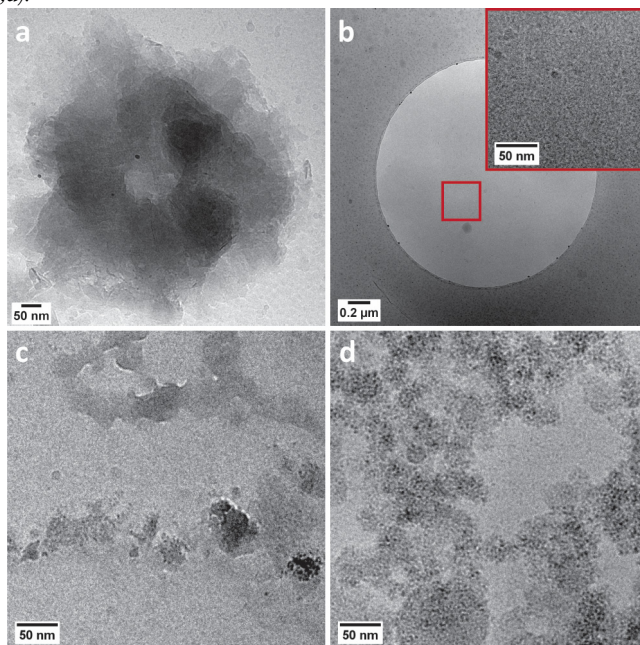


Figure 3.4 CryoTEM images of phases observed throughout the second drop in pH including: folded sheets (a), high-contrast particulated regions (b) and clusters of nanoparticles (c,d).

After the end of the second pH drop a gradual increase in pH is observed. For this stage cryoTEM shows that ZnO is the dominant species present (Fig. 3.2h). This matches pXRD data obtained after 6 h reaction time (Fig. 3.1f). During this time period, base will still be released by HMTA decomposition, whereas the pH only gradually increases from 5.8 to 5.7 (Fig. 3.2a IV). The remainder of the released base is likely consumed by the growth of the ZnO crystals present.

By using cryoTEM sampling only a fraction of the reaction volume can be investigated. Due to this fact, only local information is obtained at a specific time point. Therefore, to confidently track the evolution in sample composition accurately in a relatively small timeframe it is imperative that the transition process occurs uniformly throughout the reaction. Given that for a fast and spontaneous disintegration process a uniform transition is unlikely, it is impossible to confidently chart the disintegration of the LBZA using

cryoTEM sampling. This explains the observation of the coexisting transient phases. In fact, one of the sampling points taken close to the end of the second pH drop, shows the dominant presence of nanometer-sized particle clusters (*section A3.1, Fig. 3.4d*) which could correspond with a relative early stage of the disintegration process. These clusters are accompanied by small highly particulated sheets, which possibly correspond to the transition of LBZA into this particle phase. If the LBZA sheets would disintegrate into nanometer-sized particles, this could partially explain the spontaneous rapid decomposition of the species. These particles would be rapidly consumed by present crystals in dispersion, resulting in a rapid size increase for both species.

This leaves the question why the LBZA sheets would spontaneously and rapidly start to disintegrate and how this is accelerated by cryoTEM sampling experiments. The most probable reason is mechanical breaking of the LBZA sheets. LBZA sheets grow throughout the reaction and it is known that crystalline materials are more prone to brittle fracture with increasing size due to the occurrence of crystal defects.^[35, 36] When the crystal size surpasses this critical size, brittle fracture will occur due to stress exposure, resulting in shattering of the LBZA sheets. The resulting disintegration of some LBZA sheets will feed and accelerate the growth of other LBZA sheets and ZnO crystals in dispersion. These expanded LBZA sheets will also surpass the critical size and disintegrate, effectively resulting in a rapid autocatalytic collapse of the entire LBZA phase. In contrast, the ZnO crystals grown remain stable, resulting in the formation of a pure ZnO phase as observed by pH measurements and cryoTEM sampling. Given that growth rates will be similar for every reaction, the onset of this autocatalytic fracturing can be expected to occur at about the same reaction time, matching observations. When performing cryoTEM sampling, additional strain is added to the system, fracturing some LBZA sheets and expediting the process.

3.4. The Influence of Layered Hydroxy Salts

Similar to the use of ZnAc₂, the use of Zn(NO₃)₂ resulted in the formation of ZnO. However, in contrast to the other zinc salts used, the Zn(NO₃)₂ reaction product is predominantly formed on solid interfaces submerged in the reaction solution (on-surface growth) e.g. reaction flask and pH probe. CryoTEM sampling was used to investigate the particles formed in dispersion at both 15 and 30 min reaction time. Particles were only incidentally observed in dispersion (*Fig. A3.9*), suggesting that during the early reaction stages most of the hydroxide is consumed by the formation of either soluble zinc hydroxide or on-surface crystal growth.

To investigate if on-surface crystal growth occurs during the early stages, SEM was performed on cleaned glass plates (without a seed layer) submerged for a specific time in the reaction medium (*Fig. 3.5*). After 15 min reaction time micrometer-sized crystals were observed on the glass surface (*Fig. 3.5a*). The diameter of the particles significantly increased with reaction time (30 – 45 min, *Fig. 3.5b; A3.10*), showing that the inserted hydroxide in the reaction is consumed by the formation of crystal growth on the glass surface. Many of these crystals have a rhombic shape, which is an atypical shape for both ZnO and LZHS, but it excellently matches with wulfingite zinc hydroxide as observed by *McBride et al.*^[6] The absence of LZHS species under mild condition is not unique as *McPeak et al.*^[7] also showed a zinc hydroxide intermediary when using seeded ZnO growth from Zn(NO₃)₂. In the presence of ZnAc₂ after 30 min reaction time no crystal growth can be observed by SEM on the glass surface (*Fig. A3.11*). After 180 min the surface was covered with ZnO pillar structures (*Fig. 3.5c,d*). These hexagonal pillars are significantly smaller than the initially observed crystals implying a transition via a dissolution-precipitation mechanism or their overgrowth with ZnO crystals as the reaction progresses. They also lack a preferred growing orientation which is due to the absence of an epitaxial seeding layer^[37].

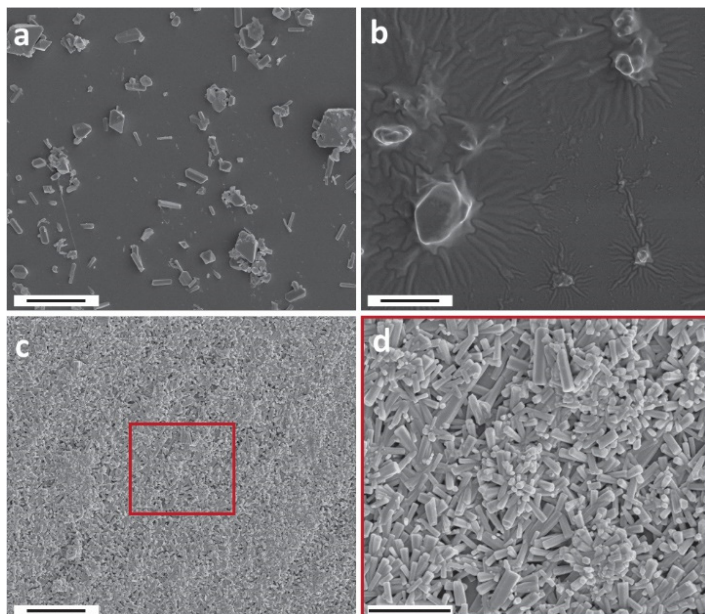


Figure 3.5 SEM images of the $\text{Zn}(\text{NO}_3)_2$ reaction product on glass plates at 15 min (a), 45 min (b) and 180 min (c,d). Scale bars are 5 μm (a-c) and 3 μm (d). A lower magnification image of (b) is shown in *Fig. A3.10*.

Discrete SEM sampling experiments provided no reasonable evidence for the formation of LBZN as a precursor for the observed surface grown ZnO crystals. *Liang et al.*^[10] observed the initial formation of LBZN in dispersion by using a 24 h incubation period at RT. Therefore, to stimulate the formation of LBZN a similar 24 h incubation time was introduced. This resulted in a gradual reduction of the starting pH from roughly 6.8 to 6.5 yet yielding a clear solution (*Fig. A3.12a*). Increasing this incubation time to several days results in the formation of a white precipitate. This matches with LBZN characteristics according to pXRD (*Fig. 3.6a; A3.12b*), confirming its formation. Performing the reaction after 24 h incubation time a turbid dispersion was obtained (*Fig. A3.13*). pH measurements (*Fig. 3.6b*) showed a second drop in pH at 25 min reaction time near the end of the typical initial pH drop. After purifying the dispersed product, pXRD and SEM (*Fig. 3.6a,c*) confirmed the formation of wurtzite ZnO in-dispersion. This shows that, for $\text{Zn}(\text{NO}_3)_2$ the preferred in-dispersion versus on-surface nucleation and growth of ZnO can be controlled by stimulating the formation of LBZN as a transient phase.

Considering the observations for all the studied zinc salts, when using ZnAc_2 , ZnCl_2 or ZnSO_4 , LZHS crystals are rapidly formed under standard reaction conditions, however, only for ZnAc_2 this LZHS phase transits into ZnO (*Fig. 3.7a,b*). Given the rapid formation of all three LZHS species their respective energy barriers are expected to be low and therefore a likely explanation for variation in evolution is the stability of these three transient phases. Although all three LZHS species can be transformed in ZnO under dry conditions by heating, this transition occurs for LBZA at 90 °C^[32, 33, 38], whereas for LBZC 160 °C and LBZS 225 °C are required, implying their greater stability^[29, 30, 39]. Additionally, when ZnO is formed in the presence of LBZA, it does not directly result in the consumption of LBZA (*Fig. 3.7b*). As shown above, LBZA initially continues to mature in the presence of ZnO, showing that ZnO is thermodynamically stable in the same range as LBZA. Given the higher stability of LBZC and LBZS precursors compared to LBZA, this could explain why these phases do not easily transform into ZnO. This does not preclude that ZnCl_2 and ZnSO_4 can be used to form ZnO via a HMTA-mediated precipitation, as this has been achieved,^[5, 23]

^{25]} but it does show that these systems will likely be more sensitive to specific reaction conditions and that their transition into ZnO might be less straightforward.

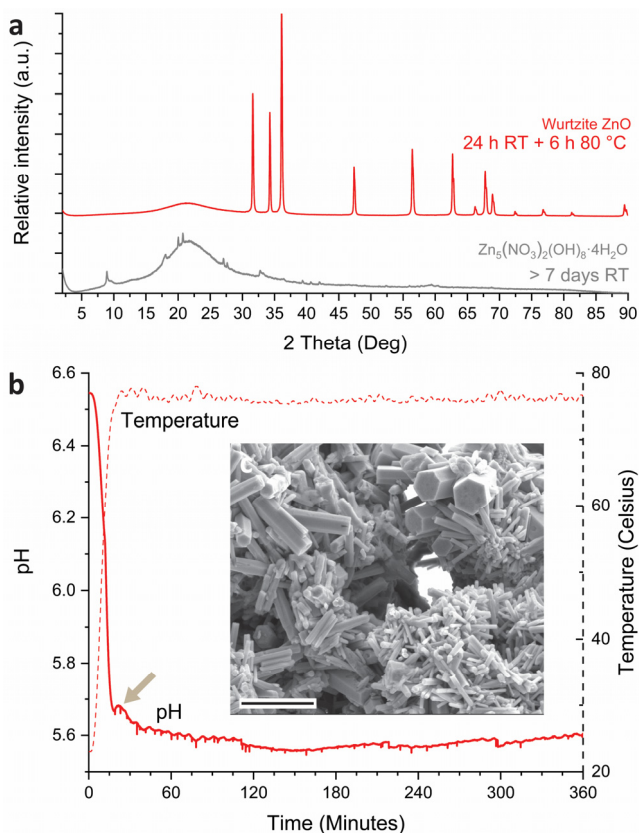


Figure 3.6 LBZN obtained after > 7 days incubated at RT and in-dispersion obtained ZnO from $Zn(NO_3)_2$ after introducing a 24 h waiting time: pXRD data (a), pH and temperature profile (b) SEM image (c) of the reaction product. The broad pXRD signals visible a about 20° are from the substrate. Arrow indicates the second drop in pH. SEM scale bar equals 2 μm.

When using $Zn(NO_3)_2$, ZnO can be formed in-dispersion after the initial formation of LBZN, suggesting a similar mechanism as for the formation of ZnO from $ZnAc_2$ (Fig. 3.7b). However, in the absence of an initial incubation period at RT, the formation of LBZN is limited compared to the heterogeneous nucleation and growth of zinc hydroxide on solid interfaces exposed to the reaction solution (Fig. 3.7c). This implies that either the energy barrier for LBZN nucleation is relatively high compared to the other LZHS or that the present nitrate molecules promote the formation of zinc hydroxide. Based on available data neither hypothesis can be excluded. In the absence of LBZN formation, hexagonal wurtzite ZnO pillars are still formed, but they are predominantly formed on surfaces present, resulting in a non-measurable quantity in the dispersion. A possible cause for this is the high concentration of zinc and hydroxide near the solid interfaces. As discussed previously, a more likely alternative is that both LBZN and LBZA play a role as ZnO nucleation template. This is supported by the similar shape, similar hexagonal spacings in the (001) plane of both species and that the main growth direction of the ZnO crystals is

perpendicular to that of the LZHS sheets. The observed occurrence of ZnO nucleation in the presence of LBZA, when using ZnAc₂, further supports this hypothesis.

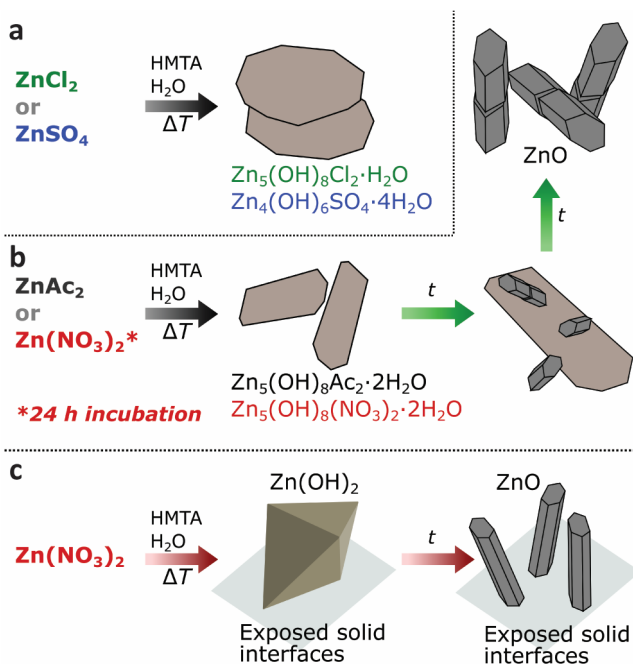


Figure 3.7 Overview of the counter-ion dependent transition into ZnO. The use of ZnCl₂ or ZnSO₄ results in the formation of stable LBZC or LBZS (a). For ZnAc₂ or for Zn(NO₃)₂ after 24 h incubation time, LBZA or LBZN are formed which subsequently transform into ZnO in-dispersion (b). For Zn(NO₃)₂ under standard conditions ZnO is formed on exposed solid interfaces (on-surface) after the initial formation of zinc hydroxide (c).

3.5. Conclusion

We have shown that for the formation of ZnO in-dispersion, a LZHS transient phase is required. The stability of this transient phase, which depends on reaction chemistry and conditions, is an essential parameter to be considered. A too stable phase, as in the case of LBZC and LBZS, can prevent the transition of this transient phase into ZnO. For LBZA under the investigated reaction conditions, pure ZnO can be formed in-dispersion. Initially, LBZA is formed, followed by a gradual formation of ZnO. During the initial formation of ZnO crystals, the LBZA crystals keep growing resulting in micrometer-sized rectangular sheets. These LBZA sheets then rapidly disintegrate (most likely by brittle fracture) resulting in an acceleration of ZnO growth. It is highly likely that the LBZA initially present acts as a nucleating template for the formation of ZnO. For Zn(NO₃)₂ initial formation or suppression of LBZN can be stimulated (aging), resulting either in ZnO dominantly formed as dispersed particles or particles on-surfaces. This not only implies that there are multiple paths for the formation of ZnO under mild reaction conditions, it also shows that the counterion has a strong effect on the formation and stability of the transient phases, in turn influencing the final reaction product and its nucleation location.

3.6. Materials and Methods

3.6.1. Materials

Ammonia (28%, GPR rechapur) was acquired from VWR, hexamethylenetetramine (HMTA, > 99.0%, ACS reagent) was acquired from Sigma-Aldrich, Zinc acetate dihydrate (ZnAc_2 , > 98%, ACS reagent), zinc chloride (ZnCl_2 , > 97%, ACS reagent), zinc nitrate hexahydrate ($\text{Zn}(\text{NO}_3)_2$, 98%, ACS reagent) and zinc sulphate heptahydrate (ZnSO_4 , 99%, ACS reagent) were acquired from Acros organics. All chemicals were used as received unless stated otherwise.

3.6.2. Methods

In a standard synthesis 50 mM of zinc salt and 25 mM of HMTA were dissolved in 50 ml pure water in a 100 ml three-neck round-bottom flask under reflux. The solution was magnetically stirred (vortexing at 450 rpm) for at least 15 minutes before the start of the reaction. The reaction pH and temperature were registered using a Metrohm unitrode pH probe. The reaction flask was suspended in an oil bath and the reaction was subsequently initiated by gradually heating to 60 or 80 °C under continued stirring. The reaction was terminated after 6 h and the final dispersion was collected. In the case that the product formed dominantly on the flask wall, ultrasonication was used to remove parts of the formed products from the flask wall. All dispersions were subsequently purified by centrifugation using an Optima L-90K ultracentrifuge equipped with a Type 70 Ti rotor at 20.000 rpm for 20 min. The pellet was redispersed in pure water followed by another centrifugation step. This procedure was performed twice. After centrifugation the solid product was dried at room temperature.

For the SEM sampling experiments, the reactions were performed in 25 ml vials using 10 ml reaction solutions. A glass cover slide (precleaned with ethanol) was diagonally suspended in the vial. The vial was suspended in an oil bath and the reaction was subsequently initiate by gradually heating to 80 °C under stirring. The reaction was terminated by removing the cover slide and rising it with pure water several times.

3.6.2.2. Analysis

Cryogenic transmission electron microscopy (CryoTEM) samples were prepared by depositing 3 μl of reaction solution on a 200 mesh Cu grid covered with a Quantifoil R 2/2 holey carbon films (Quantifoil Micro Tools GmbH, part of SPT Life Sciences group). An automated vitrification robot (Thermo Fischer Scientific, TFS, Vitrobot Mark III) preheated to 60 °C at 100% humidity was used for blotting and plunging in liquid ethane. All TEM grids were surface plasma treated for 40 seconds using a Cressington 208 carbon coater prior to use.

In case of discrete sampling at elevated temperatures the Vitrobot chamber and the used pipet tip were preheated to 60 °C to minimize sample preparation artifacts due to cooling. The TEM grid was placed in the Vitrobot several minutes before applying the sample to allow for thermal equilibration. Finally, the sample was taken directly from the reaction solution and rapidly transferred onto the grid in the Vitrobot followed by blotting and plunge freezing.

Cryo-TEM studies were performed on the TU/e cryoTITAN (TFS) which is equipped with a field emission gun (FEG), a postcolumn Gatan Energy Filter (model 2002) and a post-GIF $2k \times 2k$ Gatan CCD camera (model 794). The microscope was operated at 300 kV acceleration voltage in bright field mode with zero-loss energy filtering using an electron flux between $2 - 24 \text{ e} / \text{\AA}^2\text{s}$. and a 1s image acquisition time.

Powder X-ray diffraction (pXRD) measurements were performed on a MiniFlex 600 diffractometer operated at 40 kV and 15 mA using Cu $K\alpha$ radiation (1.54 nm),.

Scanning electron microscopy (SEM) was carried out on an Quanta 3D (TFS) equipped with a secondary electron detector and operated at 5.0 kV. SEM samples prepared on glass were sputter coated

with a 10 nm gold layer using an Emitech K575X sputter coater to improve conductivity. The samples in powder form were dispersed in pure water, 10 μL dispersion was deposited on a continuous carbon coated TEM grid with copper or gold supports (200 mesh) followed by manual blotting after 40 seconds. Samples were loaded in the SEM using an in-house build custom SEM holder that can accommodate 6 TEM grids.

3.7. Appendix A3

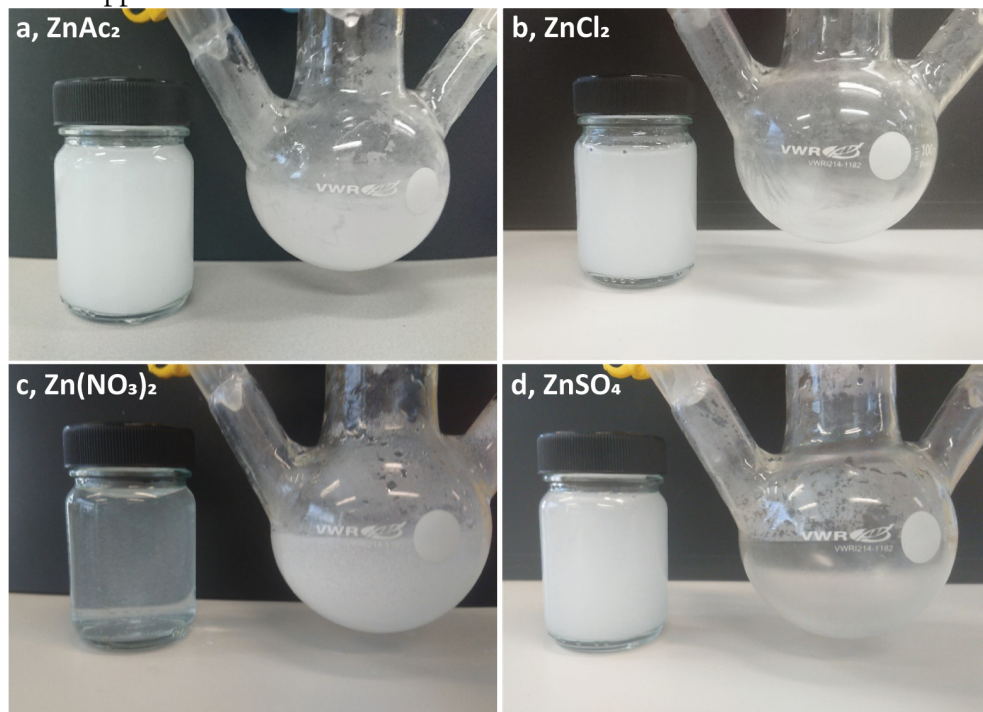


Figure A3.1 Pictures of the reaction flask and a storage jar containing the final dispersion for reactions performed with ZnAc₂ (a), ZnCl₂ (b), Zn(NO₃)₂ (c) and ZnSO₄ (d) at 80 °C.

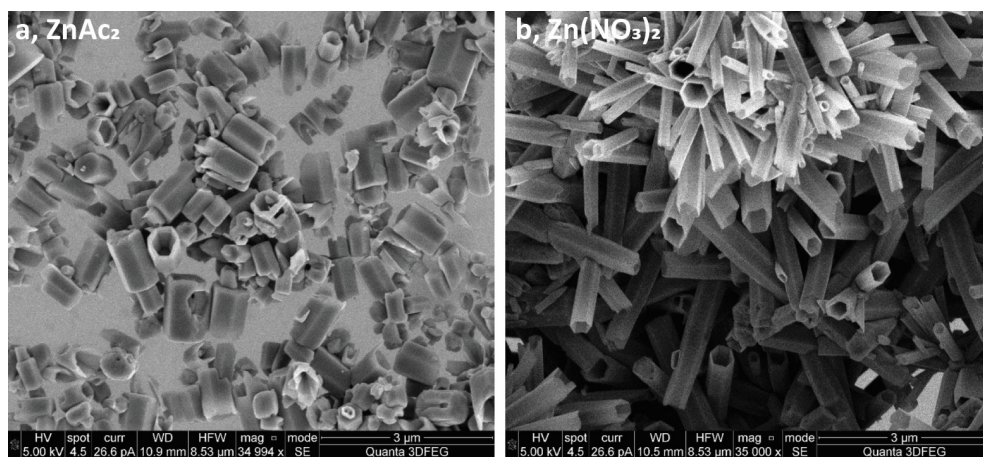


Figure A3.2 SEM images of hollow ZnO pillars synthesized from ZnAc₂ (a) and Zn(NO₃)₂ (b) purified at least 24 hours after the reaction was terminated.

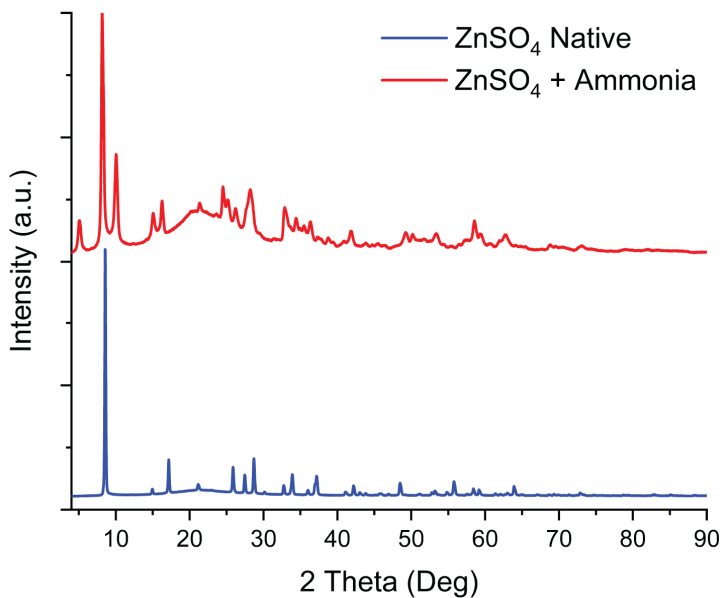


Figure A3.3 pXRD data of $\text{Zn}_4(\text{OH})_6\text{SO}_4 \cdot 4\text{H}_2\text{O}$ (blue curve) and a mixture of zinc sulphate hydroxy hydrate salts (red curve) formed from ZnSO_4 under native reaction conditions and with an initial addition of ammonia to increase the amount of base present, respectively.

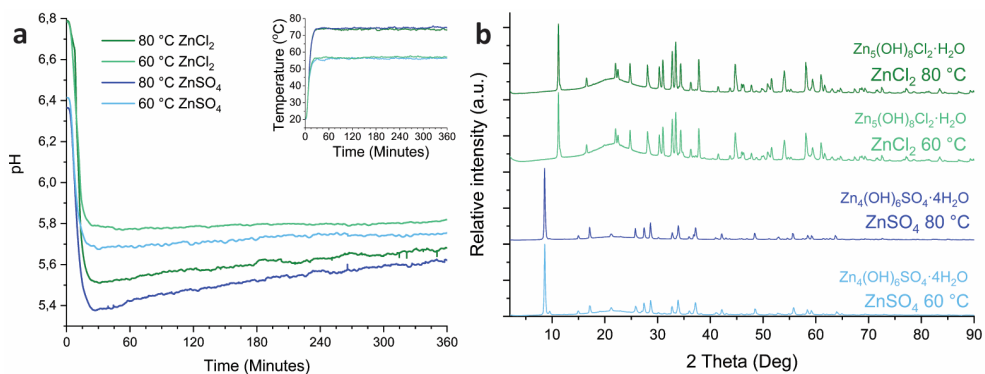


Figure A3.4 pH and temperature profiles (a) and pXRD data (b) of the reaction using ZnCl_2 and ZnSO_4 as zinc source at 60 and 80 °C reaction temperature.

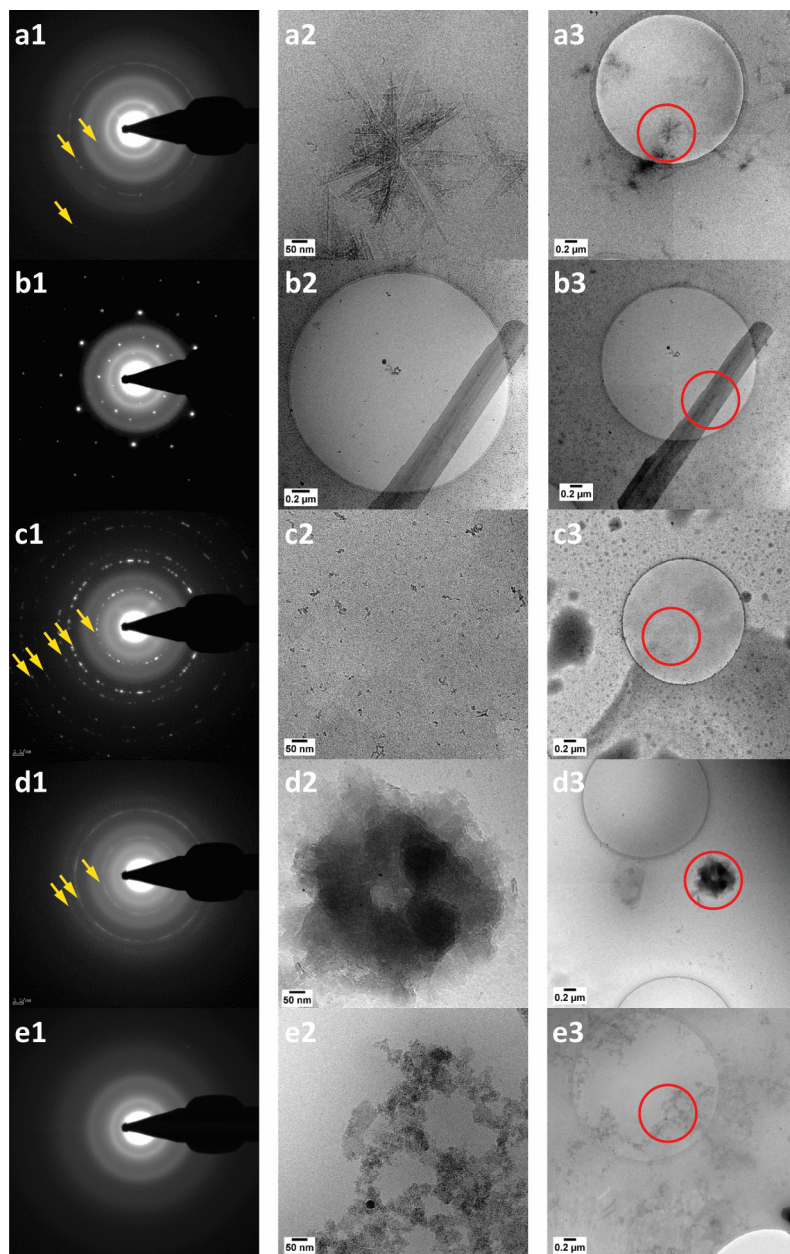


Figure A3.5 Low Dose Selected Area Electron diffraction (LDSAED) patterns (a1-e1), corresponding cryoTEM images (a2-e2) and the selected area location encircled in red (a3-e3) from the radial averaging plots showed in *Fig. 3.3*. LBZA sheets formed initially at RT (a), matured LBZA sheets (b), and species observed during the LBZA collapse; high contrast particulated regions (c), disorganized sheet clusters (d) and particle clusters (e). Diffraction rings are indicated with yellow arrows.

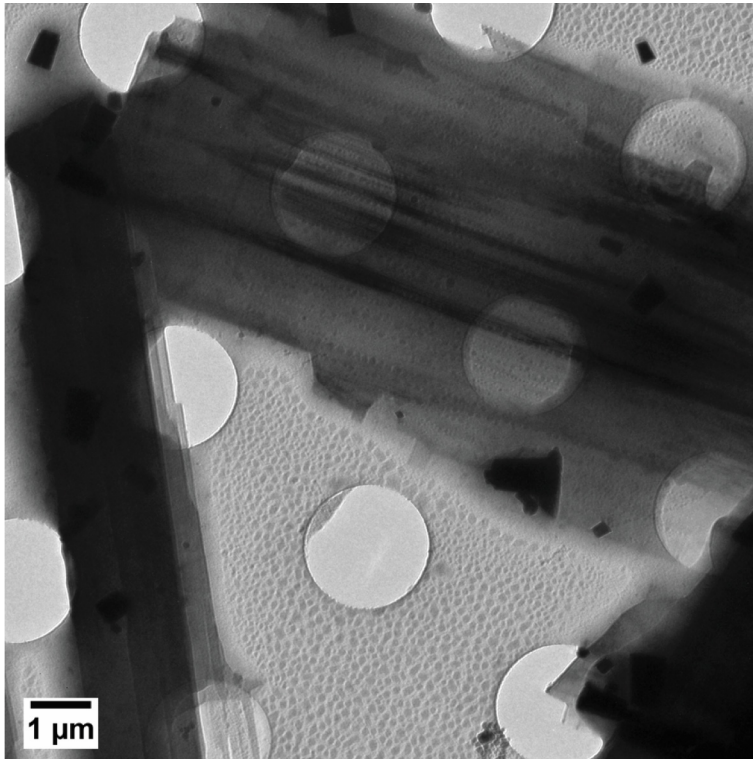


Figure A3.6 CryoTEM image of large LBZA sheets and small ZnO crystals observed in region II, see Fig. 3.2.

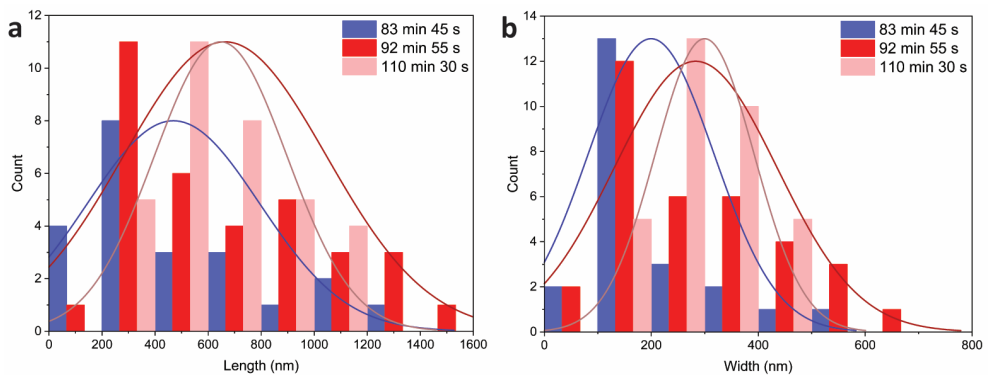


Figure A3.7 Histogram of the measured length (a) and width (b) of ZnO crystals observed by cryoTEM just before (83 min 45 s, blue), at the beginning (92 min 55 s, red) and at the end (110 min 30 s, pink) of the second ZnAc₂ pH drop. All data was taken from cryoTEM experiment 4 (section A3.1). Using a two-sided independent t -test it is found that the average length (l) at 92 min 55 s ($l = 660$ nm, $S_l = 380$ nm, $N = 34$) and 110 min 30 s ($l = 650$ nm, $S_l = 250$ nm, $N = 33$) is not equal to the average length at 83 min and 45 s ($l = 470$ nm, $S_l = 330$ nm, $N = 22$) with a probability of 95.4% and 96.4%, respectively. It was found that the average width (w) at 92 min 55 s ($w = 280$ nm, $S_w = 150$ nm, $N = 34$) and 110 min 30 s ($w = 300$ nm, $S_w = 90$ nm, $N = 33$) is not equal to the average width at 83 min and 45 s ($w = 200$ nm, $S_w = 120$ nm, $N = 22$) with a probability of 97.5% and 99.8%, respectively.

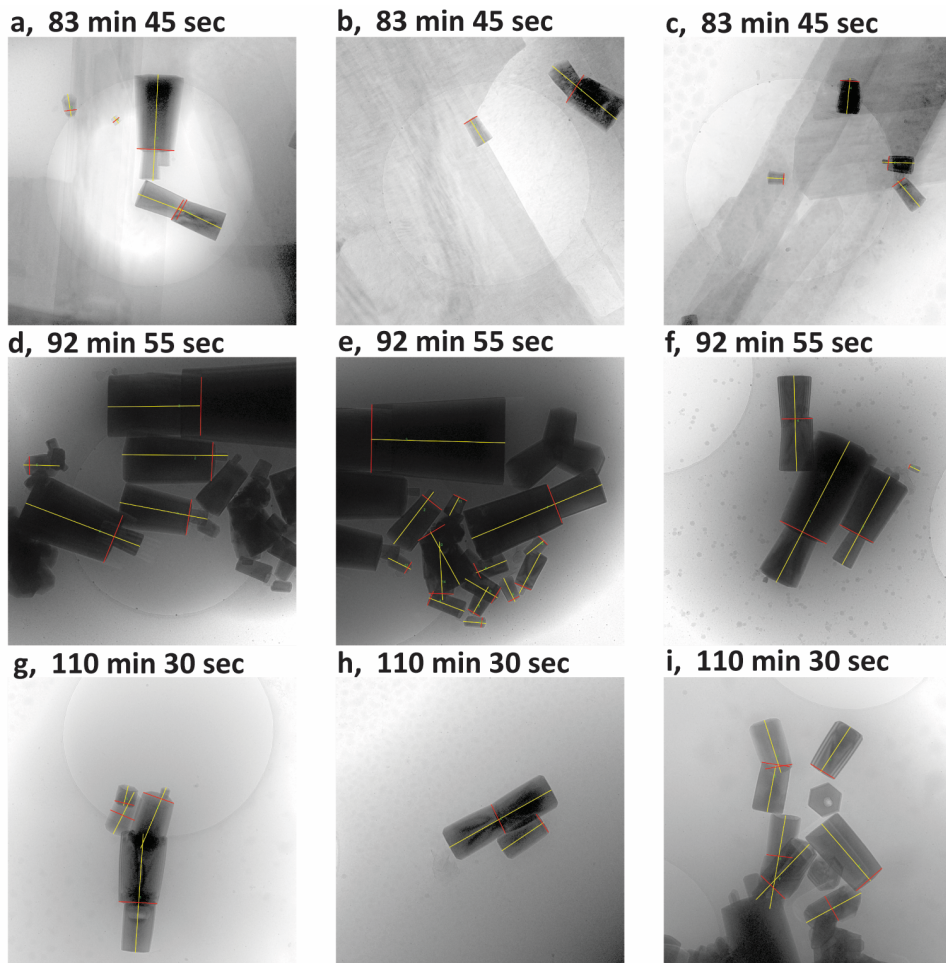


Figure A3.8 CryoTEM images at 83 min 45 s, 92 min 55 s and at 110 min 30 s sampling time used for particle size analysis. The red lines indicate measured widths and the yellow lines indicate measured lengths. The contrast was modified to distinguish between individual ZnO particles. Data collected from these images and at least 4 additional images per sampling time were used to compose the histograms in *Fig. A3.7* and the particles sizes in the main text.

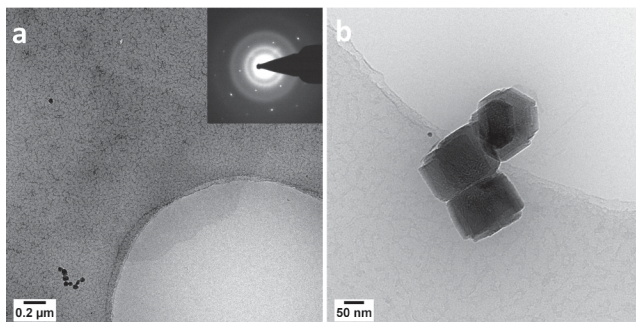


Figure A3.9 CryoTEM images of the $\text{Zn}(\text{NO}_3)_2$ reaction sampled at 15 min reaction time, showing incidentally observed particles including one LBZN sheet (a) and two twinned ZnO crystals (b).

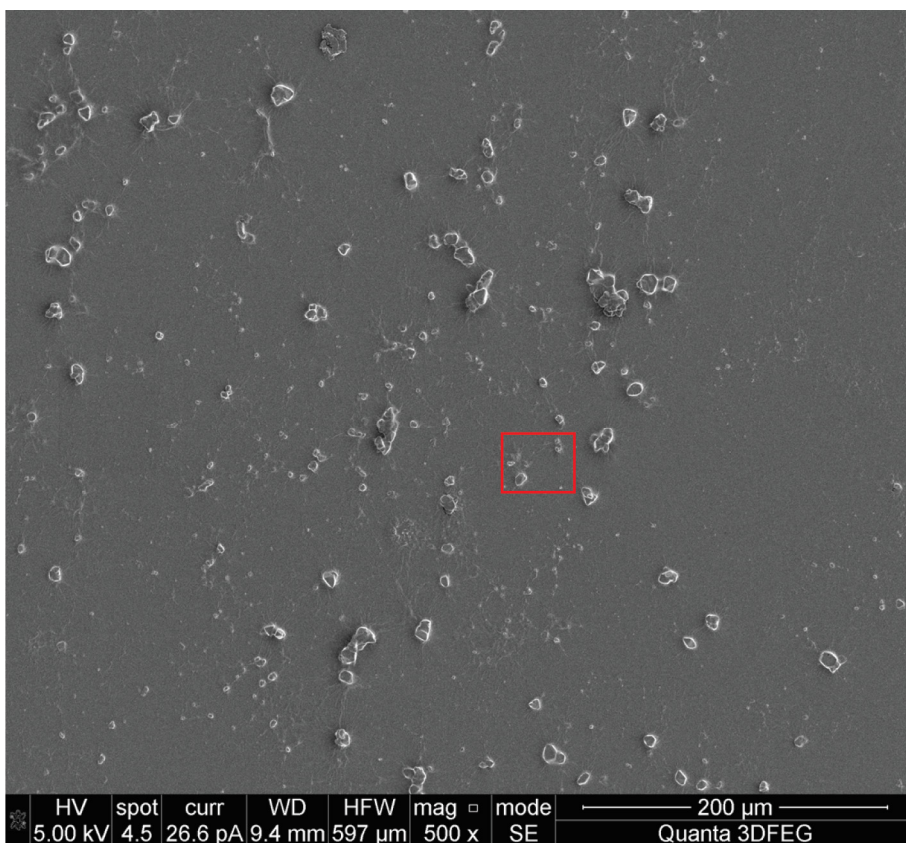


Figure A3.10 Lower magnification SEM image of the region shown in Fig. 3.5b. The location of Fig. 5b has been indicated in red.

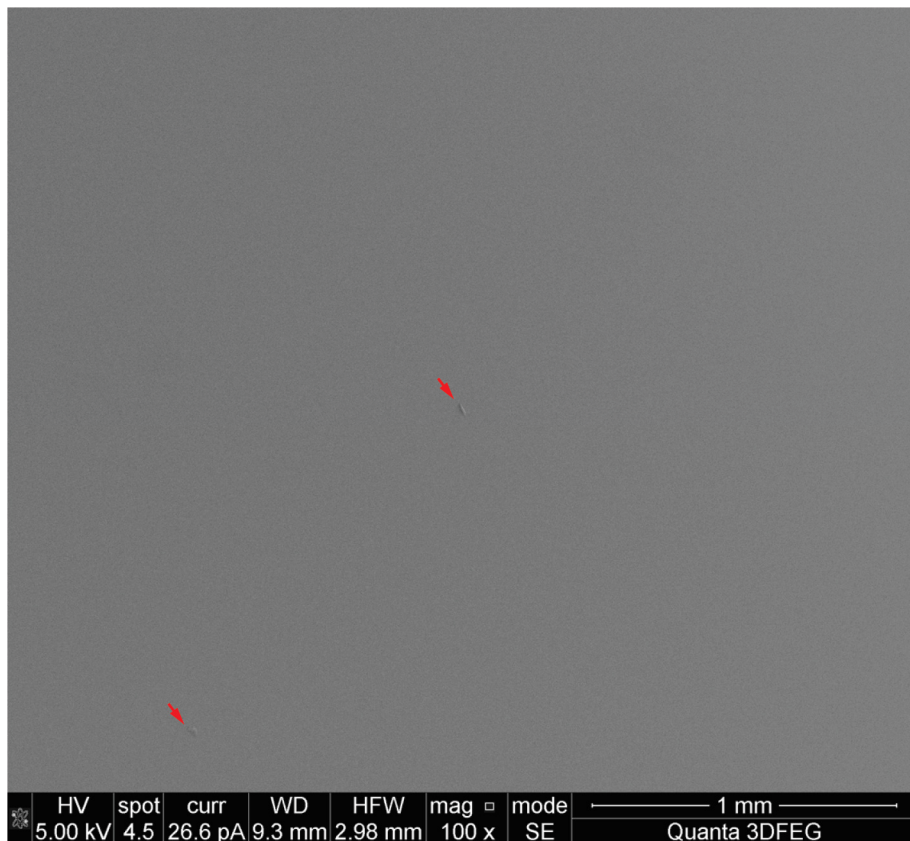


Figure A3.11 SEM images of a glass surface suspended in a ZnAc_2 reaction for the first 30 minutes, showing two particles (red arrow) in a field of about 9 mm^2 . This shows that the image is in focus and no significant surface growth occurs at this time point.

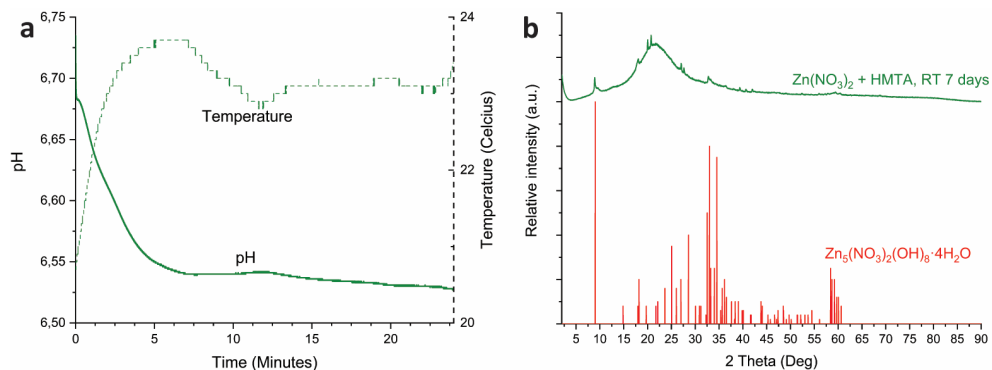


Figure A3.121 pH and temperature (a) profile of $\text{Zn}(\text{NO}_3)_2$ and HMTA in water incubated for 24h at RT. pXRD data (b) collected of the product obtained after > 7 days of incubation at RT.

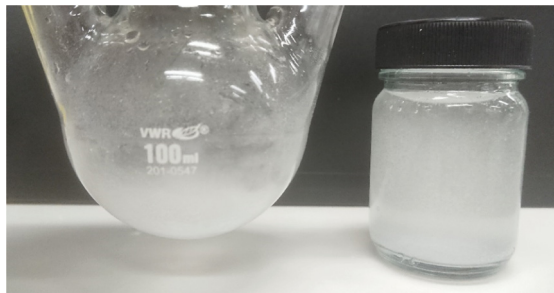


Figure A3.13 Pictures of the flask and isolated reaction product dispersion for the reaction performed with $\text{Zn}(\text{NO}_3)_2$ with an additional 24 hours incubation time.

A3.1. Additional Supporting Information

Additional supporting information can be found online with the original manuscript at: ^[40]

<https://pubs.rsc.org/--/content/articlelanding/2020/ce/d0ce00847h#!divAbstract>

The references in the text specifically correspond to ESI section 3.

3.8. References

1. J. J. De Yoreo, P. U. Gilbert, N. A. Sommerdijk, R. L. Penn, S. Whitelam, D. Joester, H. Zhang, J. D. Rimer, A. Navrotsky, J. F. Banfield, A. F. Wallace, F. M. Michel, F. C. Meldrum, H. Colfen and P. M. Dove, Crystallization by Particle Attachment in Synthetic, Biogenic, and Geologic Environments. *Science* **349**, aaa6760 (2015).
2. G. Mirabello, A. Keizer, P. H. H. Bomans, A. Kovacs, R. E. Dunin-Borkowski, N. A. J. M. Sommerdijk and H. Friedrich, Understanding the Formation Mechanism of Magnetic Mesocrystals with (Cryo-)Electron Microscopy. *Chem Mater* **31**, 7320-7328 (2019).
3. W. J. Habraken, J. Tao, L. J. Brylka, H. Friedrich, L. Bertinetti, A. S. Schenk, A. Verch, V. Dmitrovic, P. H. Bomans, P. M. Frederik, J. Laven, P. van der Schoot, B. Aichmayer, G. de With, J. J. DeYoreo and N. A. Sommerdijk, Ion-association Complexes Unite Classical and Non-classical Theories for the Biomimetic Nucleation of Calcium Phosphate. *Nat Commun* **4**, 1507 (2013).
4. Y. Xu, K. C. H. Tijssen, P. H. H. Bomans, A. Akiva, H. Friedrich, A. P. M. Kentgens and N. Sommerdijk, Microscopic Structure of the Polymer-induced Liquid Precursor for Calcium Carbonate. *Nat Commun* **9**, 2582 (2018).
5. K. Govender, D. S. Boyle, P. B. Kenway and P. O'Brien, Understanding the Factors that Govern the Deposition and Morphology of Thin Films of ZnO from Aqueous Solution. *J Mater Chem* **14**, 2575-2591 (2004).
6. R. A. McBride, J. M. Kelly and D. E. McCormack, Growth of Well-defined ZnO Microparticles by Hydroxide Ion Hydrolysis of Zinc Salts. *J Mater Chem* **13**, 1196-1201 (2003).
7. K. M. McPeak, M. A. Becker, N. G. Britton, H. Majidi, B. A. Bunker and J. B. Baxter, In Situ X-ray Absorption Near-Edge Structure Spectroscopy of ZnO Nanowire Growth During Chemical Bath Deposition. *Chem Mater* **22**, 6162-6170 (2010).
8. N. J. Nicholas, G. V. Franks and W. A. Ducker, The Mechanism for Hydrothermal Growth of Zinc Oxide. *CrystEngComm* **14**, 1232-1240 (2012).
9. W. L. Feng, B. C. Wang, P. Huang, X. D. Wang, J. Yu and C. W. Wang, Wet Chemistry Synthesis of ZnO Crystals with Hexamethylenetetramine (HMTA): Understanding the Role of HMTA in the Formation of ZnO Crystals. *Mat Sci Semicon Proc* **41**, 462-469 (2016).
10. M. K. Liang, M. J. Limo, A. Sola-Rabada, M. J. Roe and C. C. Perry, New Insights into the Mechanism of ZnO Formation from Aqueous Solutions of Zinc Acetate and Zinc Nitrate. *Chem Mater* **26**, 4119-4129 (2014).
11. B. Song, X. Cui, Y. Q. Wang, L. F. Si, Z. X. Kou, W. W. Tian, C. Yi and Y. M. Sun, Controllable Growth of Unique Three-Dimensional Layered Basic Zinc Salt/ZnO Binary Structure. *Cryst Growth Des* **16**, 4877-4885 (2016).
12. J. Lee, A. J. Easteal, U. Pal and D. Bhattacharyya, Evolution of ZnO Nanostructures in Sol-gel Synthesis. *Curr Appl Phys* **9**, 792-796 (2009).
13. E. S. Jang, J. H. Won, Y. W. Kim, Z. Cheng and J. H. Choy, Dynamic Transition Between Zn-HDS and ZnO; Growth and Dissolving Mechanism of Dumbbell-like ZnO Bipod Crystal. *CrystEngComm* **13**, 546-552 (2011).
14. T. H. Hsieh, J. Y. Chen, C. W. Huang and W. W. Wu, Observing Growth of Nanostructured ZnO in Liquid. *Chem Mater* **28**, 4507-4511 (2016).
15. S. Yin and T. Sato, Mild Solution Synthesis of Zinc Oxide Films with Superhydrophobicity and Superhydrophilicity. *J Mater Chem* **15**, 4584-4587 (2005).
16. J. G. Strom and H. W. Jun, Kinetics of Hydrolysis of Methenamine. *J Pharm Sci* **69**, 1261-1263 (1980).
17. R. Devaraj, K. Venkatachalam, K. Saravanakumar, P. M. Razad and K. Mahalakshmi, Role of Hexamine: Growth of Multiarmed ZnO Nanorods and Evidence of Merging due to Lateral Growth. *J Mater Sci-Mater El* **27**, 12201-12208 (2016).
18. G. Amin, M. H. Asif, A. Zainelabdin, S. Zaman, O. Nur and M. Willander, Influence of pH, Precursor Concentration, Growth Time, and Temperature on the Morphology of ZnO Nanostructures Grown by the Hydrothermal Method. *J Nanomater* **2011**, 1-9 (2011).
19. K. M. McPeak, T. P. Le, N. G. Britton, Z. S. Nickolov, Y. A. Elabd and J. B. Baxter, Chemical Bath Deposition of ZnO Nanowires at Near-Neutral pH Conditions without Hexamethylenetetramine (HMTA): Understanding the Role of HMTA in ZnO Nanowire Growth. *Langmuir* **27**, 3672-3677 (2011).
20. R. Parize, J. Garnier, O. Chaix-Pluchery, C. Verrier, E. Appert and V. Consonni, Effects of Hexamethylenetetramine on the Nucleation and Radial Growth of ZnO Nanowires by Chemical Bath Deposition. *J Phys Chem C* **120**, 5242-5250 (2016).
21. Y. Liu, K. P. Tai and S. J. Dillon, Growth Kinetics and Morphological Evolution of ZnO Precipitated from Solution. *Chem Mater* **25**, 2927-2933 (2013).
22. S. E. R. Tay, A. E. Goode, J. N. Weker, A. A. Cruickshank, S. Heutz, A. E. Porter, M. P. Ryan and M. F. Toney, Direct In Situ Observation of ZnO Nucleation and Growth via Transmission X-ray Microscopy. *Nanoscale* **8**, 1849-1853 (2016).
23. P. M. Perillo, M. N. Atia and D. F. Rodriguez, Studies on the Growth Control of ZnO Nanostructures Synthesized by the Chemical Method. *Materia-Brazil* **23**, e12133 (2018).
24. T. F. Long, S. Yin, K. Takabatake, P. Zhnag and T. Sato, Synthesis and Characterization of ZnO Nanorods and Nanodisks from Zinc Chloride Aqueous Solution. *Nanoscale Res Lett* **4**, 247-253 (2009).
25. M. R. Alenezi, S. J. Henley, N. G. Emerson and S. R. P. Silva, From 1D and 2D ZnO Nanostructures to 3D Hierarchical Structures with Enhanced Gas Sensing Properties. *Nanoscale* **6**, 235-247 (2014).
26. M. R. Alenezi, A. S. Alshammari, K. D. G. I. Jayawardena, M. J. Beliatas, S. J. Henley and S. R. P. Silva, Role of the Exposed Polar Facets in the Performance of Thermally and UV Activated ZnO Nanostructured Gas Sensors. *J Phys Chem C* **117**, 17850-17858 (2013).

27. C. T. Sun and D. F. Xue, Chemical Bonding Theory of Single Crystal Growth and its Application to Crystal Growth and Design. *CrystEngComm* **18**, 1262-1272 (2016).
28. C. Ou, P. E. Sanchez-Jimenez, A. Datta, F. L. Boughey, R. A. Whiter, S. L. Sahonta and S. Kar-Narayan, Template-Assisted Hydrothermal Growth of Aligned Zinc Oxide Nanowires for Piezoelectric Energy Harvesting Applications. *ACS Appl Mater Inter* **8**, 13678-13683 (2016).
29. A. Moezzi, M. B. Cortie and A. M. McDonagh, Zinc Hydroxide Sulphate and its Transformation to Crystalline Zinc Oxide. *Dalton Trans* **42**, 14432-14437 (2013).
30. A. Moezzi, M. Cortie and A. McDonagh, Transformation of Zinc Hydroxide Chloride Monohydrate to Crystalline Zinc Oxide. *Dalton Trans* **45**, 7385-7390 (2016).
31. Q. J. Yu, W. Y. Fu, C. L. Yu, H. B. Yang, R. H. Wei, M. H. Li, S. K. Liu, Y. M. Sui, Z. L. Liu, M. X. Yuan, G. T. Zou, G. R. Wang, C. L. Shao and Y. C. Liu, Fabrication and Optical Properties of Large-scale ZnO Nanotube Bundles via a Simple Solution Route. *J Phys Chem C* **111**, 17521-17526 (2007).
32. M. S. Yao, P. Hu, N. Han, F. Ding, C. L. Yin, F. L. Yuan, J. Yang and Y. F. Chen, ZnO Micro-windbreak for Enhanced Gas Diffusion. *Sensor Actuat B-Chem* **186**, 614-621 (2013).
33. Q. Y. Cui, K. Yu, N. Zhang and Z. Q. Zhu, Porous ZnO Nanobelts Evolved from Layered Basic Zinc Acetate Nanobelts. *Appl Surf Sci* **254**, 3517-3521 (2008).
34. M. N. R. Ashfold, R. P. Doherty, N. G. Ndifor-Angwafor, D. J. Riley and Y. Sun, The Kinetics of the Hydrothermal Growth of ZnO Nanostructures. *Thin Solid Films* **515**, 8679-8683 (2007).
35. H. J. Gao, B. H. Ji, I. L. Jager, E. Arzt and P. Fratzl, Materials Become Insensitive to Flaws at Nanoscale: Lessons from Nature. *Proc Nat Am Soc* **100**, 5597-5600 (2003).
36. X. Zhang, A. Vyatskikh, H. J. Gao, J. R. Greer and X. Y. Li, Lightweight, Flaw-tolerant, and Ultrastrong Nanoarchitected Carbon. *Proc Nat Am Soc* **116**, 6665-6672 (2019).
37. J. H. Kim, E. M. Kim, D. Andeen, D. Thomson, S. P. DenBaars and F. F. Lange, Growth of Heteroepitaxial ZnO Thin Films on GaN-Buffered Al₂O₃(0001) Substrates by Low-temperature Hydrothermal Synthesis at 90 Degrees C. *Adv Funct Mater* **17**, 463-471 (2007).
38. A. Moezzi, A. McDonagh, A. Dowd and M. Cortie, Zinc Hydroxyacetate and Its Transformation to Nanocrystalline Zinc Oxide. *Inorg Chem* **52**, 95-102 (2013).
39. W. X. Zhang and K. Yanagisawa, Hydrothermal Synthesis of Zinc Hydroxide Chloride Sheets and their Conversion to ZnO. *Chem Mater* **19**, 2329-2334 (2007).
40. M. M. J. van Rijt, B. M. Oosterlaken, R. R. M. Joosten, L. E. A. Wijkhuijs, P. H. H. Bomans, H. Friedrich and G. de With, Counter-ion Influence on the Mechanism of HMTA-mediated ZnO Formation. *CrystEngComm* **22**, 5854-5861 (2020).

Chapter 4

Titration-based Strategy for Controlled Aqueous ZnO Formation

Hexamethylenetetramine (HMTA) is commonly used as a base releasing agent for the synthesis of ZnO under mild aqueous conditions. HMTA hydrolysis leads to a gradual formation of base during the reaction. Use of HMTA, however, does have limitations: HMTA hydrolysis yields both formaldehyde and ammonia, it provides no direct control over the ammonia addition rate or the total amount of ammonia added during the reaction, it results in a limited applicable pH range and it dictates the accessible reaction temperatures. To overcome these restrictions, this work presents a direct base titration strategy for ZnO synthesis in which a continuous base addition rate is maintained. Using this highly flexible strategy, wurtzite ZnO can be synthesized at a pH > 5.5 using both KOH or ammonia as base source at a variety of addition rates and reaction pH. *In situ* pH measurements suggest a similar reaction mechanism as for the HMTA-based synthesis, independent of the varied conditions. The type and concentration of the base used for titration, affects the reaction product, with ammonia showing evidence of capping behavior. Optimizing this strategy, we are able to influence and direct the crystal shape and significantly increase the product yield to 74% compared to the ~13% obtained by the HMTA reference reaction.

This chapter is adapted from:

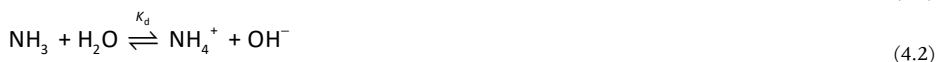
M. M. J. van Rijt, B. M. Oosterlaken, H. Friedrich and G. de With, Controlled Titration-based ZnO Formation, *CrystEngComm*, 2021, DOI: 10.1039/d1ce00222h.

“And as regards haste”, he added philosophically, “the impression that time is quickly running out is customary a warning signal enjoining one to reduce the pace, and proceed slowly and with due prudence”

Andrzej Sapkowski, *The tower of Swallows*, 1997

4.1. Limitation in Aqueous ZnO Formation

For the aqueous formation of zinc oxide (ZnO) at a mild and controlled pH, hexamethylenetetramine (HMTA) is typically used as a base releasing agent.^[1-4] Using this strategy a variety of ZnO morphologies can be synthesized^[5] ranging from hexagonal twin pillar structures^[6, 7] and ZnO arrays,^[8-10] to more complicated morphologies^[11-13] and nanocomposites.^[14] At elevated reaction temperature HMTA hydrolysis results in the gradual formation of ammonia (NH₃) and formaldehyde (CH₂O, Eq. 4.1) in the reaction medium. The produced ammonia is protonated by the water present, releasing hydroxide in the process (Eq. 4.2).^[15] The formed hydroxide is subsequently consumed as base during the formation of ZnO (Eq. 4.3).



$$k_{obs} = (k_w + k_h[\text{H}^+])f^+ \quad (4.4)$$

HMTA hydrolysis is acid catalysed, resulting in a concomitant increase in HMTA decomposition rate k with a decreasing reaction pH (Eq. 4.4), with f^+ representing the fraction of HMTA in protonated form.^[16] Combining this with a hydroxide consuming reaction, like the formation of ZnO, the system will move to an equilibrium pH where the formation of hydroxide by HMTA hydrolysis and ammonia protonation is in balance with the hydroxide consumption by the reaction, effectively making HMTA a pH buffer.^[17] Given that for a crystallization process the reaction rate is temperature dependent, the reaction pH and final HMTA decomposition rate will also be influenced by the reaction temperature. Although the decomposition of HMTA is further catalysed by the presence of strong acids,^[18] Ashfold *et al.*^[19] showed that the rate of HMTA decomposition is not catalysed or retarded by the formation of ZnO after 2 h reaction time.

Besides HMTA being used as base source and pH buffer, additional influences of HMTA on the ZnO reaction have been investigated.^[20] HMTA has been proposed to act as a capping or structure directing agent on the non-polar side facets of ZnO promoting growth along the *c*-axis^[21-23] and acting as a shell preventing the merging of nanorods^[22, 24]. However, these additional HMTA influences are under debate. Notably, *in-situ* XANES measurements showed no long lived zinc-HMTA intermediates during the reaction, whereas IR measurements showed no adsorption of HMTA on ZnO.^[25, 26] One generally overlooked aspect is the influence of the HMTA hydrolysis products ammonia, formaldehyde and hydroxide. As hydrolysis of HMTA yields all these products simultaneously, studies into product specific effects becomes highly challenging.

To overcome above mentioned limitations, a titration-based strategy may be employed that allows for the addition of any reactant at any rate, facilitating the study of the influence individual components. Furthermore, titration is not limited to a narrow equilibrium pH window during reaction (I), by the reaction temperature (II), does not need reactant refreshing steps over long reaction times (III)^[27-29] or a reaction condition dependent base addition rate (IV), disadvantages inherent to the use of HMTA. Titration-based strategies have been used previously for the formation of biomimetic magnetite,^[30, 31] silica^[32] and to limited extend for ZnO^[26], but not in context of imitating existing reaction conditions such as the HMTA-based ZnO synthesis.

Therefore, this work aims to design a HMTA-inspired base-titration strategy for the formation of ZnO in water under mild pH conditions. By investigating the contribution of HMTA decomposition products, we find that of its hydrolysis products mainly the ammonia affects the ZnO reaction product. It is further

found that the decomposition rate of HMTA is higher during the initial formation of ZnO than under native conditions. Finally, using the flexibility of the titration strategy, we show that ZnO crystal shape and size is sensitive to the reaction conditions, including the initial pH and the added base concentration. We finally demonstrate a protocol for the formation of highly faceted twin-pillared ZnO crystals with high yield.

4.2. Hydrolysis of HMTA and Experimental Design

Previous work on the formation of ZnO using HMTA showed a constant pH of 5.8 during most of the reaction.^[33] Hence, the hydrolysis of 25 mM HMTA in water at a constant pH of 5.8 was taken as a model system.^[33] For experimental details see section A4.1. The HMTA hydrolysis rate was measured by titrating 0.25 M acetic acid into the reaction vessel to maintain a constant pH (Fig. A4.1), as discussed in detail in section A4.2. These measurements showed a constant but pH dependent HMTA hydrolysis rate k_{obs} of 0.013 h^{-1} (pH 6.0), 0.018 h^{-1} (pH 5.8) and 0.023 h^{-1} (pH 5.7), which matches excellently with results from Ashfold *et al.*^[19] (Fig. 4.1a).

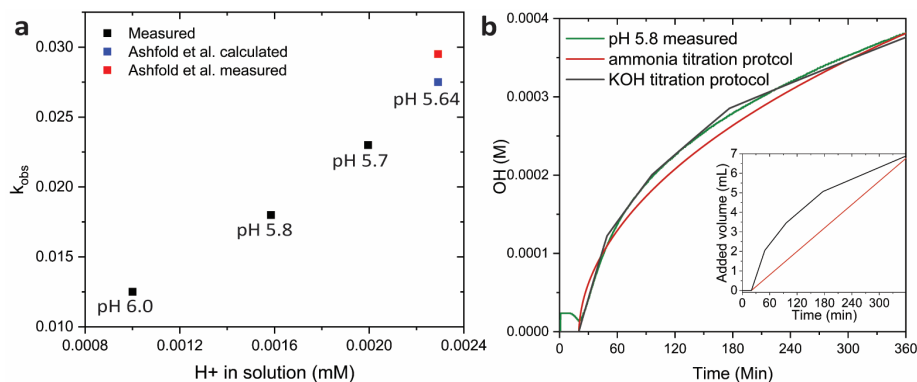


Figure 4.1 Observed hydrolysis rate (a) of HMTA at pH 6.0, 5.8 and 5.7 (black) compared to results from Ashfold *et al.*^[19] (results from Ashfold have been corrected with a factor of two to compensate for the difference HMTA starting concentration, see section A2.2). Measured formation of hydroxide ions (OH⁻) by HMTA hydrolysis (b) at pH 5.8 (green) and the calculated amount of formed hydroxide as a function of time (b), with the corresponding titration protocol, by using 73.35 mM ammonia or KOH (red) or 3.1 mM KOH (black), see inset.

To mimic the base formation rate during HMTA hydrolysis with a preprogrammed run in our titration setup, the minimal titration rate and increment steps of 0.01 mL min^{-1} of the equipment should be considered. Taking this limitation into account, two titration strategies were designed, both presuming that ZnO formation does not influence the hydrolysis of HMTA, as indicated by Ashfold *et al.*^[19] The first is based on the addition of ammonia (both with and without the simultaneous addition of formaldehyde) or KOH without taking the dissociation constant of ammonia K_{a} into account. Given the near linear hydrolysis rate of HMTA, we calculated that 73.35 mM ammonia or KOH had to be added at a constant rate of 0.02 mL min^{-1} or 146.70 mM ammonia and 221.55 mM formaldehyde, both at a constant rate of 0.01 mL min^{-1} (Fig. 4.1b, red). The second titration strategy is based on the addition of KOH while taking the K_{a} of ammonia into account.^[15, 34] For this a progressively decreasing addition rate was calculated for 3.1 mM KOH (Fig. 4.1b, black). Both strategies showed an increase in hydroxide ions that closely matched with the previously identified decomposition of HMTA (25 mM) at a pH of 5.8 (Fig. 4.1b).

4.3. Influence of Reaction Components

Upon initiating a HMTA-ZnO reference reaction by heating, *in-situ* pH measurements show a gradual pH decrease from 6.8 to 5.8 (Fig. 4.2). After this initial pH drop, the pH remains stable until 120 min reaction time. At this time a second drop of 0.1 pH is observed, which previous work has shown to indicate a rapid transition from a layered basic zinc acetate (LBZA) rich phase to predominantly wurtzite ZnO (LBZA-ZnO transition).^[33] Following the LBZA-ZnO transition the pH gradually recovered to 5.8. At the end of the reaction, a white precipitate is observed for all reactions but to a varying degree, both in dispersion and on the flask. After purification of the dispersed reaction products, a yield of 12.6% was obtained. Repeating the HMTA reaction to exclude the influence of titration itself (water, 0.2 mL min⁻¹), no significant influence on the kinetics, final product or yield was observed (Fig. A4.2a-c). pXRD and SEM analysis confirm the formation of wurtzite ZnO (Fig. A4.2d-g).

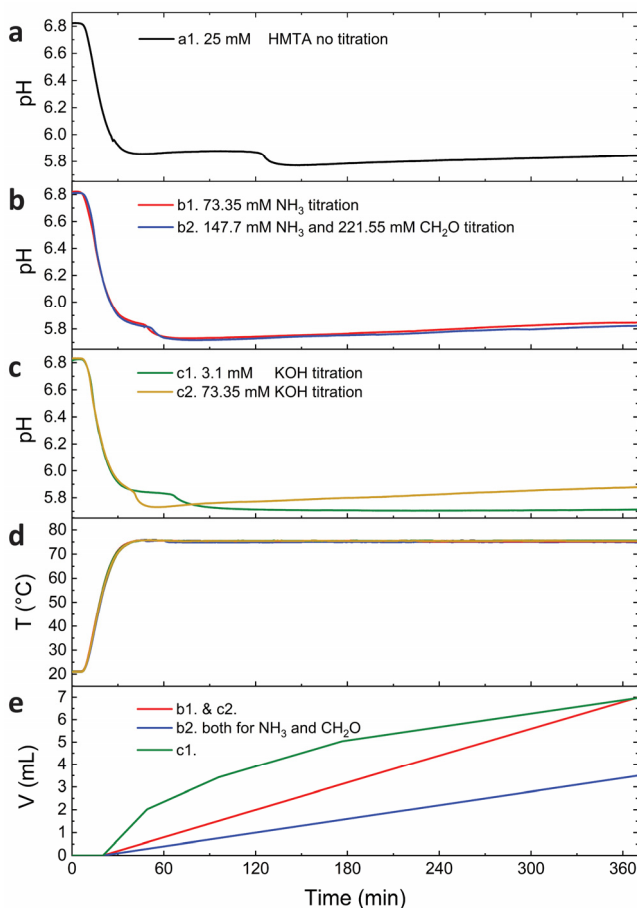


Figure 4.2 HMTA- and titration-based synthesis of ZnO from zinc acetate showing the pH evolution of the HMTA control experiment (a), the pH evolution of the ammonia-based titration experiments (b), the pH evolution of the potassium hydroxide-based titration experiments (c), the temperature T (d) and titration volume V (e) as function of time.

When titrating 73.35 mM ammonia directly (Fig. 4.2b,d-e), the pH profile showed the same features as the HMTA reference reaction with the notable difference that the LBZA-ZnO transition is observed at 51 min instead of 120 min reaction time. This indicates a significant acceleration of the reaction kinetics when using direct base-titration. Simultaneous titration of formaldehyde showed no influence on the pH evolution during the reaction. After purification, pXRD confirmed the formation of wurtzite ZnO, independent of simultaneous titration of formaldehyde (Fig. 4.3). As all pXRD reflections are sharp, we conclude that the materials formed are crystalline. The product yield was 3.5% when titrating ammonia and 3.7% when titrating in ammonia and formaldehyde.

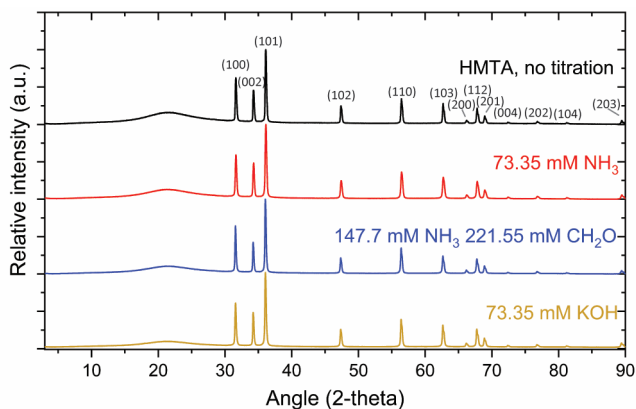


Figure 4.3 pXRD data of ZnO formed by HMTA- and titration-mediated synthesis. The pXRD data is normalized on the highest intensity signal and, the broad pXRD signal visible at about 20° is due to the substrate. All further observed spacings match with wurtzite ZnO.

The effects of direct hydroxide addition by KOH titration was investigated using the two protocols detailed above: 1) taking the K_a of ammonia into account by gradually adding 3.1 mM KOH and 2) mimicking the ammonia titration protocol using 73.35 mM KOH. Again, both strategies showed the typical pH features (Fig. 4.2c-e) as observed when using HMTA.^[33] The LBZA-ZnO transition was observed at 64 min reaction time for the 3.1 mM and 21 min reaction time for the 73.35 mM KOH titration strategy. Furthermore, when using 3.1 mM KOH the pH remained at 5.7 after the LBZA-ZnO transition, resulting in a relatively low final pH compared to all other reactions. This suggests that the added amount of hydroxide is significantly lower for this experiment than for all other investigated reactions. Indeed, after purification the yield was 0.4% for the 3.1 mM and 4.3% for the 73.35 mM KOH titration strategy. Due to the limited yield, only the 73.35 mM KOH product could be analysed by pXRD, which confirmed the formation of wurtzite ZnO (Fig. 4.3).

Comparing the experimentally obtained reaction yields to theoretically calculated values (section A4.3.), it is found that the result for the 3.1 mM KOH strategy matches well with the expected yield (0.43%) when taking the ammonia K_a into account. The 73.35 mM KOH and ammonia strategies showed a notably higher yield close to $\sim 4\%$. Given the close match between the 73.35 mM KOH and ammonia yields, we presume that almost all ammonia dissociates into ammonium during the reaction. Therefore, the result of the 73.35 mM KOH sample is expected to be close to result obtained using ammonia. This is likely caused by the formation of Zn-ammonium complexes,^[28] possibly in combination with the capping of LBZA and ZnO by ammonium.

Using SEM, the crystal size and shape were studied (Fig. 4.4; A4.3). An approximately constant crystal aspect ratio is observed for all conditions. The crystal habit of wurtzite ZnO results in either a rod-like or

twin-pillared hexagonally faceted shape.^[28] The ZnO crystals resulting from the 25 mM HMTA reaction generally show this hexagonal shape. Size measurements revealed a diameter of 400 ± 150 nm, where \pm indicates the sample standard deviation. (Fig. 4.4a). Although all four HMTA-inspired titration strategies show hexagonally shaped ZnO crystals, the hexagonal faceting is generally less well expressed as compared to crystals of similar size synthesized by using HMTA. Measuring crystal size revealed a diameter of 250 ± 40 nm when titrating ammonia (Fig. 4.4c) and 260 ± 70 nm when titrating with ammonia and formaldehyde (Fig. 4.4d). This shows that formaldehyde has no notable influence of the crystal shape or size. Titrating KOH results in a diameter of 270 ± 110 nm for the 3.1 mM (Fig. 4.4e) and 110 ± 30 nm for the 73.35 mM titration strategy (Fig. 4.4f). This indicates that the above titration-based strategies result in the formation of smaller ZnO crystals compared to the use of HMTA, especially when using KOH as base. Additional size measurements from the pXRD data, by use of the Scherrer equation, did not yield reliable results because the crystals exceed the maximum measurable crystal size imposed by instrumental limitations.^[35]

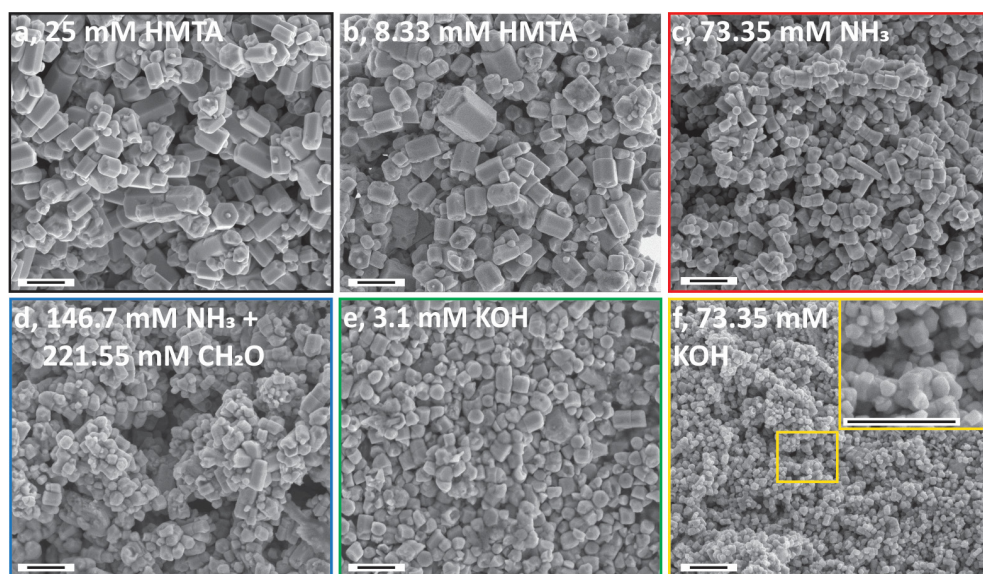


Figure 4.4 SEM images of ZnO formed using 25 mM HMTA (a) and 8.33 mM HMTA (b) as reference. Titration based-ZnO using 73.35 mM ammonia titration (c), 146.7 mM ammonia with simultaneous 221.55 mM formaldehyde titration (d) and using KOH titration 3.1 mM (e) and 73.35 mM (f). All scalebars equal 1 μ m. Size analysis is shown in Fig. A4.3.

Overall, these results show that using a HMTA-inspired direct base-titration strategy wurtzite ZnO can be synthesized under a mild and controlled pH, is formed independent of the added base (ammonia or KOH) and that the addition of formaldehyde does not seem to influence the reaction. A similar pH evolution is observed for all the titration strategies compared to the HMTA reference reaction, suggesting that the underlying ZnO formation mechanism remains unchanged, although with increased reaction kinetics. The HMTA-inspired titration-based ZnO crystals are smaller, show a loss in crystal habit definition and have a smaller yield than the HMTA reference reaction.

4.4. Increased Base Addition Rates

Given the promising results using a HMTA-inspired direct base-titration strategy, the flexibility of the approach was used to optimize the formation of ZnO. As initial step the base addition was increased by using a 1 M ammonia or KOH stock solution while maintaining a titration rate of 0.02 mL min^{-1} . After 1 h reaction time, no base was added in case that the pH was 6.0 or higher to minimize pH-induced ZnO etching.^[33]

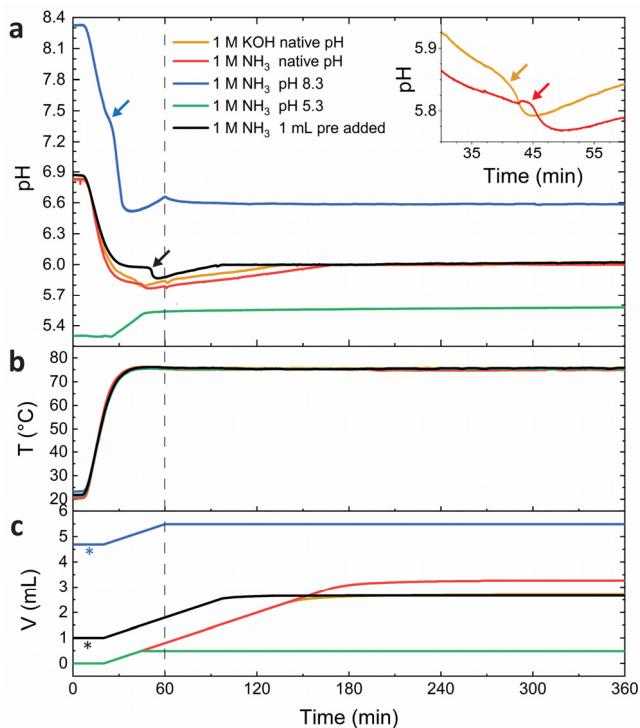


Figure 4.5 Titration-based synthesis of ZnO from zinc acetate using 1 M KOH or 1 M ammonia solutions showing the time evolution of pH (a) magnified between 30 and 50 min reaction time (inset), the temperature T (b) and the titration volume V (c). The dotted line at 1 h reaction time indicates the change in the titration protocol to a target pH of 6. The LBZA-ZnO transitions (a) are indicated using coloured arrows. * Indicates base has been gradually added prior to heating, see Fig. A4.4.

Using either 1 M KOH or ammonia solutions all typical pH features were observed (Fig. 4.5a,b). The LBZA-ZnO transition was again clearly observed in both cases at 41 min and 44 min reaction time, respectively. After the LBZA-ZnO transition the pH gradually increased (from 5.8) to 6.0 at 140 min for KOH and 169 min for ammonia. Upon reaching a pH of 6.0, the base addition rate gradually decreased to 0 mL min^{-1} , indicating that the reaction was complete. This was observed between 180–240 min reaction time. In total 2.70 mL of 1 M KOH and 3.27 mL of 1 M ammonia were required for the reaction with no base being added after 4 h reaction time (Fig. 4.5c). This new titration strategy resulted in a significantly increased yield of 31.8% using KOH and 41.3% using ammonia. pXRD confirmed the formation of pure ZnO (Fig. 4.6). For 1M KOH, SEM analysis showed the formation of crystals with a diameter of $140 \pm 30 \text{ nm}$ (Fig. 4.7b; A4.3) with some clear evidence of hexagonal faceting. For 1 M NH₃ titration, crystals with a

diameter of 240 ± 90 nm and a clear hexagonal faceting were observed (Fig. 4.7c; A4.3), however, rods tend to form clusters instead of the expected twin-pillared structure.

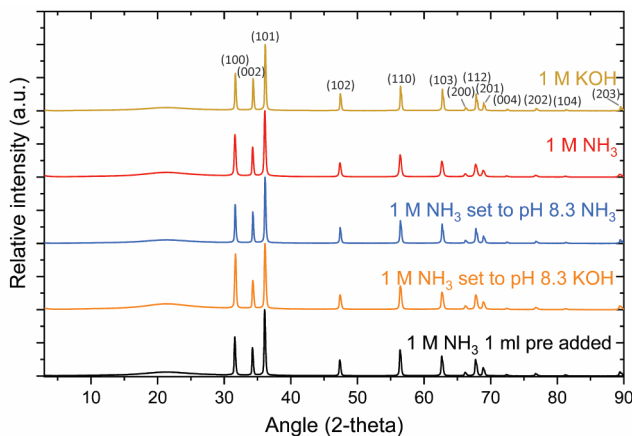


Figure 4.6 pXRD data of ZnO formed by direct base titration using 1 M NH_3 or KOH. The pXRD data is normalized on the highest intensity signal and the broad pXRD signal visible at about 20° is due to the substrate. All further observed spacings match with wurtzite ZnO.

4.5. Influence of pH and Promoting Twin-pillar ZnO Formation

Given the narrow pH range 6.8 – 5.7 using standard conditions, the influence of pH was further investigated. We used 1) a lower starting pH of 5.3 combined with a low target pH of 5.5 and 2) studied the influence of an initially higher pH of ~ 8.3 combined with a similar reaction protocol as that used at standard pH. In all cases 1 M ammonia was gradually titrated into the system.

Starting the reaction at pH 5.3, the pH gradually increased until reaching 5.5 (Fig. 4.5a,b), after which the addition of base was stopped, resulting in a further constant pH of 5.5 (Fig. 4.5c). During and after the reaction no turbidity was observed, nor could any product be obtained by post purification. This indicates that no LBZA or ZnO is formed under these conditions, suggesting that the typical reaction pH of 5.7 - 5.8 is close to the minimal pH required for the formation of ZnO.

To probe the higher pH range, the starting pH was set to 8.3 by either titrating 1 M ammonia (4.7 mL, Fig. 4.5) or KOH (4.8 mL, Fig. A4.4) to the reaction mixture (Fig. A4.5). Upon reaching pH 6.9 this instantly led to the precipitation of LBZA using either base, independently of the base addition rate (Fig. A4.6). Upon reaching pH 8.3 by titrating ammonia or KOH, a stable pH was obtained.

Upon initiating the reaction by heating (Fig. 4.5a,b; A4.4), *in-situ* pH measurements show an immediate drop in pH. For the case that ammonia was used to set the initial pH, an accelerated decrease in the pH is observed 21 minutes after starting the reaction, suggesting a very early LBZA-ZnO transition. Around 32 min, a minimum in pH of 6.6 is reached, followed by a gradual increase in pH up to 6.8 at 60 min due to the constant titration of ammonia. At 60 min, ammonia titration stops resulting in a slight drop in pH to 6.7 after which the pH remains stable for the remainder of the reaction. When adjusting the pH using KOH, a comparable pH evolution is observed with one notable difference. A small rise in pH is observed at 22 min, followed by a second pH decrease at 42 min (Fig. A4.4a). These two pH observations make it unclear when the transition for LBZA to ZnO exactly occurs. After purification an even higher

yield of 74.5 or 68.2% was obtained using respectively ammonia or KOH to set the initial pH. pXRD analysis showed the formation of wurtzite ZnO for both bases (Fig. 4.6). SEM images show the formation of twin-pillared ZnO (Fig. 4.7d,e) with the amount of ammonia used during the start of the reaction strongly affecting their morphology. The use of KOH resulted in ZnO crystals with a diameter of 220 ± 90 nm with a less defined crystal habit, in particularly visible on the side facets (Fig. 4.7e; A4.3). Using ammonia to set the pH resulted in crystals with a diameter of 390 ± 110 nm and a complete loss of crystal habit, i.e., multifaceted ZnO crystals (Fig. 4.7d; A4.3).

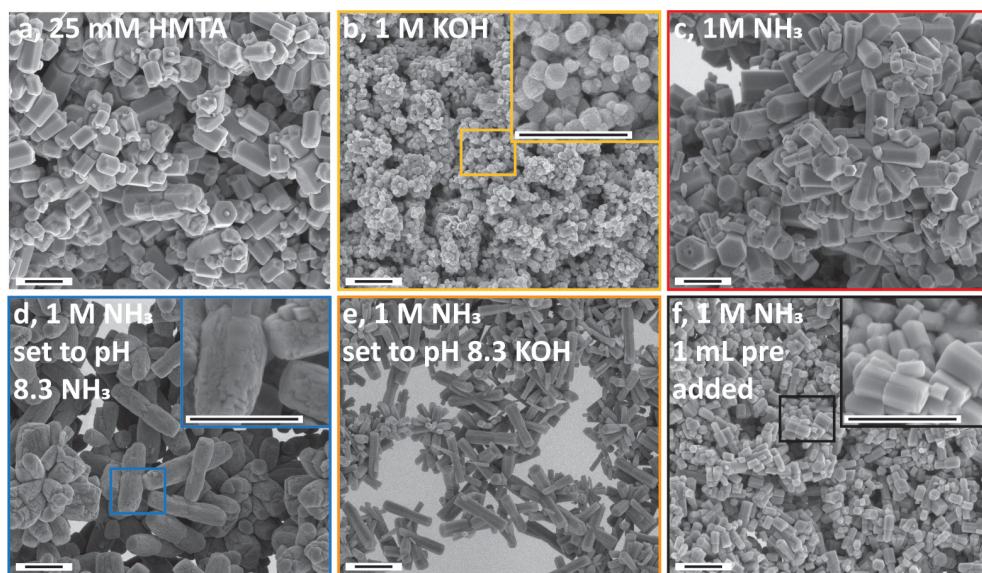


Figure 4.7 SEM images of ZnO formed by 25 mM HMTA as reference (duplicate of Fig. 4.2a), titrating 1 M KOH at native starting pH (b) and 1 M ammonia at native starting pH (c), starting at a pH of 8.3 set using ammonia (d), starting at a pH of 8.3 set using KOH (e) and titrating 1 mL of 1 M ammonia before initiating the reaction (f). The pXRD data is normalized on the highest intensity signal and the broad pXRD signal visible at about 20° is due to the substrates. All scalebars equal 1 μm .

Using this high starting pH of 8.3, predominantly twin-pillared ZnO crystals were observed whereas clusters of ZnO are predominantly formed using the milder native reaction pH. LBZA is formed upon increasing the starting pH and LBZA is believed to act as a nucleation template during the formation of ZnO in dispersion.^[6, 33] Therefore, to promote the formation of twin-pillared ZnO at a mild reaction pH, a titration reaction was designed starting at pH 6.9, after adding 1 mL of ammonia at RT to promote the initial formation of LBZA (Fig. 4.5; A4.5). This resulted in a yield of 34% wurtzite ZnO (Fig. 4.6). Indeed, after purification SEM analysis (Fig. 4.7f; A4.3) showed the presence of predominantly straight twin-pillared ZnO crystals with a diameter of 200 ± 50 nm.

In short, it was observed that titrating an increased concentration of base during the reaction results in the formation of wurtzite ZnO crystals that are similar in size and shape compared to the use of HMTA, while maintaining a similar pH evolution and range. Simultaneously, the yield increased significantly to $\sim 35\%$, when aiming at pH of 6. Decreasing the reaction pH does not result in LBZA or ZnO formation; however, upon increasing the starting pH to 8.3 the ZnO yield is increased to $\sim 70\%$. Crystals formed at elevated pH show loss of habit, especially when adding relatively large amounts of ammonia. The

formation of a twin-pillared ZnO structure over clustered pillars can be promoted by simply adding base before initiating the reaction.

4.6. Discussion

4.6.1. Yield

As mentioned, the HMTA reference reaction resulted in a yield of $\sim 13\%$. This value exceeds both the yields observed for the HMTA-inspired ammonia- and KOH-based titration strategies ($\sim 4\%$) and the expected maximum yield, based on the predicted decomposition rate of HMTA (10%, *section A4.3*). To obtain a HMTA reference with a lower yield, the initial amount of HMTA was decreased from 25 mM to 8.33 mM. However, this still resulted in a yield of 7.2%, significantly exceeding the yield of the titration reaction and the expected maximum yield ($\sim 3.3\%$, *Fig. A4.2*). Ashfold *et al.*^[19] showed that the decomposition rate of HMTA is not affected by the formation of ZnO after a reaction time larger than 2 h and these authors are on occasion cited as proving that the ZnO formation reaction does not affect the HMTA decomposition rate. However, using their data for the first 1.5 h we calculated a close to 9-fold faster decomposition rate in presence of the ZnO forming reaction (*section A4.3*). This higher initial decomposition rate of HMTA during the formation of ZnO explains the higher yield for the HMTA reference reaction compared to the 73.35 mM base titration reactions. This emphasizes the unpredictability of the HMTA reference reaction and makes the direct imitation of HMTA decomposition highly challenging.

When titrating 1 M of base, an increase in yield with reaction pH could be observed. Titrating ammonia to an equilibrium pH of 6.0 resulted in a yield of 34.0 or 41.3% with or without an initial addition of base, respectively. For the high pH reactions with a final pH of 6.6 and 6.4, a yield of respectively 74.5 or 68.2% was obtained. This suggests that the equilibrium between soluble Zn species and ZnO shifts with increasing reaction pH, allowing for a larger ZnO yield when terminating the reaction at a higher final pH. It also shows that significantly more base is added using these 1 M base titration strategies than when using HMTA.

4.6.2. Kinetics

Comparing the LBZA-ZnO transition time between experiments, we note that by titrating 73.35 mM KOH this transition is observed slightly earlier at 40 min compared to 51 min using 73.35 mM ammonia. In general, faster reaction kinetics are observed with an increase in the concentration of the base added (*Fig. 4.3; 4.5*). By increasing the added KOH concentration from 3.1 mM to 73.35 mM, the time at which the LBZA-ZnO transition occurs, decreases from 64 min to 40 min. However, further increasing the KOH concentration to 1 M does not further accelerate the occurrence of the LBZA-ZnO transition. Moreover, using 1 M ammonia, the addition of 1 mL base before initiating the reaction results in a delay of the LBZA-ZnO transition from 44 min to 50 min reaction time (*Fig. 4.5*). Given that the LBZA-ZnO transition is presumably caused by LBZA crystals exceeding a critical size,^[33] this suggests that the LBZA-ZnO transition time depends on small variations in (initial) reaction conditions influencing the LBZA growth rate and/or stability. This point is further supported by the transition time of ~ 120 min when using HMTA, close to an hour longer than all titration reactions including those with a slower base addition. However, based on the present data it cannot be excluded that the presence of HMTA itself has a retarding effect on the kinetics.

4.6.3. Particle Size, Shape and Capping

The shape of the ZnO crystals seems to be strongly influenced by the added concentration and type of base. Titration of KOH results in the formation of relatively poorly defined crystals with some hexagonal

features, independent of the titrated concentration of KOH (3.1 mM, 73.35 mM or 1 M). The size of the crystals decreases with increasing amounts of base from 270 ± 110 (at 3.1 mM) to 140 ± 30 (at 1 M). This implies that the increased presence of base in the system increases the number of nuclei resulting in smaller particles.^[36]

When using ammonia additional changes in crystal habit of the reaction product are observed. Where titration of relative low amounts of ammonia (73.35 mM, Fig. 4.4c) results in crystals with poor hexagonal faceting, the titration of higher amounts (1 M, Fig. 4.7c) results in highly defined hexagonal crystals. This suggests, especially when taking the KOH observations into account, that the ZnO crystal habit definition increases with the amount of ammonia in the system. This is further supported by the HMTA observations. This strategy adds an intermediate amount of ammonia compared to the two ammonia titration strategies and results in a less clear hexagonal habit compared to the use of 1 M ammonia titration (Fig. 4.4a; 4.7a). The influence on crystal shape due to the presence of ammonia is a strong indicator of capping behaviour. Additional evidence for the capping of ammonia is provided from the reactions starting at an elevated pH of 8.3. In contrast to KOH, using ammonia to set the initial pH results in the formation of multifaceted ZnO structures. Strikingly, Amin *et al.*^[37] observed similar multifaceted ZnO crystals for HMTA-based ZnO but at a very low starting pH of 1.8. This large difference in starting pH excludes a pH effect. However, both systems are expected to contain a large amount of ammonia before the onset of ZnO formation, either due to the initial correction of pH starting to 8.3 or by rapid HMTA decomposition when the pH is increased from 1.8 to > 5.5 to conditions under which ZnO can be formed.

The observation of capping behaviour by ammonia is not surprising. Adsorption of ammonia on ZnO is a known behaviour^[38, 39] and exploited for the use of ZnO as ammonia sensors.^[40-42] With an increasing concentration of ammonia both the (001) c-plane and the (210) m-plane become more pronounced, suggesting both planes are capped (Fig. A4.7). Wurtzite ZnO has an innate preferential growth in the [001] direction in water.^[43] Hence observation of preferred growth suggests that capping along the m-plane is either comparable to the capping of the c-plane or more pronounced. The c-plane is composed of alternating layers of Zn^+ or O^{2-} resulting in a positively or negatively charged polar surface. The m-plane has no net surface charge and is non-polar. Although the surface chemistry is different, adsorption of ammonia in the gas phase has been experimentally confirmed on both the c-plane^[44] and the m-plane^[45], supporting this hypothesis.

Besides the effect of HMTA on crystal faceting, there is an additional factor that influences both the size and shape of the ZnO crystals, namely the early formation of LBZA during the reaction. As discussed earlier, LBZA promotes the formation of twin-pillared ZnO crystals by acting as a nucleation template.^[6] Thus, if more LBZA is formed at the start of the reaction, ZnO nucleation will become more favourable compared to growth, thereby decreasing the ZnO particle size. Indeed, in this work early formation of LBZA decreased the ZnO diameter from 240 ± 90 nm to 200 ± 50 nm.

4.6.4. Direct HMTA Influences

Compared to the HMTA-inspired titration strategies, the HMTA reference reaction results in larger and more clearly faceted ZnO particles, a higher reaction yield and retarded reaction kinetics. This makes it arguable whether HMTA has a direct influence on the reaction, besides its gradual formation of ammonia. Unfortunately, given the influence of the ZnO formation reaction on the decomposition rate of HMTA, it can also be argued that all these effects are caused by variations in the base formation rate. Therefore, based on the present data no firm conclusion can be made whether HMTA directly influences the ZnO formation process. However, it should be noted that by increasing and optimizing the ammonia addition rate, ZnO crystals can be formed similar to those formed when using HMTA. This shows that, although HMTA may directly influence the formation of ZnO, the same results can be achieved by optimizing ammonia titration conditions.

4.7. Conclusion

Wurtzite ZnO was synthesized at mild pH in water using a direct base titration strategy which offers excellent control over the base addition rate. Using HMTA inspired titration rates we found that ZnO is formed independent of the added base, either ammonia or KOH. The evolution of pH in time indicates no change in ZnO formation mechanism compared to HMTA, but only changed reaction kinetics. In contrast to statements in literature, the formation of ZnO was found to influence the decomposition rate of HMTA. Formaldehyde, a byproduct of HMTA decomposition, shows no influence on the reaction.

Use of KOH as base results in relatively small crystals independent of the added amount of base. Using increasing amounts of ammonia instead, the shape and degree of faceting closely matches the typically observed hexagonal ZnO twin-pillars, which implies that ammonia caps the formed ZnO crystals.

Reducing the reaction pH to ≤ 5.5 prevented any reaction from occurring, showing that a minimal pH value is required for the reaction. In contrast, increasing the starting pH to 8.3 resulted in ZnO formation with a loss in crystal habit. Here use of ammonia to set the starting pH resulted in multifaceted ZnO crystals. The typical twin pillared ZnO crystal shape was predominantly observed when LBZA was formed before initiating the reaction. This supports the hypothesis that LBZA acts as a nucleation template for the formation of twin pillared ZnO crystals in dispersion. Given the observed influences of ammonia on the formation of ZnO in this work, it can be argued that it is the ammonia and not HMTA that further directs the formation of the ZnO crystals. Due to the direct control over base addition rates ZnO yields exceeding 74% could be achieved. This yield increases with the target pH.

Given the direct control over base addition and the entailing flexibility provided by the titration-based ZnO synthesis strategy, we believe it is a promising tool for mineralization in general. For ZnO in particular, we expect it to have further uses for heterogenous ZnO nucleation and growth, due to the high control over the growth conditions, and for the formation of ZnO at reduced temperatures thanks to the temperature independent addition of base.

4.8. Materials and Methods

4.8.1. Materials

Acetic acid (99-100%, GPR reagent) and ammonia (28 %, GPR reagent) were acquired from VWR, hexamethylenetetramine (HMTA, >99.0 %, ACS reagent) and formaldehyde (37%, ACS reagent in water 10 – 15 % methanol as stabilizer) were acquired from Sigma-Aldrich, potassium hydroxide (pellets, pure) was acquired from Merck, zinc acetate dihydrate (ZnAc_2 , 98+ %, ACS reagent) was acquired from Acros organics. All chemicals were used as received unless stated otherwise.

4.8.2. Methods

4.8.2.1. Reaction Set-up, pH and Temperature Measurements

pH and temperature measurements were conducted, respectively, using a Metrohm 6.0234.100 and 6.1110.100 pH and temperature sensor, connected to an 809 Titrando unit equipped with two 800 dosino dosing devices (10 or 20 mL) controlled by TIAMO 2.5 software.

4.8.2.2. Determining the pH Dependent HMTA Hydrolysis Rate

25 mM of HMTA was dissolved in 50 ml pure water in a 100 mL five-neck flask under reflux. The titration experiment was magnetically stirred (vortexing, 450 rpm). The titration unit was set to titrate acetic acid (0.25 M) to achieve a pH of 5.7, 5.8 or 6.0 using the optimal titration speed setting on the dosing device. 300 s after initiating the titration protocol, the reaction temperature was gradually increased to ~ 80 °C.

The experiment was continued for 22200 s (6.2 h) during which time the added volume, the pH and the reaction temperature were monitored. From this data the released amount of ammonia and hydroxide by HMTA were calculated, see *section A4.2*.

Table 4.1 Titration protocol including the titration solution composition and time specific titration rates for the HMTA imitiation and control reactions.

Protocol	Added solution	0 – 1198 s (mL·min ⁻¹)	1200 – 2958 s (mL·min ⁻¹)	2960 – 5768 s (mL·min ⁻¹)	5770 – 10598 s (mL·min ⁻¹)	10600 – 22200 s (mL·min ⁻¹)
<i>Measure</i>	None					
<i>IM</i>	Pure water	0			0.02	
<i>IM-73</i>	73.35 mM NH ₃ or KOH	0			0.02	
<i>IM-146</i>	146.70 mM NH ₃ + 221.55 mM CH ₂ O	0			0.01	
<i>IM-OH</i>	0.0310 mM KOH	0	0.07	0.03	0.02	0.01

Table 4.2 Titration protocol including the titration solution composition and time specific titration rates used for reactions with an increased base concentration.

Protocol	pH set solution	Titrated solution	0 – 1198 s (mL·min ⁻¹)	1198 – 22200 s (mL·min ⁻¹)	1198 – 3600 s (Target pH)	3600 – 22200 s (Target pH)
<i>pH 6.8</i>	None	1 M ammonia	0	0.02	7.0	6.0
<i>pH 5.3</i>	0.25 mM acetic acid	1 M ammonia	0	0.02	5.5	5.5
<i>pH 8.3</i>	1 M NH ₃ or KOH	1 M ammonia	0	0.02	8.5	6.0

4.8.2.3. Titration-based Synthesis of Zinc Oxide

50 mM zinc acetate (and when noted 8.33 or 25 mM of HMTA) was dissolved in 50 ml pure water in a 100 mL five-neck flask under reflux. The titration experiment was magnetically stirred (vortexing, 450 rpm). If stated, the pH was pre-set at RT by adding 1 M acetic acid, KOH or ammonia solution. After addition of the chemicals or the correction of the pH, the solution was stirred for 900 s. After this time titration unit was set to add base (ammonia or KOH) at a constant rate. The used titration protocol is sample specific and detailed in *Table 4.1*; *4.2*. 300 s after initiating the titration protocol, the reaction temperature was gradually increased to ~80 °C. After 22200 s (6.2. h) the reaction was terminated, and the reaction dispersions were collected. These dispersions were subsequently purified by centrifugation using an Optima L-90K ultracentrifuge equipped with a Type 70 Ti rotor at 20k or 30k rpm for 20 min. The sediment was redispersed in pure water followed by another centrifugation step. This procedure was performed twice. After centrifugation the product was dried at room temperature. An overview of all experimental results is shown in *Table 4.3*.

Table 4.3 Overview of investigated samples, their yield, LBZA-ZnO transition time, initial pH, final pH, used titration protocol and diameter as measured by SEM.

Sample	Yield %	LBZA-ZnO transition (min)	Initial pH	Final pH	Titration-protocol	Diameter (nm)
25 mM HMTA	12.6	120	6.8	5.8	measure	400±150
8.33 mM HMTA	7.2	141	6.8	5.8	measure	410±160
25mM HMTA-H ₂ O	13.2	126	6.8	5.8	IM	430±140
146.70 mM NH ₃ + 221.55 mM CH ₂ O	3.7	51	6.8	5.8	IM-146	260±70
73.35 mM NH ₃	3.5	51	6.8	5.8	IM-73	250±40
3.1 mM KOH	0.4	64	6.8	5.7	IM-OH	270±110
73.35 mM KOH	4.3	40	6.8	5.9	IM-73	110±30
1 M KOH	31.8	41	6.8	6.0	pH 6.8	140±30
1 M NH ₃ STD	41.3	44	6.8	6.0	pH 6.8	240±90
1 M NH ₃ pH 8.3 ^{*I}	63.6	21	8.3	6.6	pH 8.3	390±110
1 M NH ₃ pH 8.3 ^{*II}	74.5	22,42	8.4	6.8	pH 8.3	220±90
1 M NH ₃ pH 5.3 ^{*III}	0	-	5.3	5.5	pH 5.3	No product
1M NH ₃ STD opti ^{*IV}	34.0	50	6.9	6.0	pH 6.8	200±50

**Either the starting pH was pre-set using 1M ammonia,^I KOH^{II} or acetic acid^{III} or 1mL 1M ammonia was gradually added at RT^{IV} before initiating the reaction by heating.*

4.8.2.4. Analysis

Powder X-ray diffraction (pXRD) measurements were performed on a MiniFlex 600 diffractometer using Cu K α radiation, operating at 40 kV and 15 mA.

Scanning electron microscopy (SEM) was carried out on a Quanta 3D (Thermo Fischer Scientific) equipped with a field emission gun, secondary electron detector and operated at 5.0 kV. The samples in powder form were dispersed in pure water, 10 μ L dispersion was deposited on a continuous carbon-coated TEM grid with copper or gold supports (200 mesh), followed by manual blotting after 40 s. Samples were loaded in the SEM using an in-house build custom SEM holder that can accommodate 6 TEM grids.

Size measurements were performed on SEM images using an in-house Matlab script. For each sample the diameter of 60 clearly identifiable particles was measured (3 images, 20 particles each). For these particles the diameter was measured either at the twinning location or if not possible at the end with visually the shortest diameter.

4.9. Appendix A4

A4.1. Calculations

Calculating the release of base from HMTA using zinc acetate counter titration requires several considerations. First the molar concentration of acetic acid in solution $[\text{CH}_3\text{COOH}]_{\text{total}}$ depends on the molarity of titrated acetic acid solution $[\text{CH}_3\text{COOH}]_{\text{titrated}}$ the initial volume (V_{initial}) and the titrated volume (V_{titrated}):

$$[\text{CH}_3\text{COOH}]_{\text{total}} = \frac{[\text{CH}_3\text{COOH}]_{\text{titrated}} \times V_{\text{titrated}}}{V_{\text{initial}} + V_{\text{titrated}}} \quad (\text{A4.1})$$

Acetic acid is a weak acid therefore only part of $[\text{CH}_3\text{COOH}]_{\text{total}}$ will be deprotonated to $[\text{CH}_3\text{COO}^-]_{\text{eq}}$ depending on the dissociation constant (K_d):

$$[\text{CH}_3\text{COOH}]_{\text{total}} = [\text{CH}_3\text{COOH}]_{\text{eq}} + [\text{CH}_3\text{COO}^-]_{\text{eq}} \quad (\text{A4.2})$$

$$[\text{CH}_3\text{COOH}]_{\text{eq}} + [\text{H}_2\text{O}]_{\text{eq}} \overset{K_d}{\rightleftharpoons} [\text{CH}_3\text{COO}^-]_{\text{eq}} + [\text{H}_3\text{O}^+]_{\text{eq}} \quad (\text{A4.3})$$

This means the molar concentrations can be set against the K_d . This can be simplified by considering that the formed amount of $[\text{CH}_3\text{COO}^-]_{\text{eq}}$ is equal to the formed amount of $[\text{H}_3\text{O}^+]_{\text{eq}}$ and that in the case of a neutralization reaction with a constant pH $[\text{H}_3\text{O}^+]_{\text{eq}}$ reacts with an equal amount of released $[\text{OH}^-]_{\text{eq}}$:

$$K_d = \frac{[\text{CH}_3\text{COO}^-]_{\text{eq}} + [\text{H}_3\text{O}^+]_{\text{eq}}}{[\text{CH}_3\text{COOH}]_{\text{eq}}} = \frac{[\text{H}_3\text{O}^+]_{\text{eq}}^2}{[\text{CH}_3\text{COOH}]_{\text{eq}}} = \frac{[\text{OH}^-]_{\text{eq}}^2}{[\text{CH}_3\text{COOH}]_{\text{eq}}} \quad (\text{A4.4})$$

By substituting Eq. A4.4 into Eq. A4.2 we obtain Eq. A4.5:

$$\begin{aligned} [\text{CH}_3\text{COOH}]_{\text{total}} &= [\text{CH}_3\text{COOH}]_{\text{eq}} + [\text{CH}_3\text{COO}^-]_{\text{eq}} = [\text{CH}_3\text{COOH}]_{\text{eq}} + [\text{H}_3\text{O}^+]_{\text{eq}} = \\ &[\text{CH}_3\text{COOH}]_{\text{eq}} + [\text{OH}^-]_{\text{eq}} = \frac{[\text{OH}^-]_{\text{eq}}^2}{K_d} + [\text{OH}^-]_{\text{eq}} \end{aligned} \quad (\text{A4.5})$$

Performing these calculations for ammonia will result in Eq. A4.6:

$$[\text{NH}_3]_{\text{total}} = [\text{NH}_3]_{\text{eq}} + [\text{NH}_4^+]_{\text{eq}} = [\text{NH}_3]_{\text{eq}} + [\text{OH}^-]_{\text{eq}} = \frac{[\text{OH}^-]_{\text{eq}}^2}{K_d} + [\text{OH}^-]_{\text{eq}} \quad (\text{A4.6})$$

To determine the amount of $[\text{OH}^-]_{\text{eq}}$ effectively released to the system, Eq. A4.5 can be solved for $[\text{OH}^-]_{\text{eq}}$ using the quadratic formula:

$$[\text{OH}^-]_{\text{eq}} = \frac{-K_d \sqrt{K_d^2 + (4 \times K_d \times [\text{CH}_3\text{COOH}]_{\text{total}})}}{2} \quad (\text{A4.7})$$

The temperature dependence of K_d can be described by:

$$\text{Log } K_d = \frac{A}{T} + B \text{ Log } T + CT + D \quad (\text{A4.8})$$

$$K_d = 10^{\text{Log } K_d} = 10^{\frac{A}{T} + B \text{ Log } T + CT + D} \quad (\text{A4.9})$$

where A, B, C and D are constants, given in Table A4.1.

Table A4.1 The constants for acetic acid and ammonia in expressions 8 and 9. [15, 34, 46]

Compounds	A	B	C	D
Acetic acid	-1500.65	-6.50923	-0.0076792	18.67257
Ammonia	-1746.57	0	0.01706	-6.1848

In absence of counter titration, the released molar concentration of hydroxides $[\text{OH}^-]_{\text{eq}}$ by HMTA can be measured by the change in pH. This takes place at neutral pH, therefore, the decrease in free protons (pH) and the increase in free hydroxides (pOH) should be considered:

$$[\text{OH}^-]_{\text{eq}} = 10^{-\text{pOH}} - 10^{-\text{pH}} = 10^{-(14-\text{pH})} - 10^{-\text{pH}} \quad (10)$$

A4.2. Collecting and Transforming Experimental Data

During a typical ZnO reaction from 50 mM zinc acetate and 25 mM HMTA at $\sim 80^\circ \text{C}$, the pH remains constant, close to pH 5.8, for most of the reaction.[33] To probe the release of hydroxide under these conditions, a reference reaction containing 25 mM HMTA in water was performed while titrating 0.25 M acetic acid targeting a pH of 5.8.

The reaction pH could be controlled by acetic acid titration (Fig. A4.1a,b,d). The released amount of hydroxide was calculated by correcting for the dissociation constant (K_a , Fig. A4.1c) while taking the reaction temperature into account.[34, 46] As expected, hydroxide was released into the system at a gradually decreasing rate over time (Fig. A4.1e,f). This results in the release of 3.3×10^{-2} mmol hydroxide after 6 h reaction time, which is equivalent to 0.50 mmol ammonia (Fig. A4.1g) or $\sim 10\%$ of total amount of ammonia present in HMTA per 6 h.

The influence of slight pH deviations on the hydrolysis rate of HMTA was investigated by repeating the experiment at pH 5.7 and 6.0 (Fig. A4.1a-b,d-g). This resulted in the release of respectively 0.62 ($\sim 13\%$) mmol and 0.36 mmol ($\sim 6\%$) ammonia per 6 h. This shows clearly that slight variations in pH will have a notable influence on the hydrolysis rate of HMTA.

Both Strom et al.[16] and Ashfold et al.[19] used 50 mM HMTA to investigate the pH dependent hydrolysis rate of HMTA. Ashfold et al. predicts a HMTA hydrolysis rate (k) of 0.055 h^{-1} at a constant reaction pH of 5.64 at 90°C . After 2 h reaction time during the formation of ZnO, a rate (k_{obs}) of 0.059 h^{-1} is measured. To compare data, the concentration of HMTA (Fig. A4.1i) and the natural logarithm of the HMTA concentration (Fig. A4.1h) were determined from the calculated release of ammonia and set against the time. From this the k_{obs} could be calculated: at pH 5.7, $k_{\text{obs}} = 0.0230 \text{ h}^{-1}$, at pH 5.8, $k_{\text{obs}} = 0.0181 \text{ h}^{-1}$ and at pH 6.0, $k_{\text{obs}} = 0.0127 \text{ h}^{-1}$. Given that k_{obs} is concentration dependent the data from Ashfold et al. was corrected with a factor two presuming no difference in activity between 25 mM and 50 mM HMTA in solution. When plotting the obtained data and the corrected data from Ashfold et al. against the number of protons in solution ($10^{-\text{pH}}$), a clear match can be observed (Fig. 4.1b). Using the experimental data provided by Ashfold et al. the initial hydrolysis rate of HMTA over the first 1.5 h was calculated. During this time the HMTA concentration decreased from 0.05 M to under 0.03 M. This results in a $k_{\text{obs}} = 0.51 \text{ h}^{-1}$, close to a nine-fold increase from $k_{\text{obs}} = 0.059 \text{ h}^{-1}$ obtained after 2 h reaction time. This shows that the HMTA hydrolysis rate is significantly higher during the initial 1.5 h of the reaction.

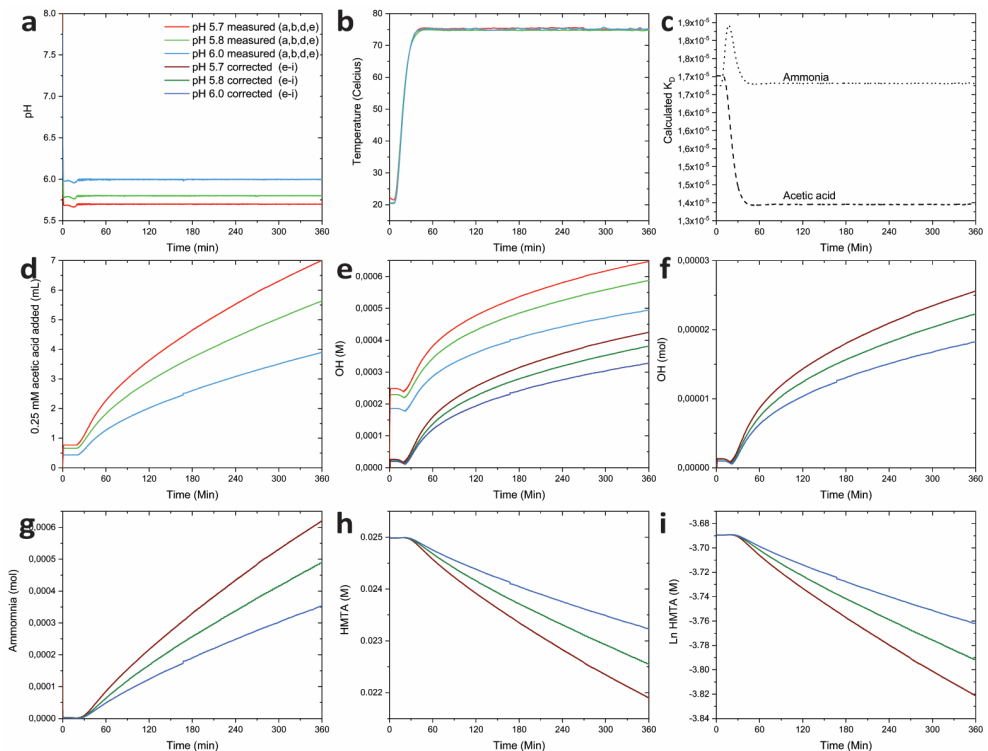


Figure A4.1 Hydrolysis of 25 mM HMTA at a constant pH of 5.7, 5.8 and 6.0, showing the evolution of pH (a) and temperature (b) of the acetic-acid counter titration as a function of time. Using the temperature evolution, the dissociation constant K_a of acetic acid and ammonia can be calculated (c). The titrated volume of acetic acid (d) is combined with the dissociation constant to calculate amount of hydroxide in M and mol (e, f), the amount of ammonia in mol released by the HMTA during the reaction (g), the concentration in M of HMTA present in solution (h) and finally the natural logarithm of the HMTA concentration (i).

A4.3. Theoretical Yield Calculations

The amount of hydroxide consumed during the reaction results from two sources: the original reaction solution (via the decrease in reaction pH) and the amount of base titrated into the system. During the investigated HMTA reference reaction and the titration reactions without an initial pH correction, the pH decreases from 6.8 to 5.8. For this pH decreases, Eq. A4.10 from section A4.1. shows the release of 1.48×10^{-3} mM hydroxide, which is a negligible amount. The amount of hydroxide released to the system via ammonia titration is dependent on the K_a of ammonia. Using data from Fig. 4.1 and taking K_a of ammonia into account, it is expected that 0.380 mM hydroxide is released over a 6 h reaction period at pH 5.8. When presuming that all the ammonia is converted into ammonium, 8.771 mM hydroxide is released (0.489 mmol ammonia in 55.64 mL). When 50 mM zinc acetate is used in the reaction after titration (7 mL to 50 mL), 43.86 mM ZnO is the maximal attainable. The formation of 1 mol ZnO requires 2 mol hydroxide. This allows for a maximum formation of 0.190 mM ZnO, a yield of 0.433% when taking the K_a of ammonia into account or a maximum formation of 4.385 mM ZnO equal to a yield of 10.00% when a full transformation of ammonia into ammonium is presumed.

A4.4. Figures

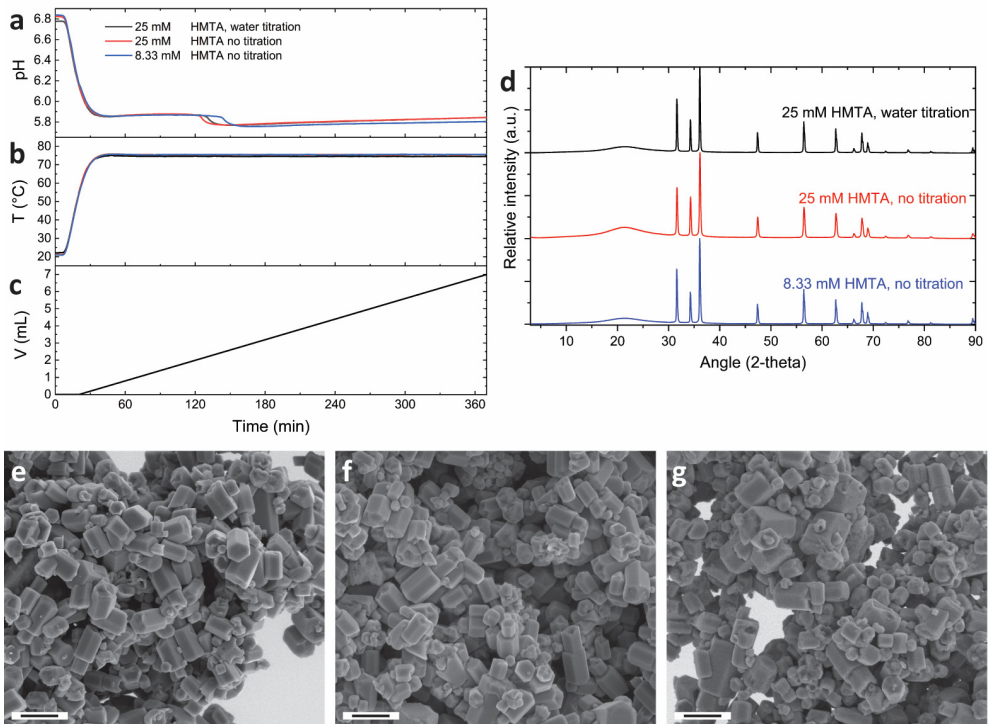


Figure A4.2 HMTA-mediated synthesis of ZnO from zinc acetate showing the evolution of pH (a), the temperature T (b) and the titration volume V (c) as a function of time combined with the pXRD results (d) and SEM images when using 25 mM HMTA with water titration (e), 25 mM HMTA without water titration (f) and 8.33 mM HMTA without water titration (g).

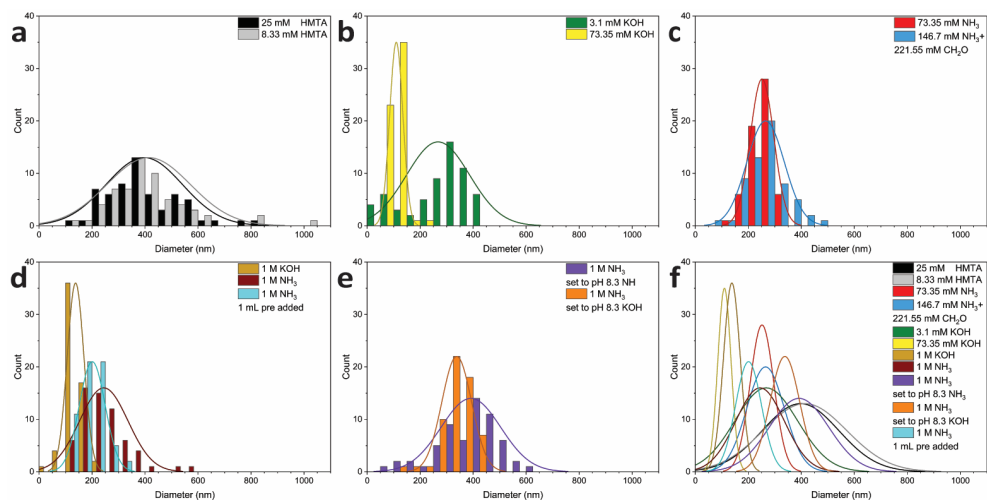


Fig. A4.3 Histograms (a-e) and size distribution plots (a-f) of diameter measurements on SEM images used to calculate the given diameter \pm sample standard deviation displayed in *Table 4.3*. This includes the HMTA references (a), the HMTA-inspired KOH titration strategy (b), the HMTA-inspired NH₃ titration strategy (c), the titration strategies with an increased base concentration at native pH (d) and at pH 8.3 (e), followed by an overview of all results (f).

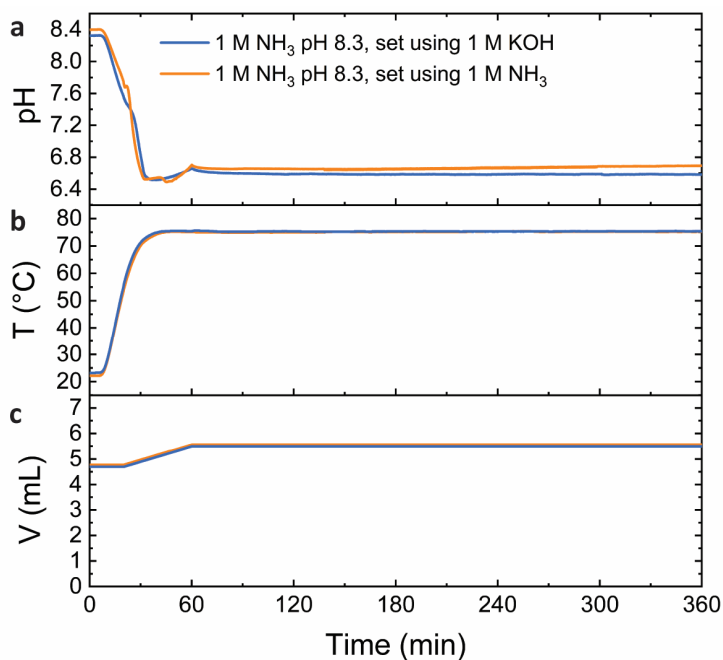


Figure A4.4 High pH titration-based synthesis of ZnO from zinc acetate showing the evolution of pH (a), temperature T (b) and titration volume V (c) as a function of time.

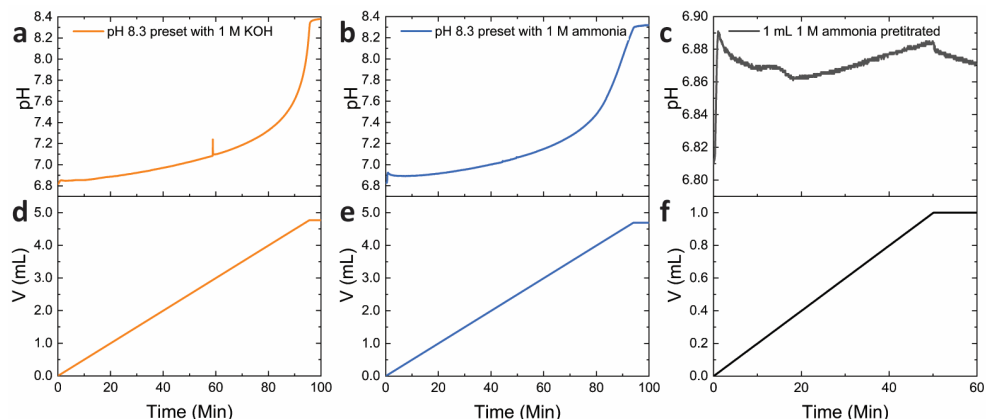


Figure A4.5 Evolution of pH (a-c) and titration volume V (d-f) as a function of time for the presetting of the zinc acetate solution to pH 8.3 using 1 M ammonia (a,d) or 1 M KOH (b,e) and for the initial addition of 1 mL ammonia (c,f). The pH was set titrating base at a rate of 0.05 mL min^{-1} (d,e). For the preformation of LBZA (c,f) a similar titration rate as the reaction of 0.02 mL min^{-1} was chosen.

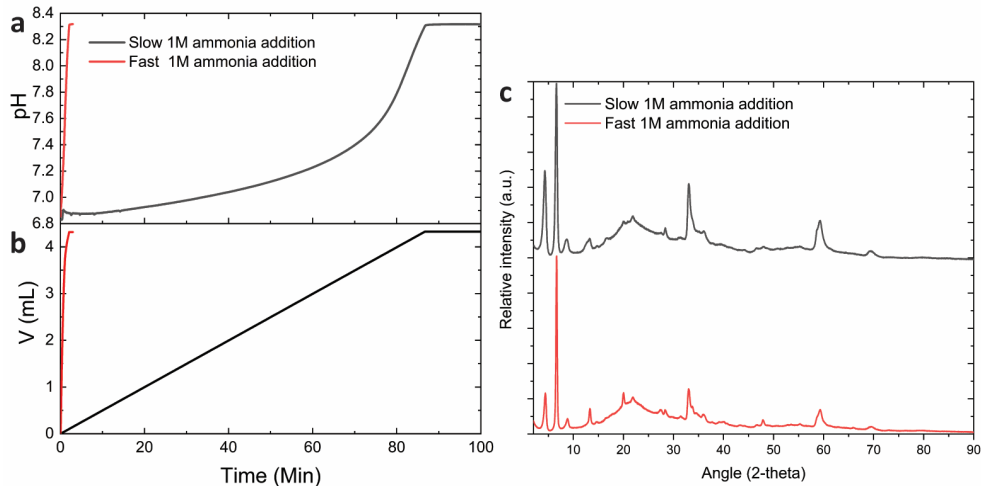


Figure A4.6 Controlled addition of 1 M ammonia to 25 mM HMTA solution showing the evolution of pH (a) and titration volume V (b) as a function of time and the pXRD (c) results of the products showing the formation of LBZA in both cases. It should be noted that sharper signals are obtained when using a faster addition rate suggesting more defined crystals with a more even crystal spacing.

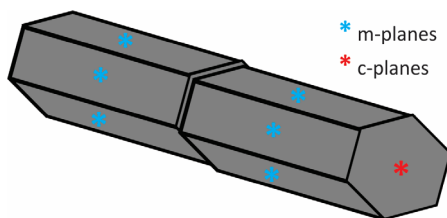


Figure A4.7 Sketch of a twin pillar ZnO structure indicating the c- and m-planes using red and blue asterisks, respectively.

4.10. References

1. K. Fujita, K. Murata, T. Nakazawa and I. Kayama, Crystal Shapes of Zinc Oxide Prepared by the Homogeneous Precipitation Method. *J. Ceram* **92**, 227-230 (1984).
2. W. L. Feng, B. C. Wang, P. Huang, X. D. Wang, J. Yu and C. W. Wang, Wet Chemistry Synthesis of ZnO Crystals with Hexamethylenetetramine (HMTA): Understanding the Role of HMTA in the Formation of ZnO Crystals. *Mat Sci Semicon Proc* **41**, 462-469 (2016).
3. S. Xu and Z. L. Wang, One-dimensional ZnO Nanostructures: Solution Growth and Functional Properties. *Nano Res* **4**, 1013-1098 (2011).
4. V. Gerbreders, M. Krasovska, E. Sledevskis, A. Gerbreders, I. Mihailova, E. Tamanis and A. Ogurcovs, Hydrothermal Synthesis of ZnO Nanostructures with Controllable Morphology Change. *CrystEngComm* **22**, 1346-1358 (2020).
5. S. Maiti, S. Pal and K. K. Chattopadhyay, Recent Advances in Low Temperature, Solution Processed Morphology Tailored ZnO Nanoarchitectures for Electron Emission and Photocatalysis Applications. *CrystEngComm* **17**, 9264-9295 (2015).
6. E. S. Jang, J. H. Won, Y. W. Kim, Z. Cheng and J. H. Choy, Dynamic Transition Between Zn-HDS and ZnO: Growth and Dissolving Mechanism of Dumbbell-like ZnO Bipod Crystal. *CrystEngComm* **13**, 546-552 (2011).
7. Z. Q. Hou, Y. X. Wang, L. H. Shen, H. Guo, G. X. Wang, Y. Li, S. F. Zhou, Q. Q. Zhang and Q. Q. Jiang, Synthesis of Dumbbell-like ZnO Microcrystals via a Simple Solution Route. *Nanoscale Res Lett* **7**, 507 (2012).
8. L. Vayssieres, Growth of Arrayed Nanorods and Nanowires of ZnO from Aqueous Solutions. *Adv Mater* **15**, 464-466 (2003).
9. S. Xu, Y. Wei, M. Kirkham, J. Liu, W. Mai, D. Davidovic, R. L. Snyder and Z. L. Wang, Patterned Growth of Vertically Aligned ZnO Nanowire Arrays on Inorganic Substrates at Low Temperature without Catalyst. *J Am Chem Soc* **130**, 14958-14959 (2008).
10. Y. Rajesh, S. K. Padhi and M. G. Krishna, ZnO Thin Film-nanowire array Homo-structures with Tunable Photoluminescence and Optical Band Gap. *RSC Adv* **10**, 25721-25729 (2020).
11. T. R. Zhang, W. J. Dong, M. Keeter-Brewer, S. Konar, R. N. Njabon and Z. R. Tian, Site-specific Nucleation and Growth Kinetics in Hierarchical Nanosyntheses of Branched ZnO Crystallites. *J Am Chem Soc* **128**, 10960-10968 (2006).
12. Z. R. Tian, J. A. Voigt, J. Liu, B. McKenzie, M. J. McDermott, M. A. Rodriguez, H. Konishi and H. Xu, Complex and Oriented ZnO Nanostructures. *Nat Mater* **2**, 821-826 (2003).
13. Y. Miao, H. J. Zhang, S. Yuan, Z. Jiao and X. D. Zhu, Preparation of Flower-like ZnO Architectures Assembled with Nanosheets for Enhanced Photocatalytic Activity. *J Colloid Interface Sci* **462**, 9-18 (2016).
14. Y. C. Liang and W. C. Zhao, Morphology-dependent Photocatalytic and Gas-sensing Functions of Three-dimensional TiO₂-ZnO Nanoarchitectures. *CrystEngComm* **22**, 7575-7589 (2020).
15. R. G. Bates and G. D. Pinching, Acidic Dissociation Constant of Ammonium Ion at 0-Degrees to 50-Degrees-C, and the Base Strength of Ammonia. *J Res Nat Bur Stand* **42**, 419-430 (1949).
16. J. G. Strom and H. W. Jun, Kinetics of Hydrolysis of Methenamine. *J Pharm Sci* **69**, 1261-1263 (1980).
17. K. Govender, D. S. Boyle, P. B. Kenway and P. O'Brien, Understanding the Factors that Govern the Deposition and Morphology of Thin Films of ZnO from Aqueous Solution. *J Mater Chem* **14**, 2575-2591 (2004).
18. H. Tada, Decomposition Reaction of Hexamine by Acid. *J Am Chem Soc* **82**, 255-263 (1960).
19. M. N. R. Ashfold, R. P. Doherty, N. G. Ndiifor-Angwafor, D. J. Riley and Y. Sun, The Kinetics of the Hydrothermal Growth of ZnO Nanostructures. *Thin Solid Films* **515**, 8679-8683 (2007).
20. P. Chettiyan, A. Chand, R. Ghosh, S. K. Sarkar, P. Das and S. Chowdhuri, Effects of Hexamethylenetetramine (HMTA) on the Aqueous Solution Structure, Dynamics and Ion Solvation Scenario: A Concentration and Temperature Dependent Study with Potential HMTA Models. *J Mol Liq* **296**, 111820 (2019).
21. A. Sugunan, H. C. Warad, M. Boman and J. Dutta, Zinc Oxide Nanowires in Chemical Bath on Seeded Substrates: Role of Hexamine. *J Solgel Sci Technol* **39**, 49-56 (2006).
22. R. Parize, J. Garnier, O. Chaix-Pluchery, C. Verrier, E. Appert and V. Consonni, Effects of Hexamethylenetetramine on the Nucleation and Radial Growth of ZnO Nanowires by Chemical Bath Deposition. *J Phys Chem C* **120**, 5242-5250 (2016).
23. R. Devaraj, K. Venkatachalam, K. Saravanakumar, P. M. Razad and K. Mahalakshmi, Role of Hexamine: Growth of Multiarmed ZnO Nanorods and Evidence of Merging due to Lateral Growth. *J Mater Sci-Mater El* **27**, 12201-12208 (2016).
24. V. Strano, R. G. Urso, M. Scuderi, K. O. Iwu, F. Simone, E. Ciliberto, C. Spinella and S. Mirabella, Double Role of HMTA in ZnO Nanorods Grown by Chemical Bath Deposition. *J Phys Chem C* **118**, 28189-28195 (2014).
25. K. M. McPeak, M. A. Becker, N. G. Britton, H. Majidi, B. A. Bunker and J. B. Baxter, In Situ X-ray Absorption Near-Edge Structure Spectroscopy of ZnO Nanowire Growth During Chemical Bath Deposition. *Chem Mater* **22**, 6162-6170 (2010).
26. K. M. McPeak, T. P. Le, N. G. Britton, Z. S. Nickolov, Y. A. Elabd and J. B. Baxter, Chemical Bath Deposition of ZnO Nanowires at Near-Neutral pH Conditions without Hexamethylenetetramine (HMTA): Understanding the Role of HMTA in ZnO Nanowire Growth. *Langmuir* **27**, 3672-3677 (2011).
27. C. Ou, P. E. Sanchez-Jimenez, A. Datta, F. L. Boughey, R. A. Whiter, S. L. Sahonta and S. Kar-Narayan, Template-Assisted Hydrothermal Growth of Aligned Zinc Oxide Nanowires for Piezoelectric Energy Harvesting Applications. *ACS Appl Mater Inter* **8**, 13678-13683 (2016).
28. A. S. Kambale, B. B. Sinha, K. Chung, M. G. Gil, V. Burungale, C. J. Park, J. H. Kim and P. S. Patil, Effect of Hydroxide Anion Generating Agents on Growth and Properties of ZnO Nanorod Arrays. *Electrochim Acta* **149**, 386-393 (2014).

29. N. Caicedo, J. S. Thomann, R. Leturcq and D. Lenoble, Aspect Ratio Improvement of ZnO Nanowires Grown in Liquid Phase by using Step-by-step Sequential Growth. *CrystEngComm* **18**, 5502-5511 (2016).
30. G. Mirabello, A. Ianiro, P. H. H. Bomans, T. Yoda, A. Arakaki, H. Friedrich, G. de With and N. Sommerdijk, Crystallization by Particle Attachment is a Colloidal Assembly Process. *Nat Mater* **19**, 391-396 (2020).
31. J. J. M. Lenders, C. L. Altan, P. H. H. Bomans, A. Arakaki, S. Bucak, G. de With and N. A. J. M. Sommerdijk, A Bioinspired Coprecipitation Method for the Controlled Synthesis of Magnetite Nanoparticles. *Cryst Growth Des* **14**, 5561-5568 (2014).
32. M. W. P. van de Put, Thesis, Technische Universiteit Eindhoven, Eindhoven (2015).
33. M. M. J. van Rijt, B. M. Oosterlaken, R. R. M. Joosten, L. E. A. Wijkhuijs, P. H. H. Bomans, H. Friedrich and G. de With, Counter-ion Influence on the Mechanism of HMTA-mediated ZnO Formation. *CrystEngComm* **22**, 5854-5861 (2020).
34. J. R. Fisher and H. L. Barnes, Ion-Product Constant of Water to 350 Degrees. *J Phys Chem-Us* **76**, 90-99 (1972).
35. K. He, N. F. Chen, C. J. Wang, L. S. Wei and J. K. Chen, Method for Determining Crystal Grain Size by X-Ray Diffraction. *Cryst Res Technol* **53**, 1700157 (2018).
36. T. Park, K. E. Lee, N. Kim, Y. Oh, J. K. Yoo and M. K. Um, Aspect Ratio-controlled ZnO Nanorods for Highly Sensitive Wireless Ultraviolet Sensor Applications. *J Mater Chem C* **5**, 12256-12263 (2017).
37. G. Amin, M. H. Asif, A. Zainelabdin, S. Zaman, O. Nur and M. Willander, Influence of pH, Precursor Concentration, Growth Time, and Temperature on the Morphology of ZnO Nanostructures Grown by the Hydrothermal Method. *J Nanomater* **2011**, 1-9 (2011).
38. T. Morimoto, H. Yanai and M. Nagao, Infrared-Spectra of Ammonia Adsorbed on Zinc-Oxide. *J Phys Chem-Us* **80**, 471-475 (1976).
39. B. Sun, X. P. Yang, D. Zhao and L. Q. Zhang, First-principles Study of Adsorption Mechanism of NH₃ on Different ZnO Surfaces on Organics Photocatalytic Degradation Purpose. *Comp Mater Sci* **141**, 133-140 (2018).
40. S. Kanaparthi and S. Govind Singh, Highly Sensitive and Ultra-fast Responsive Ammonia Gas Sensor Based on 2D ZnO Nanoflakes. *Materials Science for Energy Technologies* **3**, 91-96 (2020).
41. F. F. Franco, L. Manjakkal, D. Shakthivel and R. Dahiya, ZnO based Screen Printed Aqueous Ammonia Sensor for Water Quality Monitoring. *Ieee Sensor*, 1-4 (2019).
42. B. Chatterjee and A. Bandyopadhyay, Development of Zinc Oxide Sensors for Detecting Ammonia Gas in the Ambient Air: A Critical Short Review. *Environ Qual Manag* **26**, 89-105 (2016).
43. L. Xu, Y. L. Hu, C. Pelligra, C. H. Chen, L. Jin, H. Huang, S. Sithambaram, M. Aindow, R. Joesten and S. L. Suib, ZnO with Different Morphologies Synthesized by Solvothermal Methods for Enhanced Photocatalytic Activity. *Chem Mater* **21**, 2875-2885 (2009).
44. K. Ozawa, T. Hasegawa, K. Edamoto, K. Takahashi and M. Kamada, Adsorption State and Molecular Orientation of Ammonia on ZnO(1010) Studied by Photoelectron Spectroscopy and Near-edge X-ray Absorption Fine Structure Spectroscopy. *J Phys Chem B* **106**, 9380-9386 (2002).
45. T. Hasegawa, Y. Shirotori, K. Ozawa, K. Edamoto and K. Takahashi, Room Temperature Adsorption of NH₃ on Zn-terminated ZnO(0001). *Appl Surf Sci* **237**, 352-357 (2004).
46. H. S. Harned and R. W. Ehlers, The Dissociation Constant of Acetic Acid from 0 to 60° Centigrade. *J Am Chem Soc* **55**, 652-656 (1933).

Chapter 5

ZnO Formation at Template Friendly Conditions

For the mineralization of organic templates into organic-inorganic hybrid materials, mild mineralization strategies are required. Given that hybrid materials typically possess enhanced material properties over its individual components, inorganic phases with a variety of properties like zinc oxide (ZnO) are of interest. The aqueous synthesis of ZnO at a mild reaction pH is rather well known, however this process generally requires a reaction temperature above 60 °C which is incompatible with many organic templates. To synthesize ZnO at “template friendly” conditions, this work explores the influence of incrementally lowering the reaction temperature for the formation of ZnO by using a direct base titration strategy. Using this strategy, ZnO can be synthesized at a temperature as low as 40 °C. The presence of layered basic zinc acetate (LBZA) does become more dominant at lower reaction temperatures, depending on the initial zinc acetate concentration. The presence of ZnO can be promoted further by adding l-lysine (l-lys) to the initial reaction solution and in its presence a larger ZnO yield is obtained at shorter reaction times. Moreover, l-lys seems to promote ZnO formation even at room temperature.

"Great was Atalanta's fame and beauty, great the value of Schoeneus's kingdom and great the conviction of many fine, fit and fast young fellows that no woman could ever best them. Many made the journey to Arcadia: all were defeated and all were killed. The crowds loved it."

Steven Fry, *Heroes*, 2019

5.1. Zinc Oxide Formation at Low Temperature

Hybrid materials are composed from both organic and inorganic components. The interaction between both these material components can result in enhanced material properties.^[1, 2] An example of this is hydroxyapatite (HAp) mineralized collagen in bone which possesses the hardness and strength of HAp, without being brittle^[3, 4]. By introducing material phases like zinc oxide (ZnO) into complex organic templates other properties, including piezoelectricity^[5, 6], a high refractive index ~ 2 ^[7] and photocatalytic behavior^[8, 9] may be introduced.

The mineralization of organic templates presents several challenges. One major challenge is the sensitivity of these templates to environmental conditions including: high or low pH, elevated reaction temperatures and exposure to incompatible solvents which all can lead to denaturation, disassembly or even decomposition of the organic template^[10-12]. This makes mineralization at “template friendly” conditions essential.

Using well known strategies ZnO can be readily synthesized in aqueous solution. By using hexamethylene tetraamine (HMTA)^[13-16] as a base addition agent this reaction can be performed at a mild reaction pH^[14, 17], however this generally requires the use of elevated reaction temperatures > 60 °C. At elevated temperatures HMTA hydrolyses gradually, which provides the base required for the reaction, see *Ch. 4*. Hence decreasing the reaction temperature will also affect the formation of base. Using a direct base titration strategy as presented in *Ch. 4*, it should be possible to overcome this limitation.

Additionally, heat is presumed to promote the formation of ZnO. To overcome this need, several approaches have been investigated where direct heating has been replaced by alternative energy sources for the reaction. These include exposure to UV light^[18], exposure to ultrasound^[19], or use of elevated reaction pH^[20]. Unfortunately, these conditions can all adversely affect sensitive organic templates and, as in the case of exposure to UV light and ultrasound, may introduce a significant temperature increase. Additionally, many low temperature ZnO formations studies, perform the initial reaction at near RT conditions and are followed by a post synthetic drying or annealing step at > 100 °C. Under post-synthetic conditions, expected transient phases such as wülfingite zinc hydroxide (Zn(OH)₂)^[21] and layered zinc hydroxy salts (LZHS)^[22] are known to directly transform into ZnO. Moreover, the presence of water in a high temperature drying procedure may allow for the transition of either phase to ZnO. This makes it questionable whether the ZnO is actually formed at low reaction temperatures or during the post synthesis treatment.

In contrast, another approach makes use of small molecular additives that promote the formation of ZnO at low temperatures. Custom peptide sequences like EAHVMHKVAPRP^[23, 24] and small molecules like l-lysine (l-lys)^[25, 26] have shown promising results.

Following the latter approach, here we investigate the formation of ZnO from zinc acetate (ZnAc₂) at low temperature using a titration-based synthesis route. Reactions being performed at incrementally lower reaction temperatures, namely 60, 50 and 40 °C and avoiding any post synthesis heating steps. It is demonstrated that ZnO can be formed at 40 °C reaction temperature in the absence of additives and depending on the amount of ZnAc₂ in the initial reaction solution. Moreover, adding l-lys to the initial reaction solution does not only promote the formation of ZnO, it allows the transition to a more pure ZnO system to continue when maturing the reaction product at room temperature.

5.2. Zinc Oxide Formation at Decreasing Reaction Temperatures

To investigate the influence of temperature on ZnO formation by a titration-based strategy, a similar reaction protocol was used as that described in *Ch. 4*. In general, 1 M ammonia is titrated into the reaction solution at 0.014 mL min⁻¹ during the first 2 h of the reaction, after which ammonia is only added when

the pH of the reaction solution is below 6.0. This protocol is discussed in detail in Materials and Methods, section 5.6.2. Given the dominant presence of layered basic zinc acetate (LBZA) during the initial reaction stages at 80 °C and that its formation was promoted by increasing the reaction pH at room temperature (see *Ch. 3 and 4*), it was decided to set the starting pH to 6.4 using acetic acid in order to minimize precipitation of LBZA at the start of the reaction.

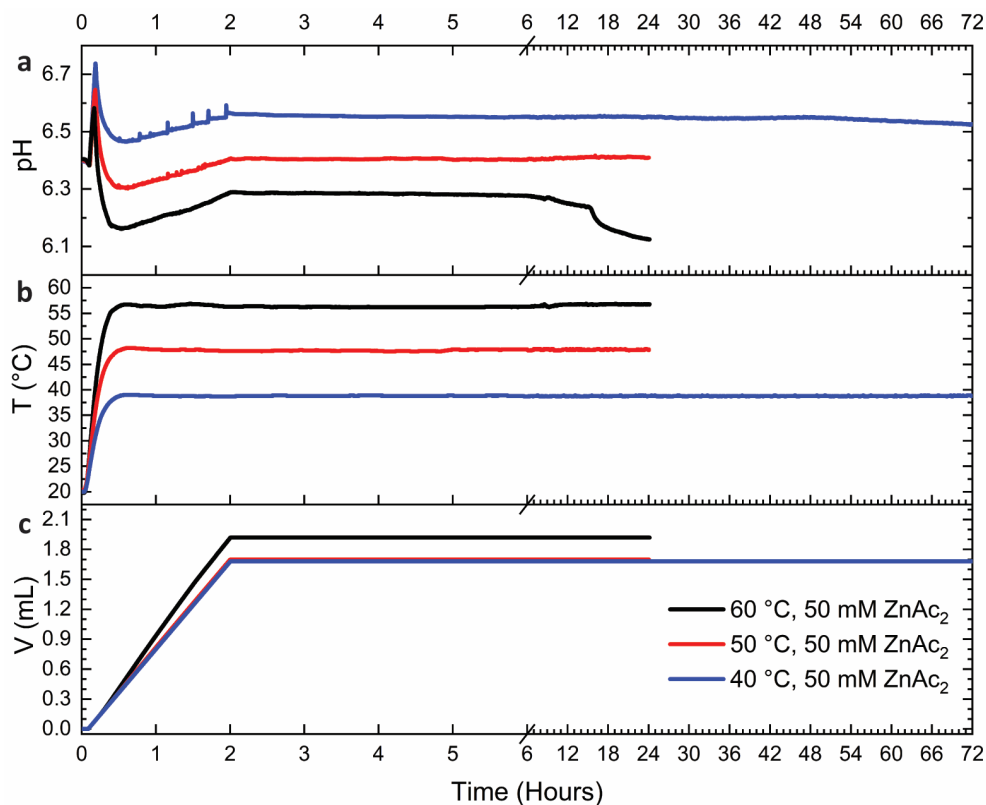


Figure 5.1 Titration based strategy for ZnO formation showing *in-situ* pH curve (a), temperature T (b) and base volume V (c) of 50 mM ZnAc₂ titrated with 1 mM ammonia at 0.014 mL min⁻¹ with a target pH of 6 after the first 2 h off the reaction time, performed at 60 °C (black), 50 °C (red) and 40 °C (blue) reaction temperature.

The reaction was performed at 60, 50 and 40 °C. During the reaction the pH and the temperature were continuously monitored using a pH and a temperature sensor. Upon initiating titration after 30 s reaction time, a sharp pH increase can be observed (*Fig. 5.1a*). This pH increase continues for the first 5 min of titration, after which a gradual drop in pH is observed for all reaction temperatures. This strong initial pH increase suggests that a minimal amount of base is consumed here. Upon reaching the initial pH maximum it is likely that layered basic zinc acetate (LBZA) starts to precipitate, as has been observed previously^[14]. The initial pH maximum is temperature dependent, occurring at pH 6.60 (60 °C), 6.64 (50 °C) and 6.74 (40 °C). The subsequent pH decrease continues until the reaction temperature stabilizes, which occurs at roughly 30 min reaction time for all temperatures (*Fig. 5.1b*). This pH minimum has a strong temperature dependence with lower reaction temperatures resulting in higher pH values: 6.16 (60 °C), 6.30 (50 °C) and

6.46 (40 °C). The pH minimum is followed by a gradual increase in pH until titration ends after 120 min reaction time (Fig. 5.1c).

After stopping the titration, an approximately constant reaction pH is obtained at all temperatures: 6.28 (60 °C), 6.40 (50 °C) and 6.55 (40 °C). Previous work showed that the transition to a predominantly ZnO phase containing reaction product is accompanied by a second decrease in pH^[14]. This second decrease is only observed at 60 °C and occurs spontaneously after 15.5 h reaction time from pH drop of 6.25 to 6.13. After purification of the reaction product formed at 60 °C, a fine white powder was obtained, whereas at both 50 and 40 °C the product has a more paint-like consistency. If consistent with work at 80 °C (Ch. 3; 4), these two observations imply that ZnO is only formed predominantly at 60 °C.

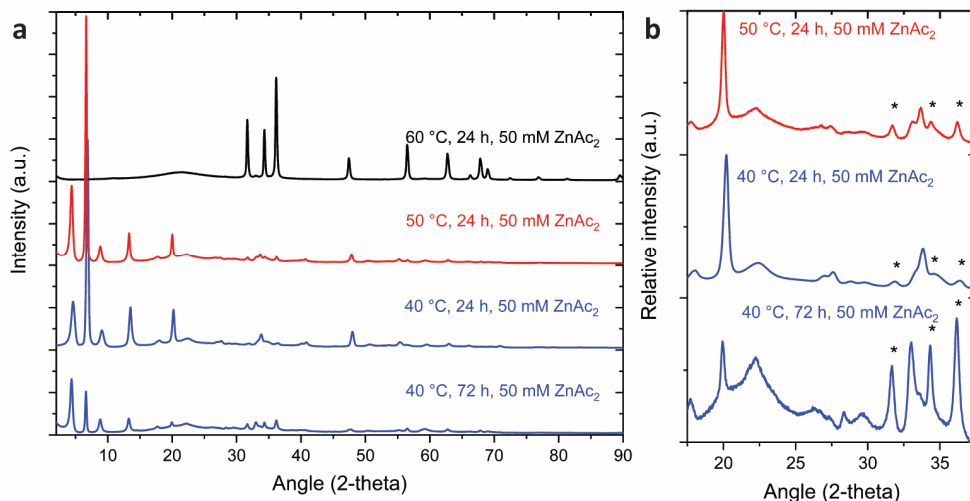


Figure 5.2 pXRD data of reaction product formed from 50 mM ZnAc₂ titrated with 1 mM ammonia at 0.014 mL min⁻¹ with a target pH of 6 after the first 2 h off reaction time at 60, 50 and 40 °C reaction temperature (a) and a zoom in between 17.5 – 37.5 2-theta with the intensity standardized over the 20 ° LBZA signal, ZnO signals are indicated with an asterisk. The broad pXRD signal visible at about 20° is from the substrate.

To verify the formation of ZnO pXRD is used (Fig. 5.2). At 60 °C, a near pure ZnO phase is obtained with only one signal at 33 ° 2-theta possibly matching LBZA. Decreasing the reaction temperature to 50 °C results in a dramatic decrease in the intensity of the ZnO signals. At this temperature, LBZA signals are predominantly observed with some minor wurtzite ZnO signals. Given that *in-situ* pH measurements did not show the typical LBZA-ZnO transition this matches with expectations (Fig. 5.2a). At 40 °C after 24 h reaction time, slightly weaker ZnO signals are observed compared to 50 °C, at both temperatures the LBZA signals are dominant (Fig. 5.2b). Increasing the reaction time at 40 °C to 72 h did result in a notable increase in ZnO signals (Fig. 5.2). This shows that ZnO can be formed at a mild near body temperature reaction conditions, given sufficient reaction time. However, even with extended reaction time LBZA is still the dominant end product.

To investigate if reduction in reaction temperature can influence the ZnO crystal shape, the ZnO crystals formed at 60, 50 and 40 °C were investigated by SEM (Fig. 5.3). This showed that the ZnO formed at 60 °C possess a rectangular and hexagonal shape (Fig. 5.3a) similar to ZnO synthesized at 80 °C in Ch. 3 and 4. For 50 and 40 °C (Fig. 5.3b,c), the underlying pillar shape can still be observed, however, with a strong increase in multiple faceting. Accordingly, instead of a rectangular shape in the long axis (c-

direction, [001]) these crystals seem to have a more cone-like shape. While a clear influence of temperature on ZnO crystal shape is observed, its origin remains unclear.

Although ZnO can be synthesized at low temperature using this reaction protocol, reproducibility proves to be an issue. The reaction using 50 mM ZnAc₂ was performed in three separate periods, one in 2019, 2020 and 2021. The experiments from 2019 provided unreliable *in-situ* pH data making it impossible to assign a general pH evolution (Section A5.1.). Reproducing this work in 2020, using the same equipment and chemicals, resulted in a significantly decreased ZnO yield compared to the formation of LBZA, especially when performing the reaction at 60 °C (Fig. A5.1). Only after all chemicals and glassware were replaced for the 2021 experiments (i.e. the data discussed in this chapter), a similar yield, as observed in the 2019 experiments, could be obtained (Fig. A5.2). Given that the exact cause of the low ZnO yield remains unclear, it needs to be emphasized that this low temperature ZnO formation protocol is rather sensitive to small variations in reaction conditions, including possibly the presence of minute amounts of impurities.

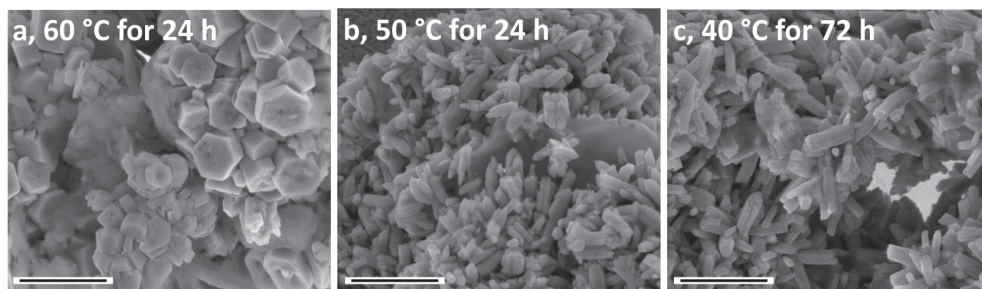


Figure 5.3 SEM images of ZnO end product synthesized at 60 (a), 50 (b) and 40 °C (c) using the 50 mM ZnAc₂ titration protocol. Scale bars are equal to 1 μm.

Overall, it is shown that by using a mild ammonia titration-based synthesis strategy, wurtzite ZnO can be formed in dispersion at a temperature as low as 40 °C. Decreasing the reaction temperature results in an increased reaction pH, namely from 6.16 (60 °C) to 6.46 (40 °C). Furthermore, at all temperatures (60 – 40 °C) LBZA is formed as a side or main product. The LBZA to ZnO transition previously observed at 80 °C is not observed below 60 °C. Indeed, the formation of LBZA becomes more dominant with decreasing reaction temperatures, showing a clear increase in LBZA formation between 60 and 50 °C. At 40 °C, increasing the reaction time from 24 to 72 h promotes the formation of ZnO over LBZA.

5.3. Influence of Reducing the Zinc Acetate Concentration

Using 50 mM ZnAc₂ results in the formation of ZnO at temperatures as low as 40 °C, next to the dominant formation of LBZA. In several cases in the literature it is observed that ZnO formation can be promoted by using relatively low zinc salt concentrations^[27]. For this reason, the ZnAc₂ starting concentration was lowered by a factor of three to 16.7 mM, accompanied by a modified ammonia titration protocol enforced by equipment limitations. The 1 M ammonia concentration was kept, but a titration rate of 0.02 mL min⁻¹ was used for the titration for the first hour, after which ammonia was only added when the pH of the reaction solution decreased below 6.0.

Performing this reaction protocol with a targeted reaction temperature of 60, 50, 40 and 30 °C, a somewhat similar pH evolution as at 50 mM ZnAc₂ was observed, however, with some notable differences (Fig. 5.4a,b). In all cases the initial pH increased to 7.0 - 7.1 which is significantly higher than pH 6.6 - 6.7 when using 50 mM ZnAc₂. It also exceeds the previously observed pH at which LBZA actively precipitates

(see *Ch. 4*). This indicates that a lower ZnAc_2 concentration will have a direct influence on the evolution of the species formed, most likely also shifting the speciation balance. The relatively high pH at low ZnAc_2 concentrations is maintained during the entire reaction at all investigated temperatures.

Looking solely at the features of the pH curve, similarities with the 50 mM ZnAc_2 reaction can be observed. After the initial pH increase a gradual pH decrease was seen to a minimum of 6.46 (60 °C) 6.60 (50 °C), 6.79 (40 °C) and 7.08 (30 °C) (*Fig. 5.4a,c*). These pH minima are followed by a rise in pH to pH 6.64 (60 °C) 6.86 (50 °C), 7.05 (40 °C) and 7.34 (30 °C) until titration ends at 1 h reaction time. After this the pH is relatively stable for several hours. In contrast to the use of 50 mM ZnAc_2 , a clear second decrease in pH is observed when performing the reaction at 60, 50 and 40 °C suggesting that a transition to a predominantly ZnO containing reaction product occurs at all three reaction temperatures. This point is supported by the observation of fine white powders formed at 60 and 50 °C. The powder obtained at 40 °C is grainier. Performing the reaction at 30 °C several decreases in pH are observed. This includes a smooth decrease at 2 h reaction time from pH 7.24 to 7.14 and a more pronounced decrease at 44.5 h reaction time from pH 7.09 to pH 6.70. At present it is unclear if any of these two pH decreases corresponds to a LBZA-ZnO phase transition. A transition is also considered unlikely as the reaction end product has a paint-like consistency, similar to the LBZA-rich reaction end products synthesized previously.

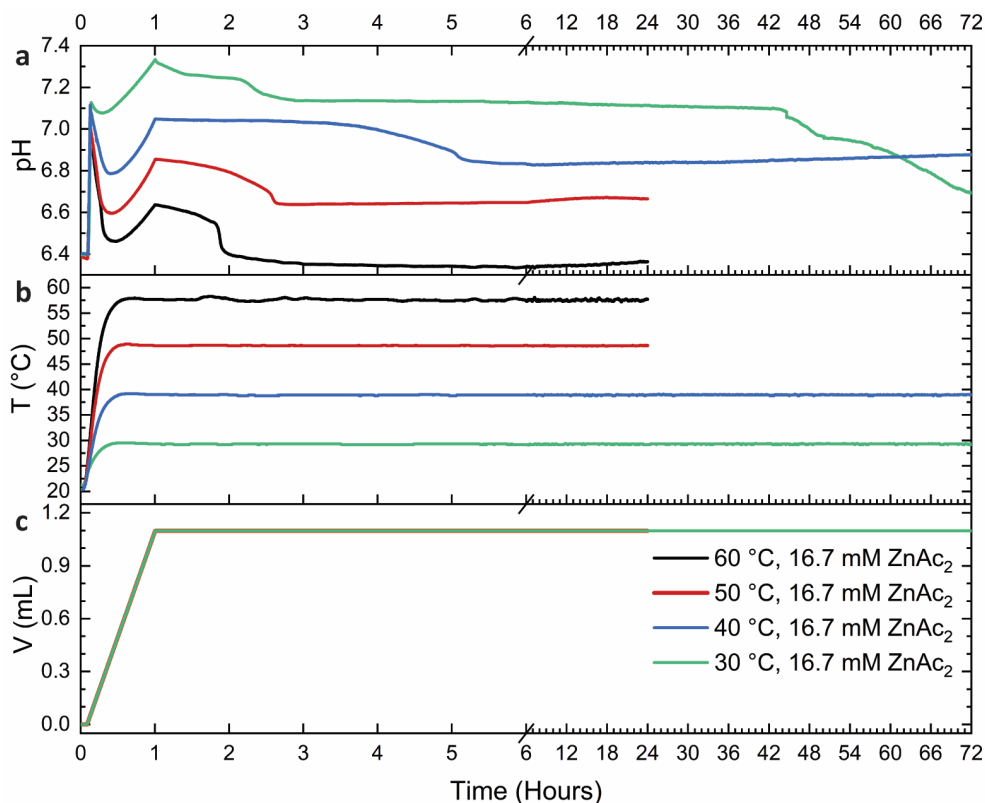


Figure 5.4 Titration based strategy for ZnO formation showing *in-situ* pH curve (a), temperature T (b) and base volume V (c) measurements of 16.7 mM ZnAc_2 titrated with 1 mM ammonia at 0.02 mL min^{-1} with a target pH of 6 after the first 1 h off the reaction time and at 60 (black), 50 (red), 40 (blue) and 30 °C (green) reaction temperature.

PXRD analysis of the reaction end product at 60 °C (Fig. 5.5) again showed the formation of a near pure ZnO phase with some minor signals before 30 ° 2-theta and one at 33 ° 2-theta that most likely correspond to LBZA. At 50 °C, pXRD analysis showed the formation of two major phases. The strongest signals correspond to wurtzite ZnO, which has more pronounced signals than those observed when using 50 mM ZnAc₂ at 50 °C. The second major set of signals matches with a wülfingite ZnOH₂ phase. Besides ZnO and wülfingite only minor signals matching LBZA could be observed. This suggests that decreasing the zinc salt concentration does promote the formation of ZnO. However, it also seems to promote the formation of wülfingite ZnOH₂. This results in a competition between the two phases.

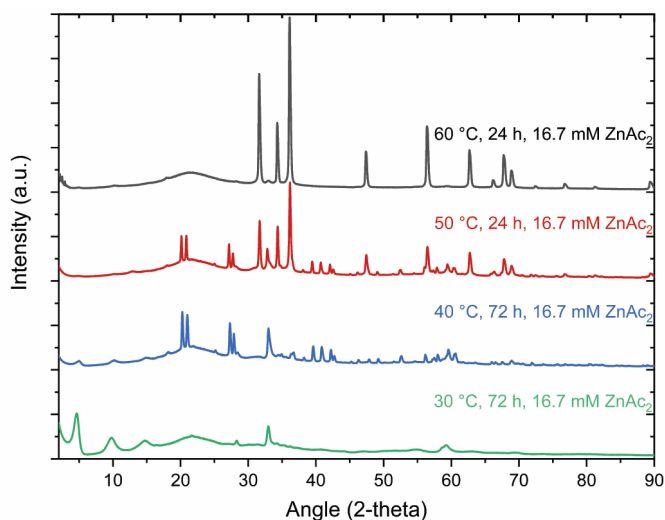


Figure 5.5 pXRD data of reaction end product synthesized from 16.7 mM ZnAc₂ titrated with 1 mM ammonia at 0.02 mL min⁻¹ with a target pH of 6 after the first 1 h off reaction time, performed at 60, 50, 40 and 30 °C reaction temperature. The broad pXRD signal visible at about 20° is from the substrate.

Analysis of the reaction performed at 40 °C, shows the predominant presence of wülfingite ZnOH₂. Only minimal signals matching with either LBZA or ZnO are observed. Given that *in-situ* pH measurements show a pH decrease typically associated with a transition from LBZA to ZnO, this does raise the question why no strong ZnO presence is observed in the end product. Therefore, the reaction at 40 °C was repeated and terminated after 1.5 h reaction time, before the second pH decrease. pXRD analysis on this intermediate product showed the dominant presence of LBZA and a minor amount of wurtzite ZnO phase (Fig. A5.3) at this initial reaction time. This shows that LBZA is initially formed using 16.7 mM ZnAc₂ at 40 °C, which makes it likely that the pH decrease does indicate a transition, however, in this case from LBZA to wülfingite ZnOH₂ instead of to ZnO. Performing the reaction at 30 °C LBZA was the dominant end product.

In summary, using a 16.7 mM ZnAc₂ instead of 50 mM results in a significantly higher reaction pH, suggesting the speciation balance does change with ZnAc₂ concentration. Performing the reaction at 50 °C promotes the formation of ZnO as compared to higher ZnAc₂ concentrations while simultaneously also forming wülfingite ZnOH₂. A clear second decrease in pH is observed at 60 – 40 °C, though this pH decrease may be assigned to a transition from LBZA to ZnO or a transition from LBZA to ZnOH₂. At 40 °C the transition to ZnOH₂ becomes dominant. Therefore, the ZnO synthesis strategy discussed in this section is ideal for a reaction temperature of ≥ 50 °C.

5.4. Influence of L-lysine

Given the promising results observed for the use of l-lys as an additive in the formation of ZnO, l-lys was employed here at 40 °C reaction temperature using both the 50 mM and 16.7 mM ZnAc₂ protocol as discussed above with a reaction time of 24 h (Section 5.2; 5.3). Due to the high pH of a 12 mM l-lys solution, l-lys was first dissolved in water and the pH was corrected to 6.4 by adding acetic acid, before adding the ZnAc₂. In both cases this resulted in a starting pH of 6.2 after adding the ZnAc₂. It is assumed that this somewhat lower starting pH will have no influence on the reaction evolution (Ch. 4). *In-situ* pH measurements showed an overall similar evolution compared to the reaction in the absence of l-lys (Fig. 5.6). Both reactions showed an initial rise to a pH maximum at 6.65 (50 mM ZnAc₂) and 7.00 (16.7 mM ZnAc₂). This is followed by a slight decrease in pH. Using 50 mM ZnAc₂, the observed pH decrease is minimal and shows a rather noisy signals, suggesting some additional process may be taking place. Subsequently, the pH rises until titration ends at 2 h and 1 h, respectively, reaching a second pH maximum at pH 6.60 (50 mM ZnAc₂) and 7.08 (16.7 mM ZnAc₂). For the remainder of both reactions this second maximum pH is maintained until the reaction is terminated at 24 h reaction time. No second pH decrease, indicative of LBZA to ZnO or LBZA to ZnOH₂ transitions, was observed.

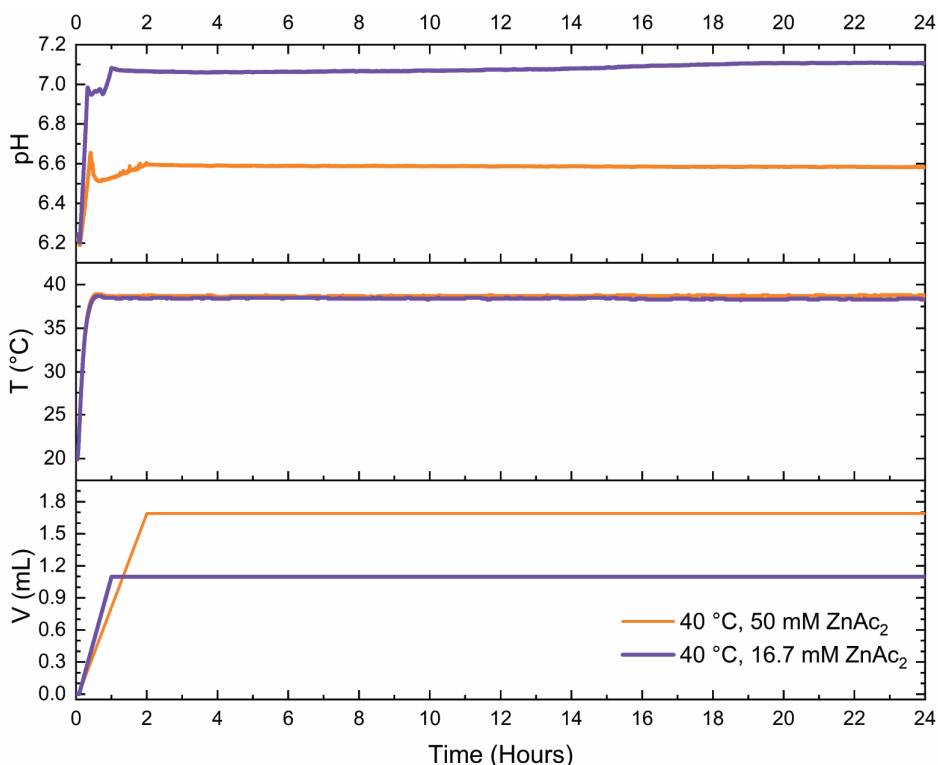


Figure 5.6 Titration based strategy for ZnO formation showing *in-situ* pH curve (a), temperature T (b) and base volume V (c) measurements of 12 mM l-lys at 40 °C in combination with 50 mM ZnAc₂ titrated with 1 mM ammonia at 0.02 mL min⁻¹ with a target pH of 6 after the first 1 h off the reaction time (orange) or 16.7 mM ZnAc₂ titrated with 1 mM ammonia at 0.02 mL min⁻¹ with a target pH of 6 after the first 1 h off the reaction time (purple), both performed at 40 °C reaction temperature.

PXRD analysis on the reaction end products (Fig A5.4), showed the preferred formation of LBZA with ZnO as a minor phase for both 50 and 16.7 mM ZnAc₂. Using 16.7 mM ZnAc₂, a stronger yet minimal ZnO signal is obtained compared to the reaction in absence of l-lys. Given that wülfingite ZnOH₂ is predominantly observed in absence of l-lys (Fig. 5.5), it is unclear whether l-lys promotes the formation of ZnO or suppresses the formation of ZnOH₂. Using 50 mM ZnAc₂, the ZnO pXRD signals are stronger than those observed in absence of l-lys at 24 h. Indeed, the relative intensity is similar to the ZnO signals observed after 72 h reaction time in presence of l-lys (Fig. 5.2). This suggests that the presence of l-lys promotes the formation of ZnO or suppresses the formation of LBZA. By increasing the reaction time to 72 h in presence of l-lys the formation of ZnO can be further improved (Fig A5.4).

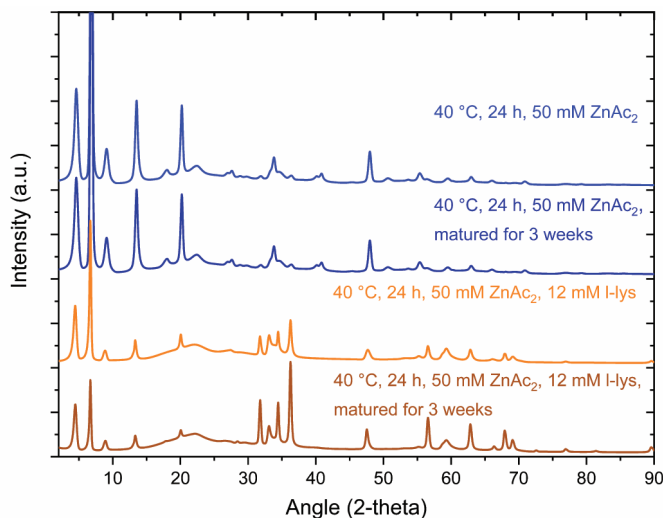


Figure 5.7 pXRD data of 50 mM ZnAc₂ titrated with 1 mM ammonia at 0.014 mL min⁻¹ with a target pH of 6 after the first 2 h off reaction time, performed at 40 °C reaction temperature in absence and in presence of 12 mM l-lys. Half of the product was directly purified and analyzed after synthesis, whereas the other half was matured for 3 weeks. broad pXRD signal visible at about 20° is due to the substrate.

Upon adding l-lys to the reaction mixture, at a mild reaction pH < 6.8, rapid formation of a white precipitate was observed in multiple cases. This suggests that l-lys has an influence at RT. To further investigate this effect, a reaction was performed 24 h at 40 °C using 50 mM ZnAc₂ both in presence and in absence of 12 mM l-lys. Subsequently, half of the reaction products was directly isolated, purified and analyzed by pXRD (Fig. 5.7). The other half of the reaction product was matured at RT for 3 weeks in a glass vial, followed by purification and pXRD analysis. In absence of l-lys, no change in pXRD signals was observed before or after maturing the product. In contrast, in presence of l-lys ZnO signals are significantly more pronounced compared to the LBZA after maturing the reaction product. This indicates that the transition from LBZA to a more ZnO pure phase continues at RT when l-lys is present. There could be due to two possible mechanisms: either l-lys destabilizes the formed LBZA over time which indirectly promotes the growth of ZnO or l-lys directly promotes the growth of ZnO. Given that it is unclear from the data if the decrease in formed ZnO after maturing is due to continued growth or dissolution and reprecipitation, it is impossible to distinguish between both mechanisms. Future studies using *in-situ* cryoTEM may give more insight in this.

Overall, these results show that the presence of l-lys promotes the formation of ZnO at low reaction temperatures. In particular, performing the synthesis of ZnO with 50 mM ZnAc₂ a similar presence of ZnO is obtained after 24 h reaction time in presence of l-lys compared to a 72 h reaction time in absence of additives. The presence of l-lys further seems to allow for continuation of the ZnO formation by maturing the reaction product at RT.

5.5. Conclusion

Using a titration-based synthesis strategy with ZnAc₂ as zinc salt and ammonia solution as base, wurtzite ZnO could be synthesized at temperatures as low as 40 °C in the absence of additives and without using any post synthetic heating steps. With decreasing reaction temperatures other species are also observed, namely LBZA and wülfingite ZnOH₂. Here, the initial ZnAc₂ concentration does influence both the crystalline species of the reaction product and their purity. Use of 50 mM ZnAc₂ only resulted in significant formation of ZnO at > 60 °C. At 50 and 40 °C ZnO became a minor phase with the major phase being LBZA. Increasing the reaction time did increase the relative amount of ZnO formed. In contrast, using 16.7 mM ZnAc₂, ZnO was the major product at 60 °C and arguably at 50 °C. At this ZnAc₂ starting concentration, significant amounts of wülfingite ZnOH₂ were observed at 50 °C and its dominant formation at 40 °C. In contrast to the use of 50 mM ZnAc₂ no ZnO was observed when performing the reaction at 40 °C using 16.7 mM ZnAc₂. Wülfingite ZnOH₂ was not formed during the initial reaction stages but likely during an observed second decrease in pH, previously only associated with the formation of ZnO at higher reaction temperatures. This suggests that under these conditions wülfingite ZnOH₂ formation is the kinetically and possibly thermodynamically more favorable pathway than the formation of ZnO.

The formation of ZnO at 40 °C could be further promoted by adding l-lys to the initial reaction solution. In presence of l-lys an increased ZnO yield was observed when using shorter reaction times. It was also found that in presence of l-lys the transition of the reaction product to containing more pure ZnO continues when maturing the reaction product at RT. Something that was not observed in absence of l-lys. Overall, this shows that ZnO can be formed at low reaction temperatures and that ZnO formation can be promoted further by selecting suitable additives.

5.6. Materials and Methods

5.6.1. Materials

Acetic acid (99-100%, GPR reagent) and ammonia (28%, GPR reagent) were acquired from VWR, l-lysine (l-lys, > 98%, purum) was acquired from Fluka and zinc acetate dihydrate (ZnAc₂, > 98%, ACS reagent) was acquired from Acros organics. All chemicals were used as received unless stated otherwise.

5.6.2. Methods

When the reaction is performed in presence of l-lys, 12 mM l-lys was dissolved in 50 mL pure water and set to pH 6.4 to 6.6 using 50 and 250 mM acetic acid solutions. Next 16.7 or 50 mM zinc acetate was dissolved in the l-lys solution or *in the case for all other reactions* in 50 mL pure water in a 100 mL five-neck flask under reflux. The reaction solution was magnetically stirred (vortexing, 450 rpm). Unless noted otherwise, the starting pH was set to 6.4 by manually adding 50 mM acetic acid solution before initiating heating. 30 s after starting pH measurements the reaction temperature was gradually increased to ~60, 50, 40 or 30 °C using an oil bath. 270 s after initiating heating 1 M ammonia is titrated into the system at 0.02

or 0.014 mL min⁻¹ for either 3300 or 6900 s, when using 16.7 or 50 mM zinc acetate respectively. After this initial titration period ammonia is only added to the reaction solution if the pH is below 6.0. 24 or 72 h after initiation, the reaction was ended and the final dispersion collected. All dispersions were subsequently purified by centrifugation using an Optima L-90K ultracentrifuge equipped with a Type 70 Ti rotor at 25,000 rpm for 20 min. The pellet was redispersed in pure water followed by another centrifugation step. This procedure was performed twice. After centrifugation the solid product was dried at room temperature.

5.6.3. Analysis

***In-situ* pH and temperature** measurements were conducted, respectively, using a Metrohm 6.0234.100 and 6.1110.100 pH and temperature sensor, connected to an 809 Titrando unit equipped with two 800 dosino dosing devices (10 or 20 mL) controlled by TIAMO 2.5 software.

Powder X-ray diffraction (pXRD) measurements were performed on a MiniFlex 600 diffractometer operated at 40 kV and 15 mA using Cu K α radiation (1.54 nm).

Scanning electron microscopy (SEM) was carried out on a Quanta 3D (Thermo Fischer Scientific) equipped with a field emission gun, secondary electron detector and operated at 5.0 kV. The samples in powder form were dispersed in pure water, 10 μ L dispersion was deposited on a continuous carbon-coated TEM grid with copper or gold supports (200 mesh), followed by manual blotting after 40 s. Samples were loaded in the SEM using an in-house build custom SEM holder that can accommodate 6 TEM grids.

5.7. Appendix A5

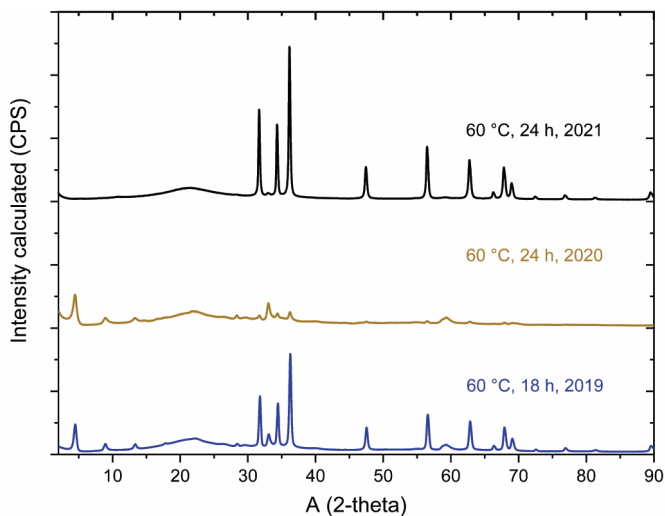


Figure A5.1 pXRD data of 50 mM ZnAc₂ titrated with 1 mM ammonia at 0.02 mL/min with a target pH of 6 after the first 2 h off reaction time, performed in 2019 (blue), 2020 (gold) and 2021 (black). The broad pXRD signal visible at about 20° is due to the substrate.

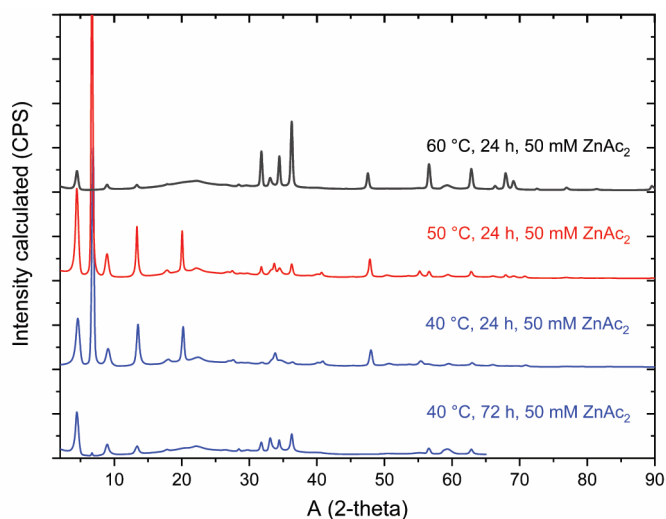


Figure A5.2 pXRD data from 2019 of 50 mM ZnAc₂ titrated with 1 mM ammonia at 0.02 mL min⁻¹ with a target pH of 6 after the first 2 h off reaction time, performed at 60 (black), 50 (red) and 40 °C (blue) reaction temperature. The broad pXRD signal visible at about 20° is due to the substrate.

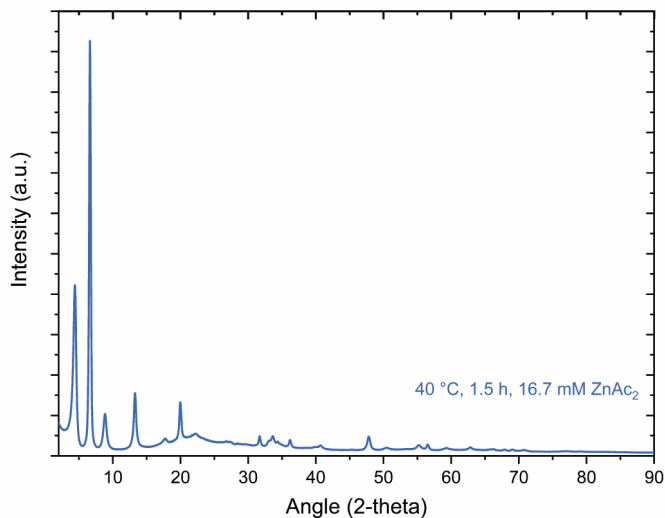


Figure A5.3 pXRD data of 16.7 mM ZnAc₂ titrated with 1 mM ammonia at 0.02 mL min⁻¹ performed at 40 °C with a 1.5 h reaction time. The broad pXRD signal visible at about 20° is due to the substrate.

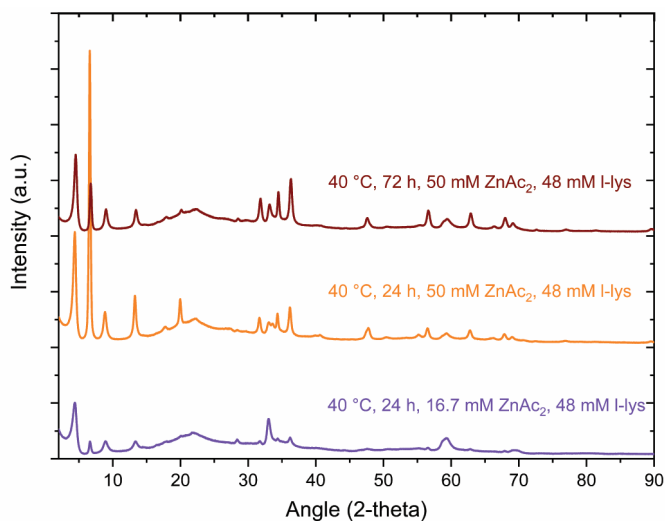


Figure A5.4 pXRD data from a 24 h (orange) and 72 h (red) reaction at 40 °C in presence of 12 mM l-lys using 50 mM ZnAc₂ titrated with 1 mM ammonia at 0.014 mL min⁻¹ and with a target pH of 6 after the first 2 h off reaction time (purple) and a 24 h reaction in presence of 16.7 mM ZnAc₂ titrated with 1 mM ammonia at 0.02 mL min⁻¹ and with a target pH of 6 after the first 1 h off reaction time (orange). The broad pXRD signal visible at about 20° is due to the substrate.

A5.1. Difficulties Using pH Probes

As mention in *section 5.3 in-situ* pH data is not presented for several of the earlier experiments. In some cases, this is due to a software issue resulting in full loss of data directly after measurements. In most cases, however, the data is not of sufficient quality to allow for reliable data interpretation. All these experiments were performed using a metrohm unitrode combined pH and temperature electrode, similar to the one used in *Ch. 3*. The specific electrode used was found to have an issue during heating (*Fig A5.5*). During the initial heating stages, the sensor detected a non-sample related spontaneous rise in pH. This pH rise was subsequently followed by a gradual pH correction over time. The occurrence of this pH rise is unpredictable and can be mistaken for the natural pH increase observed during initial titration. This makes it impossible to reliably deconvolute this artifact from pH changes present in the reaction. For this reason, it was decided to omit all pH data acquired with this probe from the data analysis process and this thesis.

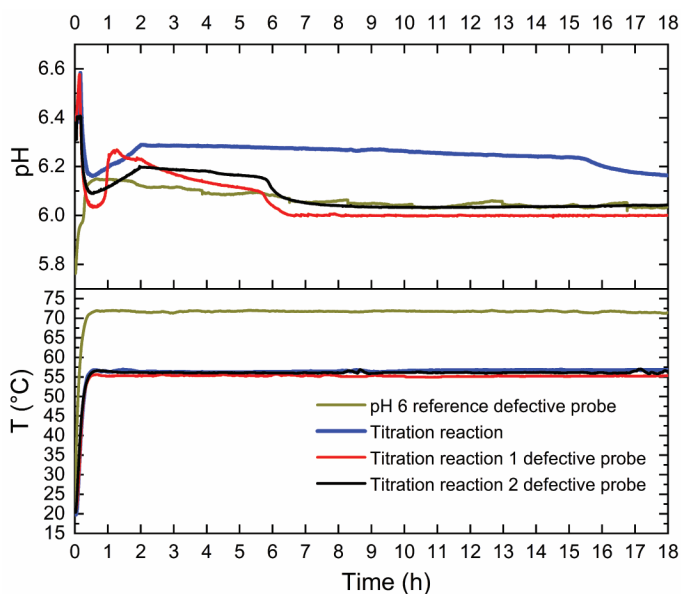


Figure A5.5 Measured pH and temperature evolution of a pH 6 buffer heated to 80 °C, and three ZnO titration reactions performed at 60 °C. For the buffer reaction and the red and black titration reactions the defective unitrode electrode was used. The remaining titration reaction blue uses a pH and temperature sensor as used for all reactions displayed in this chapter.

5.8. References

1. L. Mishnaevsky and M. Tzapatsis, Hierarchical Materials: Background and Perspectives. *MRS Bull* **41**, 661-666 (2016).
2. U. G. K. Wegst, H. Bai, E. Saiz, A. P. Tomsia and R. O. Ritchie, Bioinspired Structural Materials. *Nat Mater* **14**, 23-36 (2015).
3. J. D. Currey, Materials Science - Hierarchies in Biomineral Structures. *Science* **309**, 253-254 (2005).
4. B. M. Oosterlaken, M. P. Vena and G. de With, In Vitro Mineralization of Collagen. *Adv. Mater.*, 2004418 (2021).
5. D. Bhatia, H. Sharma, R. S. Meena and V. R. Palkar, A Novel ZnO Piezoelectric Microcantilever Energy Scavenger: Fabrication and Characterization. *Sens Biosensing Res* **9**, 45-52 (2016).
6. E. S. Nour, O. Nur and M. Willander, Zinc Oxide Piezoelectric Nano-generators for Low Frequency Applications. *Semicond Sci Tech* **32**, 064005 (2017).
7. W. L. Bond, Measurement of the Refractive Indices of Several Crystals. *J Appl Phys* **36**, 1674-1677 (1965).
8. C. B. Ong, L. Y. Ng and A. W. Mohammad, A Review of ZnO Nanoparticles as Solar Photocatalysts: Synthesis, Mechanisms and Applications. *Renew Sust Energ Rev* **81**, 536-551 (2018).
9. Z. Mirzaeifard, Z. Shariatinia, M. Jourshabani and S. M. R. Darvishi, ZnO Photocatalyst Revisited: Effective Photocatalytic Degradation of Emerging Contaminants Using S-Doped ZnO Nanoparticles under Visible Light Radiation. *Ind Eng Chem Res* **59**, 15894-15911 (2020).
10. B. R. Williams, R. A. Gelman, D. C. Poppke and K. A. Piez, Collagen Fibril Formation - Optimal Invitro Conditions and Preliminary Kinetic Results. *J Biol Chem* **253**, 6578-6585 (1978).
11. T. Hayashi and Y. Nagai, Effect of pH on the Stability of Collagen Molecule in Solution. *J Biochemie* **73**, 999-1006 (1973).
12. Y. Sun, W. L. Chen, S. J. Lin, S. H. Jee, Y. F. Chen, L. C. Lin, P. T. C. So and C. Y. Dong, Investigating Mechanisms of Collagen Thermal Denaturation by High Resolution Second-harmonic Generation Imaging. *Biophys J* **91**, 2620-2625 (2006).
13. V. Gerbreders, M. Krasovska, E. Sledevskis, A. Gerbreders, I. Mihailova, E. Tamanis and A. Ogurcovs, Hydrothermal Synthesis of ZnO Nanostructures with Controllable Morphology Change. *CrystEngComm* **22**, 1346-1358 (2020).
14. M. M. J. van Rijt, B. M. Oosterlaken, R. R. M. Joosten, L. E. A. Wijkhuijs, P. H. H. Bomans, H. Friedrich and G. de With, Counter-ion Influence on the Mechanism of HMTA-mediated ZnO Formation. *CrystEngComm* **22**, 5854-5861 (2020).
15. Y. B. Wang, S. Wang and X. Lu, In Situ Observation of the Growth of ZnO Nanostructures Using Liquid Cell Electron Microscopy. *J Phys Chem C* **122**, 875-879 (2018).
16. K. Fujita, K. Murata, T. Nakazawa and I. Kayama, Crystal Shapes of Zinc Oxide Prepared by the Homogeneous Precipitation Method. *J. Ceram* **92**, 227-230 (1984).
17. R. Parize, J. Garnier, O. Chaix-Pluchery, C. Verrier, E. Appert and V. Consonni, Effects of Hexamethylenetetramine on the Nucleation and Radial Growth of ZnO Nanowires by Chemical Bath Deposition. *J Phys Chem C* **120**, 5242-5250 (2016).
18. D. L. G. Arellano, J. Bhamrah, J. W. Yang, J. B. Gilchrist, D. W. McComb, M. P. Ryan and S. Heutz, Room-Temperature Routes Toward the Creation of Zinc Oxide Films from Molecular Precursors. *ACS Omega* **2**, 98-104 (2017).
19. O. Carp, A. Tirsoga, R. Ene, A. Ianculescu, R. F. Negrea, P. Chesler, G. Ionita and R. Birjega, Facile, High Yield Ultrasound Mediated Protocol for ZnO Hierarchical Structures Synthesis: Formation Mechanism, Optical and Photocatalytic Properties. *Ultrason Sonochem* **36**, 326-335 (2017).
20. W. Zhao, X. Y. Song, Z. L. Yin, C. H. Fan, G. Z. Chen and S. X. Sun, Self-assembly of ZnO Nanosheets into Nanoflowers at Room Temperature. *MRS Bull* **43**, 3171-3176 (2008).
21. N. J. Nicholas, G. V. Franks and W. A. Ducker, The Mechanism for Hydrothermal Growth of Zinc Oxide. *CrystEngComm* **14**, 1232-1240 (2012).
22. A. Tarat, R. Majithia, R. A. Brown, M. W. Penny, K. E. Meissner and T. G. G. Maffei, Synthesis of Nanocrystalline ZnO Nanobelts via Pyrolytic Decomposition of Zinc Acetate Nanobelts and their Gas Sensing Behavior. *Surf Sci* **606**, 715-721 (2012).
23. A. Sola-Rabada, M. K. Liang, M. J. Roe and C. C. Perry, Peptide-directed Crystal Growth Modification in the Formation of ZnO. *J Mater Chem B* **3**, 3777-3788 (2015).
24. M. Umetsu, M. Mizuta, K. Tsumoto, S. Ohara, S. Takami, H. Watanabe, I. Kumagai and T. Adschiri, Bioassisted Room-temperature Immobilization and Mineralization of Zinc Oxide - The Structural Ordering of ZnO Nanoparticles into a Flower-type Morphology. *Adv Mater* **17**, 2571-+ (2005).
25. N. Subramanian and A. Al Ghafiri, An Amino Acid-based Swift Synthesis of Zinc Oxide Nanostructures. *RSC Adv* **4**, 4371-4378 (2014).
26. N. Subramanian and A. Al Ghafiri, A Green Synthetic Route for Zinc Oxide Nanoarchitectures using L-lysine. *Mater Lett* **92**, 361-364 (2013).
27. T. F. Long, S. Yin, K. Takabatake, P. Zhnag and T. Sato, Synthesis and Characterization of ZnO Nanorods and Nanodisks from Zinc Chloride Aqueous Solution. *Nanoscale Res Lett* **4**, 247-253 (2009).

Chapter 6

Designing Stable, Hierarchical Peptide Fibers from Block Co-polypeptide Sequences

Natural materials, such as collagen, can assemble with multiple levels of organization in solution. Achieving a similar degree of control over morphology, stability and hierarchical organization with equilibrium synthetic materials remains elusive. For the assembly of peptidic materials the process is influenced by the formation of a secondary structure motifs. This formation with its underlying hydrophobic interactions and electrostatics results in a complex interplay of variables. Consequently, fine tuning the thermodynamics and kinetics of assembly remains extremely challenging. Here, we synthesized a set of block co-polypeptides with varying hydrophobicity and ability to form secondary structure. From this set we select a sequence with balanced interactions that results in the formation of high-aspect ratio thermodynamically favored nanotubes, stable between pH 2 and 12 and up to 80 °C. This stability permits their hierarchical assembly into bundled nanotube fibers by directing the pH and inducing complementary zwitterionic charge behavior. This block co-polypeptide design strategy, using defined sequences, provides a straightforward approach to creating complex hierarchical peptide-based assemblies with tunable interactions ideal as mineralization template for, for example, ZnO.

This chapter is adapted from:

M. M. J. van Rijt, A. Ciaffoni, A. Ianiro, M.-A. Moradi, A. L. Boyle, A. Kros, H. Friedrich, N. A. J. M. Sommerdijk and J. P. Patterson, Designing stable, hierarchical peptide fibers from block co-polypeptide sequences, *Chemical Science*, 2019, **10**, 9001-9008.

“All around us are people, of all classes, of all nationalities, of all ages. For three days these people, these strangers to one another, are brought together. They sleep and eat under one roof, they cannot get away from each other. At the end of three days they part, they go their several ways, never, perhaps, to see each other again.”

Agatha Christie, Murder on the Orient Express, 1934

6.1. Peptide Self-assembly

Due to their biocompatibility, biodegradability and their versatility in chemistry^[1-3], poly (amino acid) amphiphiles are widely investigated for applications including therapeutics^[4], drug delivery^[5], and scaffolding for biological growth^[6]. A wide range of strategies exist for creating peptide-based self-assembled materials including dipeptides^[7], dynamic peptide libraries^[8], spider-silk based sequences^[9], peptide amphiphiles (PA)^[10, 11] and block co-polypeptides (BCPP)^[12, 13]. These amphiphilic peptide materials have been shown to organize into various morphologies, such as spherical-^[14-17] and cylindrical micelles^[6, 8, 18], vesicles^[12, 17, 19-21], nanotubes^[22-30], nanoribbons^[25, 30-34] and hydrogel networks^[13, 35]. Nanotubes are defined as well-defined hollow cylinders with a diameter range of 0.5-500 nm and an aspect ratio exceeding five^[36]. These morphologies possess only limited levels of organization, which strongly contrast with natural materials like collagen that possess multiple levels of organization (hierarchical materials). As these hierarchical materials possess unrivalled control over structure and properties^[37], achieving hierarchical self-assembly in synthetic materials through additional complementary supramolecular interactions is an important goal in the field of bio-inspired materials.

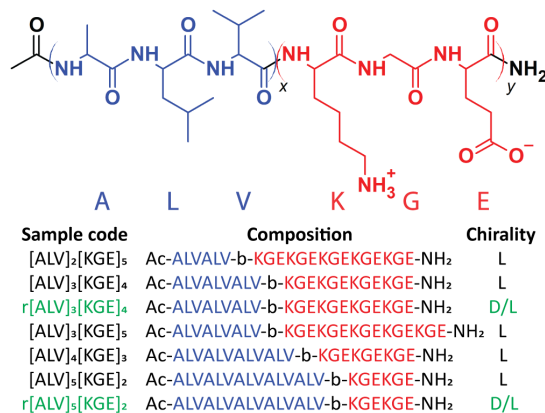
Synthetic hierarchical materials often form kinetically trapped structures, which can be very stable^[38-40], but generally are highly dependent on the preparation conditions and mostly are non-uniform in size and morphology^[41, 42]. Thermodynamically controlled assemblies that rapidly equilibrate to the lowest energy conformation tend to form well-defined and reproducible structures^[43]. However, these structures tend to rearrange upon changing solution conditions^[44], which limits their usability window and prevents control over their organization in solution. At elevated temperatures, changes or even denaturation of the peptide secondary structure can radically influence the expressed morphology resulting in, for example, peptide nanotube in helical unwinding^[29] or the devolution into spherical micelles at elevated temperatures^[25]. The pH induced protonation or deprotonation of peptide moieties has shown to induce self-assembly^[45], evolution in morphology^[18] or even the inversion of vesicular assemblies^[19]. Furthermore, variations in ionic concentration have shown to both influence the secondary structure and the fibrillar length^[6]. Therefore, realizing thermodynamically controlled assemblies that are stable in a wide range of environments with the ability to form hierarchical assemblies is an interesting challenge which requires a careful balance of system thermodynamics and kinetics^[46]. For peptide-based assemblies this requires controlling hydrophobic interactions, electrostatics and the resulting secondary structure motifs ^[11, 47]. Consequently, new approaches towards designing peptide sequences which allow control over thermodynamics and kinetics are needed.

Here we use BCPPs with a defined amino acid composition and sequence, inspired by previous observed assembly behavior^[48]. We designed a hydrophobic core sequence with the ability to form secondary structure, and a hydrophilic “stabilizer” sequence which is pH responsive. Simple variation of the peptide relative peptide block lengths and their ability to form secondary structure provides control over the system morphology, thermodynamics, and kinetics. This allows us to form well-defined peptide nanotubes which are stable between pH 2 -12, in a temperature range of 4 -80 °C and under a wide range of ionic strengths. The stability of the nanotube morphology under this broad variety of environments allows their organization in solution to be tuned by controlling inter-nanotube attraction and repulsion, resulting in the formation of bundled nanotube fibers.

Using solid-phase peptide synthesis (SPPS)^[49], we created a set of BCPPs with the generic composition [ALV]_x[KGE]_y, see *scheme 1* and *section A6.1.1*. The hydrophobic alanine - leucine - valine (ALV) sequence is designed to form a rigid secondary structure, either α -helical or β -sheet^[50, 51], which makes the formation of typical spherical or cylindrical micelles less favorable as compared to the lower curvature nanotube or vesicular morphologies^[52]. The added rigidity of the secondary structure should also provide enhanced stability to the assembled morphology compared to typically used aliphatic segments. The alternating charges in the lysine - glycine - glutamic acid (KGE) hydrophilic sequence is designed to control the

repulsion between individual chains and ultimately larger assemblies by adjusting solution pH. Based on the pH the hydrophilic stabilizer block is either dominantly positively, zwitterionically or negative charged. By varying the relative lengths of each sequence and synthesizing complementary racemic sequences, we investigate the relative contributions of secondary structure and hydrophobicity on the morphology and the thermodynamics and kinetics of the assemblies.

Scheme 1 Molecular structure of $[\text{ALV}]_x[\text{KGE}]_y$ and an overview of the investigated peptide sequences.



6.2. Control over Morphology and Assembly Kinetics by Varying the Hydrophobic-hydrophilic Balance and Secondary Structure

To initiate self-assembly, the investigated peptide sequences (scheme 1) were added directly to pure water (resulting in a pH of ~ 4) or pH 4 buffer at a concentration of 5 or 10 mg mL⁻¹. At both concentrations similar behavior was observed. For $[\text{ALV}]_5[\text{KGE}]_2$ this resulted in macroscopic phase separation. Assembly of $[\text{ALV}]_5[\text{KGE}]_2$ could be induced by a DMSO solvent switch procedure (see *section 6.6*), still yielding a turbid dispersion. The high water-incompatibility of $[\text{ALV}]_5[\text{KGE}]_2$ indicates the formation of kinetically trapped assemblies during water addition in the solvent switch procedure^[53]. Upon pure water or pH 4 buffer addition the more hydrophilic sequences $[\text{ALV}]_2[\text{KGE}]_5$, $[\text{ALV}]_3[\text{KGE}]_4$, $[\text{ALV}]_3[\text{KGE}]_5$ and $[\text{ALV}]_4[\text{KGE}]_3$ quickly formed slightly viscous, transparent solutions.

The evolution of morphology with increasing length of the hydrophobic sequence was investigated by cryoTEM. $[\text{ALV}]_2[\text{KGE}]_5$, the most hydrophilic sequence, showed no evidence of self-assembly (*Fig. A6.1a*). Using cryo-EELS analysis a significant amount of nitrogen could be detected in the solution (*Fig. A6.1c*), indicating that $[\text{ALV}]_2[\text{KGE}]_5$ peptides are solubilized as unimers, i.e. individual macromolecules. The presence of the peptide in solution was further supported by the formation of sheet-like polymer structures upon freeze drying in the TEM (*Fig. A6.2a-b*). For the $[\text{ALV}]_3[\text{KGE}]_4$ peptide, the formation of well-defined nanotubes, with lengths of $> 2 \mu\text{m}$ and diameters of $9 \pm 1 \text{ nm}$ and with an internal cavity of $4.5 \pm 0.4 \text{ nm}$ were observed by cryoTEM (*Fig. 6.1a*). This measured diameter exceeds the length of two fully extended hydrophobic sequences (6.9 nm, *section A6.2*), thereby strongly suggesting that the observed structures are hollow nanotubes (curled bilayer structures) rather than solid or hydrated cylindrical micelles. However, the observation of these small internal nanotube cavities by cryoTEM was very challenging and required optimal imaging conditions, as further discussed in *section A6.2*. SAXS measurements were performed to support the cryoTEM results. The experimental SAXS data was

compared to both form factor modelling (no least-squares minimization) and fitting (using least-squares minimization) of hollow and solid cylinders (Fig. 6.2, section A6.2). For both procedures the solid cylinder model showed a poor correlation with the experimental results. In contrast, good agreement between the SAXS data and the hollow cylinder model, with a diameter of 9 nm with an internal cavity diameter of 2 nm, is observed, confirming the formation of nanotubes. That this internal cavity shows a smaller diameter according to SAXS (2 nm) compared to cryoTEM (4.5 nm) further supports the presence of hydrated stabilizer blocks in the nanotube interior. These hydrated domains cannot be observed by cryoTEM whereas they seem to provide contrast in SAXS.

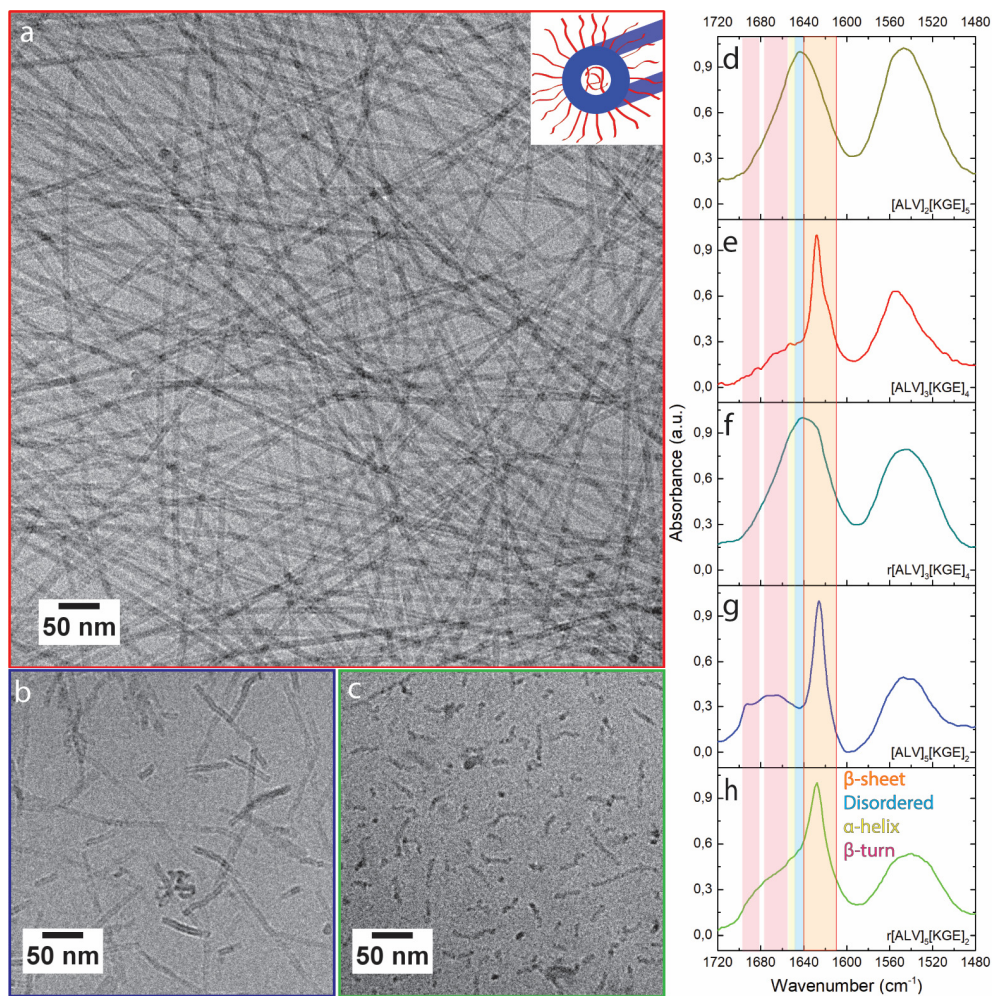


Figure 6.1 CryoTEM images (a-c) of $[\text{ALV}]_5[\text{KGE}]_4$ (a), $[\text{ALV}]_5[\text{KGE}]_2$ (b) and $r[\text{ALV}]_5[\text{KGE}]_2$ (c) combined with normalized FTIR spectra (d-h) of $[\text{ALV}]_5[\text{KGE}]_5$ (d), $[\text{ALV}]_5[\text{KGE}]_4$ (e), $r[\text{ALV}]_5[\text{KGE}]_4$ (f), $[\text{ALV}]_5[\text{KGE}]_2$ (g) and $r[\text{ALV}]_5[\text{KGE}]_2$ (h) self-assembled at 5 mg mL^{-1} . The FTIR spectra show the amide I and II signals of the peptide assemblies. Inset (a) corresponds to a sketch of the expected tubular assembly structure based on cryoTEM observations. Low magnification images of a-c can be found in section A6.1.2.

To determine if these nanotubes are equilibrium species, dialysis was used, in combination with UV-Vis measurements of the amide absorption (*section A6.3*), where the use of a 10 kDa dialysis membrane should only allow the diffusion of peptide unimers through the membrane wall. After 72 h of dialysis a strong decrease in amide absorption was observed, indicating that unimer exchange between the nanotubes and bulk solution indeed occurs, strongly indicating that the nanotubes are equilibrium species^[54]. CryoTEM showed that similar tubular assemblies were found when $[\text{ALV}]_3[\text{KGE}]_4$ was subjected to DMSO solvent switch (*section A6.1.2*). As the observation of similar structures from a different preparation method is uncommon for kinetically trapped structures^[54], this lends support to our conclusion that these are in equilibrium with unimers in solution.

To determine if the evolution from unimers to nanotubes between $[\text{ALV}]_2[\text{KGE}]_5$ and $[\text{ALV}]_3[\text{KGE}]_4$ is due to an increase of the hydrophobic (ALV) sequence, or a decrease of the hydrophilic (KGE) sequence length, $[\text{ALV}]_3[\text{KGE}]_3$ was synthesized. CryoTEM showed identical nanotube assemblies compared to $[\text{ALV}]_3[\text{KGE}]_4$ (*Fig. A6.3a*). This suggests that the increase in hydrophobic domain length is the driving force for the observed evolution in morphology.

Assembly of the $[\text{ALV}]_4[\text{KGE}]_3$ sequence resulted in a mixture of disordered curved cylindrical shaped micelles with a diameter of 5 ± 1 nm (*Fig. A6.3b*) and long nanotubes with a diameter of 9 ± 1 nm. The latter had an internal cavity of 2.5 ± 0.4 nm. The assembly of $[\text{ALV}]_4[\text{KGE}]_3$ in two distinct cylindrical populations suggest the presence of a kinetic component during self-assembly.

CryoTEM further showed that the most hydrophobic peptide $[\text{ALV}]_5[\text{KGE}]_2$, assembled into 200 nm long nanotubes with a diameter of 9 ± 1 nm (*Fig. 6.1b*) and an internal cavity of 4.4 ± 0.4 nm. Based on the previously mentioned water-incompatibility of $[\text{ALV}]_5[\text{KGE}]_2$ we conclude that these nanotubes are kinetically trapped structures. This evolution from 1) soluble unimers of $[\text{ALV}]_5[\text{KGE}]_2$, to 2) nanotubes of both $[\text{ALV}]_3[\text{KGE}]_4$ and $[\text{ALV}]_3[\text{KGE}]_5$ that are in equilibrium with the solution, to 3) kinetically trapped structures with $[\text{ALV}]_4[\text{KGE}]_3$ and finally 4) phase separation of $[\text{ALV}]_5[\text{KGE}]_2$ (which can be assembled by solvent switch into kinetically trapped nanotubes) indicates that both the morphology and the energetics of the formation pathways can be controlled by the relative block lengths of the $[\text{ALV}]_x[\text{KGE}]_y$ system.

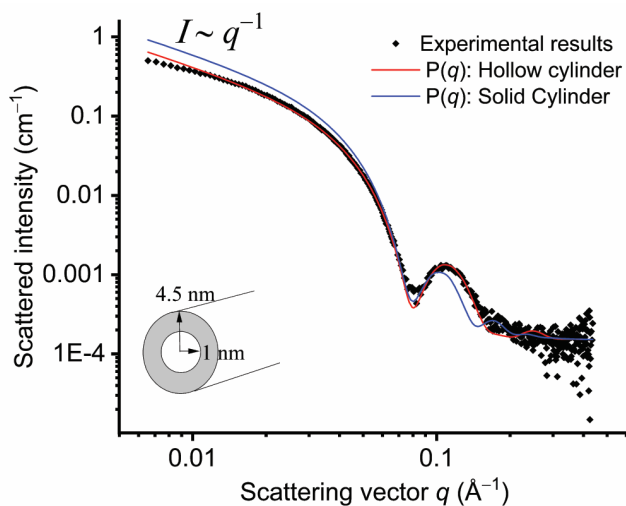


Figure 6.2 SAXS scattered intensity(I) plot against the scattering vector (q) for $[\text{ALV}]_3[\text{KGE}]_4$ assembled at 5 mg mL^{-1} in pH 4 buffer by direct dissolution (black) versus the fitted model for solid (blue) and hollow (red) cylindrical shaped micelles.

For all assembled samples, strong light scattering of the aggregates prevented the use of circular dichroism, therefore the secondary structure (i.e. folding behavior) of these macromolecules was investigated using Fourier transform infrared (FTIR) spectroscopy, by analyzing the Amide I vibrations (Fig. 6.1d-h; A6.3c). Hand-in-hand with the observed evolution in morphology, an evolution in secondary structure was observed: $[\text{ALV}]_2[\text{KGE}]_5$ showed an amide I maximum at 1644 cm^{-1} corresponding to disordered folding behavior; $[\text{ALV}]_3[\text{KGE}]_4$, $[\text{ALV}]_3[\text{KGE}]_5$ and $[\text{ALV}]_4[\text{KGE}]_3$ showed a dominant β -sheet folding behavior represented by an amide I maximum at 1627 cm^{-1} ; while $[\text{ALV}]_5[\text{KGE}]_2$ showed an amide I maxima at 1626 cm^{-1} and a mixed signal between 1665 cm^{-1} , and 1693 cm^{-1} corresponding to a mix of β -sheet and β -turn folding behavior^[55].

To identify the influence of secondary structure both on morphology and equilibrium behavior of the assemblies we synthesized the racemically randomized peptides $r[\text{ALV}]_3[\text{KGE}]_4$ and $r[\text{ALV}]_5[\text{KGE}]_2$. Both could be dispersed by direct dissolution. Similar to $[\text{ALV}]_3[\text{KGE}]_4$, $r[\text{ALV}]_3[\text{KGE}]_4$ quickly formed a slightly viscous, transparent solution. However, where the optically pure $[\text{ALV}]_3[\text{KGE}]_4$ formed well-defined nanotubes, cryoTEM analysis showed virtually no self-assembly for $r[\text{ALV}]_3[\text{KGE}]_4$ (Fig. A6.1b), with exception of some small populations of cylindrical shaped micelles (Fig. A6.4). After *in-microscope* freeze drying large amounts of micrometer-sized polymer sheets were observed (Fig. A6.2c-d), that were not observed previously by cryoTEM or by dispersion turbidity. This indicates they were formed during freeze-drying and that most of the peptide was present in solution as unimers. For FTIR of $r[\text{ALV}]_3[\text{KGE}]_4$ (Fig. 6.1f; A6.5) the amide I maximum was observed at 1642 cm^{-1} corresponding to disordered folding behavior, similar to that observed for $[\text{ALV}]_2[\text{KGE}]_5$.

The more hydrophobic sequence $r[\text{ALV}]_5[\text{KGE}]_2$ required multiple hours of stirring to obtain a transparent solution, but in contrast to the optically pure $[\text{ALV}]_5[\text{KGE}]_2$, it could still be dispersed by direct dissolution. $r[\text{ALV}]_5[\text{KGE}]_2$ showed the formation of disordered curved cylindrical shaped micelles with a diameter of $7 \pm 1\text{ nm}$ (Fig. 6.1c). No internal cavities could be observed by cryoTEM, suggesting that cylindrical micelles are formed instead of nanotubes. This is supported by the measured decrease in diameter from 9 to 7 nm compared to $[\text{ALV}]_5[\text{KGE}]_2$ (Fig. A6.6). This diameter is reasonable for cylindrical micelles formation based hydrophobic sequence length (section A6.2). FTIR (Fig. 6.1h; A6.5) showed an amide I maximum at 1627 cm^{-1} with a broad shoulder towards the higher wavenumbers.^[55] This suggests a combination of β -sheet and disordered folding behavior after self-assembly, and hence that β -sheet formation is an important stabilizing factor for the nanotubes.

The observation that these two racemic systems behave distinctly different from their optically active counterparts strongly suggests that the rigid β -sheet core folding is responsible for directing the nanotube structure in $[\text{ALV}]_3[\text{KGE}]_4$, $[\text{ALV}]_3[\text{KGE}]_5$, $[\text{ALV}]_4[\text{KGE}]_3$ and $[\text{ALV}]_5[\text{KGE}]_2$. At the same time β -sheet formation reduces the solubility of $[\text{ALV}]_5[\text{KGE}]_2$ compared to $r[\text{ALV}]_5[\text{KGE}]_2$ such that direct dissolution is not possible, and also unimer exchange is disfavoured.⁴⁴

The above results stress the fine balance in composition required for the formation of equilibrium nanotube structures in water in the $[\text{ALV}]_3[\text{KGE}]_4$ system, making this peptide system an ideal candidate for studying the stability and responsive behavior of peptide aggregates.

6.3. Thermal Stability and Thermodynamic Control

To investigate if the $[\text{ALV}]_3[\text{KGE}]_4$ nanotubes are in equilibrium with the solution we performed controlled heating and cooling (thermal annealing) experiments monitoring structure formation with static light scattering (SLS) measurements. CryoTEM studies at room temperature before and after thermal annealing and for a reheated part of the sample to $58\text{ }^\circ\text{C}$ (equipment limit) during vitrification were used to provide further insight into the system behavior.

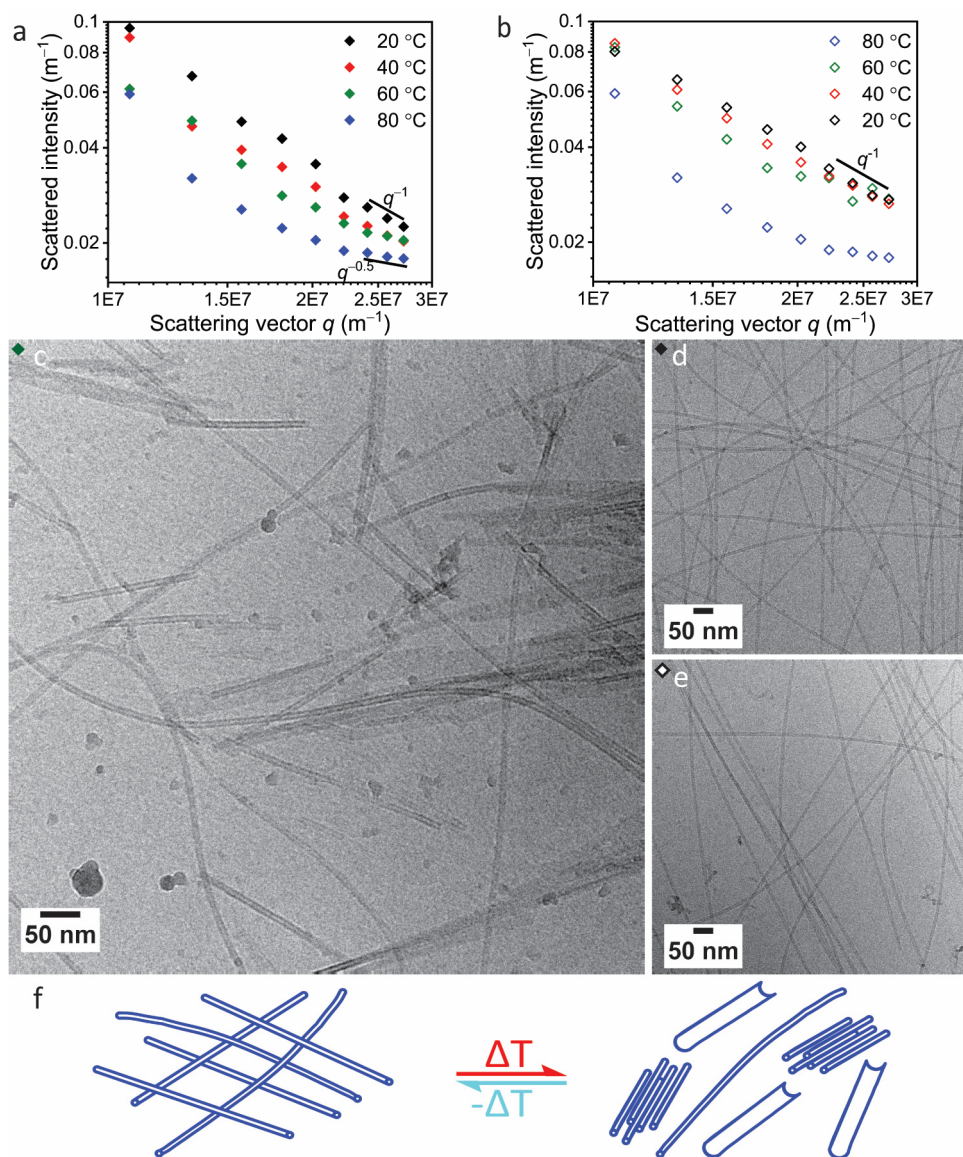


Figure 6.3 SLS results for $[\text{ALV}]_3[\text{KGE}]_4$ at 0.5 mg mL^{-1} in pH 4 buffer collected at 20, 40, 60 and 80 °C, during heating (a) and cooling (b). CryoTEM of $[\text{ALV}]_3[\text{KGE}]_4$ heated to 58 °C during vitrification (c), before heating (d) and after the SLS heating procedure (e). Scheme of observed species (f) before / after heating (left) and during at ~ 60 °C (right).

During each heating step the total light scattering intensity at 90° was measured to determine the equilibration time. This showed that during every step full system equilibration occurred within 80 s after reaching the target temperature (Fig. A6.7). At room temperature SLS shows that the logarithm of the excess Rayleigh ratio $\log_{10}R(q)$ scales linearly with the logarithm of the scattering vector $\log_{10}q$, with a

slope close to -1 , corresponding to the presence of cylindrical shaped assemblies or nanotubes with a fractal dimension of 1.^[56]

With increasing temperature, the scattering intensity decreased (*Fig. 6.3a*) indicating a progressive decrease in nanotube length with temperature. Simultaneously, we observed an increase in the slope at low q values ($< 2 \cdot 10^7 \text{ m}^{-1}$), indicating a progressive increase in attractive interactions between individual cylinders with increasing temperature. This strongly implies a tendency of the cylinders to form bundles at high temperatures. This trend is observed with a single exception at $60 \text{ }^\circ\text{C}$ at a q -value of $1.1 \cdot 10^7 \text{ m}^{-1}$, likely due to the presence of intermediate aggregates. At $58 \text{ }^\circ\text{C}$ cryoTEM indeed showed the presence of large populations of bundles of relative short nanotubes. These bundles were present alongside a minor population of long ($> 2000 \text{ nm}$) curved nanotubes and some sheet like structures which possibly resulted from the unfolding of nanotubes (*Fig. 6.3c, A6.8*).

In contrast, during gradual cooling from 80 to $20 \text{ }^\circ\text{C}$ the SLS curve (*Fig. 6.3b*) did not show a gradual transition. Instead, the decrease in intensity showed a strong hysteresis, although the curve recorded at $20 \text{ }^\circ\text{C}$ again matched that of the sample before heating, the observed hysteresis suggests that although the nanotubes show fully reversible aggregation behavior, the kinetics of aggregation are different from those of the de-aggregation process^[57, 58]. CryoTEM showed similar long nanotube assemblies both before and after thermal annealing (*Fig. 6.3d,e*), and after thermal annealing unfolded nanotubes were no longer observed. This confirms that the SLS observations are indeed in accord with a fully recovered morphology and suggests that long nanotubes are the thermodynamically favored product^[6].

At elevated temperatures peptide nanotubes tend to morphologically rearrange^[25, 29]. For $[\text{ALV}]_3[\text{KGE}]_4$, both SLS and cryoTEM suggest that the nanotube morphology is conserved even at high temperatures. The decrease in tube length can be explained by a shift in the thermodynamic equilibrium between unimers and assemblies at higher temperatures, and the concomitant dissolution of the unimers from the nanotube ends that have higher surface energies^[59]. The additional formation of bundled structures indicates an increase in interaction between individual nanotubes. This is likely due to thermal dehydration of the hydrogen-bonding groups in the hydrophilic stabilizer blocks, decreasing their solubility and leading to the loss of the hydration layer around the individual nanotubes, making lateral aggregation more favorable. Evidence for dehydration was indeed observed by cryoTEM which showed that at $58 \text{ }^\circ\text{C}$ (*Fig. 6.3c*) the nanotube wall gave a higher contrast compared to RT observations (*Fig. 6.3d,e*). The increase in nanotube wall density is consistent with the expulsion of water from the hydrophilic stabilizer block. Together SLS and cryoTEM suggest $[\text{ALV}]_3[\text{KGE}]_4$ nanotubes show significant temperature stability and form under thermodynamic control.

6.4. pH Responsive Behavior and Hierarchical Assembly

The $[\text{ALV}]_x[\text{KGE}]_y$ peptides are designed with a complementary zwitterionic hydrophilic stabilizer possessing alternating positive and negative charges. This should ensure stability of the assemblies at both low and high pH, where the stabilizer blocks will be positively charged or negatively charged, respectively, while promoting interactions between assemblies at intermediate pH. To investigate nanotube stability over a range of pH values, and to investigate whether pH modulation can activate the formation of higher order species without compromising the underlying nanotube morphology, $[\text{ALV}]_3[\text{KGE}]_4$ was assembled in buffers of pH 2, 6 and 12 (10 mg mL^{-1} , direct dissolution). FTIR showed the formation of dominant β -sheet arrangements in all cases with amide I maxima between $1628\text{--}1624 \text{ cm}^{-1}$ (*Fig. A6.9*), suggesting a core folding similar to β -sheet formation observed at pH 4.

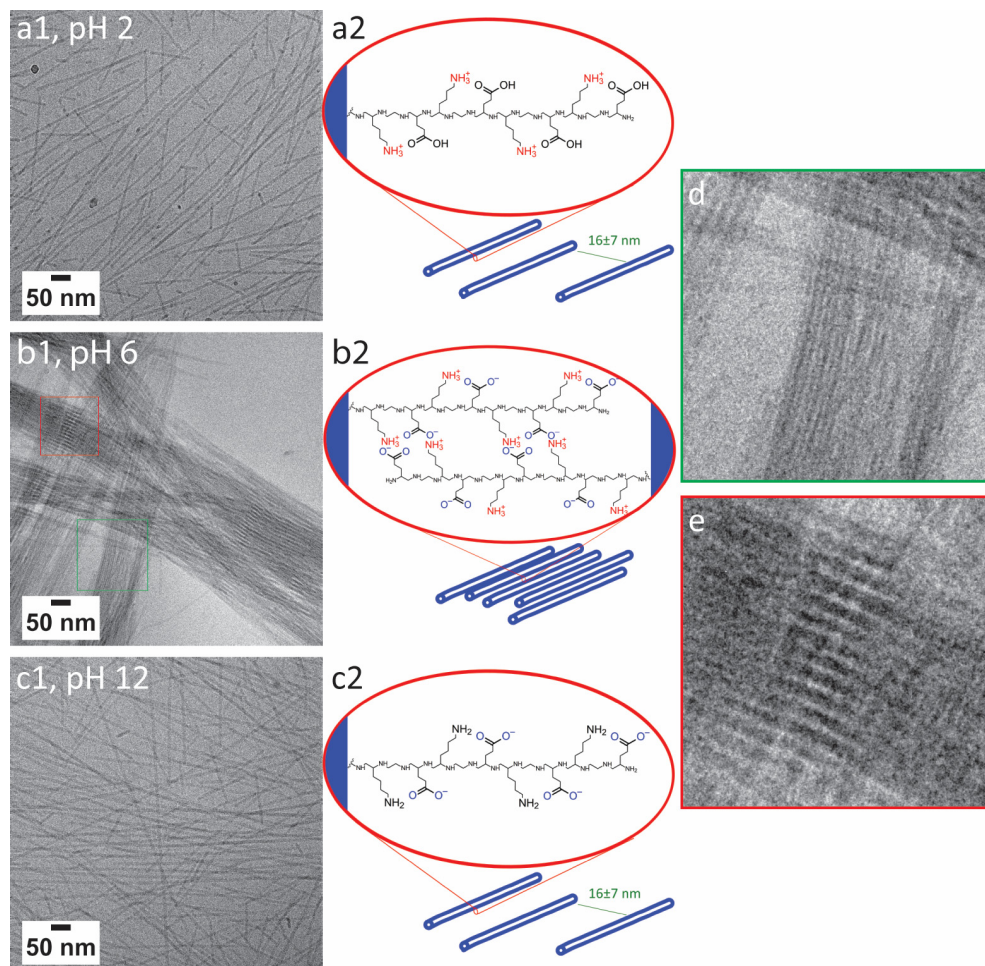


Figure 6.4 CryoTEM images (1) and schemes (2) of $[\text{ALV}]_3[\text{KGE}]_4$ assembled via direct dissolution at 10 mg mL^{-1} in pH 2 (a), 6 (b) and 12 (c) buffer. Zoom-in of b showing the bundled composition out of nanotubes (d) and an organization-induced interference pattern (e).

At both pH 2 and pH 12 (Fig. 6.4a,c) cryoTEM showed the formation of straight dispersed nanotubes with an external diameter of 8 ± 1 and 9 ± 1 nm, respectively, indicating that the nanotube morphology is highly stable over a wide range of pH values. The length of the nanotubes appears to vary with pH (Fig. 6.1a; 6.4b,c), where more significant populations of short nanotubes are present at pH 2 and 12. As the energy difference between long and short nanotubes will be small (aspect ratios > 20) it is likely that the distribution of lengths is determined stochastically by the nanotube nucleation rate, which is likely pH dependent. At pH 6 the system becomes rather viscous and turbid, suggesting the presence of larger assemblies. CryoTEM in combination with cryogenic electron tomography (cryoET) indeed revealed the formation of large fibers of closely packed nanotubes (Fig. 6.4b; A6.11). CryoET specifically confirmed that the fibers are three-dimensional structures composed of individual nanotubes with a diameter of 9 ± 1 nm (Fig. A6.10, section A6.1.3). Although the resolution of the reconstructions was not sufficient to observe

the inner cavity of the nanotubes, their hollow nature could be confirmed from cryoTEM images (*Fig. 6.4d; A6.11*). The conservation of the nanotube morphology shows that the β -sheet secondary structure provides strong enough intermolecular interactions that are not affected by the changed charge behavior of the hydrophilic stabilizer block. Most fibers were relatively thin (composed of < 30 nanotubes per fiber) yet highly ordered as observed as interference patterns in cryoTEM (*Fig. 6.4e*). We propose that this order originates from the attractive forces between neighboring nanotubes that in combination with steric interactions induce their parallel alignment.

To substantiate this proposition, we consider the pK_a s of the amino acids constituting the hydrophilic stabilizer blocks. Glutamic acid and lysine have pK_a s of 4.25 and 10.53, respectively^[60]. At pH 6 both are expected to be charged, leading to zwitterionic peptide chains with strong mutual interactions. Diluting fibers formed at 10 mg mL^{-1} at pH 4 to 5 mg mL^{-1} at pH 6 results in the formation of high density nanotube patches in which nanotube alignment is preserved despite the dilution (*Fig. A6.12a,b*). Note that: only dispersed nanotubes are observed when samples are prepared at 1 mg mL^{-1} (*section A6.1.2*). However, when increasing the pH from 6 to 8, to a regime in which the lysine groups start to be deprotonated the alignment is lost and the fibers reorganize to form dispersed nanotubes, similar to those prepared directly at pH 8 (*section A6.1.2*, *Fig. A6.12c*). Consequently, sequences for which glutamic acid was replaced with lysine or vice versa should show dispersed fibers at pH 6; this was indeed confirmed by cryoTEM (*Fig. A6.13*).

Hence, fiber formation appears to be controlled by electrostatic interactions between the hydrophilic stabilizer blocks. At pH 6 these will be in a zwitterionic state, allowing their interdigitation as proposed by Chen et al.^[18] Indeed, cryoET shows that within the fibers the inter-nanotube distance is $2.5 \pm 0.8 \text{ nm}$, which is significantly shorter than the length of a fully extended hydrophilic stabilizer sequence (4.4 nm), and supports the proposed interdigitation of the hydrophilic sequences as the driving force for fiber formation.

6.5. Conclusion

Controlling thermodynamics and kinetics of molecular self-assembly to design objects with pre-designed morphology and hierarchical structure is a key challenge for the creation of soft and complex materials. Here, we achieved this by the variation of the number and type of the amino acids in the hydrophilic and hydrophobic blocks of a block co-poly peptide. We demonstrated that by composing the appropriate hydrophobic core and hydrophilic stabilizer blocks we can create well-defined and thermodynamically stable nanotubes that can reversibly assemble into fibers as a function of pH.

Varying the amino acid composition of the different blocks allowed us – beyond tuning the hydrophobic/hydrophilic balance - to modulate two parameters that were key to the assembly of these hierarchical structures: 1) The introduction of secondary structure (β -sheets) in the hydrophobic block, that provides the nanotubes with the required stability under different self-assembly conditions, 2) The reversible introduction of a zwitterionic regime in the hydrophilic blocks that allowed to direct the inter-nanotube interactions through pH variation.

Importantly, the thermodynamic stability of the nanotube morphology is a key factor in their uniform formation, which, together with their high aspect ratios make this system an ideal candidate for further investigation as a peptide hydrogel system.^[52] Moreover, we anticipate that our approach can be used to design and control the thermodynamics, kinetics and morphology of peptide based assemblies for a range of applications notably as templates for “ZnO” mineralization.

6.6. Materials and Methods

6.6.1. Materials

Acetic acid (99-100%, GPR reagent) was acquired from VWR, potassium chloride (KCl, > 99%, BioXtra), potassium hydroxide (KOH, > 85%, ACS reagent), sodium acetate anhydrous (CH₃COONa, 99%, FCC), sodium hydroxide (NaOH, > 98%, BioXtra) and hydrochloric acid (HCl, 37%, ACS reagent) were acquired from Sigma Aldrich, dimethylsulfoxide (DMSO, > 99.7%, AR) was acquired from Biosolve, potassium dihydrogen phosphate (KH₂PO₄, > 99 %, extra pure) and sodium hydrogen carbonate (NaHCO₃, 99.5%, EMPROVE) were acquired from Merck. All chemicals were used as received unless stated otherwise.

The peptides were synthesized by solid phase peptide synthesis (SPPS) using either a Liberty 1 or a Liberty Blue microwave-assisted automated peptide synthesizer. Peptides were synthesized on either ChemMatrix Rink amide resin (if the Liberty 1 was used) or TentaGel Rink amide resin (if the Liberty Blue was used). Standard Fmoc chemistry was employed, with deprotection facilitated by 20% piperidine in DMF and coupling achieved using either HCTU with DIPEA as base (with the Liberty 1) or DIC with Oxyma as base (Liberty Blue). Peptides were manually acetylated upon completion of synthesis using acetic anhydride and pyridine, before cleavage from the resin was facilitated using a mixture of TFA:TIPS:H₂O (95:2.5:2.5). The cleaved peptide was collected by precipitating into ice-cold diethyl ether, the resulting dispersion was centrifuged and the supernatant was removed. The pellet was resuspended in a mixture of MeCN and H₂O before being freeze-dried.

The pH buffers were prepared as shown in table 6.1.^[61]

Table 6.1 Measured pH and composition of used pH buffers.

pH		M	A	ml	M	B	ml	Salt (mM)
Target	Measured							
2	1.6	0.1	KCl	50	0.1	HCl	13.0	79.4
4	3.9	0.1	Acetic acid	164	0.1	CH ₃ COONa	36.0	72.0
6	5.9	0.1	KH ₂ PO ₄	100	0.1	NaOH	11.6	89.6
8	7.9	0.1	KH ₂ PO ₄	100	0.1	NaOH	93.4	51.7
10	9.8	0.05	NaHCO ₃	100	0.1	NaOH	21.4	41.2
12	12.4	0.2	KCl	50	0.2	NaOH	12.0	161.3

6.6.2. Methods

High-performance liquid chromatography (HPLC) was conducted using a Shimadzu system with two LC-8A pumps and an SPD-10AVP UV-Vis detector. All peptides were purified using a Gemini 3 μm C18 column (150 × 21.2 mm). Peptides were eluted using a gradient of 10-90% B over 30 min at a flow rate of 12 mL min⁻¹, where A is H₂O containing 0.1% TFA, and B is MeCN containing 0.1% TFA. Collected fractions were analyzed using LC-MS and the fractions deemed to be > 95% pure were pooled and freeze-dried.

Liquid chromatography mass spectrometry (LC-MS) was conducted on a Thermo Scientific LC-MS equipped with a Gemini® 3 μm C18 LC column (50 × 4.6 mm). MS and relative abundance measurements were conducted using a TSQ Quantum Access MAX MS chamber.

Self-assembly by direct dissolution (DD) was performed unless stated otherwise. Typically, ≤ 100 μl of pure water or buffer was added directly to the peptide powder, followed by overnight stirring using a

magnetic stirring bar. When mentioned, 50 v% diluted systems were made by adding $\leq 30 \mu\text{l}$ of the assembled peptide system with $\leq 30 \mu\text{l}$ dilutant followed by overnight stirring.

Self-assembly by solvent switch (SS) in DMSO was performed by dissolving peptide powder at 2 times the target concentration in DMSO. Pure water was added dropwise under heavy stirring giving the system time to stabilize. DMSO was removed by dialysis using a ThermoScientific Slide-A-Lyzer® 2 kDa mini dialysis unit.

The pH measurements were conducted using a Mettler Toledo seven compact pH/ion sensor or a Metrohm (6.0234.100) 125 mm pH probe.

Cryogenic transmission electron microscopy (Cryo-TEM) samples were prepared by depositing 3 μl sample on a 200 mesh Cu grids with Quantifoil R 2/2 holey carbon films (Quantifoil Micro Tools GmbH, part of SPT Life Sciences group). An automated vitrification robot (Thermo Fischer Scientific, TFS, Vitrobot Mark III) was used for plunging in liquid ethane. All TEM grids were surface plasma treated for 40 s using a Cressington 208 carbon coater prior to use. Cryo-TEM studies were performed on the TU/e cryoTITAN (TFS) operated at 300 kV, equipped with a field emission gun (FEG), a post-column Gatan Energy Filter (model 2002) and a post-GIF 2k \times 2k Gatan CCD camera (model 794).

Freeze-drying is performed to confirm the presence of peptide on the grid, if no structures are observed during cryoTEM. Either these structures are removed during blotting or the peptides are present in unimer form. During freeze-drying, present peptides crash out of solution resulting in typically dense fibrous networks or sheets that can be observed by TEM. Freeze-drying is conducted in-microscope by gradually heating the samples on the grid in the autoloader to room temperature conditions overnight.

TEM image size analysis have been conducted using an in-house Matlab script. Rod diameters are estimated based on ideally 60 measurements from three representative micrographs (3 \times 20). Clearly distinguishable cross sections are selected and measured at random. Where possible separate assemblies are measured targeting local maxima and minima. The interspacing distance of aligned rods determined, by averaging the distances between the lowest intensity of the typical nanotube W-shape from intensity line plots gathered from at least three representative micrographs. The lengths of directional rods are estimated based on 10 end-to-end length measurements from a single representative micrograph. A length of > 2000 or > 1000 nm is indicated if respectively no rod end or a single rod end is typically observed.

Cryogenic electron energy loss spectroscopy (Cryo-EELS) was conducted on the TU/e cryoTITAN in EELS mode at 390 eV with a 20 eV slit. The carbon layer of the TEM grid was avoided where possible. Spectra were collected between 3 s and 10 s. Beam damage was investigated by taking an image before and after EELS. EELS is used to identify present elements by looking at the loss energy of registered electrons. For nitrogen, which is only present in the Ac-(ALV)_x-b-(KGE)_y-NH₂ peptides the K loss edge is at 401 eV.

Cryogenic tomography series were collected between $\pm 66^\circ$ using 3° increments, with a total electron dose below $60 \text{ e}^- \text{ \AA}^{-2}$. Tilt series acquisition was performed with Inspect3D software (TFS). Alignment and reconstruction of the series were carried out using IMOD software^[62, 63].

Attenuated total reflectance Fourier transform infrared spectroscopy (ATR-FTIR) measurements were conducted on a Varian 670-IR spectrometer using golden gate MCT setup taking 100 scans with a resolution of either 2 or 4 cm^{-1} between 4000 and 650 cm^{-1} . A 2 μl sample droplet was placed over the crystal without closing the golden gate. The environmental signals were deconvoluted from the peptide signals by subtracting a reference measurement.

Small angle x-ray scattering (SAXS) measurements were performed on a SAXSLAB GANESHA 300 XL SAXS system equipped with a GeniX 3D Cu Ultra Low Divergence micro focus sealed tube source producing X-rays with a wavelength of $\lambda = 1.54 \text{ \AA}$ at a flux of 10^8 photons s^{-1} . The instrument was equipped with a Pilatus 300 K silicon pixel detector. Two configurations with sample-to-detector distance of 713 mm and 1513 mm, respectively, have been used to access a q -range of $0.015 \leq q \leq 0.447 \text{ \AA}^{-1}$ and $0.007 \leq q \leq$

0.212 Å⁻¹, with wave vector $q = 4\pi(\sin \theta/2)/\lambda$. Each sample was measured for 2 hours in each configuration. Silver behenate was used for calibration of the beam center and the q range. Samples were placed in 2 mm quartz capillaries (Hilgenberg, Germany).

The two-dimensional SAXS patterns were brought to an absolute intensity scale using the calibrated detector response function, known sample-to-detector distance, measured incident and transmitted beam intensities, and azimuthally averaged to obtain one-dimensional SAXS profiles. The scattering curves of the sample were obtained by subtraction of the scattering contribution of the solvent and quartz capillaries. Data was modelled with SasView 3.1.2 (<http://www.sasview.org/>) using pre-developed form factors for homogeneous^[64], and hollow-cylinders^[65]. The solvent electron length density $\rho_{\text{H}_2\text{O}} = 9.47 \cdot 10^{-6}$ have been determined with the SasView dedicated utility.

Static light scattering (SLS) measurements were performed on an ALV CGS-3 instrument equipped with a 532 nm green laser and an ALV-LSE5004 digital correlator. To minimize excluded volume interactions a freshly prepared sample of [ALV]₃[KGE]₄ self-assembled by direct dissolution at 0.5 mg ml⁻¹ in pH 4 buffer has been used. Based on cryoTEM measurements this low concentration does not influence self-assembly behavior compared to assembly at 5-10 mg ml⁻¹, see *section A6.1.2*. Analysis was conducted using quartz NMR tube between 30 and 150 degrees with angular step of 10 degrees. For each angle three runs of 60 seconds have been performed and were averaged over time to obtain the static values $I(q)_{\text{samp}}$, where $q = 4\pi n_s \sin \theta / \lambda$ is the wave vector (with n_s the refractive index of the solvent, θ is half of the scattering angle and λ is the wavelength of the laser). The same procedure has been followed to measure the static intensities of the pH 4 $I(q)_{\text{solv}}$ buffer and of a toluene standard $I(q)_{\text{st}}$. These values have been used to bring $I(q)_{\text{samp}}$ on absolute scale (the so-called Rayleigh ratio) according to the relation:

$$I(q) = \frac{I(q)_{\text{samp}} - I(q)_{\text{solv}}}{I(q)_{\text{st}}} R_{\text{st}} \frac{n_s^2}{n_{\text{st}}^2} \quad (6.1)$$

Here n_{st} and R_{st} are the refractive index and the Rayleigh ratio of the standard (for toluene at 532 nm $n_{\text{st}} = 1.47$, $R_{\text{st}} = 2.10 \times 10^{-3} \text{ m}^{-1}$). The measurements were repeated at different temperatures from 20 °C to 80 °C and back to 20 °C with a temperature step of 20 °C.

Ultraviolet-visible spectroscopy (UV-vis) measurements were conducted on a Jasco V-650 spectrophotometer using quartz cuvettes. The wavelength was probed between 340 nm and 800 nm with a scanning speed of 100 nm/min, a band width of 1 nm and a data interval of 0.5 nm with a medium response time.

6.7. Appendix A6

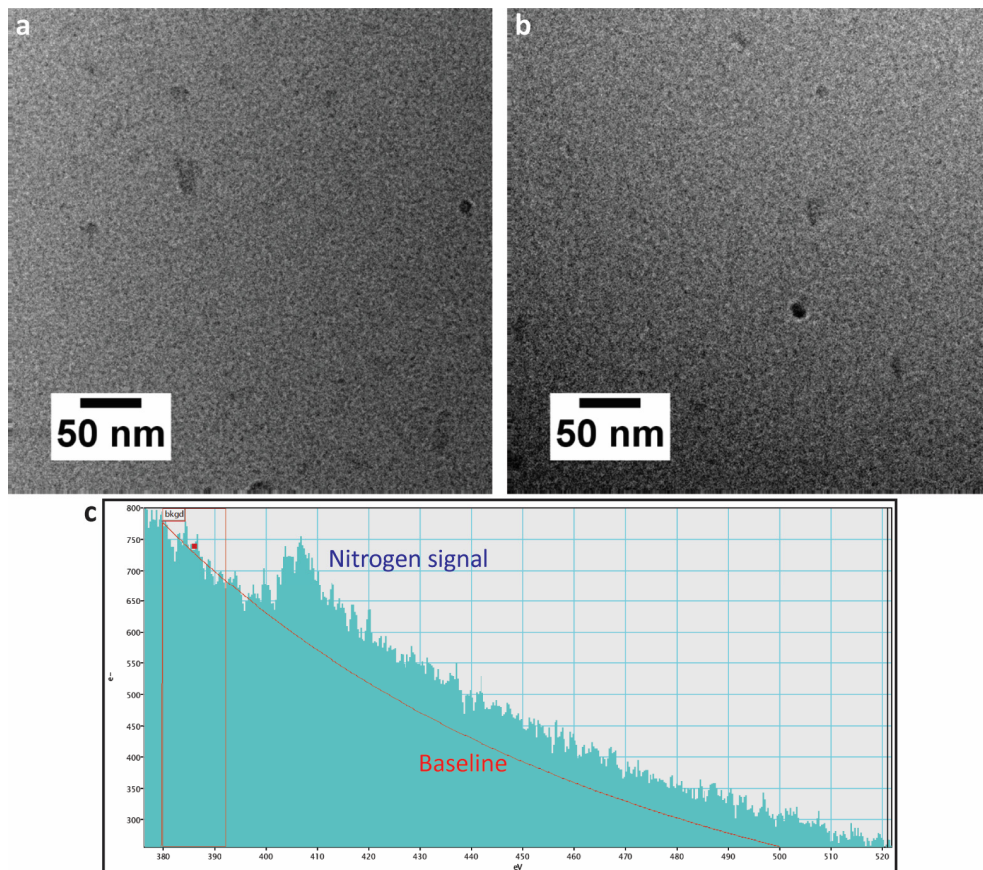


Figure A6.1 CryoTEM images of $[\text{ALV}]_2[\text{KGE}]_5$ (a), $\tau[\text{ALV}]_3[\text{KGE}]_4$ (b) assembled at 5 mg ml^{-1} in pH 4 buffer. Cryo electron energy loss spectroscopy (EELS, c) between 380 and 520 eV of $[\text{ALV}]_2[\text{KGE}]_5$, in a similar region as Fig A6.1a. The signal at $\sim 400 \text{ eV}$ indicates the presence of nitrogen. The only source of nitrogen present in the system is $[\text{ALV}]_2[\text{KGE}]_5$, confirming its presence in the viewing area.

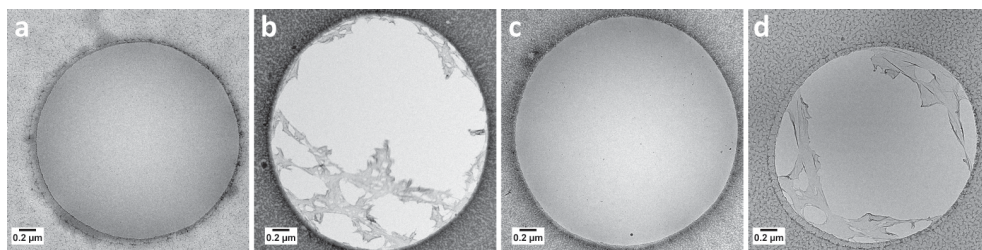


Figure A6.2 CryoTEM (a,c) and post freeze drying images (b,d) of $[\text{ALV}]_2[\text{KGE}]_5$ (a,b) and $r[\text{ALV}]_3[\text{KGE}]_4$ (c,d) assembled in water at 5 mg ml^{-1} . If no self-assembled structures are observed during cryoTEM there are two possibilities. Either these structures are removed during blotting or the peptides are present in unimer form. During freeze-drying present peptides crash out of solution resulting in typically dense fibrous networks or sheets that can be observed by TEM.

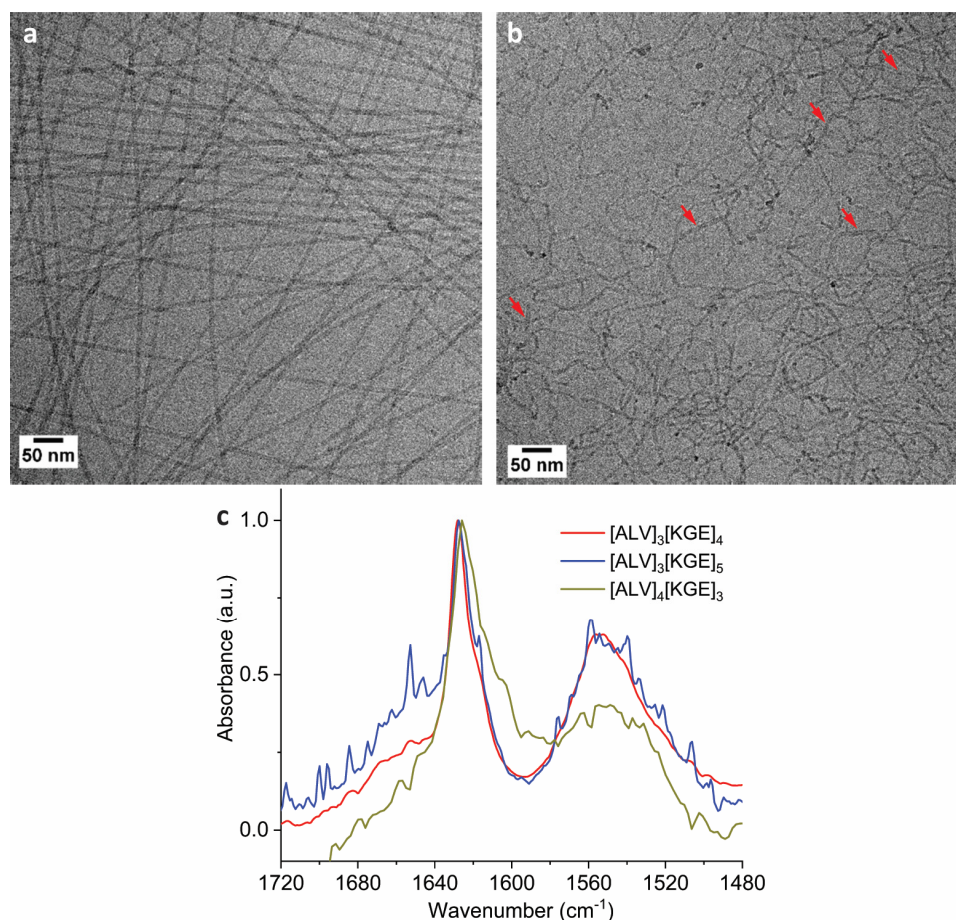


Figure A6.3 CryoTEM image of $[\text{ALV}]_3[\text{KGE}]_5$ (a) nanotubes and $[\text{ALV}]_4[\text{KGE}]_3$ (b) cylindrical shaped micelles and several nanotubes (red arrows) assembled at 5 mg ml^{-1} in pH 4 buffer. Normalized FTIR spectra of $[\text{ALV}]_3[\text{KGE}]_5$, $[\text{ALV}]_3[\text{KGE}]_4$ and $[\text{ALV}]_4[\text{KGE}]_3$ show strong β -sheet formation for all systems.

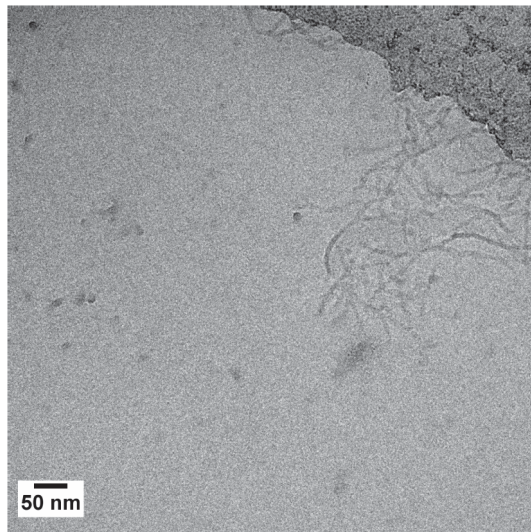


Figure A6.4 CryoTEM image of observed $r[ALV]_5[KGE]_4$ cylindrical micelles assembled at 5 mg ml^{-1} in pH 4 buffer. This is most likely due to strong self-sorting behavior of the racemic peptide sequences.

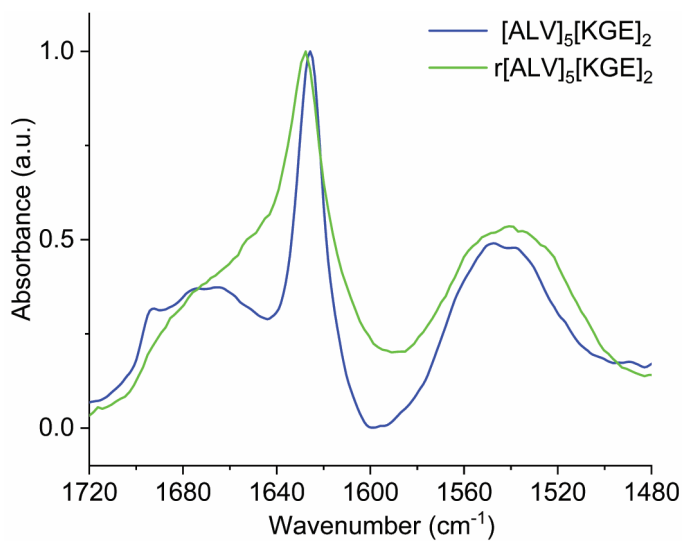


Figure A6.5 Normalized FTIR spectra of $r[ALV]_5[KGE]_2$ and $r[ALV]_5[KGE]_2$.

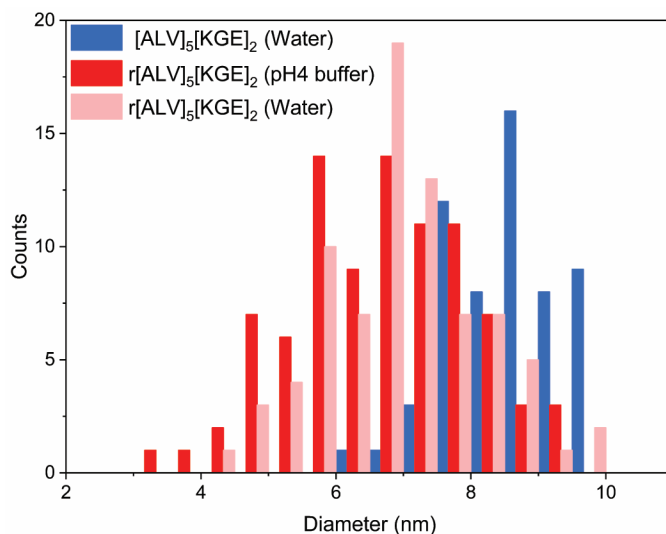


Figure A6.6 Measured diameter of $[\text{ALV}]_5[\text{KGE}]_2$ assembled in pure water by a DMSO solvent switch (Blue) vs $r[\text{ALV}]_5[\text{KGE}]_2$ cylindrical shaped micelles assembled in pure water and pH 4 buffer via direct dissolution (Red).

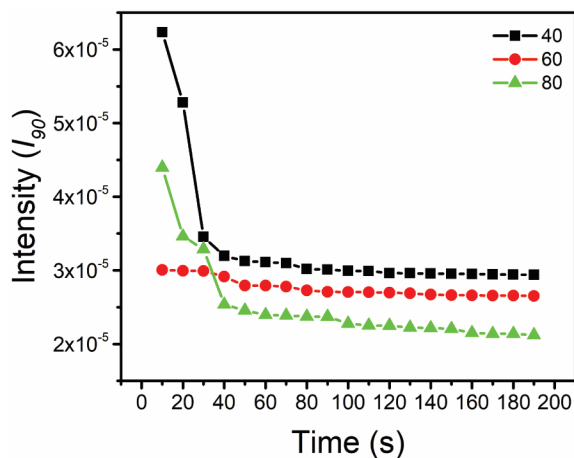


Figure A6.7 Equilibration time with temperature for each SLS heating step (20-40, 40-60 and 60-80 °C), total scattering intensity measured at a set collection angle at 90 °C.

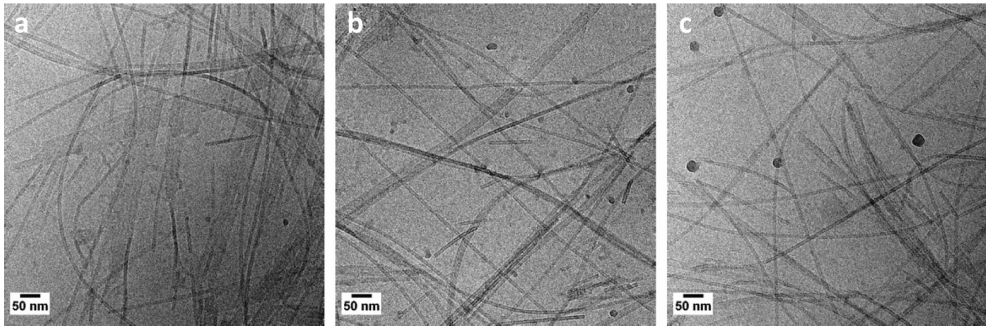


Figure A6.8 CryoTEM images (a-c) of $[\text{ALV}]_3[\text{KGE}]_4$ assembled at 0.5 mg ml^{-1} heated to $58 \text{ }^\circ\text{C}$ during vitrification.

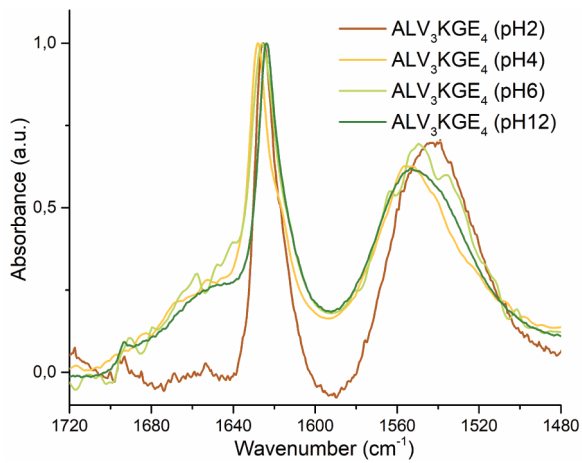


Figure A6.9 Normalized FTIR spectra of $[\text{ALV}]_3[\text{KGE}]_4$ assembled at 10 mg ml^{-1} in pH 2, 4, 6 and 12 buffers via direct dissolution.

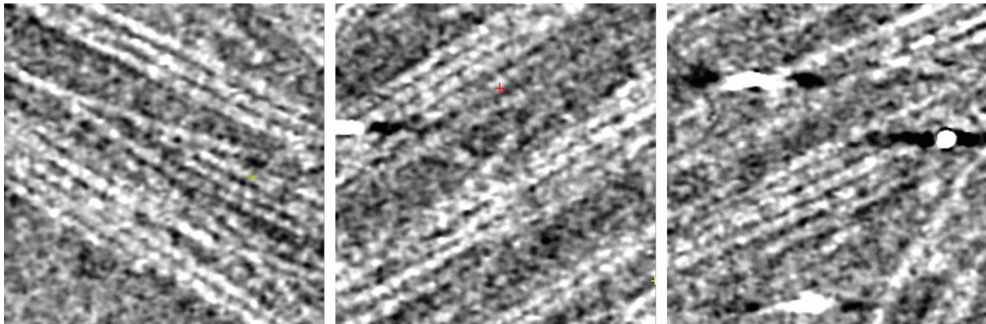


Figure A6.10 Inverted contrast slices from the cryotomography reconstruction data of $[\text{ALV}]_3[\text{KGE}]_4$ assembled via direct dissolution at 10 mg ml^{-1} in pH 6 buffer.

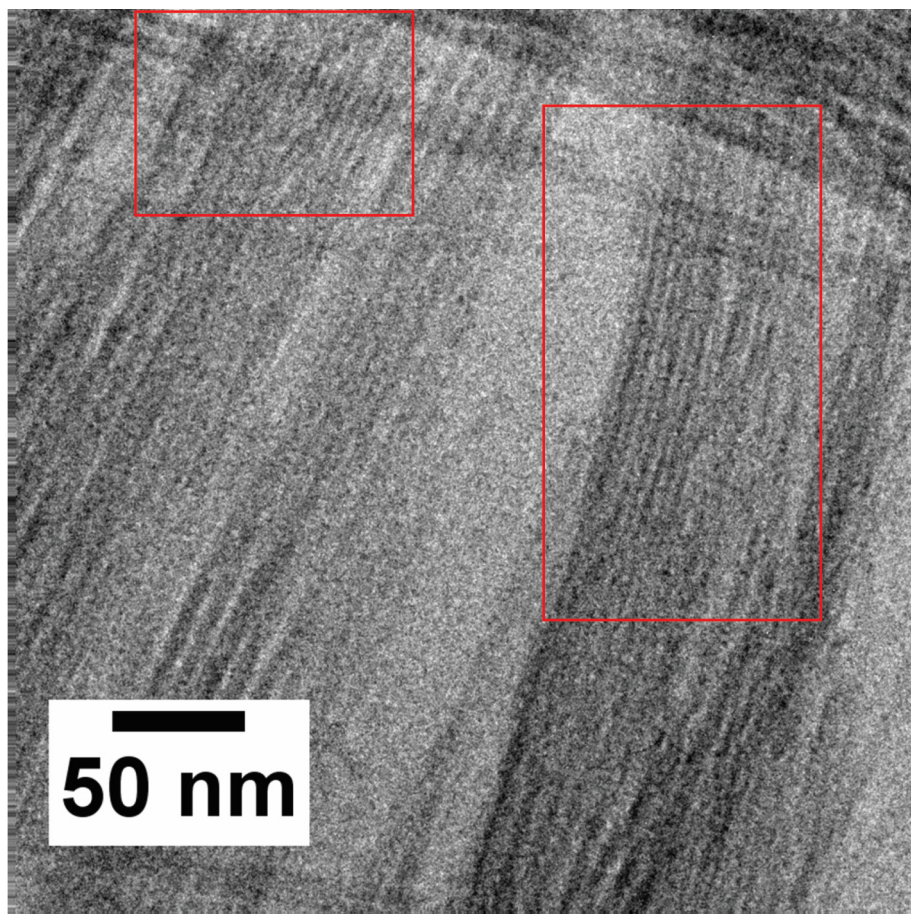


Figure A6.11 Magnified *Fig 6.4d*. Regions showing nanotubes with observable internal cavities are highlighted in red.

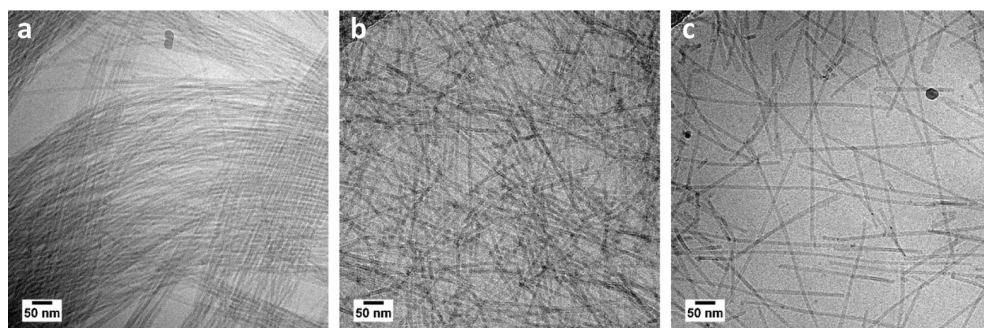


Figure A6.12 CryoTEM images of $[\text{ALV}]_3[\text{KGE}]_4$ assembled at 10 mg ml^{-1} in pH 6 buffer (a), diluted to 5 mg ml^{-1} to pH 6 (b) and diluted to 5 mg ml^{-1} at pH 8 (c).

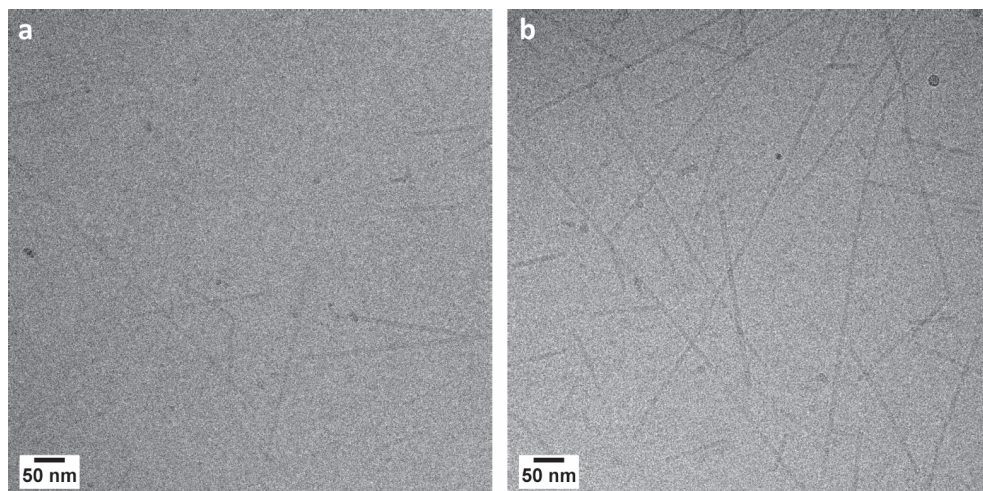


Figure A6.13 CryoTEM images of $[\text{ALV}]_3[\text{KGK}]_4$ (a) and $[\text{ALV}]_3[\text{EGE}]_4$ (b) assembled at 5 mg ml^{-1} in pH 6 buffer.

A6.1. Additional Supporting Information

Additional supporting information can be found online with the original manuscript at: ^[66]
<https://pubs.rsc.org/en/content/articlelanding/2019/sc/c9sc00800d#!divAbstract>

A6.1.1.

This section corresponding with ESI section 3 of the original manuscript.

A6.1.2.

This section corresponding with ESI section 4 of the original manuscript.

A6.1.3.

This section corresponding with both supporting videos of the original manuscript.

A6.2. Observance of Hollow Assemblies by CryoTEM

Most cylindrical structures of $[\text{ALV}]_3[\text{KGE}]_4$ and $[\text{ALV}]_5[\text{KGE}]_2$ imaged by cryoTEM show a lower electron transmission at the edge of the cylinder than in the center. This behavior is typical for hollow structures, strongly suggesting that the cylindrical structures are nanotubes, see *Fig A6.14*. That these typical features for hollow structure are not observed in every assembly and in every cryoTEM image can be explained by three factors; 1) resolution, 2) layer-thickness of the vitrified water and the 3) imaging defocus value.

First, $[\text{ALV}]_3[\text{KGE}]_4$ nanotubes show an outer diameter of 9 nm and an inner diameter, measured in between the points of lowest intensity, of $4.5 \pm 0.4 \text{ nm}$. Under our standard imaging conditions, the pixel size is 0.39 nm. This means that the inner diameter spans 10 - 11 pixels. This minimal number of pixels for the nanotube interior can make it hard to distinguish the wall from the nanotube center. Secondly, in cryoTEM imaging of organic assemblies, contrast is mainly generated due to difference in mean inner potential between the object electron path and the electron path of its surrounding. In cryoTEM vitrified water surrounds the sample on all sides, with vitrified water layers ranging from a couple of nanometers to over a micrometer in thickness. For a nanotube assembly this means that the observed difference in the core and wall contrast would be generated by: the contrast from the wall thickness + the interior water layer + the exterior water layer versus the contrast from the core thickness + the exterior water layer. With the difference in diameter thickness between the peptide nanotube core and the wall of just close to 3 nm the interaction between the electron beam and a thick (200 nm +) vitrified water layers will be dominant. This makes the contrast difference between the peptide nanotube core and the wall difficult to

detect. Thirdly, in TEM the resolution and phase contrast are inversely related depending on the defocus. It was found that at our standard imaging conditions a defocus of close to $-4 \mu\text{m}$ is optimal to observe most features. Below this defocus range the loss in contrast due to filtering by contrast transfer makes it harder to distinguish function the assemblies from the environment. Above this defocus value, too much resolution is lost to distinguish between the nanotube core and wall. Because the nanotubes are not perfectly aligned to the grid and multiple layers of nanotubes can be present, therefore, a difference in height between different nanotubes and segments of individual nanotubes. Although minimal, this difference in height may influence the effective defocus value resulting in the observation of hollow behavior in some nanotubes and regions while not in others.

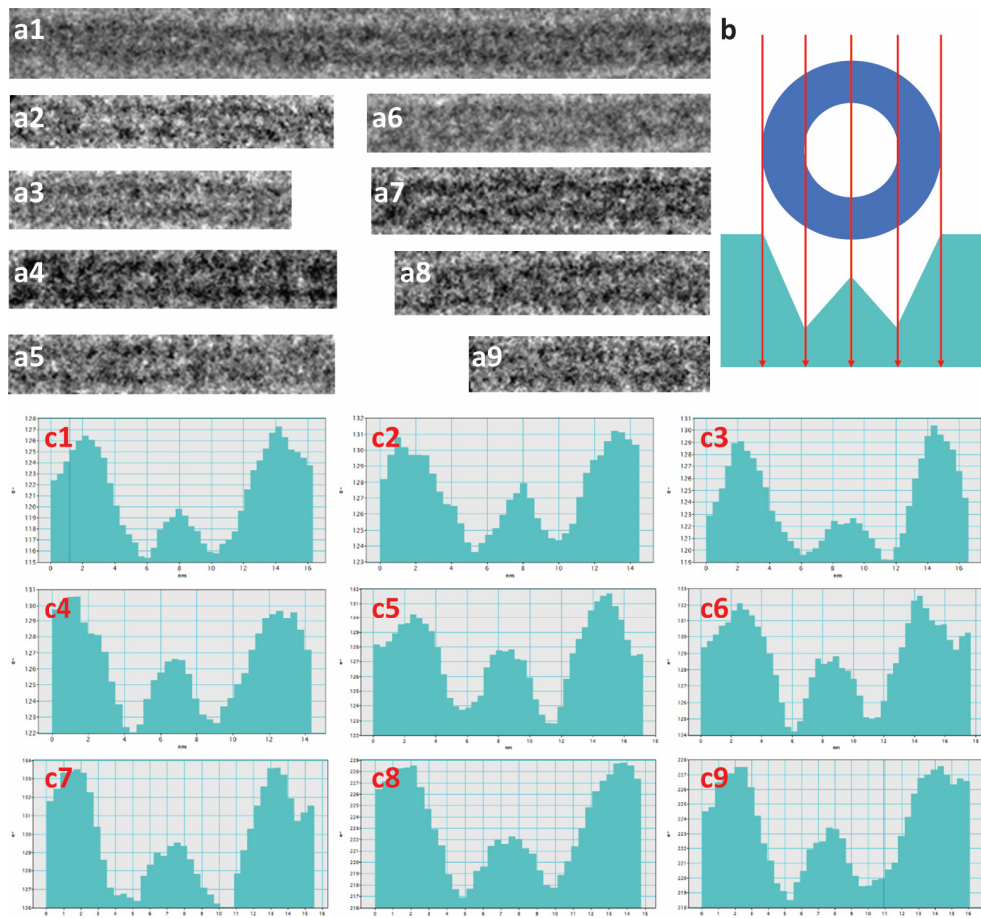


Figure A6.14 Selected cryoTEM nanotubes from several different $[\text{ALV}]_3[\text{KGE}]_4$ samples assembled by direct dissolution in pH 4 buffer (a1-a9). A schematic of the cross-section and the corresponding transmission signal of a hollow cylindrical object. The line plots, over a length of at least 58.5 nm, of the shown $[\text{ALV}]_3[\text{KGE}]_4$ nanotubes (c1 – c9).

A6.2.1. Peptide Molecular Configuration

In their native extended state amino acid repeats have a length of $\sim 3.5 \text{ nm}$ ^[67]. This means that the length of a single KGE or ALV repeat is equal to $\sim 1.05 \text{ nm}$. With two C-C bonds ($\text{C-C} = 1.53 \text{ \AA}$)^[60] the length of

the extended acetate core block is estimated at roughly 3.0 Å. This is an overestimation as it does not take the bond angles nor the presence of half a bond length in the final amino acid repeat into account. On the same bases the amide stabilizer block ending is estimated at 1.5 Å (C-N = 1.46 Å)⁶⁰. Using these chosen values the core, stabilizer and full sequence length of the investigated BCPP can be calculated, *table A6.1*. Based on these calculations the maximum diameter of a rod comprising out of two fully extended hydrophobic [ALV]_x blocks is 6.9, 6.9 and 11.1 nm for [ALV]₃[KGE]₄, [ALV]₃[KGE]₅ and [ALV]₅[KGE]₂, respectively. The measured diameter of the assemblies of all these peptides in cryoTEM are 9 ± 1 nm. This means that the peptide core block of both [ALV]₃[KGE]₄ and [ALV]₃[KGE]₅ is not long enough to assemble into cylindrical micelles. However, they are long enough to assemble in nanotubes with a wall radius of about 2 - 3 nm.

Table A6.1 Formula and calculations for the maximum core, stabilizer and sequence length for [ALV]₃[KGE]₄ and [ALV]₃[KGE]₅.

Maximum length	Formula	[ALV] ₃ [KGE] ₄ (x = 3, y = 4)	[ALV] ₃ [KGE] ₅ (x = 3, y = 5)
Core (nm)	$L_{\text{core}} = 0.30 + x1.05$	3.45	5.55
Stabilizer (nm)	$L_{\text{stabilizer}} = 0.15 + y1.05$	4.35	2.25
Full sequence (nm)	$L_{\text{sequence}} = L_{\text{core}} + L_{\text{stabilizer}}$	7.80	7.80

A6.2.2. Evidence of Nanotube Formation with SAXS

Two different approaches have been followed to analyze the SAXS patterns: form factor modeling and form factor fitting. The first approach (*Fig. A6.15a*) consisted of comparing the experimentally obtained SAXS profiles with the theoretical form factors of a full cylinder having a cross sectional radius of 4.5 nm and the one of a hollow cylinder with an external cross sectional radius of 4.5 nm and an internal radius of 1 nm. In both models the length of the cylinder was set to 400 nm, which is much larger than the larger length scale accessible experimentally. The baseline and the electron length density of the cylinders have been adjusted manually (no fitting procedure involved) to obtain the best agreement of the curves with the experimental data. The same electron length density value has been used for the solid and the hollow cylinders.

The second approach (*Fig. A6.15b*) consisted of fitting the experimental data with the theoretical form factors of full and hollow cylinders respectively. The cylinder length was set as constant (400 nm) while the cross-sectional radius (internal and external in the case of the hollow cylinder), the background and the electron length density of the cylinders have been used as fitting parameters. Cross-sectional Gaussian polydispersity is accounted for in the fitting, with a polydispersity value of 0.08 in both cases. The best fitting was obtained with the form factor of a solid cylinder having cross sectional radius of 4.7 nm and with the form factor of a hollow cylinder having an external cross-sectional radius of 4.5 nm and internal radius of 1 nm.

As expected, the main differences between the solid and the hollow models can be observed in the q range associated with typical length scales which are comparable to the cylinder thickness ($0.08 \leq q \leq 0.2 \text{ \AA}^{-1}$ in our case). At lower q values (larger length scales) both models follow the classical scaling power law associated with cylindrical objects $I \sim q^{-1}$. The deviation of the experimental data from the theoretical curves at low q might be related with the contribution of the form factor, and is indicative for the presence of repulsive interactions between the cylinders, which might be caused by presence of charge groups at the sides of the cylinders.

In both applied procedures the best agreement with the experimental results was obtained with the hollow cylinder model (*Fig. A6.15*). Furthermore, the typical sizes obtained by fitting the data with this model are in good agreement with the ones derived from the cryoTEM analysis. Hence the SAXS analysis confirms that the cylinders are hollow.

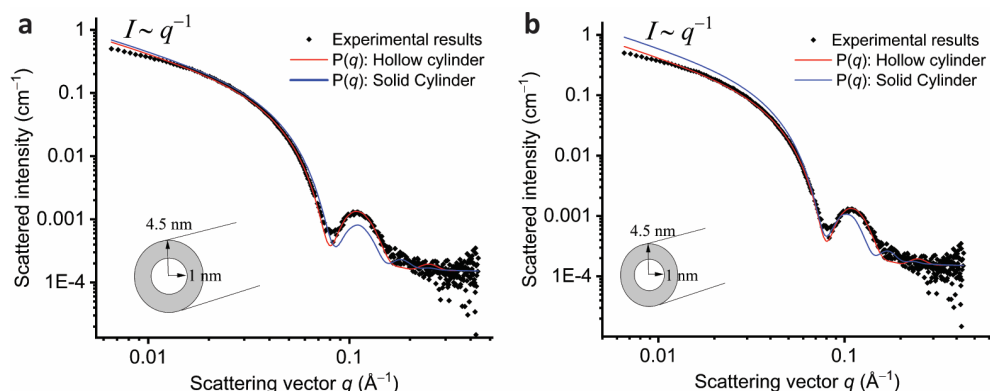


Figure A6.15 Analysis of the SAXS profiles performed via a) form factor modeling and b) form factor fitting.

A6.3. Dynamic Self-assembly

To prove unimer exchange between the assemblies and solution, $[\text{ALV}]_3[\text{KGE}]_4$ was assembled in a pH 4 buffer at 1 mg ml^{-1} by direct dissolution. The resulting slightly viscous transparent liquid was dialyzed (10 kDa membrane) for 72 h against 900 ml of the pH 4 buffer. Pre-dialysis cryoTEM confirmed self-assembly into nanotubes (Fig. A6.16a). UV-vis analysis (Fig. A6.16b) conducted against a pH 4 buffer background, pre-dialysis, showed an absorption maxima at 203 nm of 1.93 Abs, identified as the amide group in $[\text{ALV}]_3[\text{KGE}]_4$. Post-dialysis UV-vis analysis showed an absorption maxima at 197 nm of 0.25 Abs, indicating a signal decrease of 87% ($1 - (0.25 - 1.93) \times 100$). During dialysis the sample volume inside the membrane increased from 0.98 g to 1.19 g, indicating a dilution of only 22% ($= (1.19/0.98) \times 100 - 100$), which is significantly lower than the observed decrease in absorbance. Therefore, the strong decrease in observed absorbance of the UV maxima suggests a significant decrease in $[\text{ALV}]_3[\text{KGE}]_4$ peptide concentration after dialysis. The 10 kDa pores (2.5 nm in diameter) are too small to fit assemblies with a diameter of 9 nm. However, a single $[\text{ALV}]_3[\text{KGE}]_4$ molecule would easily transfer through the membrane, suggesting that $[\text{ALV}]_3[\text{KGE}]_4$ can exchange unimers in water.

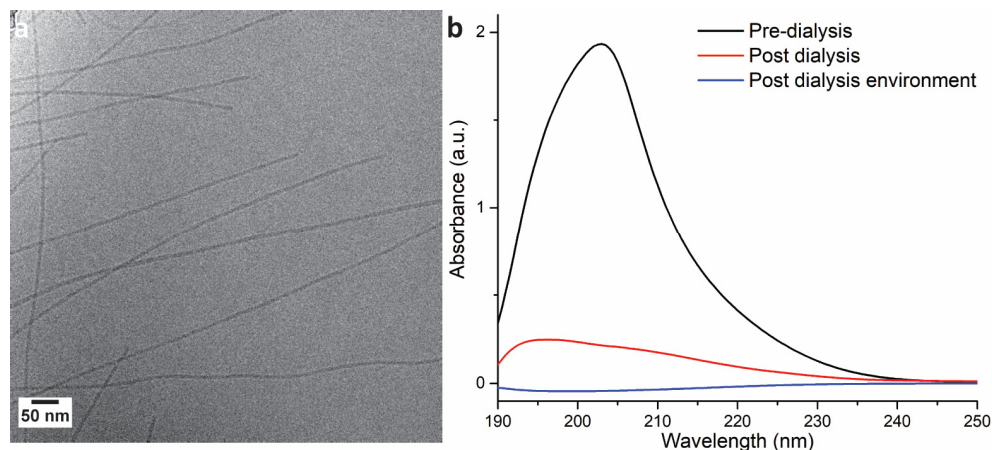


Figure A6.16 CryoTEM image of $[\text{ALV}]_3[\text{KGE}]_4$ at 1 mg ml^{-1} assembled by DD before dialysis (a) and the measured UV spectra (b) of this sample pre-dialysis (black), post dialysis (red) and the outer membrane environment post-dialysis (Blue).

6.8. References

1. E. De Santis and M. G. Ryadnov, Peptide Self-assembly for Nanomaterials: the Old New Kid on the Block. *Chem Soc Rev* **44**, 8288-8300 (2015).
2. N. Habibi, N. Kamaly, A. Memic and H. Shafice, Self-assembled Peptide-based Nanostructures: Smart Nanomaterials Toward Targeted Drug Delivery. *Nano Today* **11**, 41-60 (2016).
3. J. Wang, K. Liu, R. Xing and X. Yan, Peptide self-assembly: thermodynamics and kinetics. *Chem Soc Rev* **45**, 5589-5604 (2016).
4. M. T. Jeena, L. Palanikumar, E. M. Go, I. Kim, M. G. Kang, S. Lee, S. Park, H. Choi, C. Kim, S.-M. Jin, S. C. Bae, H. W. Rhee, E. Lee, S. K. Kwak and J.-H. Ryu, Mitochondria localization induced self-assembly of peptide amphiphiles for cellular dysfunction. *Nat Commun* **8**, 26 (2017).
5. B. S. Lee, A. T. Yip, A. V. Thach, A. R. Rodriguez, T. J. Deming and D. T. Kamei, The Targeted Delivery of Doxorubicin with Transferrin-conjugated Block Copolyptide Vesicles. *Int J Pharm* **496**, 903-911 (2015).
6. F. Tantakitti, J. Boekhoven, X. Wang, R. V. Kazantsev, T. Yu, J. Li, E. Zhuang, R. Zandi, J. H. Ortony, C. J. Newcomb, L. C. Palmer, G. S. Shekhawat, M. O. de la Cruz, G. C. Schatz and S. I. Stupp, Energy Landscapes and Functions of Supramolecular Systems. *Nat Mater* **15**, 469-476 (2016).
7. Z. Fan, L. Sun, Y. Huang, Y. Wang and M. Zhang, Bioinspired Fluorescent Dipeptide Nanoparticles for Targeted Cancer Cell Imaging and Real-time Monitoring of Drug Release. *Nat Nanotech* **11**, 388-394 (2016).
8. C. G. Pappas, R. Shafi, I. R. Sasselli, H. Siccardi, T. Wang, V. Narang, R. Abzalimov, N. Wijerathne and R. V. Ulijn, Dynamic Peptide Libraries for the Discovery of Supramolecular Nanomaterials. *Nat Nanotech*, 1-9 (2016).
9. O. S. Rabotyagova, P. Cebe and D. L. Kaplan, Self-Assembly of Genetically Engineered Spider Silk Block Copolymers. *Biomacromolecules* **10**, 229-236 (2009).
10. K. Sato, W. Ji, L. C. Palmer, B. Weber, M. Barz and S. I. Stupp, Programmable Assembly of Peptide Amphiphile via Noncovalent-to-Covalent Bond Conversion. *J Am Chem Soc* **139**, 8995-9000 (2017).
11. H. G. Cui, M. J. Webber and S. I. Stupp, Self-Assembly of Peptide Amphiphiles: From Molecules to Nanostructures to Biomaterials. *Biopolymers* **94**, 1-18 (2010).
12. E. P. Holowka, V. Z. Sun, D. T. Kamei and T. J. Deming, Polyarginine Segments in Block Copolypeptides Drive both Vesicular Assembly and Intracellular Delivery. *Nat Mater* **6**, 52-57 (2007).
13. Y. T. Sun, A. L. Wollenberg, T. M. O'Shea, Y. X. Cui, Z. H. Zhou, M. V. Sofroniew and T. J. Deming, Conformation-Directed Formation of Self-Healing Diblock Copolypeptide Hydrogels via Polyion Complexation. *J Am Chem Soc* **139**, 15114-15121 (2017).
14. J. A. Hanson, Z. Li and T. J. Deming, Nonionic Block Copolypeptide Micelles Containing a Hydrophobic Rac -Leucine Core. *Macromolecules* **43**, 6268-6269 (2010).
15. T. A. T. Lee, A. Cooper, R. P. Apkarian and V. P. Conticello, Thermo-reversible Self-assembly of Nanoparticles Derived from Elastin-mimetic Polypeptides. *Adv Mater* **12**, 1105-1110 (2000).
16. M. R. Dreher, A. J. Simnick, K. Fischer, R. J. Smith, A. Patel, M. Schmidt and A. Chilkoti, Temperature triggered self-assembly of polypeptides into multivalent spherical micelles. *J Am Chem Soc* **130**, 687-694 (2008).
17. D. Pati, S. Das, N. G. Patil, N. Parekh, D. H. Anjum, V. Dhaware, A. V. Ambade and S. Sen Gupta, Tunable Nanocarrier Morphologies from Glycopolypeptide-Based Amphiphilic Biocompatible Star Copolymers and Their Carbohydrate Specific Intracellular Delivery. *Biomacromolecules* **17**, 466-475 (2016).
18. Y. Chen, H. X. Gan and Y. W. Tong, pH-controlled Hierarchical Self-assembly of Peptide Amphiphile. *Macromolecules* **48**, 2647-2653 (2015).
19. J. Rodriguez-Hernandez and S. Lecommandoux, Reversible Inside-out Micellization of pH-responsive and Water-soluble Vesicles Based on Polypeptide Diblock Copolymers. *J Am Chem Soc* **127**, 2026-2027 (2005).
20. M. Ueda, A. Makino, T. Imai, J. Sugiyama and S. Kimura, Transformation of Peptide Nanotubes into a Vesicle via Fusion Driven by Stereo-complex Formation. *Chem Commun* **47**, 3204-3206 (2011).
21. E. G. Bellomo, M. D. Wyrsta, L. Pakstis, D. J. Pochan and T. J. Deming, Stimuli-responsive Polypeptide Vesicles by Conformation-specific Assembly. *Nat Mater* **3**, 244-248 (2004).
22. J. D. Hartgerink, Self-Assembly and Mineralization of Peptide-Amphiphile Nanofibers. *Science* **294**, 1684-1688 (2001).
23. M. Reches and E. Gazit, Casting Metal Nanowires Within Discrete Self-Assembled Peptide Nanotubes. *Science* **300**, 625-627 (2003).
24. Ç. Ç. Cenkler, P. H. H. Bomans, H. Friedrich, B. Dedeoğlu, V. Aviyente, U. Olsson, N. A. J. M. Sommerdijk and S. Bucak, Peptide Nanotube Formation: a Crystal Growth Process. *Soft Matter* **8**, 7463 (2012).
25. L. Ziserman, H. Y. Lee, S. R. Raghavan, A. Mor and D. Danino, Unraveling the Mechanism of Nanotube Formation by Chiral Self-assembly of Amphiphiles. *J Am Chem Soc* **133**, 2511-2517 (2011).
26. C. R. Gao, H. H. Li, Y. Li, S. Kewalramani, L. C. Palmer, V. P. Dravid, S. I. Stupp, M. O. de la Cruz and M. J. Bedzyk, Electrostatic Control of Polymorphism in Charged Amphiphile Assemblies. *J Phys Chem B* **121**, 1623-1628 (2017).
27. N. C. Burgess, T. H. Sharp, F. Thomas, C. W. Wood, A. R. Thomson, N. R. Zaccai, R. L. Brady, L. C. Serpell and D. N. Woolfson, Modular Design of Self-Assembling Peptide-Based Nanotubes. *J Am Chem Soc* **137**, 10554-10562 (2015).
28. Y. Zhao, W. Yang, D. Wang, J. Wang, Z. Li, X. Hu, S. King, S. Rogers, J. R. Lu and H. Xu, Controlling the Diameters of Nanotubes Self-Assembled from Designed Peptide Amphiphiles. *Small* **14**, 1703216 (2018).

29. I. W. Hamley, A. Dehsorkhi, V. Castelletto, S. Fuzeland, D. Atkins, J. Seitsonen and J. Ruokolainen, Reversible Helical Unwinding Transition of a Self-assembling Peptide Amphiphile. *Soft Matter* **9**, 9290-9293 (2013).
30. I. W. Hamley, A. Dehsorkhi and V. Castelletto, Self-assembled Arginine-coated Peptide Nanosheets in Water. *Chem Commun* **49**, 1850-1852 (2013).
31. Y. Xie, Y. Wang, W. Qi, R. Huang, R. Su and Z. He, Reconfigurable Chiral Self-Assembly of Peptides through Control of Terminal Charges. *Small* **13**, 1700999 (2017).
32. S. Mondal, L. Adler-Abramovich, A. Lampel, Y. Bram, S. Lipstman and E. Gazit, Formation of Functional Super-helical Assemblies by Constrained Single Heptad Repeat. *Nat Commun* **6**, 8615 (2015).
33. V. Castelletto, S. Kirkham, I. W. Hamley, R. Kowalczyk, M. Rabe, M. Reza and J. Ruokolainen, Self-Assembly of the Toll-Like Receptor Agonist Macrophage-Activating Lipopeptide MALP-2 and of Its Constituent Peptide. *Biomacromolecules* **17**, 631-640 (2016).
34. M. J. Krysmann, V. Castelletto, J. E. McKendrick, L. A. Clifton, I. W. Hamley, P. J. F. Harris and S. A. King, Self-assembly of Peptide Nanotubes in an Organic Solvent. *Langmuir* **24**, 8158-8162 (2008).
35. V. Castelletto, A. Kaur, R. M. Kowalczyk, I. W. Hamley, M. Reza and J. Ruokolainen, Supramolecular Hydrogel Formation in a Series of Self-Assembling Lipopeptides with Varying Lipid Chain Length. *Biomacromolecules* **18**, 2013-2023 (2017).
36. X. Y. Gao and H. Matsui, Peptide-based Nanotubes and Their Applications in Bionanotechnology. *Adv Mater* **17**, 2037-2050 (2005).
37. C. Sanchez, H. Arribart and M. M. G. Guille, Biomimetism and Bioinspiration as Tools for the Design of Innovative Materials and Systems. *Nat Mater* **4**, 277-288 (2005).
38. H. B. Qiu, Z. M. Hudson, M. A. Winnik and I. Manners, Multidimensional Hierarchical Self-assembly of Amphiphilic Cylindrical Block Comicelles. *Science* **347**, 1329-1332 (2015).
39. X. H. Yan, J. B. Li and H. Möwald, Self-Assembly of Hexagonal Peptide Microtubes and Their Optical Waveguiding. *Adv Mater* **23**, 2796+ (2011).
40. Z. L. Yu, A. Erbas, F. Tantakitti, L. C. Palmer, J. A. Jackman, M. O. de la Cruz, N. J. Cho and S. I. Stupp, Co-assembly of Peptide Amphiphiles and Lipids into Supramolecular Nanostructures Driven by Anion- π Interactions. *J Am Chem Soc* **139**, 7823-7830 (2017).
41. D. B. Wright, J. P. Patterson, N. C. Gianneschi, C. Chassenieux, O. Colombani and R. K. O'Reilly, Blending block copolymer micelles in solution; Obstacles of blending. *Polym Chem-Uk* **7**, 1577-1583 (2016).
42. Y. Yan, J. B. Huang and B. Z. Tang, Kinetic Tapping - a Strategy for Directing the Self-assembly of Unique Functional Nanostructures. *Chem Commun* **52**, 11870-11884 (2016).
43. R. M. da Silva, D. van der Zwaag, L. Albertazzi, S. S. Lee, E. W. Meijer and S. I. Stupp, Super-resolution Microscopy Reveals Structural Diversity in Molecular Exchange among Peptide Amphiphile Nanofibres. *Nat Commun* **7**, 11561 (2016).
44. M. F. J. Mabeoone, A. J. Markvoort, M. Banno, T. Yamaguchi, F. Helmich, Y. Naito, E. Yashima, A. R. A. Palmans and E. W. Meijer, Competing Interactions in Hierarchical Porphyrin Self-Assembly Introduce Robustness in Pathway Complexity. *J Am Chem Soc* **140**, 7810-7819 (2018).
45. G. M. Kim, Y. H. Bae and W. H. Jo, pH-induced Micelle Formation of Poly(histidine-co-phenylalanine)-block-poly(ethylene glycol) in Aqueous Media. *Macromolecular bioscience* **5**, 1118-1124 (2005).
46. R. Freeman, M. Han, Z. Alvarez, J. A. Lewis, J. R. Wester, N. Stephanopoulos, M. T. McClendon, C. Lynsky, J. M. Godbe, H. Sangji, E. Luijten and S. I. Stupp, Reversible Self-assembly of Superstructured Networks. *Science* **362**, 808-813 (2018).
47. T. J. Deming, Polypeptide Hydrogels via a Unique Assembly Mechanism. *Soft Matter* **1**, 28 (2005).
48. V. Dmitrovic, J. J. M. Lenders, H. R. Zope, G. de With, A. Kros and N. A. J. M. Sommerdijk, Library of Random Copolypeptides by Solid Phase Synthesis. *Biomacromolecules* **15**, 3687-3695 (2014).
49. B. E. I. Ramakers, J. C. M. van Hest and D. W. P. M. Löwik, Molecular Tools for the Construction of Peptide-based Materials. *Chem Soc Rev* **43**, 2743-2756 (2014).
50. Y. Shen, J. Maupetit, P. Derreumaux and P. Tufféry, Improved PEP-FOLD Approach for Peptide and Mini-protein Structure Prediction. *J Chem Theory Comput* **10**, 4745-4758 (2014).
51. P. Thevenet, Y. Shen, J. Maupetit, F. Guyon, P. Derreumaux and P. Tuffery, PEP-FOLD: an Updated de Novo Structure Prediction Server for both Linear and Disulfide Bonded Cyclic Peptides. *Nucleic Acids Res* **40**, 288-293 (2012).
52. M. P. Hendricks, K. Sato, L. C. Palmer and S. I. Stupp, Supramolecular Assembly of Peptide Amphiphiles. *Accounts Chem Res* **50**, 2440-2448 (2017).
53. D. B. Wright, J. P. Patterson, N. C. Gianneschi, C. Chassenieux, O. Colombani and R. K. O'Reilly, Blending Block Copolymer Micelles in Solution; Obstacles of Blending. *Polym Chem-Uk* **7**, 1577-1583 (2016).
54. T. Nicolai, O. Colombani and C. Chassenieux, Dynamic Polymeric Micelles versus Frozen Nanoparticles Formed by Block Copolymers. *Soft Matter* **6**, 3111-3118 (2010).
55. J. T. Pelton and L. R. McLean, Spectroscopic Methods for Analysis of Protein Secondary Structure. *Anal Biochem* **277**, 167-176 (2000).
56. J. S. Pedersen and P. Schurtenberger, Scattering Functions of Semiflexible Polymers with and without Excluded Volume Effects. *Macromolecules* **29**, 7602-7612 (1996).
57. J. Wang, K. Liu, R. Xing and X. Yan, Peptide self-assembly: thermodynamics and kinetics. *Chem Soc Rev*, (2016).
58. P. A. Korevaar, C. J. Newcomb, E. W. Meijer and S. I. Stupp, Pathway Selection in Peptide Amphiphile Assembly. *J Am Chem Soc* **136**, 8540-8543 (2014).
59. J. N. Israelachvili, *Intermolecular & Surface Forces*. (Academic Press Limited, ed. 3rd, 1991).

60. G. L. E. Turner, *Crc Handbook of Chemistry and Physics - a Ready-Reference Book of Chemical and Physical Data*, 70th Edition - Weast, R. C., Lide, D. R. *Ann Sci* **48**, 496-497 (1991).
61. R. A. Robinson and R. H. Stokes, *Electrolyte Solutions: Second Revised Edition. Electrolyte Solutions: Second Revised Edition*, (1968).
62. J. R. Kremer, D. N. Mastrorade and J. R. McIntosh, Computer Visualization of Three-dimensional Image Data using IMOD. *J Struct Biol* **116**, 71-76 (1996).
63. D. N. Mastrorade, Dual-axis Tomography: An Approach with Alignment Methods that Preserve Resolution. *J Struct Biol* **120**, 343-352 (1997).
64. A. Guinier and G. Fournet, *Small-Angle Scattering of X-Rays*. (John Wiley and Sons, New York, 1955).
65. L. A. Feigin and D. I. Svergun, *Structure Analysis by Small-Angle X-Ray and Neutron Scattering*. (Plenum Press, New York, 1987).
66. M. M. J. van Rijt, A. Ciaffoni, A. Ianiro, M.-A. Moradi, A. L. Boyle, A. Kros, H. Friedrich, N. A. J. M. Sommerdijk and J. P. Patterson, Designing Stable, Hierarchical Peptide Fibers from Block Co-polypeptide Sequences. *Chem Sci* **10**, 9001-9008 (2019).
67. P. Yurkanis Bruice, Organic Chemistry. *Chem. Eur. J.*, 1263 (2007).

Chapter 7

Exposure of Collagen to Zinc Species

Collagen mineralization has extensively been investigated with hydroxyapatite, silica and iron oxides. To extend the range of inorganic minerals for collagen mineralization, a material with a wide variety in properties like zinc oxide (ZnO) is an interesting choice. ZnO can be readily synthesized under aqueous conditions, yet ZnO formation at low temperature conditions required for collagen mineralization remains a challenge. Therefore, this work explores the exposure of collagen to zinc acetate and layered basic zinc acetate for an extended time at 37 °C, both in presence and absence of charged additives. This shows that extended exposure to these zinc species (> 6 weeks) does not adversely affect the collagen. Although none of the investigated conditions resulted in the mineralization of collagen with zinc species, the use of l-lysine (l-lys) does show promising results. In the presence of l-lys predominantly zinc nanoparticles are observed that may be ideal for collagen mineralization, independent of the zinc starting material. This suggest that further optimalization of the mineralization process in presence of l-lys, or a polymer (> 5 kDA) similar to l-lys, may result in collagen mineralization.

7.1. Collagen Mineralization

Collagen mineralized with hydroxyapatite (HAp) such as found in bone and teeth is one of the most well-known natural hybrid materials^[1]. The interplay between the hierarchical organic collagen template and the inorganic HAp phases is what gives these materials their excellent mechanical properties^[2-4]. *In-vivo* collagen mineralization is aided by a complex range of non-collagenous proteins^[5]. *In vitro*, this process can be imitated by use of charged polymers^[6, 7] like poly aspartic acid (pAsp)^[8, 9] and poly acrylic acid (pAA)^[7, 10] or poly allylamine hydrochloride (pAH)^[11], which are believed to promote collagen mineralization by sufficiently suppressing crystallization in solution^[12]. Utilizing these strategies, collagen has been mineralized with a range of alternative phases including calcium carbonate^[13], yttria-stabilized zirconia^[14], silica and iron oxides^[15].

Given the organic nature of collagen, low reaction temperatures are essential. Collagen mineralization is typically performed at or below 37 °C, with higher temperatures adversely affecting collagen fibers^[16, 17]. Infiltration or mineralization process that require a higher reaction temperature, like the crystallization process from amorphous yttria-stabilized zirconia can result in destruction or removal of the organic collagen phase^[14]. Therefore, to achieve a hybrid collagen material, a mild reaction temperature of ~37 °C is essential.

Zinc oxide (ZnO) is a mineral with a great variety of characteristics including but not limited to piezoelectric^[18, 19], photocatalytic^[20, 21] and antimicrobial^[22] properties. This makes ZnO an interesting choice for collagen mineralization. Although ZnO can be synthesized near ~37 °C, these processes do not yet yield pure ZnO at these mild reaction conditions and can be rather complex for small reaction volumes, see *Ch. 5*. Alternatively, previous work at higher temperature showed that layered basic zinc acetate (LBZA) is formed as a transient phase during the formation of ZnO from Zinc acetate (ZnAc₂), *Ch. 3*^[23]. After the LBZA phase reaches a critical size it is believed to collapse or dissolve, catalyzing the formation of ZnO in the process. Therefore, isolation of LBZA close to its critical size may result in its transition into ZnO at low reaction temperatures.

Hence, this work investigates the mineralization with zinc species by exposing collagen for an extended period to either a ZnAc₂ solution or a LBZA dispersion in presence of pAA or l-lysine (l-lys) to promote mineralization. Although this work does not result in mineralized collagen, there is no indication that these processes adversely affect the collagen. Moreover, the use of l-lys shows promising results, so that the mineralization may be obtained in a more optimized mineralization process.

7.2. Collagen Exposure to Zinc Acetate and Layered Basic Zinc Acetate

In this work two collagen mineralization strategies are explored. For all strategies the reaction is performed three ways, namely, in presence of 12 mM pAA functional groups, in presence of 12 mM l-lys and in absence of additives. Initially, the use of high molecular weight 450 kDa pAA was investigated; however, this resulted in complete phase separation at low pH upon mixing. For this reason, a 5.1 kDa pAA was used instead. After preparation of the reaction solutions they were all matured for > 6 weeks in a 37 °C water bath.

For the first strategy 12.5 mM ZnAc₂, 1 mg mL⁻¹ collagen and the selected additive were mixed. For the second strategy, LBZA was formed by using a titration strategy from *Ch. 4*. Here, 50 mM ZnAc₂ was heated to 80 °C while titrating in 1 M ammonia at 0.02 mL min⁻¹. After 30 minutes part of this reaction solution was added to a mixture of 1 mg mL⁻¹ collagen and the selected additive, so that the LBZA dispersion was diluted 4 times as compared to the added LBZA dispersion. The methods are described in detail in *section 7.5*.

Ideally, for low temperature collagen mineralization a titration-based ZnO synthesis procedure at $\sim 40^\circ\text{C}$ should be used similar as the ones discussed in *Ch. 5*. Unfortunately, due to the smaller reaction scale and current uncertainties for that procedure, this did not prove to be possible. This point is discussed in detail in *section 7.3*.

After maturing the reaction solutions, a white precipitate was obtained under all investigated reaction conditions. Given the absence of stirring during the maturing protocol, the resulting dispersions were composed of a transparent supernatant with a white sediment at the bottom of the reaction flask. Upon shaking the reaction vessel, a homogenous dispersion was obtained. The reaction products were analyzed by conventional TEM on dried samples, indicated as TEM for the remainder of this chapter. This analysis confirmed that assembled collagen fibers were present under all conditions. In none of the cases overhydration, dehydration or disassembly of the collagen fibers was observed.

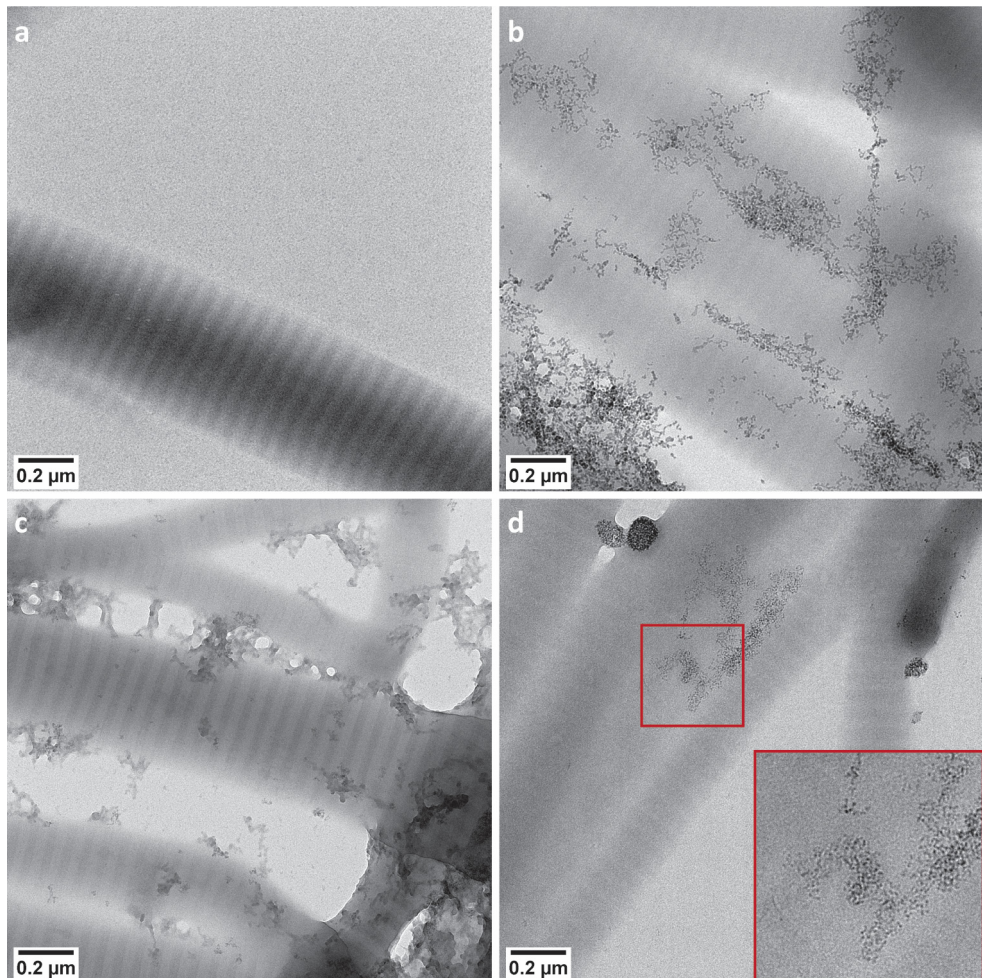


Figure 7.1 Dry TEM images of a collagen fibril dispersed in pure water (a) and of collagen fibrils after exposure to a ZnAc_2 solution for over 6 weeks at 37°C with an initial pH of 6.7 in absence of additives (b), in presence of 12 mM 5.1 kDa pAA (c) and in presence of 12 mM l-Lys (d) dried on a carbon support.

7.2.1. Collagen - Zinc Acetate Interaction

After maturing the collagen - ZnAc_2 solutions, TEM studies on reaction product showed no evidence of interfibrillar crystalline species in any of the collagen fibrils, independent of the reaction composition or starting pH. The results are shown in *Fig. 7.1*, accompanied by a water dispersed collagen reference (*Fig. 7.1a*). Comparing the products it was notable that relatively small non-uniform particles were observed in absence of additives (*Fig. 7.1b*) and in presence of pAA (*Fig. 7.1c*). Using selected area electron diffraction (SAED, not shown), these particles were identified as LBZA. In contrast, when using l-lys, nanoparticles and organized clusters of nanoparticles were observed (*Fig. 7.1d*).

Beside the influence on the products in dispersion, the use of additives seems to show some effect on the collagen fibrils. In particular, when using pAA the interface between the collagen gap and overlap zones seem rather sharp (*Fig. 7.1c*). This is not observed for the collagen reference or for the other reaction conditions (*Fig. 7.1a,b,d*). This might indicate that Zn^{2+} ions are present in the collagen fibrils when using pAA, acting as a stain. However, there is currently no conclusive experimental evidence to support this claim.

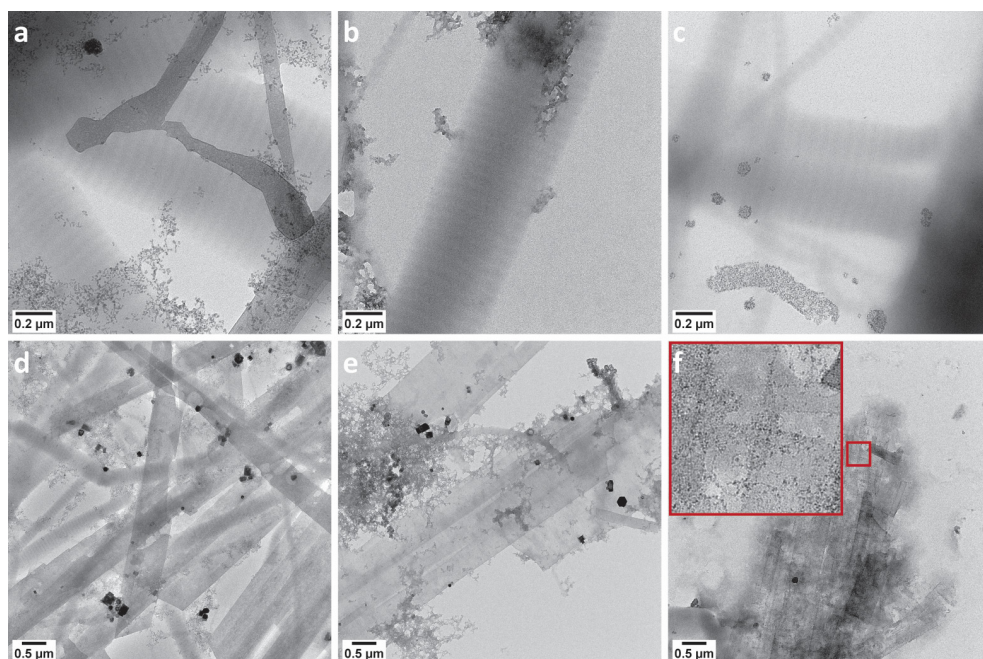


Figure 7.2 TEM images of collagen fibrils (a-c) and a more general sample overview (d-f) after exposure to the initial stages (at 30 min) of a ZnO forming reaction at 80 °C which was subsequently matured for over 6 weeks at 37 °C in absence of additives (a,d), in presence of 12 mM 5.1 kDa PAA (b,e) and in presence of 12 mM l-Lys (c,f) dried on a carbon support.

7.2.2. Collagen - Layered Basic Zinc Acetate Interaction

Similar to the ZnAc_2 reaction show above, mixing a predominantly LBZA phase with collagen did not result in interfibrillar mineralization of collagen (*Fig. 7.2a-c*). In all cases, similar looking collagen fibrils were observed as compared to the water dispersed collagen reference (*Fig. 7.1a*). The resulting extrafibrillar zinc-based reaction products proved to have a rather complex composition and for this reason only the

phases that are dominantly observed throughout the sample are discussed. As reference, previous TEM and cryoTEM sampling (*Ch. 3*) of initial LBZA-rich reaction phases during ZnO synthesis strategies showed the predominant presence of LBZA with some hexagonal ZnO crystals exposing multiple distinct morphologies depending on the present additive^[23]. Performing the collagen maturing procedure in absence of additives or in presence of pAA did indeed predominately result in the observation of large micrometer scale LBZA sheets and some hexagonal crystals, presumably ZnO (*Fig. 7.2d,e*). Besides these products, some relatively small non-uniform particles were observed, similar to those found when using ZnAc₂ in the previous section (*Section 7.3.1*). This suggests that in presence of collagen at 37 °C minimal evolution of the zinc phases seems to take place.

In contrast, when l-lys is added, the predominant zinc phases do change. First, no hexagonal crystals were observed during the TEM study. This suggests that ZnO crystals that were formed during the initial reaction protocol and observed in presence of pAA and in absence of additives may have dissolved or transformed. Moreover, only two major phases, besides collagen, were observed in this system. First, micrometer sized LBZA sheets. However, these sheets look different in TEM compared to typical LBZA sheets as observed for the other reaction conditions. Higher magnification TEM images show that these LBZA sheets are composed out of smaller nanometer-sized particles accompanied by clearly visible defects in the LBZA structure (*Fig. 7.3*). The second phase consists of free and clustered zinc nanoparticles like the ones observed when using ZnAc₂ as zinc source in presence of l-lys.

7.2.3. Discussion on L-lysine to Promote Collagen Mineralization

Both when using ZnAc₂ or LBZA as zinc source in presence of l-lys, nanoparticles were observed in dispersion. Moreover, when starting with LBZA as zinc source, the addition of l-lys seems to result in the deconstruction of the LBZA phase into nanoparticles directly, whereas in absence of l-lys the LBZA phase remained stable. This shows that l-lys has a strong and active role in this process. Although ZnO formation in *Ch. 5* in presence of l-lys is investigated, differences in procedure between this work and the work presented in *Ch. 5* makes it hard to directly compare the results. Therefore, the exact influence of l-lys on these zinc rich solutions and the underlying mechanism remains unclear.

Previous work showed that nanoparticles are an ideal intermediate for collagen mineralization^[8]. This suggests that the use of l-lys promotes the mineralization of collagen with zinc species. It does raise the question, however, why no mineralized collagen can be observed when using l-lys. There are two likely reasons for this. The first is the absence of stirring during most of the reaction. This means that the motion of the nanoparticles is purely based on diffusion and therefore rather slow, reducing the probability of their infiltration into collagen. The more so because under these conditions the larger collagen fibrils visibly sediment to the bottom of the flask, whereas nanoparticles can be expected to remain homogeneously dispersed throughout the solution. This combined effect will strongly reduce the probability of mineralization. The second reason may be the size of the l-lys. Song *et al.*^[7] demonstrated that for 2 kDa pAA, interfibrillar hydroxyapatite (HAp) mineralization can be prevented, because these small polymers can enter the collagen fibril and suppress HAp mineralization. Given that the l-lys used is significantly smaller than 2 kDa, it can be assumed l-lys molecules can enter the collagen fibers and potentially prevent interfibrillar mineralization. Therefore, using a > 5 kDa poly l-lys in future work may circumvent this possibility.

Overall, by exposing collagen to ZnAc₂ at 37 °C with a starting pH of 6.4 or 8.0 or to LBZA, no interfibrillar collagen mineralization is observed. The use of additives in this procedure does show promise though. The presence of l-lys results in nanoparticle formation which may be ideal for collagen mineralization whereas the use of pAA may result in Zn²⁺ ion loading of the collagen fibrils.

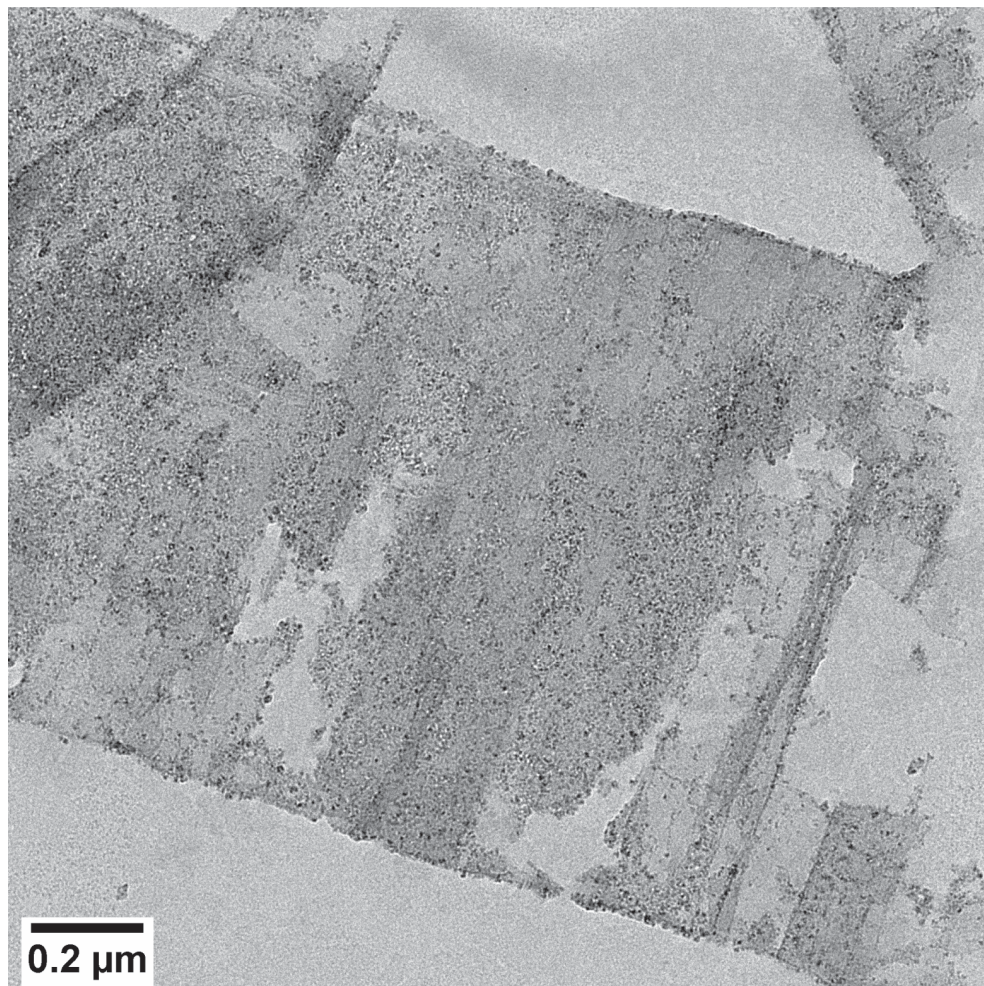


Figure 7.3 TEM image of a LBZA sheet composed of nanoparticles with clearly observable holes in the structure, after exposure to the initial stages (at 30 min) of a ZnO forming reaction at 80 °C which was subsequently matured for over 6 weeks at 37 °C in presence of 12 mM l-lys dried on a carbon support.

7.3. Discussion on Possible Future Work

As mentioned above the current procedures do have limitations that may prevent the interfibrillar mineralization of collagen. The first limitation is the synthesis of the ZnO. Ideally, a titration strategy based on the low temperature ZnO formation discussed in *Ch. 5* would be used. To minimize the amount of collagen used per experiment, relatively small reaction volumes (~ 2.5 mL) were used. However, this requires such a low titration rate of base of near 0.001 mL min^{-1} that cannot be reached with the current equipment. Moreover, at this time it is unclear if and how this decrease in reaction volume would affect this procedure, making it unclear if it can be directly applied to smaller volumes. Therefore, this strategy

could not be used in this current work. As an ideal setup for future work, we suggest the optimization of a low volume titration protocol as shown in *Fig. 7.4* equipped to a low rate titration set-up for the initial stages of the reaction.

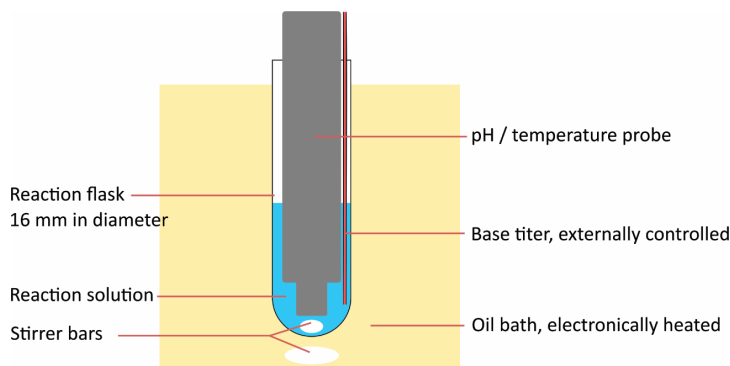


Figure 7.4 Proposed reaction setup for collagen mineralization with ZnO using a base-titration strategy.

Besides the base addition limitation during the initial reaction, a major disadvantage in the current procedure is the absence of shaking or stirring during maturing. This limits particle motion to diffusion, and it ensures that the collagen fibrils sediment to the bottom of the flask, minimizing exposure to zinc particles that may infiltrate and mineralize the collagen fibrils. The use of a water bath that allows for magnetic stirring or is equipped with a shaking option should solve this.

7.4. Conclusion

Exposure of collagen to zinc species for > 6 weeks at 37 °C did not adversely affect the collagen, but it did not result in clear evidence of collagen mineralization. In presence of pAA or in absence of additives, exposure of collagen to a ZnAc₂ solution predominantly resulted in the formation of small non-uniform LBZA particles in solution. TEM imaging did suggest that in the presence of pAA some zinc infiltration may have occurred into the collagen fibrils. If so, this did not result in the mineralization of the collagen fibers. Similar to the exposure of collagen to a ZnAc₂ solution, exposure of collagen to a LBZA dispersion under these conditions showed formation of some new small non-uniform LBZA particles. However, most of the initially present phase composed of large LBZA sheets and some ZnO crystals did not show any sign of evolution during this process.

Exposing collagen to ZnAc₂ or LBZA resulted in presence of l-lys in the formation of amorphous nanoparticles. Specifically, when starting from LBZA, the LBZA sheets seem to deconstruct into the nanoparticles, suggesting that nanoparticle formation is highly favorable. While collagen mineralization with HAP and iron oxides showed that a nanoparticle phase acts as a step towards collagen infiltration and mineralization, in this work this seems not to be the case. The most probable reason for this is a combination of the small size of l-lys, which allows this molecule to enter the collagen fibril pores, in combination with weaknesses in the current mineralization procedure. Hence, by using > 5 kDa poly l-lys combined with a more optimized mineralization procedure, zinc infiltrated and possibly mineralized collagen may be obtained.

7.5. Materials and Methods

7.5.1. Materials

Ammonia (28%, GPR reagent) was acquired from VWR, Zinc acetate dihydrate (ZnAc_2 , > 98%, ACS reagent) was acquired from Acros organics, Resorbable Collagen Tape (RCT, bovine Achilles tendon collagen) was acquired from ACE Surgical Supply Co., L-Lysine (L-Lys, > 98%, purum) was acquired from Fluka, 5.1 kDa (pAA, GPC) and 450 kDa poly acrylic acid (pAA) were acquired from Sigma-Aldrich. All chemicals were used as received unless stated otherwise.

7.5.2. Methods

7.5.2.1 Preparation of Stock Solutions

In all cases the stock solutions were prepared immediately before the final sample preparation.

To prepare a collagen stock dispersion, a ceramic mortar was cooled down to cryogenic temperatures by filling it with liquid nitrogen. Next a piece of resorbable collagen tape (RCT) hydrated with pure water and placed in the mortar filled with liquid nitrogen. Using a pestle, the RCT was crushed into a fine powder, collected and dried overnight under vacuum. The resulting RCT powder was vigorously redispersed into 15 mL pure water, 2 mg mL^{-1} via both sonication and magnetic stirring.

A ZnAc_2 stock solution was created by dissolving 50 mM ZnAc_2 in pure water followed by vigorous stirring.

A LBZA stock dispersion was synthesized by using a titration based ZnO synthesis protocol detailed in *Ch. 4*. Here, 50 mM ZnAc_2 was dissolved in 50 ml pure water in a 100 ml five-neck flask under reflux. The titration experiment was magnetically stirred (vortexing, 450 rpm). After 900 s, the reaction was initiated by gradually increasing the reaction temperature to 80 °C, using an oil bath. Starting 300 s after initiating heating ammonia was titrated into the solution at a constant rate of 0.02 mL min^{-1} . After 1800 s the reaction was terminated by collecting the reaction dispersion in a flask and submerging this flask in an ice bath for several minutes.

A L-lys and a pAA solution was created by dissolving 48 mM of, respectively, l-lys and pAA in 25 mL pure water. The pH of these solutions was subsequently set to 7.0 by adding acetic acid or ammonia solutions to lower or raise the pH.

7.5.2.1. Maturing the Collagen-zinc Dispersions

Collagen mineralization samples containing ZnAc_2 stock were prepared by mixing 1.250 mL of the collagen stock with 0.625 mL ZnAc_2 stock and either 0.625 mL l-lys stock, pAA stock or pure water in a borosilicate test tube, followed by vigorous stirring.

Collagen mineralization samples containing LBZA stock were prepared by mixing 1.250 mL of the collagen stock with 0.625 mL LBZA stock and either 0.625 mL l-lys stock, pAA stock or pure water in a borosilicate test tube, followed by vigorous stirring.

The test tubes containing either the ZnAc_2 or LBZA dispersions were placed in a custom-made stainless-steel flask holder, located in a Lauda Ecoline 019 water bath which was preheated to 37 °C. All samples were matured for > 6 weeks, after which the test tubes were removed from the water bath. Following this, using a pipet most of the liquid phase was removed from the reaction flasks and the sediment was dispersed in the remaining supernatant. TEM samples were prepared by placing 10 μl of the dispersion on a continuous carbon coated grids with gold supports that had been glow discharged for 40 s. Excess liquid was removed after 40 s by manual blotting from the side using a filter paper.

7.5.3. Analysis

pH measurements were conducted using a Metrohm unitrode pH probe connected to an 867 pH module.

Transmission Electron Microscopy (TEM) and selected area electron diffraction (SAED) images were collected on a Tecnai T20 (Thermo Fischer Scientific) operated at 200 kV, equipped with a 4096×4096 pixels CETA CMOS camera.

7.7. References

1. B. M. Oosterlaken, M. P. Vena and G. de With, In Vitro Mineralization of Collagen. *Adv. Mater.*, 2004418 (2021).
2. J. D. Currey, Materials Science - Hierarchies in Biomineral Structures. *Science* **309**, 253-254 (2005).
3. M. Goldberg, A. B. Kulkarni, M. Young and A. Boskey, Dentin: Structure, Composition and Mineralization. *Front Biosci (Elite Ed)* **3**, 711-735 (2011).
4. S. Weiner, W. Traub and H. D. Wagner, Lamellar Bone: Structure-function Relations. *J Struct Biol* **126**, 241-255 (1999).
5. F. Nudelman, A. J. Lausch, N. A. J. M. Sommerdijk and E. D. Sone, In Vitro Models of Collagen Biomineralization. *J Struct Biol* **183**, 258-269 (2013).
6. D. Toroian, J. E. Lim and P. A. Price, The Size Exclusion Characteristics of Type I Collagen - Implications for the Role of Noncollagenous Bone Constituents in Mineralization. *J Biol Chem* **282**, 22437-22447 (2007).
7. Q. Song, K. Jiao, L. Tonggu, L. G. Wang, S. L. Zhang, Y. D. Yang, L. Zhang, J. H. Bian, D. X. Hao, C. Y. Wang, Y. X. Ma, D. D. Arola, L. Breschi, J. H. Chen, F. R. Tay and L. N. Niu, Contribution of Biomimetic Collagen-ligand Interaction to Intrafibrillar Mineralization. *Sci Adv* **5**, eaav9075 (2019).
8. F. Nudelman, K. Pieterse, A. George, P. H. H. Bomans, H. Friedrich, L. J. Brylka, P. A. J. Hilbers, G. de With and N. A. J. M. Sommerdijk, The Role of Collagen in Bone Apatite Formation in the Presence of Hydroxyapatite Nucleation Inhibitors. *Nat Mater* **9**, 1004-1009 (2010).
9. C. Y. Shao, R. B. Zhao, S. Q. Jiang, S. S. Yao, Z. F. Wu, B. Jin, Y. L. Yang, H. H. Pan and R. K. Tang, Citrate Improves Collagen Mineralization via Interface Wetting: A Physicochemical Understanding of Biomineralization Control. *Adv Mater* **30**, 1704876 (2018).
10. Y. P. Qi, Z. Ye, A. Fok, B. N. Holmes, M. Espanol, M. P. Ginebra and C. Aparicio, Effects of Molecular Weight and Concentration of Poly(Acrylic Acid) on Biomimetic Mineralization of Collagen. *ACS Biomater Sci Eng* **4**, 2758-2766 (2018).
11. L. N. Niu, S. E. Jee, K. Jiao, L. Tonggu, M. Li, L. Wang, Y. D. Yang, J. H. Bian, L. Breschi, S. S. Jang, J. H. Chen, D. H. Pashley and F. R. Tay, Collagen Intrafibrillar Mineralization as a Result of the Balance between Osmotic Equilibrium and Electroneutrality. *Nat Mater* **16**, 370-378 (2017).
12. D. Kim, B. Lee, S. Thomopoulos and Y. S. Jun, The Role of Confined Collagen Geometry in Decreasing Nucleation Energy Barriers to Intrafibrillar Mineralization. *Nat Commun* **9**, 962 (2018).
13. H. Ping, H. Xie, Y. M. Wan, Z. X. Zhang, J. Zhang, M. Y. Xiang, J. J. Xie, H. Wang, W. M. Wang and Z. Y. Fu, Confinement Controlled Mineralization of Calcium Carbonate within Collagen Fibrils. *J Mater Chem B* **4**, 880-886 (2016).
14. B. Zhou, L. N. Niu, W. Shi, W. Zhang, D. D. Arola, L. Breschi, J. Mao, J. H. Chen, D. H. Pashley and F. R. Tay, Adopting the Principles of Collagen Biomineralization for Intrafibrillar Infiltration of Yttria-Stabilized Zirconia into Three-Dimensional Collagen Scaffolds. *Adv Funct Mater* **24**, 1895-1903 (2014).
15. Y. Xu, F. Nudelman, E. D. Eren, M. J. M. Wirix, B. Cantaert, W. H. Nijhuis, D. Hermida-Merino, G. Portale, P. H. H. Bomans, C. Ottmann, H. Friedrich, W. Bras, A. Akiva, J. P. R. O. Orgel, F. C. Meldrum and N. Sommerdijk, Intermolecular Channels Direct Crystal Orientation in Mineralized Collagen. *Nat Commun* **11**, 5068 (2020).
16. B. R. Williams, R. A. Gelman, D. C. Poppke and K. A. Piez, Collagen Fibril Formation - Optimal Invitro Conditions and Preliminary Kinetic Results. *J Biol Chem* **253**, 6578-6585 (1978).
17. Y. Sun, W. L. Chen, S. J. Lin, S. H. Jee, Y. F. Chen, L. C. Lin, P. T. C. So and C. Y. Dong, Investigating Mechanisms of Collagen Thermal Denaturation by High Resolution Second-harmonic Generation Imaging. *Biophys* **91**, 2620-2625 (2006).
18. D. Bhatia, H. Sharma, R. S. Meena and V. R. Palkar, A Novel ZnO Piezoelectric Microcantilever Energy Scavenger: Fabrication and Characterization. *Sens Biosensing Res* **9**, 45-52 (2016).
19. E. S. Nour, O. Nur and M. Willander, Zinc Oxide Piezoelectric Nano-generators for Low Frequency Applications. *Semicond Sci Tech* **32**, 064005 (2017).
20. C. B. Ong, L. Y. Ng and A. W. Mohammad, A Review of ZnO Nanoparticles as Solar Photocatalysts: Synthesis, Mechanisms and Applications. *Renew Sust Energ Rev* **81**, 536-551 (2018).
21. Z. Mirzaeifard, Z. Shariatinia, M. Jourshabani and S. M. R. Darvishi, ZnO Photocatalyst Revisited: Effective Photocatalytic Degradation of Emerging Contaminants Using S-Doped ZnO Nanoparticles under Visible Light Radiation. *Ind Eng Chem Res* **59**, 15894-15911 (2020).
22. M. Alavi and A. Nokhodchi, An Overview on Antimicrobial and Wound Healing Properties of ZnO Nanobiofilms, Hydrogels, and Bionanocomposites based on Cellulose, Chitosan, and Alginate Polymers. *Carbohydr* **227**, 115349 (2020).
23. M. M. J. van Rijt, B. M. Oosterlaken, R. R. M. Joosten, L. E. A. Wijkhuijs, P. H. H. Bomans, H. Friedrich and G. de With, Counter-ion Influence on the Mechanism of HMTA-mediated ZnO Formation. *CrystEngComm* **22**, 5854-5861 (2020).

Chapter 8

Epilogue: Connecting ZnO to Organic Templates

"He was going to live forever, or die in the attempt."
Joseph Heller, *Catch-22*, **1961**.

Mineralization of organic templates is a complex and difficult process. Apart from the results obtained as described in this thesis, several other studies were conducted that ultimately did not make it into this booklet, including mineralization of liquid crystals networks, track-etched membranes and collagen with zinc oxide (ZnO) using more traditional HMTA based ZnO formation strategies at > 80 °C. The results obtained generally showed a loss in materials performance of the organic templates. For example, attempts to mineralize 6OBA liquid crystals resulted in a general loss of the alignment of the liquid crystal network, without resulting in successful mineralization of the pores^[1, 2], mineralization of light actuating azobenzene-doped liquid crystal networks resulted in a loss of actuation due to exposure to elevated temperatures^[3] and, after performing a ZnO mineralization protocol at 80 °C on crosslinked collagen, only a single partially disassembled collagen fiber was observed during TEM analysis. These studies demonstrate the great need for mild, low-temperature conditions for successful mineralization of organic templates. Therefore, the research described in this thesis focuses on the efforts necessary to mineralize ZnO at mild low temperature condition. To obtain the necessary tools for ZnO mineralization, in this thesis three different approaches have been explored.

8.1. Direct Ion-Exchange of Minerals

The first part of this thesis describes the investigation into the formation of ZnO from hydroxyapatite (HAp) crystals via an ion-exchange procedure. The first and crucial step, the exchange of the Ca^{2+} ions with Zn^{2+} ions into Zn-HAp, is investigated in **Chapter 2**. This work shows that close to 20 mol% of Zn^{2+} ions can be incorporated into Zn-HAp within 10 s of exposure time, while preserving both crystallinity and crystal shape. Optimization of reaction conditions, however, only yielded a minimal increase in Zn^{2+} ion incorporation at best, and in certain cases even full dissolution and reprecipitation of the HAp crystals into hopeite. The most probable explanation for this is the limited stability of Zn-HAp, which is too soluble under aqueous conditions in absence of additional stabilizers.

This does not mean that the crystal formation via ion-exchange is without promise. Essentially, this work highlights that apatites are not an ideal starting material for an ion-exchange strategy. The main problem with apatites is their relatively high lattice energy, which limits the number of viable exchange pathways. This characteristic, combined with those of intermediates like Zn-HAp that has a limited stability, creates a large amount of challenges. Future work should focus on the exchange of crystals with a lower lattice energy, like carbonates as starting material, which probably has major advantages. The relative ease with which ions in these materials can be exchanged with other ions should mean that they can be rapidly and easily converted into other crystalline species. In this case, all ion-exchange accessible crystals could be obtained in a complex shape or mineralized into a complex template, after the initial crystal can be synthesized in the shape or location of interest.

8.2. Understanding and Controlling Aqueous Zinc Oxide Formation

In the second part, this thesis describes our efforts aimed at understanding and controlling the formation of ZnO under aqueous conditions. **Chapter 3** details a study into the mechanism of HMTA-based ZnO formation, using a constant reaction protocol but with varying zinc salts. This study demonstrates that, independent of the selected zinc counterion, a layered zinc hydroxy salt (LZHS) can be formed. This transient phase has a fundamental influence on the final product. In the case of zinc nitrate, the LZHS has a relative high barrier of formation, resulting in ZnO formation on reaction interface surfaces. Using zinc acetate under typical conditions or zinc nitrate with an extended incubation time, allows for the LZHS to act as a ZnO nucleation template, resulting in dispersed ZnO crystals. The transition from LZHS to ZnO

corresponds with a spontaneous decrease in pH. This allows for *in-situ* pH measurements to track the reaction progress. Finally, LZHS species, such as those formed from zinc chloride and zinc sulphate, are found to be too stable, thus, preventing the transition to ZnO. This shows that the reaction chemistry is an important factor in the formation process of ZnO. The use of HMTA, however, prevents full control over the reaction chemistry by moderating the base release.

To remove this limitation, a base titration strategy for the formation of ZnO is introduced in **Chapter 4**. Above a reaction pH of 5.5, the use of this titration strategy resulted in the formation of ZnO independent of the type of added base and the base addition rate, while the pH transition proved to be very similar to the pH transition when using HMTA. Although ZnO was formed under all conditions, highly faceted twin-pillar ZnO crystals were mainly observed when large amounts of ammonia were added. This makes it arguable that ammonia, and not HMTA, directs the formation of ZnO. Moreover, the direct addition of base further allowed for a doubling the reaction yield.

For the mineralization of organic templates, mild reaction conditions are required to prevent damage to the template. Whereas the formation process of ZnO in Chapters 3 and 4 uses a mild reaction pH, the reaction temperature close to 80 °C, is incompatible with many organic materials. Therefore, efforts to probe the influence of a lower reaction temperature on the titration protocol introduced in Chapter 4 are described in **Chapter 5**. The results show that, with a reaction temperature as low as 40 °C, ZnO can indeed be formed. With decreasing reaction temperature, a LZHS phase is more dominantly observed. The presence of l-lysine (l-lys) promotes the formation of ZnO and allows for the continued transition of LZHS to ZnO at RT after ending the reaction. By decreasing the initial zinc acetate concentration, the formation of ZnO becomes more favorable at 50 °C, but the side effect of this is the formation of wülfingite zinc hydroxide (ZnOH₂). At 40 °C ZnOH₂ phase becomes the dominant phase.

These observations demonstrate that, by using a mild reaction pH to form ZnO in dispersion, a LZHS transient phase is formed under various reaction conditions, with pH measurements being able to detect this phase transition. The ZnO formation process proved to be rather sensitive to reaction conditions. The exact reaction composition, including the type of zinc counterion, the selected base and the addition pathway of the base, can influence the shape and size of the ZnO crystals dramatically and in some cases prevent the formation of ZnO completely. Using a controlled titration setup, this sensitivity can be turned into an advantage so that greater control over the formation process and the final product can be obtained. However, at lower reaction temperatures this sensitivity can affect reproducibility.

Given the immense flexibility of the titration-controlled base addition route, this strategy has potential for general applicability in crystal formation, for ZnO and other minerals. The exact control over base addition does not only allow for having the exact reaction solution composition and pH, it also, for example, relieves the need of refreshing steps of the reaction mixture which is used in the formation of ZnO growth on surfaces. This can make this strategy a relevant alternative to traditional HMTA strategies.

The main limitation of the current approach lies in the inability to form high purity ZnO at low temperatures and the reproducibility at lower reaction temperature. Based on the results presented in this work, it is unlikely that a simple decrease in reaction temperature at a mild pH will result in reliable ZnO formation within a reasonable reaction time. Future work should, therefore, focus on expanding the use of additives for low temperature ZnO formation. Given the promising results obtained using l-lys, its use and the use of similar additives should be expanded upon.

8.3. Hierarchical Organic Mineralization Templates and Templated Mineralization

The third and final part of this thesis discusses the development and mineralization of hierarchical organic templates with ZnO. In **Chapter 6** a self-assembling [ALV]_x-b-[KGE]_y block copolypeptide system is

developed and studied. By balancing the relative hydrophilic and hydrophobic domain lengths, assembly into thermodynamically stable peptide nanotubes with constant chain length results. Besides showing great uniformity, these peptide nanotubes are stable in a wide pH range of 2 - 12 and are stable at a temperature as high as 80 °C. This stability combined with the zwitterionic nature of the peptide nanotubes allows their hierarchical self-assembly into peptide fibers at mild pH, which makes this a material of interest as an organic mineralization template.

For the mineralization of organic templates with ZnO, collagen is investigated as a model system in **Chapter 7**. Exposing collagen to zinc salt or a pre-formed LZHS phase does not result in mineralization of the collagen fibers, both in absence and presence of charged additives. Exposure to these zinc species showed no adverse effect on the collagen fibers and in the presence of poly acrylic acid (pAA) some loading of the collagen fibers with Zn²⁺ ions may have occurred. Especially promising are the results obtained in the presence of l-lys, which mediates the formation of nanoparticles when starting from a zinc salt and which seemed to deconstruct the original LZHS phase in zinc nanoparticles as well.

To obtain ZnO mineralization of hierarchical templates, the organic template is currently not the limiting factor. Indeed, besides the existing biological templates, stable yet controllable peptide-based templates can be synthesized. The current limiting factor is the ZnO mineralization strategy. In part this is due to the current limitations posed by the available synthesis strategies as discussed in Chapter 5 and section 8.2., which should be further developed before continuing efforts on the mineralization of organic templates with ZnO.

Besides this, the implementation of these mineralization strategies needs to be revisited as well. The absence of stirring or shaking during the current maturing step means that infiltration is mainly dependent on diffusion which can be rather slow. Moreover, the resulting sedimentation of collagen creates a macroscopically heterogeneous system, which further complicates collagen infiltration. The presence of l-lys seems to stabilize the zinc phases into nanoparticles, which may be ideal carriers for collagen infiltration. The exact underlying process does remain unclear and might warrant further studies. In spite of these promising results, l-lys may infiltrate the collagen fibrils and prevent interfibrillar mineralization. Therefore, by using a sufficiently large poly l-lys (> 5 kDa), the advantages of l-lys may be maintained without impairing the mineralization process. Thus, implementing these changes in combination with a more effective ZnO formation strategy at low reaction temperature is likely to yield mineralization of collagen and other organic templates with zinc species, perhaps with ZnO as well.

8.4. References

1. B. M. Oosterlaken, Y. F. Xu, M. M. J. van Rijt, M. P. da Cunha, G. H. Timmermans, M. G. Debije, H. Friedrich, A. P. H. J. Schenning and N. A. J. M. Sommerdijk, Nanohybrid Materials with Tunable Birefringence via Cation Exchange in Polymer Films. *Adv Funct Mater* **30**, 1907456 (2020).
2. Y. F. Xu, H. P. C. van Kuringen, D. J. Mulder, A. P. H. J. Schenning and N. A. J. M. Sommerdijk, Smectic Liquid Crystal Polymers as a Template for Ultrathin CaCO₃ Nanolayers. *RSC Adv* **6**, 13953-13956 (2016).
3. M. P. da Cunha, Y. Foelen, R. J. H. van Raak, J. N. Murphy, T. A. P. Engels, M. G. Debije and A. P. H. J. Schenning, An Untethered Magnetic- and Light-Responsive Rotary Gripper: Shedding Light on Photoresponsive Liquid Crystal Actuators. *Adv Opt Mater* **7**, (2019).

List of Publications

M. M. J. van Rijt†, S. W. Nooteboom†, A. van der Weijden, W. L. Noorduin and G. de With, Stability-limited Ion-exchange of Calcium with Zinc in Biomimetic Hydroxyapatite, *Materials & Design*, 2021, *under peer review*.

B. M. Oosterlaken, M. M. J. van Rijt, R. R. M. Joosten, H. Friedrich and G. de With, Time-resolved cryo-TEM study on the formation of iron hydroxides in a collagen matrix, *ACS Biomaterials Science & Engineering*, 2021, *under peer review*.

M. M. J. van Rijt, B. M. Oosterlaken, H. Friedrich and G. de With, Controlled Titration-based ZnO Formation, *CrystEngComm*, 2021, DOI: 10.1039/d1ce00222h.

M.-A. Moradi†, D. Eren†, M. Chiappini, S. Rzakiewicz, M. Goudzwaard, M. M. J. van Rijt, A. D. A. Keizer, A. F. Routh, M. Dijkstra, G. de With, N. A. J. M. Sommerdijk, H. Friedrich, and J. P. Patterson, Spontaneous organization of supracolloids into three-dimensional structured materials, *Nature Materials*, 2021, **20**, 541-547.

M. M. J. van Rijt, B. M. Oosterlaken, R. R. M. Joosten, L. E. A. Wijkhuijs, P. H. H. Bomans, H. Friedrich and G. de With, Counter-ion influence on the mechanism of HMTA-mediated ZnO formation, *CrystEngComm*, 2020, **22**, 5854-5861.

E. A. Egorova, M. M. J. van Rijt, N. A. J. M. Sommerdijk, G. S. Gooris, J. A. Bouwstra, A. L. Boyle and A. Kros, One Peptide for Them All: Gold Nanoparticles of Different Sizes Are Stabilized by a Common Peptide Amphiphile, *ACS Nano*, 2020, **14**, 5874-5886.

B. M. Oosterlaken, Y. F. Xu, M. M. J. van Rijt, M. P. da Cunha, G. H. Timmermans, M. G. Debije, H. Friedrich, A. P. H. J. Schenning and N. A. J. M. Sommerdijk, Nanohybrid Materials with Tunable Birefringence via Cation Exchange in Polymer Films, *Advanced Functional Materials*, 2020, **30**, 1907456.

M. M. J. van Rijt, A. Ciaffoni, A. Ianiro, M.-A. Moradi, A. L. Boyle, A. Kros, H. Friedrich, N. A. J. M. Sommerdijk and J. P. Patterson, Designing stable, hierarchical peptide fibers from block co-polypeptide sequences, *Chemical Science*, 2019, **10**, 9001-9008.

A. Ianiro†, H. Wu†, M. M. J. van Rijt, M. P. Vena, A. D. A. Keizer, A. C. C. Esteves, R. Tuinier, H. Friedrich, N. A. J. M. Sommerdijk and J. P. Patterson, Liquid-liquid phase separation during amphiphilic self-assembly, *Nature Chemistry*, 2019, **11**, 320-328.

A. Ianiro, J. Patterson, Á. González García, M. M. J. van Rijt, M. M. R. M. Hendrix, N. A. J. M. Sommerdijk, I. K. Voets, A. C. C. Esteves and R. Tuinier, A roadmap for poly(ethylene oxide)-block-poly- ϵ -caprolactone self-assembly in water: Prediction, synthesis, and characterization, *Journal of Polymer Science Part B: Polymer Physics*, 2018, **56**, 330-339.

† Authors contributed equally.

Curriculum Vitae



Mark van Rijt was born on November the 3rd 1991 in Eindhoven, the Netherlands. After completing his secondary education in 2010 at the Peellandcollege in Deurne he moved to Fontys University of Applied Science where he obtained his bachelor's degree (BAsc) in 2014. During this study he performed two internships. One 7 months internship at TNO, in Eindhoven, working on Lower Critical Solution Temperature Hydrogels (2012) and a second 7.5 months internship at the research group of prof. Steven P. Armes at the University of Sheffield working on Well-defined Organic Vesicular Templates for Hybrid Core-shell Nanoparticles (2014). In 2017 Mark obtained his master's degree (MSc) at Eindhoven

University of Technology (TU/e), *met grote waardering*, writing his thesis in the laboratory of Materials and Interface Chemistry under supervision of prof. Nico A. J. M. Sommerdijk and dr. Joe P. Patterson on the Self-Assembly of Defined Block Copolypeptides. Following this he obtained a PhD position at the TU/e Laboratory of Physical Chemistry under supervision of prof. Gijsbertus de With and dr. Heiner Friedrich on the NWO "Bi-Hy" research grant. During his PhD he worked towards the mineralization of organic templates with zinc oxide.

Acknowledgements

It has been a long journey and yet, when I look back, I do not think about all the projects and the time I spend on them, but I think about all the people I had the privilege to work and spend time with.

First off, I would like to thank my first promotor **Bert de With** and my copromotor **Heiner Friedrich**. Bert, thank you so much for the last couple of years. I know doing science is like a hobby for you, which might make coming out of retirement not the worst thing for you personally, but without all our fruitful and pleasant discussions this thesis would have been a shell of what it is now. Heiner, I'll never forget our first project meeting when you asked me what the project should be about. Looking back, it is amazing that almost all the big ideas we came up with in the following months ended up in this thesis one way or another. Besides the scientific discussion I want to thank you for all chats about life and the universe at the F.O.R.T and all the Thursday "BEERS" calls.

I would also like to thank **Nico Sommerdijk** for accepting me on the "Bi-Hy" project and for the two very good years I had at SMG, **Remco Tuinier** for welcoming me to SPC and **NWO** for funding the project. On a special note, I would like to thank **Emiel Hensen**, **Kitty Nijmeijer** and **Laurent Nelissen** for everything they did for me and the rest of SMG.

The goal of any PhD project is to defend it at the end. Therefore, I would like to thank **Kitty Nijmeijer** chairing my committee. I'm also very grateful to all my committee members **Emiel Hensen**, **Lara Estroff**, **Jeffrey Rimer**, **Thomas Weber** and **Wim Noorduyn** for finding the time to join my defense committee, reading my thesis and, in advance, for the challenging discussion during my defense.

A lot of the work presented in this thesis was only possible thanks to a lot of great colleagues and collaborators to whom I want to express my gratitude and without whom my PhD project would have been way less fun. I would like to start by thanking **Imanda** and **Pleunie** for always arranging everything, often before I knew something had to be done. **Ingeborg**, thank you for all the help on the lab and always making time when there was a problem. **Rick** and **Paul** (prof. Bomans!) thank you for teaching me all the ins and outs of the Sphera and the Titan, and especially for being available at all the weird times when the Titan decided to go on strike. **Anne** and **Pauline**, thank you for all the nice chats and the brainstorms ranging from staining samples to optimizing the FTIR.

Chapter 2 was only possible thanks to the collaboration with AMOLF. My thanks go to **Wim Noorduyn** for making this possible. Wim, I'm still amazed at the stories you told during the GRC on biomineralization, even if only half of it would be true. My thanks also go to **Arno van der Weijden** for all his experimental help, suggestions and for continuing until after regular hours so we could process all the samples during my visits. The "not so spicey" Indian food we ordered the last time was particularly memorable.

Chapter 6 was only possible thanks to the collaboration with the group of **Alexander Kros** at Leiden University. Alexander, thank you for your continued support and suggestions on this project over the last years. I would like to thank **Adriano Ciaffoni** and **Denis Aschmann** for synthesizing the peptides and **Aimee Boyle** for all her help in analyzing and processing the data. I would further like to thank **Joe Patterson** for his suggestions and insights on this work and **Alessandro Ianiro** for all his "scattering" help.

Over the last years I had the privilege of supervising four students. **Leon**, **Rob**, **Lisette** and **Sjoerd**, thank you all for your hard work, your trust in me and of course for putting up with my supervision.

Leon, our work on the actuating ZnO films confirmed the need for much of the other work in this thesis. **Rob**, our work inspired parts of chapter 3 and 7. **Lisette**, our work led to chapter 5, but thanks to your enthusiasm you influenced many more parts of this thesis. **Sjoerd**, our work resulted in Chapter 2. It ended up a bit different than we hoped at the start, but that just means we learned a lot more from it.

Over the years I've had quite a few officemates: **Xufeng**, **Artur**, **Mohammad S** (I still feel bad for the time I locked you up in the office, and for all the following times I did it again...), **Rob** (Postdoc Rob), **Michiel**, **Remco** (I do miss our endless complaining rants about everything) and "super" **Machi**. Thank you all for the good times in the office!

Yifei, thank you for your help in getting the project started and our many interesting, though sometimes intense, discussions. **Hanglong**, thank you for your endless positivity and your infinite willingness to help. **Jeroen**, we have known each other since the beginning of our bachelors and somehow, we keep ending up on each other's paths. I just want you to know that, if I see a copy of this thesis ending somewhere it shouldn't be, I know it was you! **Simon**, thank you for all the walks and talks. It is a pity that we couldn't chat as often during the last year. **Laura**, when I have a crazy idea most people try to talk me out of it, as they should, instead of actually going along with it or suggesting something even crazier, thank you for the great times. Take care of my Tomolab! **Deniz** and **Mohammad M**, always when you two were quietly discussing work in the corridors and Mohammad was wearing his beanie, I heard the gangsta's paradise song in my mind. Thank you both for all the nice meaningful chats and for the great times working together on projects. **Marina**, at the start of our PhD's we had all these ambitious ideas for collaborations and, of course, despite all the time we spend on it, none of it did work. The nice thing about all of this is that I got a good friend in return. Thank you for everything and I'll see you for the next run around the park!

The next two colleagues I would like to thank, my two paranymphs, were there for me during the good and the bad times of this PhD. **Paula**, you were the first person I saw the moment I finished my master thesis and over the following years we have only become better friends. I could always trust on you doing unpredictable things at the right moment and talk to you about anything. **Bernette**, a bit over four years ago we started on the same project only weeks apart. Since then I had someone at work who was always there for me; be it as the person reminding me about meetings, the person joining me for conferences, the person distracting me for hours when we actually should have worked or the person who was always there when I needed a friendly face. I can't imagine how the last four years would have been without either of you!

There are many more **current and previous colleagues at SMG, SPC and TU/e** that all deserve my gratitude. I know it has been a custom to mention everyone's name, but I'm too afraid that I'll miss one or two of you. Thank you all for the great atmosphere, the fun at coffee breaks, borrels, group trips and random work-avoiding chats. I wish you all the best!

Er zijn natuurlijk veel mensen die ik al lang kende voordat ik aan dit PhD avontuur begon. Ik wil mijn **familie en vrienden** bedanken voor al jullie gezelligheid, interesse en steun over de laatste jaren. Zeker de epische discussies tijdens feestjes over helemaal niets waren altijd een goede afleiding, ik hoop dat we dat snel weer mogen oppakken. **Pa en Ma**, tot slot wil ik jullie bedanken voor jullie steun en begrip tijdens al die jaren "school", dank jullie wel voor alles.

